Deposition and Characterisation of SnS Thin Films for Application in Photovoltaic Solar Cell Devices

PATRICK AKATA NWOFE

Ph.D

2013

Deposition and Characterisation of SnS Thin Films for Application in Photovoltaic Solar Cell Devices

PATRICK AKATA NWOFE

A thesis submitted in partial fulfilment
of the requirements of the
University of Northumbria at Newcastle
for the degree of
Doctor of Philosophy

Research undertaken in the
School of Computing, Engineering and Information Sciences

October 2013

Abstract

Thin films of SnS have been deposited onto heated glass substrates using the thermal evaporation method and the chemical and physical properties of the layers determined and correlated to the deposition conditions and to post-deposition heat treatments. In particular scanning electron microscopy, energy dispersive X-ray analysis, X-ray diffractrometry and Raman studies were used to determine the material properties, transmittance and reflectance spectroscopy to determine the optical constants and 4-probe and van der Pauw measurements to determine the electrical properties. The results indicate that for a wide range of deposition conditions it is possible to produce high quality layers of SnS that are free from pin-holes and cracks, that are made of densely packed grains, and that adhere strongly to the substrate. For substrate temperatures between 280 °C to 360 °C it is possible to produce single phase SnS layers. The energy bandgap of these layers was in the range 1.3 eV to 1.35 eV, was direct, and had an optical absorption coefficient $\alpha > 10^5 \mathrm{cm}^{-1}$ for photons with energies greater than the energy bandgap. The electrical properties indicate that all the layers are p-conductivity type with resistivities in the range 40 Ω cm to 100 Ω cm. Solar cell devices were fabricated in the superstrate and substrate configurations using n-type cadmium sulphide (CdS) and zinc indium diselenide (ZIS) buffer layers to partner the p-type SnS. The devices were investigated by measuring the I-V characteristics in the dark, to determine the predominant conduction mechanisms, the I-V characteristics under illumination to determine the open-circuit voltage V_{oc}, the short circuit current density J_{sc}, the fill factor FF and solar conversion efficiency of the devices, C-V studies to determine the doping profile in the SnS and the built-in voltage at the junction and spectral response measurements to determine the minority carrier diffusion length in the p-SnS. Devices made with CdS as the n-type partner had a high density of interface states ($1.36 \times 10^{11} FC^{-1} cm^{-2}$) with low photovoltaic parameters and a negative

band offset of $-0.36\,\mathrm{eV}$ obtained (as measured using x-ray photoelectron spectroscopy). The best devices made were substrate configuration solar cells in which the back contact on glass was molybdenum and the buffer layer was ZIS. These devices have $V_{oc} = 472$ mV, $J_{sc} = 16.1$ mA/cm^2, FF $= 0.38$ and a solar conversion efficiency of 2.9%. This is a world record efficiency for SnS-based solar cells at the time of submission of this PhD thesis.

List of Contents

List of Figures

List of Tables

Acknowledgements

I would like to thank my supervisory team immensely for their roles throughout the journey. In particular my principal supervisor, Professor R. W. Miles on his great mentorship and guidance over the years. Dr J. K. Tan and Dr I. Forbes have also made great contributions.

I would like to express my indebtedness to Northumbria University for sponsorship of the PhD programme, and Ebonyi State University, Abakaliki for support through Education Trust Fund (ETF), Nigeria. I strongly acknowledge the contributions of Professor K.T. Ramakrishna Reddy and Professor N. Pearsall. To Dr G. Zoppi, Dr N. Beattie, Dr D. Johnston, Bob Best and Ogah E. Ogah, I say a big thank you for your help.

I also thank my wife, children and parents for their understanding, support and prayers.

Finally, I thank God Almighty, who made all things possible.

Author's Declaration

I declare that the work contained in this thesis has not been submitted for any other award and that it is all my own work. I also confirm that this work fully acknowledges opinions, ideas and contributions from the work of others.

The research presented in this thesis did not contravene any of the ethics considerations given by the University Ethics Committee and it was therefore appropriate to enter not applicable on the forms.

Name: Patrick Akata Nwofe

Signature: .....

Date: October 2013

Chapter 1

Introduction

The photovoltaic effect is the direct conversion of sunlight into electricity using either an electrochemical junction or a p-n (or p–i-n) junction made using semiconductor materials. The photovoltaic effect was first discovered by Becquerel in 1839 when he found that if he illuminated platinum electrodes immersed in a solution of dilute sulphuric acid a voltage was produced [1]. The first solid state solar cell was later made by Adams and Day in 1877, a diode device based on the use of the chemical element, selenium [2]. It was not however until 1954 that a practical solar cell was produced at Bell Telephone Laboratories by Chapin et al. [3]. They made a p-n junction device by diffusing boron impurities into a n-conductivity type silicon wafer cut from a Czochralski grown boule and found they could produce devices with an efficiency of 6%. The first applications of the solar cells were to provide power in remote locations for communications systems and later weather monitoring systems. Also in the 1950's and 1960's, it was realised that solar cells had excellent potential for use to power satellites and space vehicles [4–6]. The stagflation caused by the 1970 energy crisis triggered serious consideration of using solar cells for terrestrial applications. Since then, the technology as noted has continued to permeate to a different range of applications such as supplying power for consumer products such as electronic calculators, clocks and toys and for providing power in remote locations both, in the developed and developing world [6, 7]. In the past decade photovoltaics has become a major contender for producing power on a large scale, either in centralised power stations or integrated into buildings (BIPV, "building integrated photovoltaics") [6–9]. It should be noted that in the late 1954 Reynolds et al. produced a cuprous sulphide/cadmium

sulphide heterojunction solar cell, also with an efficiency of 6% [10]. This work stimulated interest in developing thin film solar cell devices as it was realised that solar cells could be produced much more cheaply using the thin film approach rather than making bulk silicon devices [10].

1.1 Silicon Solar Cells

Silicon is a group IV element. It is an indirect bandgap material with an energy bandgap of about 1.1 eV. Solar cell technology is still largely dominated by cells based on the use of monocrystalline and multicrystalline silicon, the former material produced using the Czochralski method and the latter material produced using a block casting method. These account for 38% and 46% of modules sold respectively [11]. However both monocrystalline and multicrystalline silicon have an indirect energy bandgap resulting in low optical absorption coefficient $\alpha \approx 100\,cm^{-1}$, such that a large thickness of silicon (typically 100–200 μm) is needed to absorb most of the incident solar radiation [6, 12, 13]. Owing to the long absorption length, a long minority carrier diffusion length is always required so that carriers generated deep within the silicon can diffuse to the junction, without encountering too much in the way of recombination losses. This entails that the silicon should be of high material purity and for the densities of crystal defects to be minimal. Achieving both these objectives adds processing steps and hence cost. Silicon solar cells are hence expensive because of high material and processing costs. Monocrystalline silicon (c-Si) solar cells are mostly fabricated with an initial step of growing the silicon wafers by the Czochralski method and subsequent conversion of the wafers to p–type or n–type using appropriate doping materials. A p–n junction is then formed by diffusing-in impurities of the opposite doping type. Electrical contacts are then applied by either screen printing or sputtering to complete the device. A number of designs are commonly used and these include "buried contact solar cells", often referred to as "UNSW" solar cells [14], "passivated emitter rear locally diffused" (PERL) solar cells [15] and passivated rear emitter floating junction (PERF) solar cells [16]. Efficiencies $> 24\%$ have been achieved for monocrystalline solar cells [17, 18]. For making multicrystalline silicon (mc-Si) solar cells, silicon is melted and then poured into cubic moulds. This results in ingots consisting of large randomly

oriented grains, a few mm in diameter. Although cells made using mc-silicon are not as efficient as those made using c-Si, the fabrication method leads to a substantial reduction in capital costs and other variables, compared to cells made from monocrystalline silicon. Both monocrystalline and multicrystalline silicon solar cells are single-junction devices with efficiencies limited by thermodynamic considerations. According to Shockley and Quiesser, the maximum theoretical solar conversion efficiency is approximately 31% [19]. Single crystalline and multicrystalline solar cells constitute what are now referred to as first generation solar cells. The production costs associated with cutting the crystalline and multicrystalline silicon ingot into wafers can be lowered by employing the "ribbon fed growth methods" [20], but the resulting device and module efficiencies are much lower than those achieved using conventional c-Si and mc-Si solar cells. Recently Sanyo have demonstrated high efficiency by using a radially new design, the HIT (Heterojunction with Intrinsic Thin layer) cell [21]. This device hybridizes conventional Si-technology with amorphous silicon technologies.

1.2 III-V Solar Cells

The most exploited III-V materials used to make solar cells are gallium arsenide (GaAs), indium phosphide (InP) and gallium antimonide (GaSb). GaAs/$CuInSe_2$ and InGaP/GaAs/Ge have also been used to make multijunction devices. The latter devices consist of different energy bandgap cells stacked one on top of the other with the wider energy bandgap cell facing the sunlight. This arrangement more effectively absorbs the solar radiation than a single junction cell, minimising thermalisation losses, such that the devices can exceed the Shockley-Queisser limit. In fact the most efficient solar cell produced to date is a III-V multijunction device with an efficiency $> 44\%$ [22]. The III-V cells are used as space cells due to their high conversion efficiencies, high power/weight ratio and improved radiation resistance [12]. However, the constituent elements gallium and indium are known to be rare and expensive and these materials are difficult to produce, keeping device costs very high.

1.3 Thin Film Solar Cells

In order to reduce production costs thin film solar cells have been developed. Such devices are fabricated by the deposition of thin films of materials unto cheap substrates or superstrates. Generally, thin film solar cells use direct energy bandgap materials such as hydrogenated amorphous silicon (αSi:H), cadmium telluride (CdTe) or copper indium gallium diselenide (CIGS). These materials have energy bandgaps near the optimum for solar energy conversion and very high optical absorption coefficients such that only few microns of material are needed to absorb most of the incident light, minimising material and production costs. Also because the light is absorbed within or near to the junction region, a long minority carrier diffusion length is not required, relaxing the need for high purity and crystallinity and hence reducing processing costs. Thin film solar cells also lend themselves to large scale, low cost production, resulting in shorter energy payback times (1 year compared to 3-4 years for silicon [7]). The first commercially produced thin film solar cells developed were based on the use of amorphous silicon. These are made using the plasma enhanced chemical vapour deposition (PECVD) method using gases containing silane (SiH_4) [23]. Despite being able to produce single junction cells with initial efficiencies $> 10\%$, it has consistently been found that the efficiency degrades in illuminated cells, over a period of months, to an efficiency $< 5\%$ due to the so-called "Stäbler-Wronski effect" [24]. The stability and efficiency are improved by the development of double junction, triple junction and micro-morph devices with the best efficiencies just over 10% [12, 23, 25].

CdTe has a direct energy bandgap of 1.5 eV and consequently a high optical absorption coefficient for photons with energies > 1.5 eV. The energy bandgap is near the optimum for PV solar energy conversion. For making solar cells the CdTe is usually doped p-conductivity type and partnered with n-conductivity type cadmium sulphide (CdS). A typical fabrication step could be by the deposition of suitable transparent conducting oxide (TCO) on the superstrate, followed by the CdS window layer, the CdTe absorber layer, and then finished off with the back contacts. The typical thickness of the absorber layer is in the range 3–10 μm compared to the 100–200 μm used in silicon technologies. Although cells with efficiencies $> 18\%$ have been achieved [22], some problems remain. The environmental acceptability of using cadmium is still uncertain in some part of the world. For example, the

risks associated to the use of cadmium can be evidenced from the Toyama Prefecture "Ouch Ouch disease" in Japan which was widely believed to be caused by "cadmium poisoning" resulting from cadmium waste water from mining sites [26, 27]. This also points to the grave consequences of the disposal of CdTe-based modules on the environment. The low abundance of tellurium in the earth crust has been established [28] and this could hinder large scale deployment in the future.

CIGS solar cells were developed following modifications on solar cells from the chalcopyrite compounds such as copper indium selenide (CIS). Typical CIGS solar cells are mostly fabricated in the "substrate configuration" with the cell components in the order; sodalime glass, metallic back contact (molybdenum) deposited mostly by RF sputtering, CIGS absorber layer mostly grown using co-evaporation of the constituent elements or by the "three stage process", CdS (n–type buffer layer) usually deposited by chemical bath deposition, TCO (mostly aluminium doped zinc oxide) by RF sputtering and a metallic Ni/Al contact grids [29]. Other buffer layers are also used. Despite the production of cells with efficiencies $> 20\%$ being reported [30], the lack of abundance and high cost of gallium and indium are expected to limit the large scale deployment of the CIGS-based devices. To avoid this problem kesterite ($CuZnSnS_4$) solar cells are being developed. In some laboratories devices with efficiencies $> 10\%$ have been produced [31]. However kesterites are known to be prone to the formation of secondary phases during film growth and this could substantially limit device performance.

1.3.1 SnS-Based Thin Film Solar Cells

SnS is a novel IV-VI compound. It is closely related to the more familiar IV-VI compounds such as PbS, PbSe and PbTe which are commonly used as infrared detector materials due to their narrow energy bandgaps and excellent stability. SnS has largely been ignored as a PV material until the past decade due to limited research funds worldwide mainly being directed toward developing CdTe and CIGS solar cell devices. SnS has attracted recent significant interest in the photovoltaic community because [32–35]:

(i) SnS has an energy bandgap of 1.35 eV very close to the optimum for photovoltaic solar energy conversion.

(ii) SnS has direct energy bandgap with a high optical absorption coefficient $\alpha > 10^5 \text{cm}^{-1}$ for photons with energies greater than the energy bandgap and this minimises the thickness needed to absorb the incident light hence relaxing the need for long minority carrier diffusion lengths.

(iii) SnS consists of highly abundant elements.

(iv) SnS, Sn and S are environmentally acceptable.

(v) SnS can be doped both n-type and p-type, giving flexibility to device design and the possibility of grain boundary passivation by counter-doping the grain boundaries.

(vi) Wide energy bandgap, n-type SnO_2 can be formed by oxidising SnS to passivate the grain boundaries and surfaces of SnS.

(vii) Large scale production methods already exist for depositing Sn and in sulphidisation of metals.

(viii) SnS can be fabricated using different low-cost deposition technologies.

1.3.2 Aims of the Work Presented

(i) To deposit thin films of SnS onto glass substrates using the thermal evaporation method,

(ii) To determine the composition, structure, optical and electrical properties of the layers and to correlate the data to the growth variables,

(iii) To investigate how post-deposition annealing of the layers in various environments affects the chemical and physical properties of the layers, in particular how annealing increases the grain size, densifies the layers and alters the stoichiometry of the SnS,

(iv) To fabricate solar cell devices using CdS buffer layers to complete the device and to determine how the cell performance varies with the deposition variables,

(v) To identify a suitable cadmium–free replacement for the CdS, to characterise such devices and to optimise them to improve their PV performance.

1.3.3 Structure of Thesis

(i) Chapter 2 presents the background theory relevant to understanding the principles of operation of solar cell devices, in particular the dependence of solar cell performance on the properties of the materials used,

(ii) Chapter 3 reviews the history of the development of SnS and SnS-based solar cells,

(iii) Chapter 4 outlines the experimental methods used to produce the layers used and to characterise the layers and devices produced,

(iv) Chapter 5 presents the results, analysis and discusses the significance of the results,

(v) Chapter 6 presents conclusions and recommendations for future work.

References

[1] A. E. Becquerel. "Mémoires sur les effets électriques produits sous l'influence des rayons solaires". In: *Comptes Rendus de l'Academie des Sciences* 9 (1839), pp. 561–567 (cit. on p. 1).

[2] W. G. Adams and R. E. Day. "The action of light on selenium". In: *Proceedings of the Royal Society* A25 (1877), p. 113 (cit. on p. 1).

[3] D. M. Chapin, C. S. Fuller, and G. L. Pearson. "A new silicon p-n junction photocell for converting solar radiation into electrical power". In: *Journal of Applied Physics* 25 (1954), pp. 676–677 (cit. on p. 1).

[4] D. A. Jenny, J. J. Loferski, and P. Rappaport. "Photovoltaic effect in GaAs pn junctions and solar energy conversion". In: *Physical Review* 101 (1956), pp. 1208–1212 (cit. on p. 1).

[5] R. L. Easton and M. J. Votaw. "Vanguard I IGY Satellite (1958 Beta)". In: *Review of Scientific Instruments* 30 (1959), pp. 70–75 (cit. on p. 1).

[6] R. W. Miles, G. Zoppi, and I. Forbes. "Inorganic photovoltaic cells". In: *Materials Today* 10 (2007), pp. 20–27 (cit. on pp. 1, 2).

[7] R. W. Miles. “Photovoltaic solar cells: Choice of materials and production methods”. In: *Vacuum* 80 (2006), pp. 1090–1097 (cit. on pp. 1, 4).

[8] M.A. Green. *Third generation photovoltaics: advanced solar energy conversion.* Springer-Verlag, Berlin, 2006 (cit. on p. 1).

[9] M. A. Green. “Consolidation of Thin-film Photovoltaic Technology: The Coming Decade of Opportunity”. In: *Progress in Photovoltaics: Research and Applications* 14 (2006), pp. 383–392 (cit. on p. 1).

[10] D. C. Reynolds, G. Leies, L. L. Antes, and R. E. Marburger. “Photovoltaic effect in cadmium sulfide”. In: *Physical Review* 96 (1954), pp. 533–534 (cit. on p. 2).

[11] Paul D. Maycock. “World Cell Production in 2006”. In: *PV News* 26 (2006), pp. 4–10 (cit. on p. 2).

[12] R. W. Miles, K. M. Hynes, and I. Forbes. “Photovoltaic solar cells: An overview of state-of-the-art cell development and environmental issues”. In: *Progress in Crystal Growth and Characterization of Materials* 51 (2005), pp. 1–42 (cit. on pp. 2–4).

[13] D. Ginley, M. A. Green, and R. Collins. “Solar Energy Conversion Toward 1 Terawatt”. In: *Materials Research Bulletin* 33 (2008), pp. 355–364 (cit. on p. 2).

[14] M. A. Green. *Silicon solar cells-Advanced theory and practice.* Bridge Printerey, Sydney, 1995 (cit. on p. 2).

[15] J. Zhao, A. Wang, P. Altermatt, and M. A. Green. “Twenty-four percent efficient silicon solar cells with double layer antireflection coatings and reduced resistance loss”. In: *Applied Physics Letters* 66 (1995), pp. 3628–3636 (cit. on p. 2).

[16] M. A. Green. *Clean Electricity from Photovoltaics.* Ed. by M. D. Archer and R. Hill. Imperial College Press, London, 2001, pp. 391–394 (cit. on p. 2).

[17] J. Zhao, A. Wang, M.A. Green, and F. Ferazza. “Novel 19.8% efficient “honeycomb” textured multicrystalline and 24.4% monocrystalline silicon solar cells.” In: *Applied Physics Letters* 73 (1998), pp. 1991–1993 (cit. on p. 2).

[18] J. Zhao, A. Wang, and M. A. Green. “24.5% efficiency silicon PERT cells on MCZ substrates and 24.7% efficiency PERT cells on FZ substrates”. In: *Progress in Photovoltaics* 7 (1999), pp. 471–474 (cit. on p. 2).

[19] W. Shockley and H. J. Queisser. “Detailed Balance Limit of Efficiency of p–n Junction Solar Cells”. In: *Journal of Applied Physics* 32 (1961), pp. 510–519 (cit. on p. 3).

[20] A. Eyer, A. Raeuber, and A. Goetzberger. “Silicon sheet materials for solar cells”. In: *Optoelectronics* 5 (1990), pp. 239–257 (cit. on p. 3).

[21] K. Kawamoto, T. Nakai, T. Baba, M. Taguchi, H. Sakata, S. Tsuge, K. Uchihashi, M. Tanaka, and S. Kiyama. “A High-Efficiency HIT Solar Cell (21.0% 100 cm^2) with Excellent Interface Properties”. In: *Technical Digest of the 12th International Photovoltaic Science and Engineering Conference*. 2001, pp. 853–856 (cit. on p. 3).

[22] M. A. Green, K. Emery, Y. Hishikawa, W. Warta, and D. D. Ewan. “Solar cell efficiency tables”. In: *Progress in Photovoltaics Research and Applications* 21 (2013), pp. 1–11 (cit. on pp. 3, 4).

[23] C. R. Wronski and D. E. Carlson. *Clean Electricity from Photovaltaics:* ed. by M. D. Archer and R. Hill. Imperial College Press, London, 2001, pp. 199–236 (cit. on p. 4).

[24] D. L. Stäbler and C. R. Wronski. “Reversible conductivity changes in discharge-produced amorphous Si”. In: *Applied Physics Letters* 31 (1977), pp. 292–294 (cit. on p. 4).

[25] J. H. Petermann, D. Zielke, J. Schmidt, F. Haase, E.G. Rojas, and R. Brendel. “19% efficient and 43μm thick crystalline Si solar cell from layer transfer using porous silicon”. In: *Progress in Photovoltaics* 20 (2011), pp. 1–5 (cit. on p. 4).

[26] B. T. Emmerson. ““Ouch-ouch” disease:the osteomalacia of cadmium nephropathy”. In: *Annals of Internal Medicine* 73 (1970), pp. 854–855 (cit. on p. 5).

[27] M. Kasuya. “Recent epidermiological studies on itai-itai disease as a chronic cadmium poisoning in Japan”. In: *Water Science Technology* 42 (2000), pp. 147–155 (cit. on p. 5).

[28] S. R. Taylor and S. M. McLennan. *The continental crust: its composition and evolution: an examination of the geochemical records preserved in sedimentary rocks*. Blackwell Sceintific Publication, Oxford, 1985 (cit. on p. 5).

[29] K. Ramanathan, M. A. Contreras, C. L. Perkins, S. Asher, F. S. Hasoon, J. Keane, D. Young, M. Romero, W. Metzger, and R. Noufi. "Short communication: accelerated publication: properties of 19.2% efficiency ZnO/CdS/$CuInGaSe_2$ thin-film solar cells". In: *Progress in Photovoltaics* 11 (2003), pp. 225–230 (cit. on p. 5).

[30] P. Jackson, D. Hariskos, E. Lotter, S. Paetel, R. Wuerz, R. Menner, W. Wischmann, and M. Powalla. "New world record efficiency for Cu(In,Ga)Se_2 thin film solar cells beyond 20%". In: *Progress in Photovoltaics: Research and Applications* 19 (2011), pp. 894–897 (cit. on p. 5).

[31] D. Aaron, R. Barkhouse, O. Gunawan, T. Gokmen, T. K. Todorov, and D. B. Mitzi. "Device characteristics of a 10.1% hydrazine-processed $Cu_2ZnSn(Se, S)_4$ solar cell". In: *Progress in Photovoltaics: Research and Applications* 20 (2012), pp. 6–11 (cit. on p. 5).

[32] M. Devika, K. T. Ramakrishna Reddy, N. Koteeswara Reddy, K. Ramesh, R. Ganesan, E. S. R. Gopal, and K. R. Gunasekhar. "Microstructure dependent physical properties of evaporated tin sulfide films". In: *Journal of Applied Physics* 100 (2006), p. 23518 (cit. on p. 5).

[33] K. T. Ramakrishna Reddy, P. Purandhra Reddy, P. K. Datta, and R. W. Miles. "Formation of polycrystalline SnS layers by a two-step process". In: *Thin Solid Films* 403 (2002), pp. 116–119 (cit. on p. 5).

[34] M. Devika, N. K. Reddy, D. S. Reddy, S. V. Reddy, K . Ramesh, E. S. R. Gopal, K. R. Gunasekhar, V. Ganesan, and Y. B. Hahn. "Optimization of the distance between source and substrate for device-grade SnS films grown by the thermal evaporation technique". In: *Journal of Physics: Condensed Matter* 19 (2007), p. 306003 (cit. on p. 5).

[35] M. Devika, N. Koteeswara Reddy, K. Ramesh, H. R. Sumana, K. R. Gunasekhar, E. S. R. Gopal, and K. T. Ramakrishna Reddy. "The effect of substrate surface on the physical properties of SnS films". In: *Semiconductor Science and Technology* 21 (2006), pp. 1495–1501 (cit. on p. 5).

Chapter 2

Background Theory

2.1 The Solar Spectrum and Atmospheric Effects

The sun is a sphere of an intensely hot gaseous matter with a diameter of 1.39 x $10^9 m$, a mean earth-sun distance of 1.5 x $10^{11} m$ and an effective blackbody surface temperature of 5777 K powered by a predominant hydrogen-helium fusion reaction [1]. The fusion energy is then transferred outward by radiation and convection and lastly radiated into space in the form of electromagnetic waves as a continuous spectrum of radiation that spans from the ultraviolet to the infra-red region (0.2 µm to 3 µm). The intensity of solar radiation in free space at the mean earth-sun distance (total energy in the spectrum) is termed the "solar constant". It has a value of 1367 W m^{-2} [2–4].

Solar radiation can undergo substantial modification both in the extra-terrestrial and terrestrial regions. These are illustrated in Figure 2.1 and Figure 2.2 respectively. Modifications in the extra-terrestrial region are mostly due to the eccentricity of the earth and the revolution of the earth around the sun. In the terrestrial regions the variation in solar radiation is mostly due to attenuation effects caused by atmospheric absorption and scattering. The air mass (AM) i.e. the amount of atmosphere which solar radiation must pass through to reach the surface of the earth depends on the position of the sun while the air mass number is an indicator of the distance travelled by solar radiation in the earth's atmosphere. It decreases with an increase in altitude above sea level. To assess the performance of a solar cell two standardised spectra are used, the AM0 and the AM1.5 spectra.

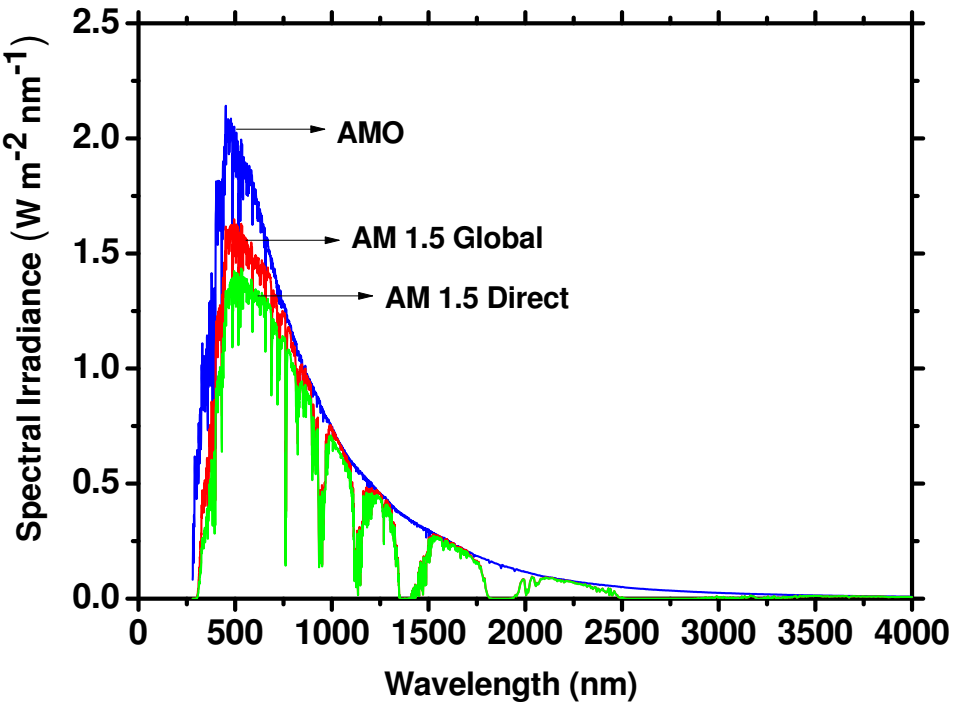

Figure 2.1: AM0 and AM1.5 Spectra (reproduced from ASTM G173-03 Reference Spectra [3]).

The AM0 spectrum is that incident just outside the earth's atmosphere, and is used for space applications. The AM1.5G spectrum is that incident after passing through an air mass of 1.5 times the thickness of the earth's atmosphere, and is utilised in terrestrial applications.

The relationship between photon energy in electron-volts (eV) and the wavelength of the incident light in micrometers is given as:

$$E(eV) = \frac{1.24}{\lambda(\mu\text{m})} \tag{2.1}$$

Atmospheric absorption is commonly caused by ozone (O_3), oxygen (O_2), nitrogen (N_2), carbon (iv)oxide (CO_2), carbon(ii)oxide (CO) and water vapour (H_2O) while scattering is mostly caused by aerosols, air molecules (Rayleigh scattering), dust and water droplets.

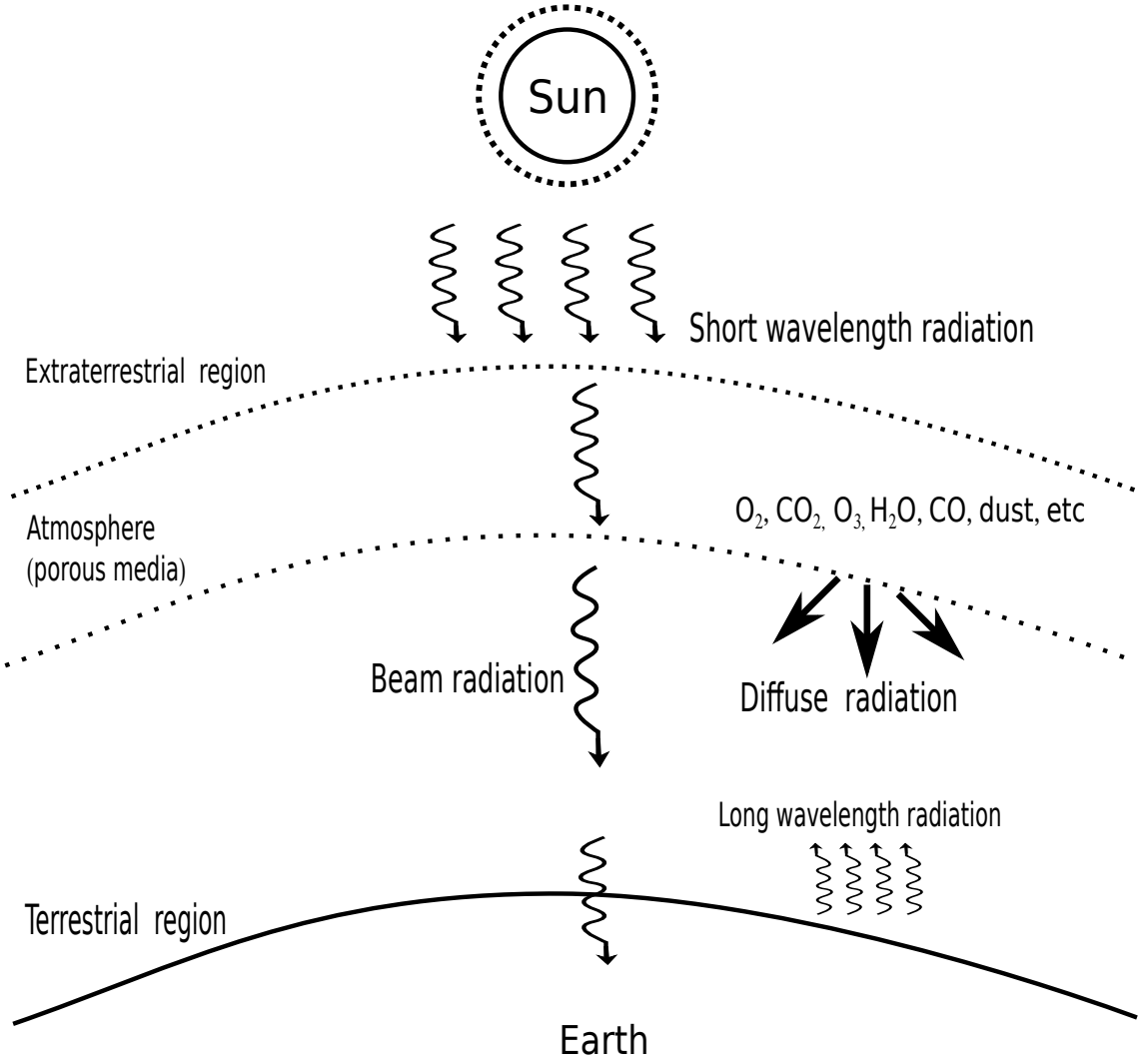

Figure 2.2: Terrestrial, Extraterrestrial Regions and Atmospheric Effects (adapted from [1]).

2.2 Light Absorption and Carrier Generation

A semiconductor is generally characterised by a bandgap energy E_g, the energy needed to create an electron-hole (e-h) pair. The energy of each packet of light, the photon is related to the light wavelength as earlier defined in Equation (2.1). The degree of light absorption is generally defined by an absorption constant $\alpha(\lambda)$ which depends strongly on the wavelength of the incident light. In terms of the photon energy, the absorption coefficient $\alpha(h\nu)$ can be defined as the relative rate of decrease in light intensity $L(h\nu)$ along its path of propagation [5] such that:

$$\alpha = \frac{1}{L(h\nu)} \frac{d[L(h\nu)]}{dx} \tag{2.2}$$

Optical absorption can be intrinsic, when energy of each absorbed photon is consumed by raising an electron from the valence band to the conduction band thereby creating an electron-hole pair or extrinsic in which case absorption is via deep localised states. Intrinsic absorption occurs in both direct and indirect bandgap materials. In direct bandgap materials the conduction band (CB) minimum and valence band (VB) maximum occur at the same value of crystal momentum, $\underline{k}$ and momentum is conserved when an electron is promoted from the top of the VB to the bottom of the CB. For such material, α is related to E_g as [5]:

$$\alpha(h\nu) = B[h\nu - E_g]^{0.5} \tag{2.3}$$

where B is an energy-independent constant that depends on the refractive index of the material and hole and electron effective masses respectively [6]. α is generally zero for $h\nu < E_g$ and $> 10^4 cm^{-1}$ for large $h\nu$. Direct bandgap materials are characterised by a sharp change in α from zero for $h\nu < E_g$ to values $> 10^4 cm^{-1}$ for $h\nu > E_g$ [7]. For forbidden direct transitions,

$$\alpha(h\nu) = B^{/}[h\nu - E_g]^{1.5} \tag{2.4}$$

where $B^{/} \neq B$ but depends on the same variables as B [6]. In indirect bandgap materials, the CB minimum and VB maximum do not occur at the same value of $\underline{k}$ and hence momentum is not conserved in band-band transitions. Since the transition requires a change in momentum a two-step process is needed, involving scattering by a phonon to conserve $\underline{k}$. The range of α for indirect transitions is between $10^{-1} - 10^2 cm^{-1}$ [8] and hence the reason why a substantial thickness and a long minority carrier diffusion length are needed when such materials are used in fabricating solar cell devices.

2.2.1 Carrier Generation

In a solar cell carrier generation is the outcome of an optical absorption process.

(i) For h$\nu = E_g$, e–h pairs are generated.

(ii) For h$\nu > E_g$, e–h pairs are generated and also the excess energy (h$\nu - E_g$) is wasted as heat.

(iii) For h$\nu < E_g$, e–h pairs are not generated under intrinsic conditions. However under extrinsic condition, a photon will be absorbed because of the available energy states in the forbidden gap due to chemical impurities or physical defects. These processes are illustrated in Figure 2.3 [9].

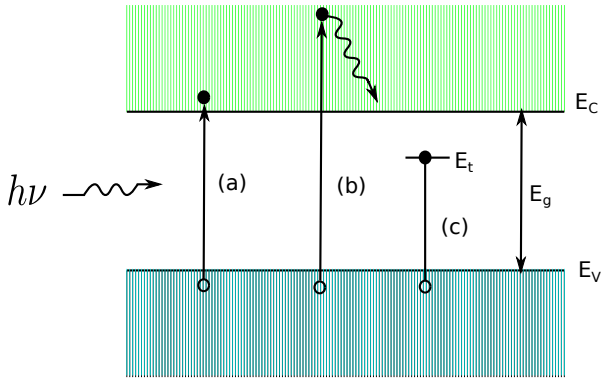

Figure 2.3: Photon Transitions in a Semiconductor for (a) $h\nu = E_g$ (b) $h\nu > E_g$ and (c) $h\nu < E_g$.

The dependence of carrier generation-rate per unit area (photon-absorption rate) as a function of E_g derives from the above criteria, added with the spectral distribution of solar radiation.

2.2.2 Recombination

Recombination is the reverse of generation and acts to restore the equilibrium condition of the carriers. It can be radiative/band-to-band recombination, when an electron recombines with a hole to emit a photon or non-radiative recombination, carrier recombination through traps or localised energy states in the forbidden gap. Auger recombination can occur when the electron recombining with a hole gives off its excess energy to a second electron in the CB or VB without emitting radiation while the second electron drops back to its

original energy with an emission of a phonon. Auger recombination is an inverse of impact ionisation, the creation of e-h pair when a high-energy electron collides with an atom and breaks the bond. Surface recombination also occurs from the discontinuities that arises due to large number of localised energy states or generation-recombination centres introduced at the surface owing to the abrupt discontinuity of the lattice structure at the surface [9]. In general, radiative recombination is common in direct bandgap materials, indirect recombination in indirect energy bandgap materials while Auger recombination is common in heavily doped materials. Radiative and non-radiative recombination processes are illustrated in Figure 2.4 respectively.

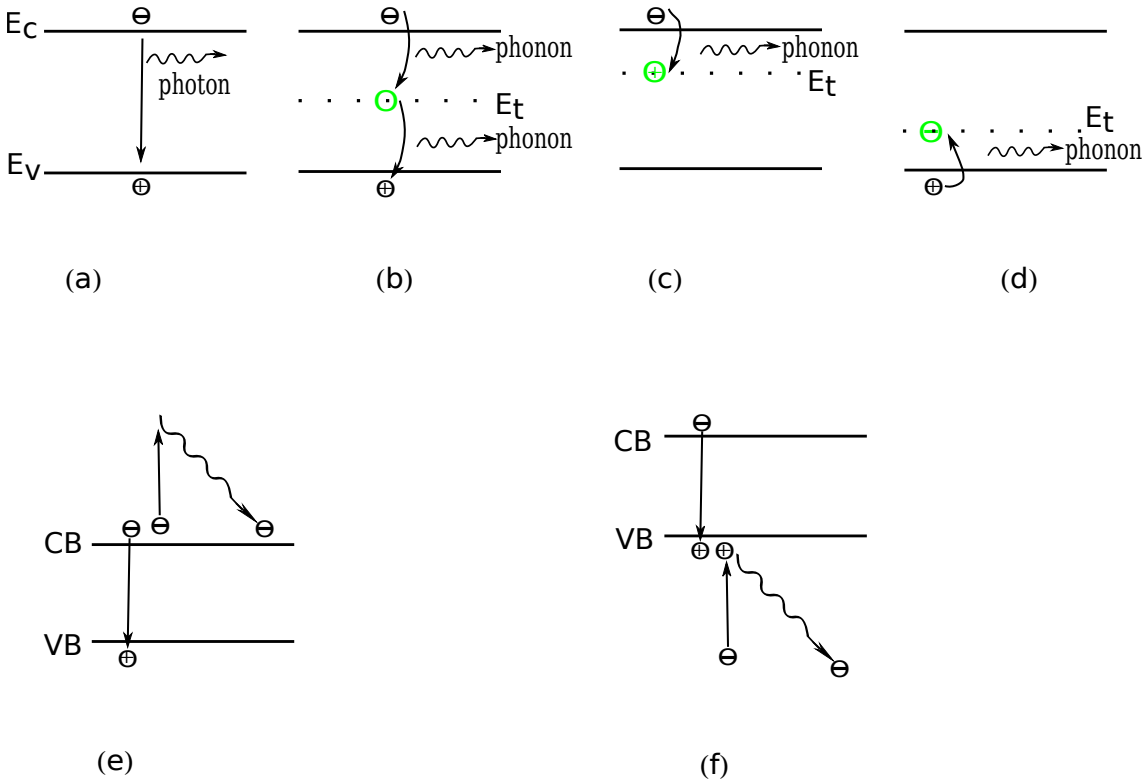

Figure 2.4: Radiative Recombination (a), and Non-radiative Recombination at: (b) Recombination Centre (c) Electron Trap (d) Hole Trap, and Auger Recombination at (e) CB (f) VB [7, 10, 11].

2.3 p-n Junction

The p-n junction is the heart of all semiconductor solar cells. Generally all photovoltaic cells contains some built-in asymmetry (making both sides different from each other). If such asymmetry consists of a p-type and n-type semiconductor material that are brought

into intimate contact, a p-n junction is formed. Owing to the differences in the electron and hole concentrations in the opposite sides (large concentration gradient), there is a tendency for electrons to diffuse from the n-type side to the p-type side and holes from the p-type side to the n-type side. This results in a build-up of positive charges on the n-type side and that of negative charges on the p-type side. The resultant double layer of charges (space charge region or depletion region) sets up an electric field that stops the further flow of the carriers. Under equilibrium conditions, the drift current flow will be balanced by the opposing diffusion current such that the net current flow is zero and the Fermi level E_F is constant across the entire material. The electrostatic potential (junction or built-in potential) V_{bi} set up by the electric field across the junction is related to the doping concentrations, and the magnitude of this electrostatic potential is the sum of the magnitude of the potentials on the n-side (V_n) and the p-side (V_p). Figure 2.5 illustrates these processes for a typical p-n junction. In the neutral p-region, the difference in energy between E_F and E_i (intrinsic Fermi-level) on the p-side of the junction is qV_p, hence

$$qV_p = (E_i - E_F) \tag{2.5}$$

From basic semiconductor theory, it is well known that:

$$p = n_i \exp\left(\frac{E_i - E_F}{kT}\right) \tag{2.6}$$

or

$$n = n_i \exp\left(\frac{E_F - E_i}{kT}\right) \tag{2.7}$$

which implies that putting Equation (2.6) in Equation (2.5) and assuming a complete ionisation of acceptors ($\mathrm{p} = \mathrm{N}_A$), gives:

$$|V_p| = \frac{kT}{q} \ln \frac{N_A}{n_i} \tag{2.8}$$

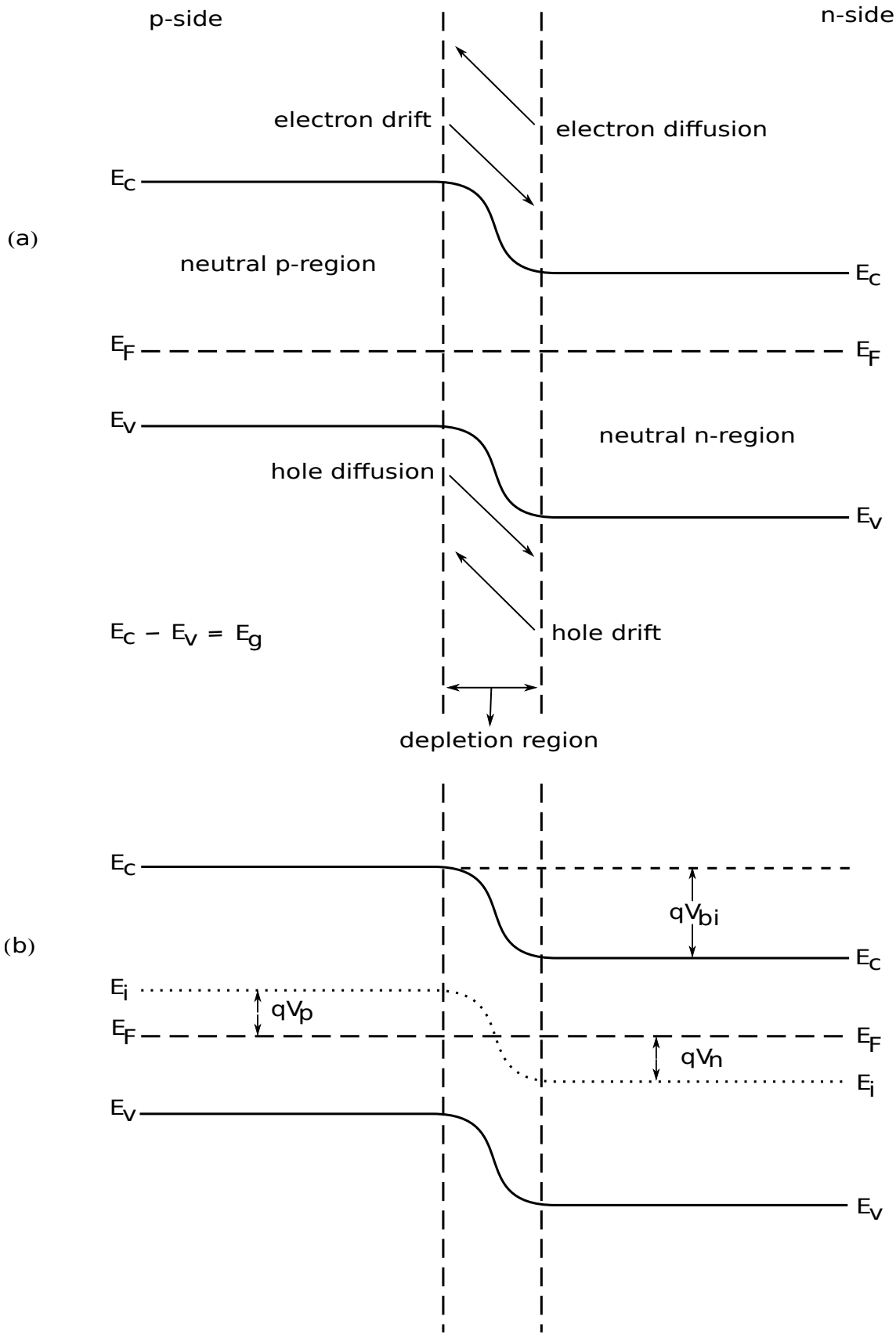

Figure 2.5: (a) p-n Junction Energy Diagram Indicating Direction of Current Flow (b) the Junction at Thermal Equilibrium [12].

At the neutral n-side of the junction, applying the same argument with respect to n yields:

$$|V_n| = \frac{kT}{q} \ln \frac{N_D}{n_i} \tag{2.9}$$

Adding Equation (2.8) and Equation (2.9) gives:

$$V_{bi} = \frac{kT}{q} \ln \frac{N_A N_D}{n_i^2} \tag{2.10}$$

where N_A and N_D are the acceptor and donor impurity densities respectively and n_i^2 is the intrinsic carrier density. Equation (2.10) shows that V_{bi} depends strongly on the doping concentrations in the p and n regions respectively. For the overall space charge neutrality of the semiconductor to be maintained, the total negative charge per unit area on the p-side must be equal to the total positive charge per unit area on the n-side and hence:

$$N_A x_p = N_D x_n \tag{2.11}$$

where x_p is the penetration of the depletion region into the p-material and x_n is the penetration of the depletion region into the n-material. The width of the depletion region w is given by:

$$w = x_p + x_n \tag{2.12}$$

The equalisation of Fermi levels throughout the material at thermal equilibrium results in a unique space charge distribution at the junction which is adequately described by Poisson's equation [13, 14]:

$$\frac{d^2\psi}{dx^2} \equiv -\frac{d\mathcal{E}}{dx} = -\frac{\rho_s}{\epsilon_s} = -\frac{q}{\epsilon_s}(N_D - N_A + p - n) \tag{2.13}$$

When a region is completely depleted such that $p = n = 0$, Equation (2.13) becomes:

$$\frac{d^2\psi}{dx^2} = \frac{q}{\epsilon_s}(N_A - N_D) \tag{2.14}$$

Figure 2.6 gives a typical picture of the space charge distribution of an abrupt junction.

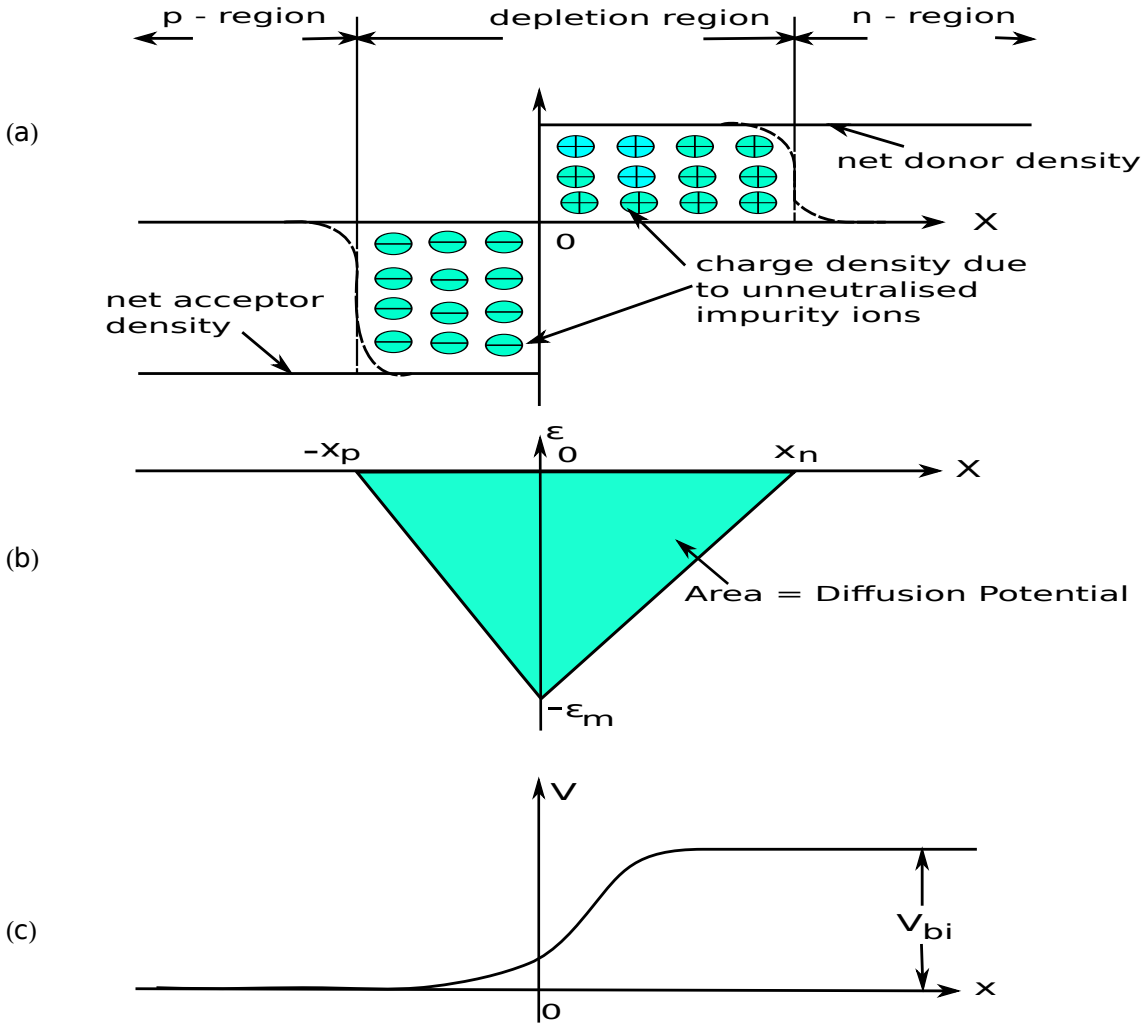

Figure 2.6: (a) Rectangular Approximation of the Space Charge Distribution (b) Electric Field Distribution (c) Potential Difference Distribution [12, 15].

Owing to the total depletion of the free carriers, Poisson's equation changes to:

$$\frac{d^2\psi}{dx^2} = +\frac{qN_A}{\epsilon_s} \quad for \quad -x_p \leq x < 0 \tag{2.15}$$

and

$$\frac{d^2\psi}{dx^2} = -\frac{qN_D}{\epsilon_s} \quad for \quad 0 < x \leq x_n \tag{2.16}$$

Using the abrupt junction approximation, integration of these Poisson's equations gives the electric field as [13, 15]:

$$\mathcal{E}(x) = -\frac{d\psi}{dx} = -\frac{qN_A(x+x_p)}{\epsilon_s} \quad for \quad -x_p \leq x < 0 \tag{2.17}$$

and

$$\mathcal{E}(x) = -\mathcal{E}_m + \frac{qN_D x}{\epsilon_s} = \frac{qN_D}{\epsilon_s}(x - x_n) \quad for \quad 0 < x \leq x_n \tag{2.18}$$

where $\mathcal{E}_m$ is the maximum of the field at $x = 0$ given by:

$$\mathcal{E}_m = \frac{qN_D x_n}{\epsilon_s} = \frac{qN_A x_p}{\epsilon_s} \tag{2.19}$$

The potential distribution V(x) and the junction potential V_{bi} is obtained by integrating Equations (2.17) and (2.18) over the depletion region hence:

$$V(x) = \mathcal{E}_m \left(x - \frac{x^2}{2w} \right) \tag{2.20}$$

and the contact potential is given by:

$$V_{bi} = \frac{1}{2}\mathcal{E}_m w \equiv \frac{1}{2}\mathcal{E}_m(x_n + x_p) \tag{2.21}$$

If $\mathcal{E}_m$ is eliminated from Equations (2.19) and (2.21), an expression for the depletion width

of a two-sided abrupt junction is obtained as [15]:

$$w = \sqrt{\frac{2\epsilon_s}{q}\left(\frac{N_A + N_D}{N_A N_D}\right) V_{bi}} \tag{2.22}$$

A one-sided abrupt junction is formed when one side of the junction is more heavily doped than the other and in most cases for solar cell, $N_D \gg N_A$ such that Equation (2.22) reduces to:

$$w = \sqrt{\frac{2\epsilon_s V_{bi}}{qN_B}} \tag{2.23}$$

where $N_B = N_A$. Equation (2.23) implies that the depletion layer width could be increased by decreasing the doping concentration on the p-type side of such device. However possible consequences are that the bulk resistance of the p-type side and the specific contact resistance of the electrical contact to the p-type side will be increased thereby increasing the series resistance of the device. Figure 2.7 shows the depletion region, space charge and electric field distribution accordingly. The energy band diagram given previously in Figure 2.5(b) and Figure 2.6(c) reveal that the total electrostatic potential across the junction is V_{bi} hence if a positive voltage V_F is applied to the p-side with respect to the n-side, the p–n junction becomes forward biased as shown in Figure 2.8(a). The total electrostatic potential reduces by V_F (i.e. to $V_{bi} - V_F$), indicating that forward bias has the effect of narrowing the depletion layer width. When a positive voltage V_R is applied to the n-side with respect to the p-side as shown in Figure 2.8(b), the junction now becomes reverse biased and the total electrostatic potential across the junction increases by V_R (i.e. to $V_{bi} + V_R$), implying that reverse bias has the effect of widening the depletion layer width. When these observed changes for the junction potential are included in Equation 2.23, an expression showing the depletion layer width as a function of applied voltage for both case is obtained as:

$$w = \sqrt{\frac{2\epsilon_s(V_{bi} \pm V)}{qN_B}} \tag{2.24}$$

where V = V_R or V_F.

Table 2.1 summarises the differences and similarities between a forward-biased and reverse-

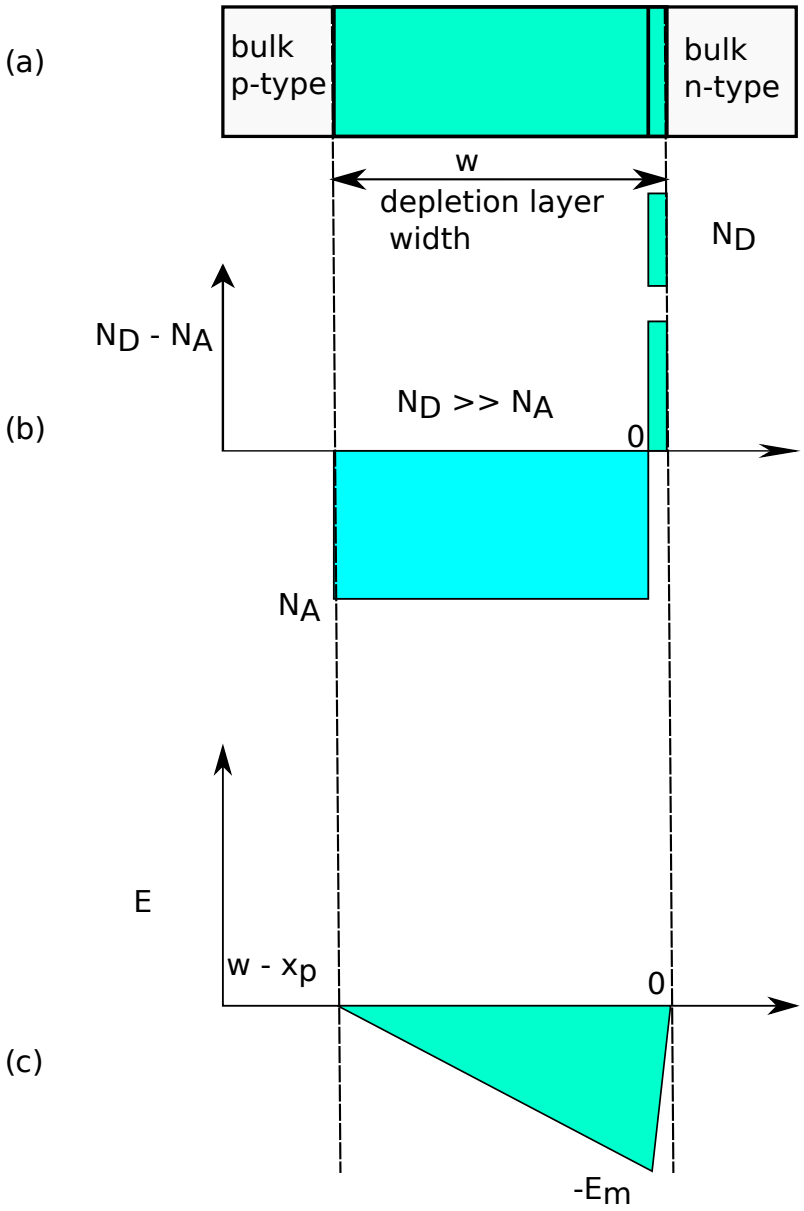

Figure 2.7: One Sided Abrupt Junction ($N_D \gg N_A$): (a) Depletion Region (b) Space Charge Distribution (c) Distribution of Electric Field [9, 16].

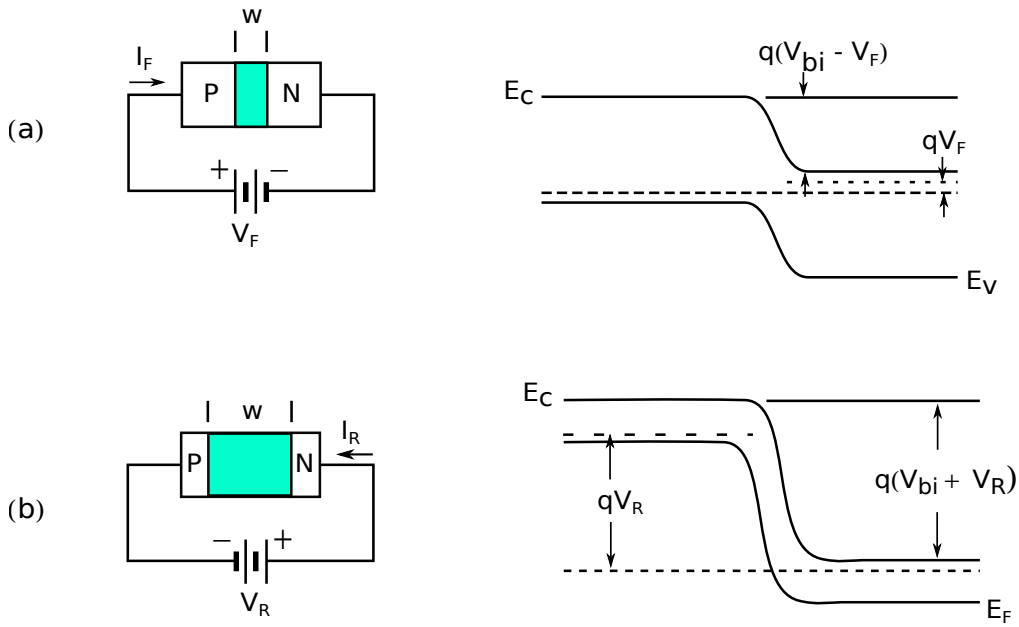

Figure 2.8: Energy Band Diagrams of a p–n Junction Under (a) Forward-bias Condition (b) Reverse-bias Condition [9].

biased p-n junction.

2.3.1 Capacitance-Voltage Analysis

It has been established that the depletion layer of a p-n junction is analogous to a parallel-plate capacitor in which the depletion layer width is equivalent to the spacing between the two plates i.e the capacitance C, is given by [9, 10]:

$$C = \frac{\varepsilon_s \varepsilon_o \mathrm{A}}{w} \tag{2.25}$$

where w is the depletion layer width, A is the junction area, ε_s and ε_o are the static dielectric constant of the material and permittivity of free space respectively. Substituting Equation (2.24) for the reverse bias case in Equation (2.25) and assuming a p^+ -n diode in which $N_A \gg N_D$, gives:

$$C = \frac{\varepsilon_s \varepsilon_o \mathrm{A}}{\sqrt{\dfrac{2\varepsilon_s \varepsilon_o (V_{bi} + V)}{qN_D}}} \tag{2.26}$$

Forward bias	Reverse bias
Connection is from positive terminal to p-side.	Connection is positive terminal to n-side.
Reduction in junction potential.	Increase in junction potential.
Increased electron diffusion from n-side to p-side compared with the steady-state condition.	Reduction in electron diffusion from n-side to p-side compared with the steady-state condition.
Increased hole diffusion from p-side to n-side compared with the steady-state condition.	Reduction in hole diffusion from p-side to n-side compared with the steady-state condition.
Flow of drift current is the same as in steady state condition.	Flow of drift current is the same as in steady state condition.
Flow of a large diffusion current is observed.	Flow of a very small reverse saturation current is observed.

Table 2.1: Differences and Similarities Between Forward-biased and Reverse-biased p-n Junction.

Rearranging Equation (2.26) gives:

$$\frac{1}{C^2} = \frac{2V_{bi}}{\varepsilon_s \varepsilon_o q N_D A^2} + \frac{2V}{\varepsilon_s \varepsilon_o q N_D A^2} \tag{2.27}$$

Equation (2.27) is of the form Y = c + mx hence a graph of $1/C^2$ against V gives the following information:

- At $1/C^2 = 0$, V = -V_{bi}
- $N_D = 2/q\varepsilon_s\varepsilon_o A^2 \times$ slope
- $N_A = n_i{}^2/N_D \exp(qV_{bi}/kT)$
- $w = \varepsilon_s\varepsilon_o A/C$
- $x_n = wN_A/(N_A + N_D)$
- $x_p = wN_D/(N_A + N_D)$

It is pertinent to mention that for an abrupt p^+n or n^+p heterojunction device, the intercept on the V-axis for $1/C^2 = 0$ in most cases do not correspond to V_{bi} due to the presence of interface states at the heterojunction. In such cases, V_{bi} can be deduced using the

expression [17]:

$$V_{intercept} = V_{bi} - \Psi_m - \beta Q_{IS}^2 \tag{2.28}$$

where Q_{IS} is the charge on the interface states and Ψ_m is the electric dipole at the interface.

2.4 Current-Voltage Characteristics

2.4.1 Ideal Diodes

The major assumptions that determine the ideal current-voltage characteristics of a p–n junction are [18, 19]:

- The depletion region has abrupt boundaries and outside the boundaries the semiconductor material is assumed to be neutral.
- The injected minority carrier densities are small compared to the majority carrier densities.
- The carrier densities at the boundaries are related by the built-in potential across the junction.
- Within the depletion region, neither generation nor recombination currents exist, implying that the electron and hole currents are constant throughout the space charge region.

Under steady state conditions, the doping concentration is equal to the majority carrier density hence the built-in potential (Equation (2.10)) is given by:

$$V_{bi} = \frac{kT}{q} \ln \frac{p_{po} n_{no}}{n_i^2} = \frac{kT}{q} \ln \frac{n_{no}}{n_{po}} \tag{2.29}$$

where p_{no} and p_{po} are the equilibrium hole densities in the n- and p- sides and n_{no} and n_{po} are the equilibrium electron densities in the n- and p- sides. From Equation (2.29):

$$n_{no} = n_{po} e^{\frac{qV_{bi}}{kT}} \tag{2.30}$$

and:

$$p_{po} = p_{no} e^{\frac{qV_{bi}}{kT}} \tag{2.31}$$

Considering Equations (2.30) and (2.31), it can be observed that the electron and hole densities are related to the built-in potential at thermal equilibrium and even when a voltage is applied across the junction, this relation remains invariant. As indicated in Figure 2.8 and Table 2.1, application of forward or reverse bias changes the electrostatic potential difference by $V_{bi} - V_F$ and $V_{bi} + V_R$ such that, Equation (2.30) now changes to [9]:

$$n_n = n_p e^{\frac{q(V_{bi}-V)}{kT}} \tag{2.32}$$

where n_n and n_p are the non-equilibrium electron densities at the depletion layer boundaries on the n- and p- sides respectively. Under steady state conditions, the injected minority carrier density is negligible compared to the majority carrier density, hence $n_n \simeq n_{no}$. The electron density at the edges of the depletion region on the p-side can be obtained by putting this relation and Equation (2.30) into Equation (2.32):

$$n_p = n_{po} e^{\frac{qV}{kT}} \tag{2.33}$$

or

$$n_p - n_{po} = n_{po}(e^{\frac{qV}{kT}} - 1) \tag{2.34}$$

Also,

$$p_n = p_{no} e^{qV/kT} \tag{2.35}$$

or alternatively

$$p_n - p_{no} = p_{no}(e^{\frac{qV}{kT}} - 1) \tag{2.36}$$

at $x = x_n$ for the n-type boundary.

The combined effect of drift, diffusion and recombination in a semiconductor can be described by the steady state continuity equation. The general expression for a minority carrier (in this case a hole in an n-type material) under low injection conditions is related as [9]:

$$\frac{\partial p_n}{\partial t} = -p_n\mu_p\frac{\partial \mathcal{E}}{\partial x} - \mu_p\mathcal{E}\frac{dp_n}{\partial x} + D_p\frac{\partial^2 p_n}{\partial x^2} + G_p - \frac{p_n - p_{no}}{\tau_p} \tag{2.37}$$

Alternatively for an electron in a p-type material,

$$\frac{\partial n_p}{\partial t} = n_p\mu_n\frac{\partial \mathcal{E}}{\partial x} + \mu_n\mathcal{E}\frac{dn_p}{\partial x} + D_n\frac{\partial^2 n_p}{\partial x^2} + G_n - \frac{n_p - n_{po}}{\tau_n} \tag{2.38}$$

The absence of generation or recombination currents (zero drift and diffusion current) in the depletion layer implies that all the currents are assumed to be coming from the neutral regions since there is no electric field in the neutral regions; hence Equation (2.38) reduces to [9]:

$$\frac{d^2 p_n}{dx^2} - \frac{p_n - p_{no}}{D_p\tau_p} = 0 \tag{2.39}$$

Using the boundary conditions of Equation (2.36) with $p_n(x = \infty) = p_{no}$ gives

$$p_n - p_{no} = p_{no}(e^{qV/kT} - 1)e^{-(x-x_n)/L_p} \tag{2.40}$$

where $L_p \equiv \sqrt{D_p\tau_p}$, is the minority diffusion length of holes in the n-region. For $x = x_n$,

$$\mathbf{J}_p(x_n) = -qD_p\frac{dp_n}{dx}\bigg|_{x_n} = \frac{qD_p p_{no}}{L_p}(e^{qV/kT} - 1) \tag{2.41}$$

Also for the neutral p-region:

$$n_p - n_{po} = n_{po}(e^{qV/kT} - 1)e^{(x+x_p)/L_n} \tag{2.42}$$

and

$$\mathbf{J}_n(-x_p) \;=\; -qD_n\frac{dn_p}{dx}\bigg|_{-x_p} \;=\; \frac{qD_n n_{po}}{L_n}(e^{qV/kT}-1) \tag{2.43}$$

where L_n, the minority diffusion length of electrons is defined by $L_n \equiv \sqrt{D_n\tau_n}$. Because

$$D_n = \;\frac{kT}{q}\mu_n \;\text{(Einstein relation)} \tag{2.44}$$

it follows that

$$L_n = \;\sqrt{\frac{kT}{q}\mu_n\tau_n} \tag{2.45}$$

The sum of the current density which is constant throughout the device can be obtained by adding Equation (2.41) and (2.43):

$$\mathbf{J} \;=\; \mathbf{J}_p(x_n)+\mathbf{J}_n(-x_p) \;=\mathbf{J}_s(e^{qV/kT}-1) \tag{2.46}$$

$$\mathbf{J}_s \;\equiv\; \frac{qD_p p_{no}}{L_p}+\frac{qD_n n_{po}}{L_n} \tag{2.47}$$

or

$$\mathbf{J}_s = qN_C N_V\left[\frac{1}{N_A}\sqrt{\frac{D_n}{\tau_n}}+\frac{1}{N_D}\sqrt{\frac{D_p}{\tau_p}}\right]e^{\frac{-E_g}{kT}} \tag{2.48}$$

where $\mathbf{J}_s$ is the saturation current density. Equation (2.46) is often called the *Shockley equation* or the *ideal diode equation* [20]. In current form, Equation (2.46) could be written as

$$\mathbf{I} \;=\mathbf{I}_s(e^{qV/kT}-1) \tag{2.49}$$

2.4.2 Real Diodes

2.4.2.1 Generation-Recombination Effects

In real diodes, most of the idealised situations indicated earlier do not hold true in all cases due to the effects of generation and recombination of carriers. Under forward bias condition, for diodes made from semiconductors with $E_g > 1$ eV, recombination in the depletion region dominates at 300 K and for $V > 3kT/q$, the recombination current is given as [14]:

$$I_F = \frac{n_i q w}{2\tau_r} e^{qV/2kT} \tag{2.50}$$

where τ_r is the *recombination lifetime.*

A combined current flow due to diffusion and recombination mechanisms occurs for a certain range of temperatures when the total forward current is given by:

$$I_F = q\sqrt{\frac{D_p}{\tau_p}}\frac{{n_i}^2}{N_D} e^{qV/kT} + \frac{n_i q w}{2\tau_r} e^{qV/2kT} \tag{2.51}$$

It has been established that in general [14]:

$$I_F \propto e^{qV/AkT} \tag{2.52}$$

where A is known as the *ideality factor* and usually has a value between 1 and 2. For semiconductors with $E_g > 1$ eV, the behaviour is as indicated in Figure 2.9. When the diffusion current dominates, $A = 1$ and when recombination dominates, $A = 2$ but when both diffusion and recombination are comparable, A has a value between 1 and 2. Under reverse bias condition, the carrier concentrations are well below their equilibrium concentrations and electron-hole emissions are dominant hence the generation current is given by:

$$I_g = \frac{n_i q w}{\tau_g} \tag{2.53}$$

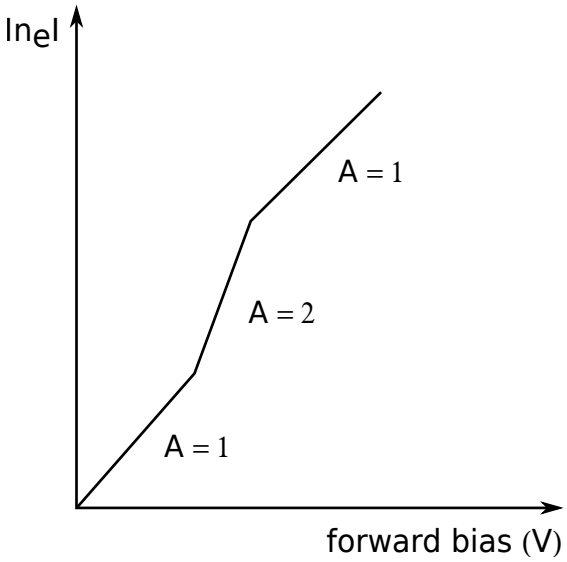

Figure 2.9: Forward Current-voltage Characteristics.

where g is the *generation lifetime*. The total generation current in reverse bias can be approximated as:

$$I_{\mathrm{R}} = q\sqrt{\frac{D_p}{\tau_p}}\frac{{n_i}^2}{N_D} + \frac{n_i q w}{\tau_g} \tag{2.54}$$

2.4.2.2 Effects of Temperature

Device performance is strongly influenced by temperature effects because of the dependence of the diffusion and recombination-generation currents on temperature, independent of the biasing mode. Under forward bias, the ratio of the diffusion current to the recombination-generation current is given by the relation:

$$\frac{I_{\mathrm{diffusion}}}{I_{\mathrm{recombination}}} = 2\,\frac{n_i}{N_D}\,\frac{L_P}{w}\,\frac{\tau_r}{\tau_p}\,e^{qV/2kT} \sim \exp\left[-\frac{E_g - qV}{2kT}\right] \tag{2.55}$$

Equation (2.55) indicates that the dominant process depends on the energy bandgap and on temperature. Considering a silicon diode at room temperature (see Figure 2.10), if the forward bias voltage is small, the recombination current is dominant while at higher forward bias voltages, the diffusion voltage usually predominates [9]. The diffusion current increases at a greater rate than the recombination current as temperature increases at any value of the forward bias voltage. For a wide range of forward bias voltages, this behaviour is consistent with Equation(2.46). For a one-sided abrupt $p^+ - n$ junction with $A = 1$, the

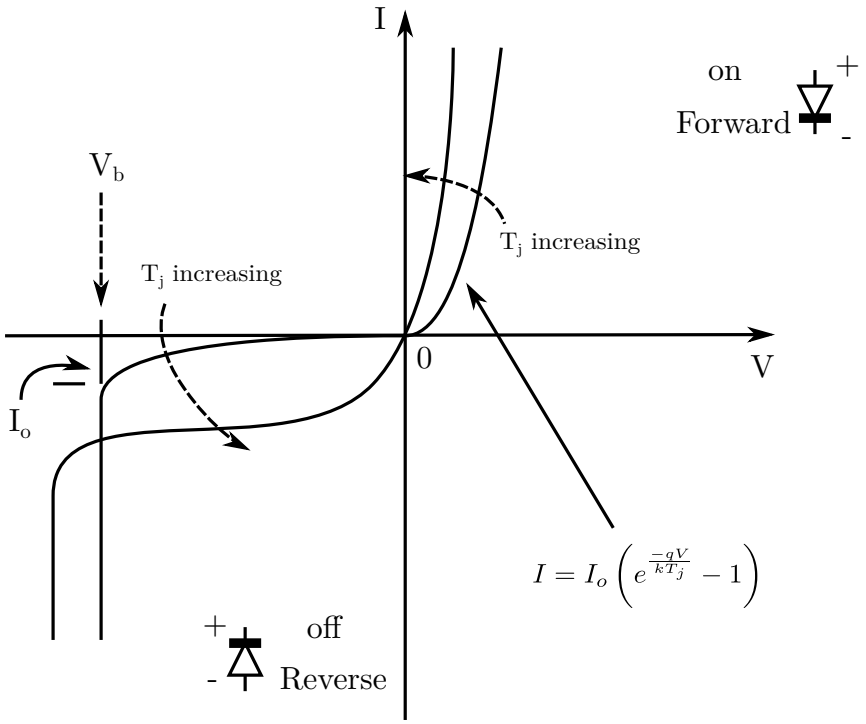

Figure 2.10: Junction Temperature T_j Effects on a Silicon p–n Junction Diode.

saturation current density is related to the temperature by:

$$\mathbf{J_s} \approx \frac{qD_pP_{no}}{L_p} \sim n_i^2 \sim \exp\left[-\frac{E_g}{kT}\right] \tag{2.56}$$

Equation (2.56) is of the form Y = mx + c and hence the slope of a graph of $\mathbf{J_s}$ versus $\frac{1}{\mathbf{T}}$ will give an activation energy that corresponds to the energy bandgap. If a reverse bias voltage is applied to an asymmetrical $p^+ - n$ junction, the ratio of the diffusion current to the generation current is

$$\frac{I_{\text{diffusion}}}{I_{\text{generation}}} = \frac{n_iL_p}{N_Dw}\frac{\tau_g}{\tau_p} \tag{2.57}$$

Equation (2.57) indicates that the ratio is directly proportional to the intrinsic carrier density n_i. In general, the generation current dominates at low temperatures while diffusion current becomes dominant at higher temperatures [10, 16].

2.4.2.3 Large Reverse Voltage Effects (Junction Breakdown)

The effect of tunnelling and avalanche multiplication mechanisms can result in the p–n junction exhibiting a non-destructive breakdown when a sufficiently large reverse bias voltage is applied on the junction. This is shown on Figure 2.11(a)–(b). For tunnelling

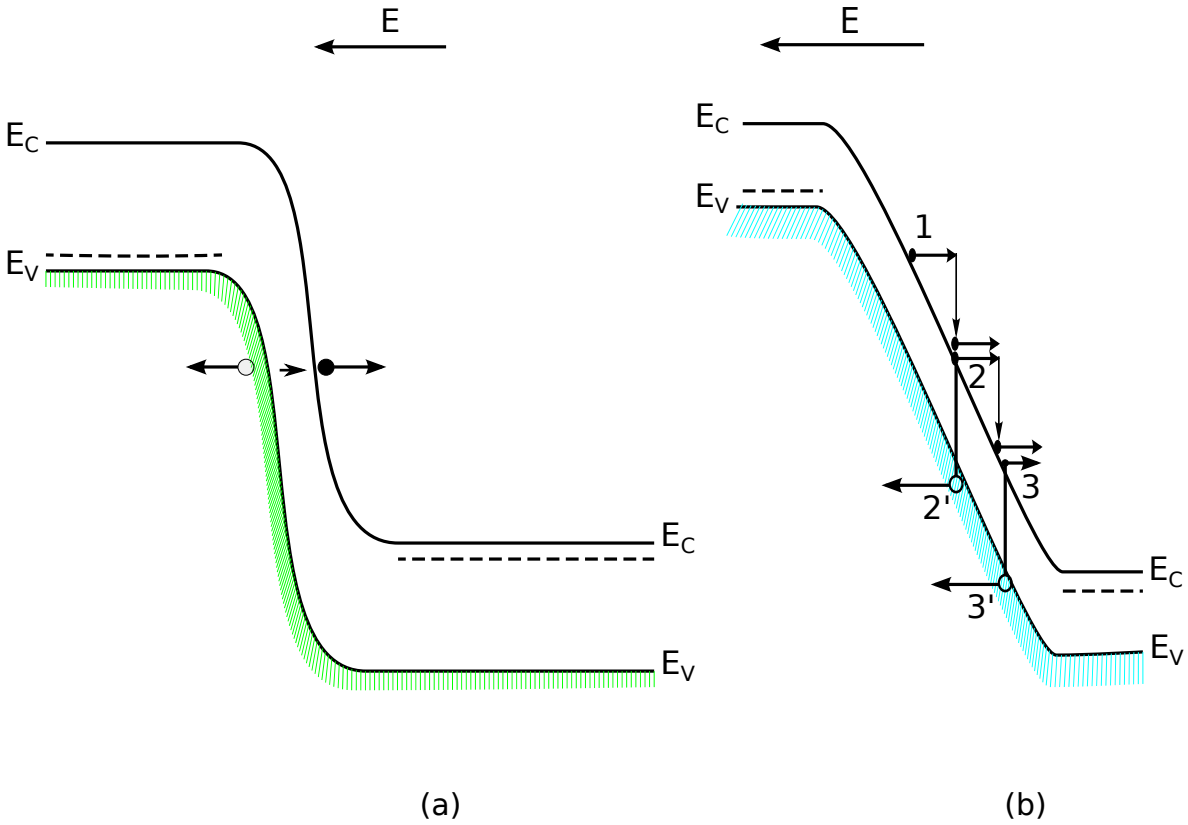

Figure 2.11: Junction Breakdown (a) Tunnelling Effect (b) Avalanche Breakdown.

to occur, a very high electric field, typically of the order of $10^7\,\mathrm{V\,cm^{-1}}$ or higher, is applied to the junction in the reverse direction. This can be achieved by having high doping concentrations ($> 5 \times 10^{17}\,\mathrm{cm^{-3}}$) in the quasi-neutral regions of the device [9]. The tunnelling process is illustrated in Figure 2.11(a). Impact ionisation mechanism is the major cause of an avalanche multiplication process. Figure 2.11(b) indicates a moderately doped asymmetrical $p^+ - n$ abrupt junction under reverse bias, exhibiting an avalanche breakdown process. When an electron denoted by 1 gains kinetic energy from the electric field and this field is high enough, it can gain sufficient energy such that it can break the lattice bonds creating an e-h pair ($2'$ and 2). Further new collisions are induced by the newly created e-h pairs when they acquire enough kinetic energy from the field resulting

in the generation of other e-h pairs ($3'$ and 3). These generative processes constitute what is known as avalanche multiplication. However, it is possible for the two to occur independently or simultaneously. In general, diode junctions that break down below 5 V are mostly associated to tunnelling effect but for junction breakdown above 5 V, avalanche process dominates. Within 5 V, junction breakdowns are explained by a combination of both effects [16, 21]. Increased junction temperature are known to reduce tunnelling breakdown voltage but increases the avalanche breakdown voltage.

2.5 Homojunctions

A homojunction consists of a junction of the same semiconductor material with different doping types and densities on each side of the device. The formation of a reasonable potential difference at the junction is achieved through altering the doping of the different sides of the material in question. This arrangement gives room for obtaining the required asymmetry in resistance that is needed for solar photovoltaic conversion in that the junction behaves as a selective barrier to the flow of the charge carriers. The main advantages of a homojunction device is the absence of interface effects due to there being no mismatch of lattice constants at the junction. However significant surface recombination can limit device performance substantially.

2.5.1 Homojunction Dark-current Analysis

The major current transport mechanisms in a forward biased p-n junction are: (*i*) diffusion of the carriers over the junction (carrier injection) (*ii*) recombination of carriers within the depletion region (*iii*) multi-step tunnelling and recombination through extrinsic states. The dark current-voltage behaviour of a solar cell is a useful tool in understanding the dominant current transport since it is understood that if a forward biased solar cell is supplying power, a dark current that opposes the photocurrent is always present. The possible current transport mechanisms are shown on Figure 2.12 [22]. In general, the total dark current contribution is the sum of diffusion, recombination and tunnelling currents. The major difference between diffusion and recombination currents lies in their temperature, voltage and energy bandgap dependence as earlier highlighted in subsection 2.4.2. The

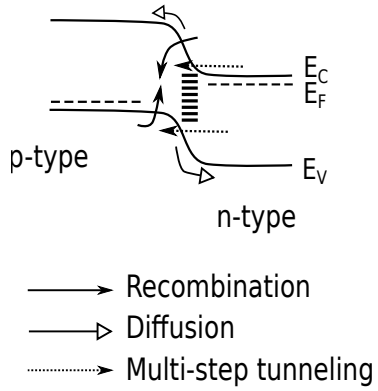

Figure 2.12: Forward biased p-n Homojunction Current Transport Mechanism.

dark depletion region recombination current density under forward bias is given as [22]:

$$J = \frac{qn_i w}{\sqrt{\tau_p \tau_n}} \frac{2sinh(qV/2kT)}{e^{(V_{bi}-V)}/kT} f(b) \tag{2.58}$$

where f(b) is an integral function which can be simplified further to give information on the trap level and intrinsic Fermi level. For forward bias voltages $>$ 2kT/q and for $N_D \gg N_A$ Equation (2.58) reduces to [22]:

$$J = J_o(e^{qV/2kT}) \tag{2.59}$$

where

$$J_o = J_{oo}(e^{-E_g/2kT}) \tag{2.60}$$

and

$$J_{oo} = kT\sqrt{\frac{2N_C N_V \epsilon_s (V_{bi} - V)}{qN_A \tau_p \tau_n}} f(b) \tag{2.61}$$

For multi-step tunnelling through extrinsic states, the availability of intermediate energy states makes it possible for electrons to tunnel from the conduction band to such energy levels within the forbidden gap, across the junction or an amalgam of recombination and tunnelling as shown in Figure 2.12.

2.6 Heterojunctions

A heterojunction is formed when two materials of different energy bandgap ($\mathbf{E}_{g1} \neq \mathbf{E}_{g2}$) and electron affinities ($\chi_1 > \chi_2$) are brought into intimate contact. It could be in the form of a semiconductor (p-n or p-i-n) or metal-semiconductor configuration. It could also be formed in semiconductor-liquid junction or excitonic solar cells (dye sensitised solar cells) and in this case, additional parameters of interest are the chemical potential, redox potential and effective work function. Abrupt heterojunctions can be grouped into anisotype (when the two materials have different conductivity types i.e. n and p type) and isotype when the semiconductors have the same conductivity type (i.e. n–n or p–p).

If the two semiconductors with required asymmetry are brought into intimate contact with each other, charge is transferred until Fermi levels are equalised across the two layers. When such contact occurs, it gives rise to three different band alignments (a) the straddled alignment or Type I alignment (b) the staggered alignment or Type II alignment (c) the broken-gap alignment or Type III alignment. The different band alignments are illustrated in Figure 2.13. Different models have been proposed in a bid to understand the energy

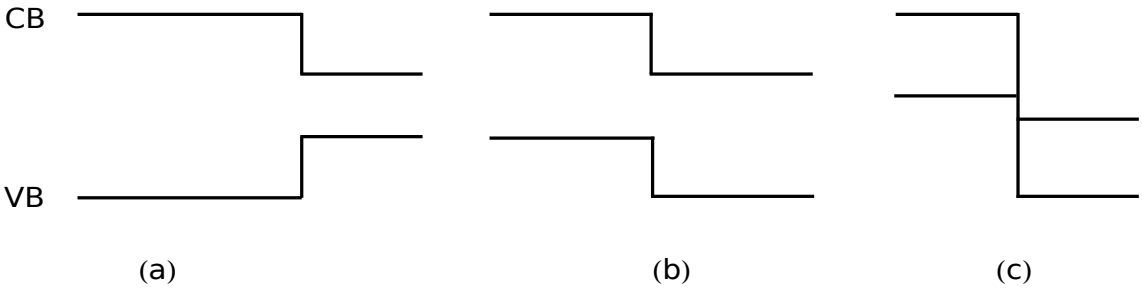

Figure 2.13: Semiconductor Heterojunction Band Alignments (a) Straddled Alignment (b) Staggered Alignment (c) Broken-gap Alignment.

band offsets and other processes taking place in heterojunctions. This is because carrier transport in heterojunctions are governed by different mechanisms in the interface region namely; recombination, tunnelling or combinations of the two involving energy levels near the interface. This makes heterojunction theory quite complex due to the presence of discontinuities in the conduction and valence bands as well as interface dipole layers, coupled with the distortion of the junction profile by the distribution of active interface states. Additionally, the properties of interface varies from one material to the other and also depends to a large extent on how they were formed. Models based on anisotype

heterojunctions are discussed below.

2.6.1 Anderson Model

The first most comprehensive model for representing the energy band diagram of a heterojunction can be traced to Anderson [23]. The model is based on the following assumptions;

- the absence of interface states at the junction
- the current transport is through injection into the quasi-neutral regions or by recombination-generation in the depletion layer
- the junction is abrupt.

The major basis of Anderson's model was to account for the discontinuities in material properties using the bandgap ($\mathbf{E_g}$), electron affinity (χ) and work function (ϕ). Figure 2.14 gives two semiconductors before and after junction formation [17]. The work function depends on the doping levels but the energy bandgap and electron affinity are assumed constant for the two semiconductors. In a n-type semiconductor, the work function ϕ is given as:

$$\phi = \chi_n + \delta_n \tag{2.62}$$

where δ_n is the energy separation between the Fermi level and the conduction band. Assuming a n-type non-degenerate semiconductor, this energy separation is given as [15]:

$$\delta_n = \left(-\frac{kT}{q}\right) \ln\left(\frac{N_D}{N_C}\right) \tag{2.63}$$

where N_D is the donor concentration and N_C is the effective density of states at the conduction band-edge. Also for a p-type semiconductor, the work function becomes:

$$\phi_p = \chi_p + Eg_p - \delta_p \tag{2.64}$$

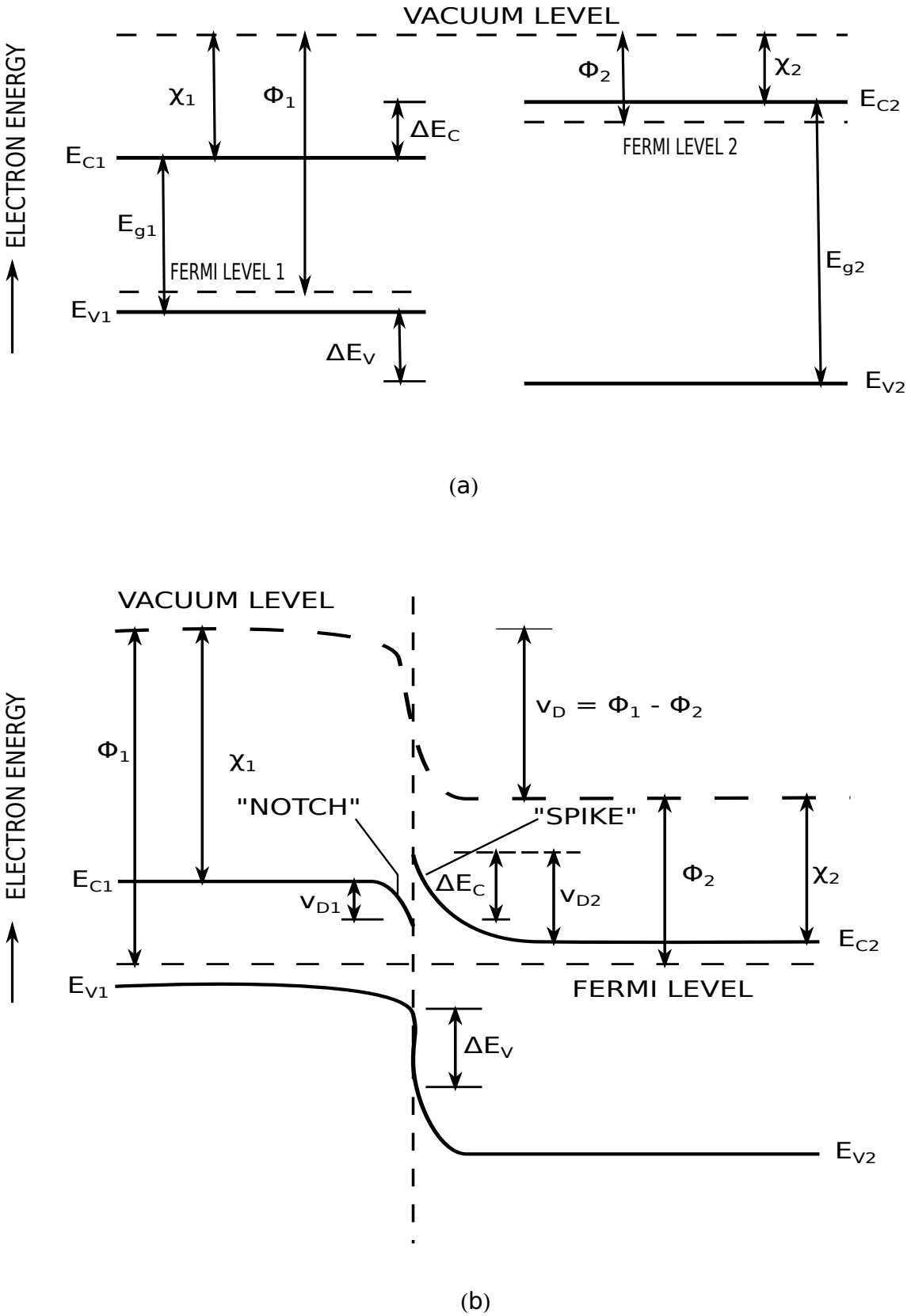

Figure 2.14: Anderson Model of two Dissimilar Semiconductors (a) Before Junction Formation (b) After Formation of the Junction.

where δ_p now refers to the energy separation between the valence band-edge and the Fermi level. For a non-degenerate p-type semiconductor, δ_p is given by:

$$\delta_p = \left(-\frac{kT}{q}\right) \ln\left(\frac{N_A}{N_V}\right) \tag{2.65}$$

where N_A and N_V are the acceptor concentration and effective density of states at the valence band-edge respectively. The conduction band-edge discontinuity is given by [22]:

$$\Delta E_{\mathrm{C}} = \chi_p - \chi_n \tag{2.66}$$

Equation (2.66) relates the electron affinities and the energy bandgaps of the two semiconductor materials hence ΔE_{V} can be given by:

$$\Delta E_{\mathrm{V}} = (Eg_n - Eg_p) - \Delta E_{\mathrm{C}} \tag{2.67}$$

The built in voltage due to the difference in work functions can be expressed as:

$$V_{\mathrm{D}} = \phi_p - \phi_n \tag{2.68}$$

or

$$V_{\mathrm{D}} = Eg_p + \Delta E_{\mathrm{C}} - \delta_p - \delta_n \tag{2.69}$$

Anderson model excluded interface states hence a depletion region is formed on either side of the junction which indicates that the width of this space-charge region could be obtained as usual by solving Poisson's equation on either side of the boundary [15], thus:

$$x_p = \sqrt{\frac{2\varepsilon_n\varepsilon_p N_{\mathrm{D}} V_{\mathrm{D}}}{qN_{\mathrm{A}}(\varepsilon_n N_{\mathrm{D}} + \varepsilon_p N_{\mathrm{A}})}} \tag{2.70}$$

$$x_n = \sqrt{\frac{2\varepsilon_n\varepsilon_p N_{\mathrm{A}} V_{\mathrm{D}}}{qN_{\mathrm{D}}(\varepsilon_n N_{\mathrm{D}} + \varepsilon_p N_{\mathrm{A}})}} \tag{2.71}$$

the total depletion width becomes

$$w = x_p + x_n = \sqrt{\frac{2\varepsilon_n\varepsilon_p V_{\mathrm{D}}(N_{\mathrm{A}} + N_{\mathrm{D}})^2}{qN_{\mathrm{A}}N_{\mathrm{D}}(\varepsilon_n N_{\mathrm{D}} + \varepsilon_p N_{\mathrm{A}})}} \tag{2.72}$$

for $N_{\mathrm{D}} \gg N_{\mathrm{A}}$ then the depletion width approximates to

$$w = \sqrt{\frac{2\varepsilon_p V_{\mathrm{D}}}{qN_{\mathrm{A}}}} \tag{2.73}$$

Also the junction capacitance could be obtained as:

$$C_{\mathrm{J}} = \sqrt{\frac{q\varepsilon_n\varepsilon_p N_{\mathrm{A}}N_{\mathrm{D}}}{2(\varepsilon_n N_{\mathrm{D}} + \varepsilon_p N_{\mathrm{A}})V_{\mathrm{D}}}} \tag{2.74}$$

Applying the same single-sided junction approximation $N_{\mathrm{D}} \gg N_{\mathrm{A}}$, Equation (2.74) changes to

$$C_{\mathrm{J}} = \sqrt{\frac{q\varepsilon_s N_{\mathrm{A}}}{2V_{\mathrm{D}}}} \tag{2.75}$$

Using the Anderson model, the $J - V$ relation of Figure 2.14 gives [17, 24]:

$$J = J_{oo} \exp\left[-\frac{q(\Delta E_{\mathrm{C}} + V_{\mathrm{D}})}{kT}\right] \times \left[\exp\left(\frac{qV}{kT}\right) - 1\right] \tag{2.76}$$

for an applied bias V, where

$$J_{oo} = qXN_{\mathrm{D}}\sqrt{\frac{D_{\mathrm{N}}}{\tau_n}} \tag{2.77}$$

X is the transmission co-efficient for electrons to cross the interface, D_{N} is the minority carrier diffusion co-efficient and τ_n is the minority carrier lifetime of the electrons in the p-type material.

It should be noted that when the two semiconductors are placed intimately close together, a "spike" and a "notch" appear at the junction between the two interfaces and this "spike" can act to block the collection of photogenerated carriers. In Anderson's model, the observed experimental values are much smaller than the predicted values and this he attributed to a high reflection of charge carriers at the interface.

2.6.1.1 Emission Model (Perlman and Feucht)

This model takes into account both the low values of transmission coefficient observed in the Anderson's model and the effects of the conduction band spike [25]. Assuming the case of a p–n heterojunction of the abrupt type in which the movement of charges are mostly by electrons, two different processes are expected for the *I-V* behaviour: (*i*) metal-semiconductor behaviour where current passage is lowered by the potential barrier on the n-side of the device, and (*ii*) homojunction type behaviour in which the build up of minority carriers at the edge of the depletion region obstructs the flow of current. When there is a large reverse potential barrier V_R as shown in Figure 2.15, metal-semiconductor behaviour dominates while homojunction type behaviour becomes dominant in situations where the spike lies below the conduction band of p-type material outside the space-charge region. Supposing the generation and recombination within the depletion region are negligible, the

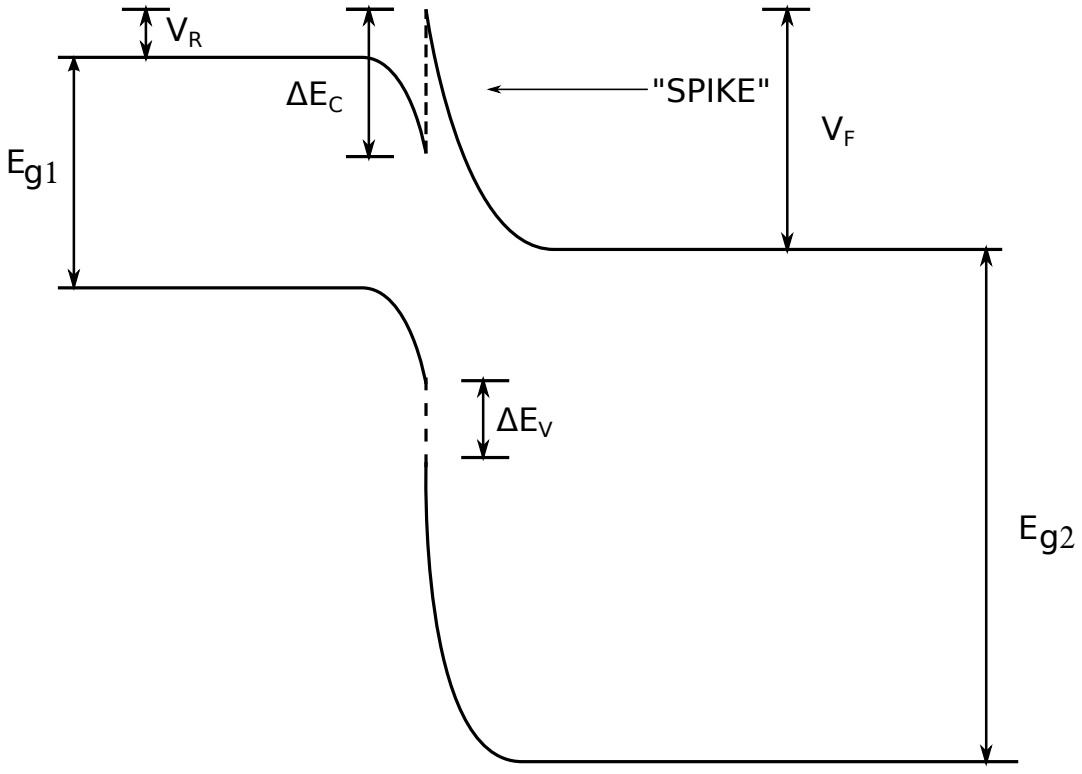

Figure 2.15: Perlman and Feucht Transport Model.

current-voltage characteristics can be defined as [25]:

$$J = J_o(\exp^{qV/kT} - 1) \tag{2.78}$$

where J_o is given as

$$J_o = \frac{1}{2} q X_m N_{\mathrm{D}} \sqrt{\frac{2kT}{\pi m_n{}^*}} \exp^{-q(V_F - V)/kT} \tag{2.79}$$

for cases in which metal-semiconductor type behaviour predominates, where $m_n{}^*$ is the effective mass of the electrons in the n-type material, V_{F} is the forward barrier height, and X_m is the transmission co-efficient. When homojunction type behaviour dominates,

$$J_o = q N_{\mathrm{D}} \sqrt{\frac{D_n}{\tau_n}} \tag{2.80}$$

where D_n and τ_n are the diffusion constant and lifetime of electrons in the p-type material. The emission model also has its setbacks in that the predicted exponential variation of reverse current followed by saturation at higher voltages is not in agreement with experiments [17].

2.6.1.2 Emission-Recombination Model (Dolega's Model)

The emission-recombination model is based on the assumption that there is thermal emission into and then fast recombination of electrons and holes within a thin layer at the metallurgical interface, the fast recombination being due to a high density of interface states within the junction region [26]. Such rapid recombination in the interface layer means that rectification does not exist unless the depletion region is wider than this layer. In this case, the p–n heterojunction is modelled as a series connection of the two metal-semiconductor contacts in which the bias voltage is controlling the boundary concentrations of the current carriers. According to Van Opdorf [17] a simple expression for the forward J-V characteristics is given as:

$$J = J_o(\exp^{qV/AkT} - 1) \tag{2.81}$$

and

$$J_o = J_{oo} \exp^{(-qV_{\mathrm{D}}/AkT)} \tag{2.82}$$

where J_{oo} is weakly temperature dependent. The diode factor A in Equation 2.81 and Equation 2.82 varies between $\exp^{(qV/kT)}$ and $\exp^{(qV/2kT)}$ (i.e. between A = 1 and A = 2) respectively, and depends on the ratio of the doping densities in the constituent semiconductors (p-type and n-type).

2.6.1.3 Tunnelling Model (Rediker, Stopek and Ward)

This model assumes that tunnelling through the "spike" of an abrupt p–n heterojunction limits the current flow [27]. Earlier work by Price [28], indicated that the electrons in the conduction band have to pass through or cross over the potential barrier in order to traverse the junction (see Figure 2.16) and hence electron flow under forward bias is mostly due to tunnelling through the barrier or thermal emission over it. Multiplying the

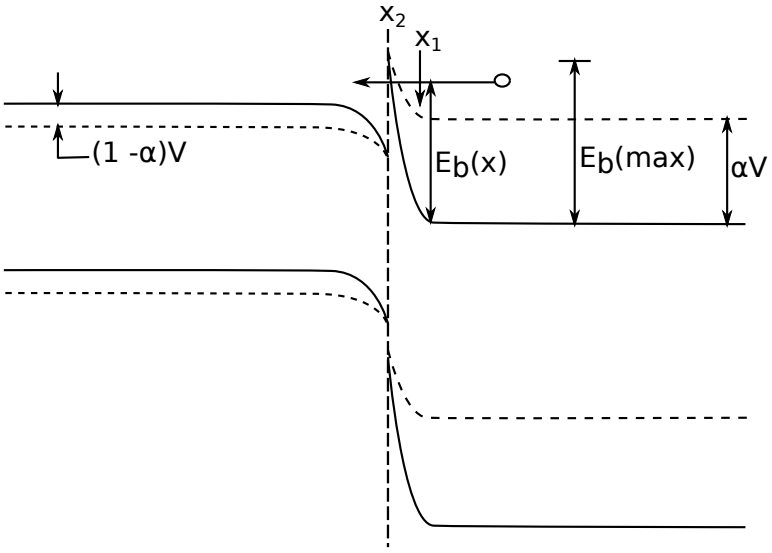

Figure 2.16: Rediker, Stopek and Ward Tunnelling Model.

incident electron flux with the expression for the tunnelling probability gives the tunnelling current in the heterojunction implying that the tunnelling phenomenon is much greater than thermal emission over the potential barrier. Hence the J-V characteristics under forward bias can be expressed by [29]:

$$J = J_o\left(T\right)\exp\left(\frac{V}{V_{\mathrm{o}}}\right) \tag{2.83}$$

where $J_o(T)$ varies slightly with temperature and V_{o} is a constant.

Attempts by Rediker et al. [27] did not indicate any expression for the dependence of

$J_o(T)$ on temperature. Later Newman [30] affirmed that $J_o(T)$ was proportional to $\exp(\frac{T}{T_o})$ modifying Equation(2.83) to

$$J = J_{oo} \exp\left(\frac{T}{T_o}\right) \exp\left(\frac{V}{V_o}\right) \tag{2.84}$$

where J_{oo}, T_o, and J_o are all constants.

2.6.1.4 Tunnelling-recombination Model (Donnelly and Milnes)

Donnelly and Milnes [31] proposed a variant of the tunnelling–recombination model as shown in Figure (2.17). They proposed that current transport in p-n heterojunctions

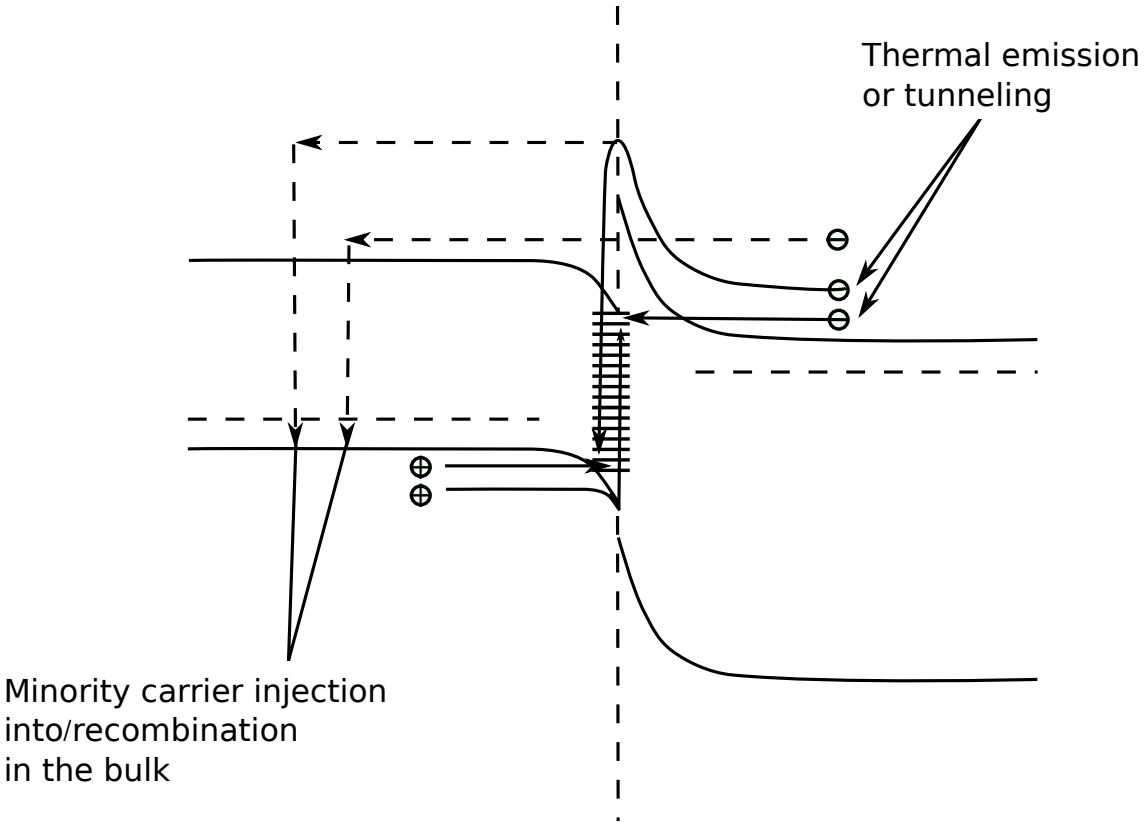

Figure 2.17: Donnelly and Milnes Tunnelling-recombination Model [17].

occur simultaneously and noted that it begins with the minority carrier injection into and recombination in the bulk of the lower E_g material (p-type), followed by recombination at the interface of both charge carriers transported by thermal emission over or by tunnelling through their respective barriers. The current contribution arising from thermal emission or tunnelling from the wider bandgap side to the smaller bandgap where minority carrier

injection into/recombination in the bulk is in dominance is given by:

$$I = I_o(\exp^{qV/AkT}) = I_{oo} \exp^{(-\Phi/kT)} \exp^{(qV/AkT)} \tag{2.85}$$

where I_{oo} = qASN$_B$ and S = V$_{th}$Q$_{IS}$N$_{IS}$, S is the surface recombination velocity, V$_{th}$ is the thermal velocity, N$_{IS}$ is the density of interface states, Q$_{IS}$ is the capture cross-section of the interface states and Φ is the activation energy.

2.6.2 Rectifying and Non-Rectifying Contacts

In general, Schottky barrier contacts results in a depletion region in the semiconductor which restricts the flow of current in one direction and prevents carrier injection in the other. Schottky barrier contacts are characterised by the following features [32, 33]:

- Minority carrier injection does not exist in the metal-semiconductor junction.
- There is no recombination in the depletion region.
- Ideality factor is approximately unity.
- In the metal, only electrons exists, there are no holes.
- Hence only depletion capacitance exists, there is no diffusion capacitance.
- Because of the absence of diffusion capacitance, Schottky diodes are very fast, hence their use in fast switching applications.

A metal-semiconductor contact whose contact resistance is very small when compared to the bulk resistance of the semiconductor material is referred to as an Ohmic contact. The non-rectifying behaviour is because Ohmic contacts form an accumulation layer of carriers in the semiconductor which allow current to flow in both directions. Figure 2.18 gives a typical I-V curve for an Ohmic contact and a Schottky barrier diode. Ohmic contacts are mostly preferred when fabricating solar cells because the contacts to the cell should not restrict current flow and also supply this current with a voltage drop that is adequately small relative to the voltage drop across the active region of the device. An ohmic contact is formed in a n-type material if the work function of the metal is smaller than that of

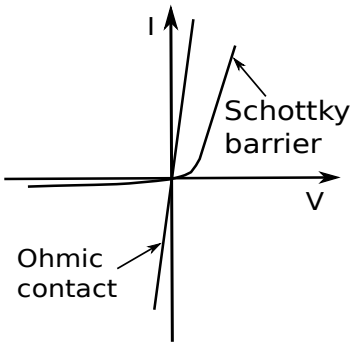

Figure 2.18: Typical I-V Characteristics for an Ohmic Contact and a Schottky Barrier Diode.

the semiconductor i.e. ($\phi_m < \phi_n$), whereas for a p-type material, the work function of the metal is larger than that of the semiconductor [19, 34]. The dominant transport mechanism depends on the doping concentration. A low doping concentration favours thermionic emission currents while tunnelling currents dominate for a high doping concentration.

2.7 Principles of Operation of Solar Cells (Photovoltaic Effect)

Solar cells are materials that convert sunlight into electricity using the photovoltaic effect. The photovoltaic effect involves the creation of a voltage or current in a device when light is shone on it. Under illumination, photons with h$\nu > E_g$ of the semiconductor are absorbed, resulting in the excitation of electrons from the valence band to the conduction band leaving equal number of holes in the valence band. When the e-h pairs are generated within the p-n junction or within a minority carrier diffusion length from the edge of each depletion region, the electric field in the space charge region separates them and drives them to an external circuit where they are collected. A diagram of a typical p-n junction solar cell is shown in Figure 2.19 while Figure 2.20 shows the energy band diagram of a solar cell under irradiation. The current-voltage characteristics of a p–n junction can be closely modelled by the ideal diode equation in the dark given by:

$$I = I_o(exp^{qV/AkT} - 1) \tag{2.86}$$

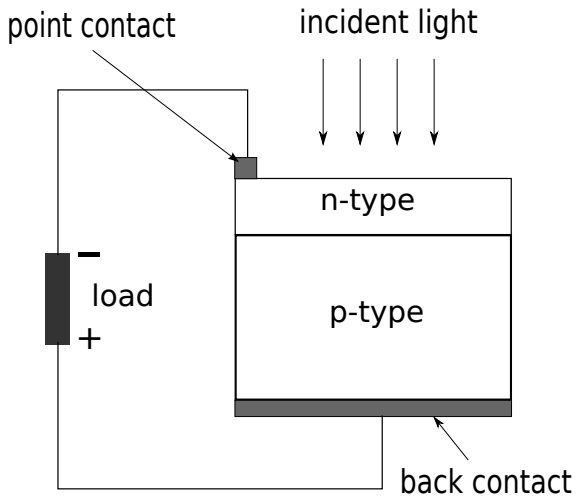

Figure 2.19: Schematic Diagram of a Solar Cell.

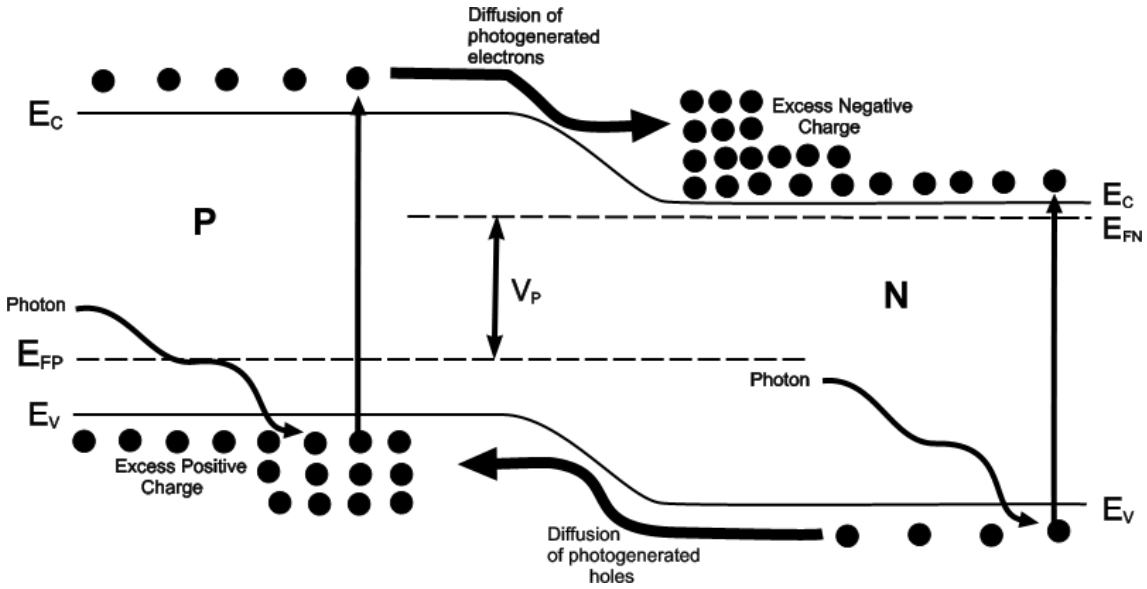

Figure 2.20: Band Diagram of Solar Cell Under Illumination.

Under solar irradiation, the photogenerated current is opposite in direction to the dark current and hence Equation 2.86 becomes [11]:

$$I = I_o(exp^{qV/AkT} - 1) - I_L \tag{2.87}$$

It is the photocurrent term I_L that manifests the shifting of the I-V curve vertically downwards as denoted in Figure 2.21. I_L is defined as:

$$\mathbf{I}_L = qAG(L_p + w + \mathbf{L}_n) \tag{2.88}$$

where G is the number of e-h pairs generated per unit volume per second, L_n and L_p are the minority carrier diffusion lengths in the p-side and n-side, w is the depletion region width and A is the cross-sectional area [4, 11, 13, 16].

Figure 2.22 shows the I-V and P-V (power-voltage) curves and the optimum point for the photovoltaic parameters of a solar cell. Electrically, a solar cell can be closely approximated by a circuit in which a current generator is placed in parallel with an asymmetric non-linear resistive element such as a diode. Figure 2.23 shows such scenario while Figure 2.24 gives the equivalent circuit of a non-ideal solar cell.

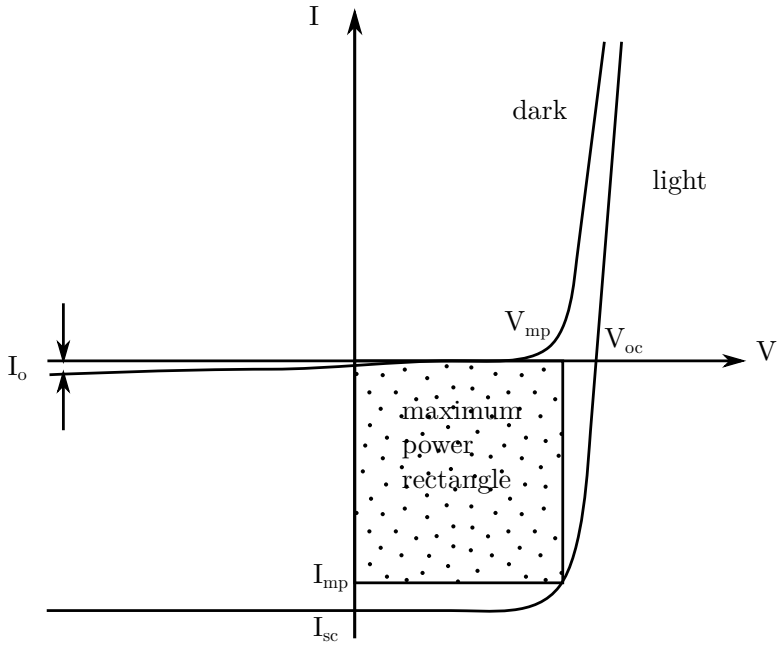

Figure 2.21: Typical I–V Characteristics of a p–n Junction in the Dark and Under Illumination.

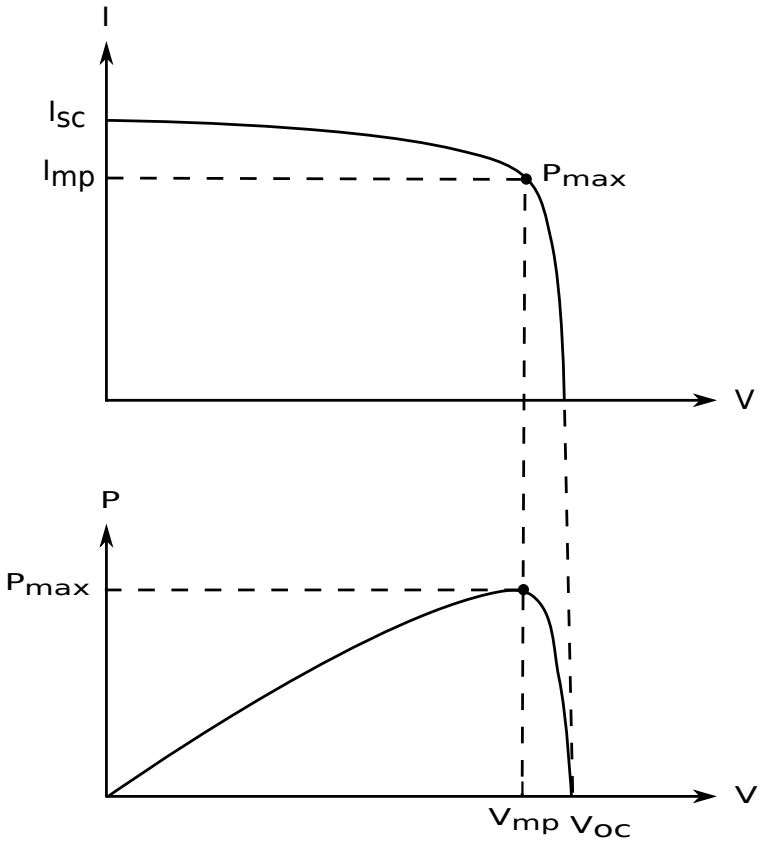

Figure 2.22: Typical I-V and P-V Curves of a Solar Cell.

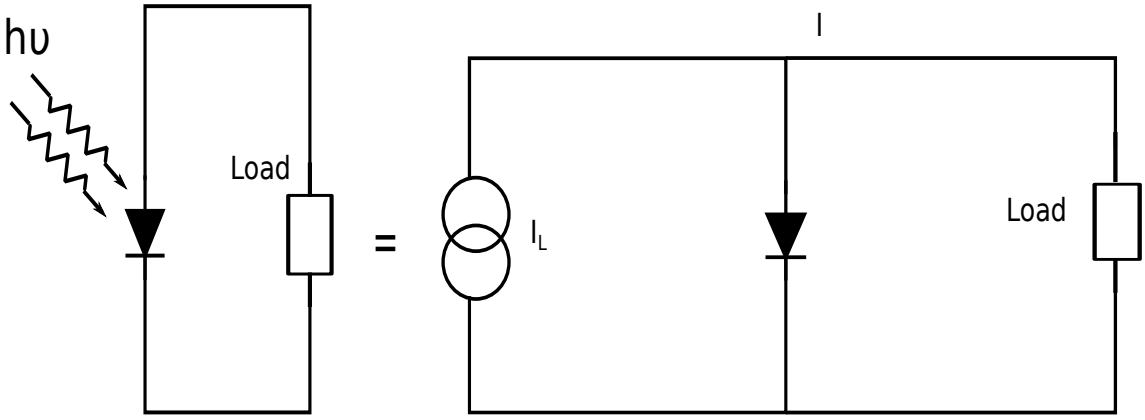

Figure 2.23: Equivalent Circuit of an Ideal p–n Junction.

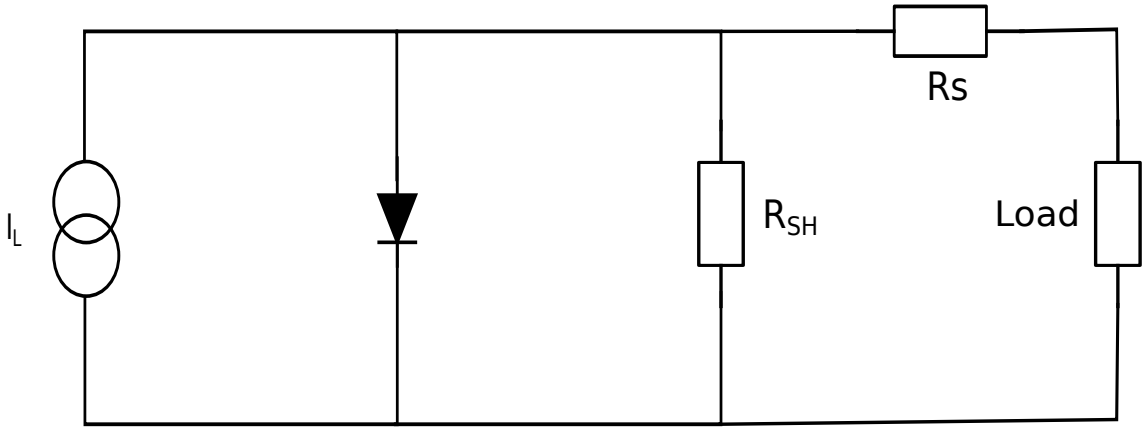

Figure 2.24: Equivalent Circuit of a Non-ideal Solar Cell [35].

2.7.1 Solar Cell Parameters (Solar Cell Figures of Merit)

The solar cell figures of merit are those parameters that enables the full interpretation of the I–V characteristics of a solar cell. These parameters include: the short-circuit current I_{sc}, the open-circuit voltage V_{oc}, the fill factor FF, and the solar conversion efficiency η.

- Short-circuit current: This is the maximum current that flows in the device at zero voltage (i.e. the current generated in the cell when the load resistance is zero). Considering the ideal case in which the effects of R_S and R_{SH} are ignored, substituting the I_{sc} conditions in Equation (2.87) reduces to Equation (2.88). This shows that I_{sc} is directly proportional to the incident light. In non-ideal solar cells, series and shunt resistances are always present and hence Equation (2.87) changes to [36]:

$$I = I_o\left(exp\frac{q(V - IR_s)}{AkT} - 1\right) + \left(\frac{V - IR_s}{R_{sh}}\right) - I_L \tag{2.89}$$

- Open-circuit voltage: This is the maximum voltage that the cell can deliver at zero current (i.e. the voltage produced when the load resistance is infinite). It is found to increase logarithmically with increase of the intensity of the incident solar illumination. From Equation (2.87), the open circuit voltage can be written as:

$$V_{\mathrm{OC}} = \frac{AkT}{q}\ln\left[\frac{I_{\mathrm{L}}}{I_{\mathrm{O}}} + 1\right] \tag{2.90}$$

Because $I_{\mathrm{L}} \gg I_{\mathrm{O}}$:

$$V_{\mathrm{OC}} \approx \frac{AkT}{q} \ln\left[\frac{I_{\mathrm{L}}}{I_{\mathrm{O}}}\right] \tag{2.91}$$

Equation (2.91) shows that V_{oc} not only depends strongly on the current generation and recombination mechanisms but also on I_o i.e. it depends on the nature of the junction transport current.

- Fill Factor: This indicates the "squareness" or sharpness of the knee of the $I-V$ curve i.e. how well the maximum power rectangle fits the area covered by the $I-V$ curve. It is an indicator of the junction quality and the degree of R_S present in the cell. It increases with increased V_{oc} and decreases at higher R_S. In real devices, maximum power cannot be extracted by operating the solar cell in short or open circuit conditions. When designing a solar cell, the ideal is to obtain a maximum power value $P_{max} = I_{max}V_{max}$ while ensuring that I_{max} and V_{max} are as close to the short circuit current and open circuit voltage as possible, the ratio of which is expressed by the fill factor [37, 38]:

$$FF = \frac{I_{max}V_{max}}{I_{sc}V_{oc}} \tag{2.92}$$

- Efficiency: This is the ratio of the power generated by the cell to the power of the incident light and expressed mathematically as:

$$\eta = \frac{I_{max}V_{max}}{P_{in}} = \frac{I_{sc}V_{oc}FF}{P_{in}} = \frac{I_{sc}V_{oc}FF}{\text{Area of the cell} \times \text{incident solar illumination}} \tag{2.93}$$

The efficiency of a solar cell can be improved by maximising I_{sc}, V_{oc} and FF. These parameters are obtained under standard test conditions of AM 1.5 global spectrum for terrestrial applications, a cell temperature of 25 °C, and an incident power density of $1000\,\mathrm{W\,m^{-2}}$.

2.7.2 Spectral Response/Quantum Efficiency

The spectral response (collection efficiency) of a solar cell is a measure of the photocurrent collected at each wavelength relative to the number of photons incident on the cell surface at that wavelength. At any given wavelength λ, the current responsivity $R_{I,\lambda}$ is given by:

$$\text{Current Responsivity, } R_{I,\lambda} = \frac{J_{sc}(\lambda)}{I_{\lambda}} \tag{2.94}$$

where $J_{sc}(\lambda)$ is the total photogenerated short circuit current density at any given λ and $I(\lambda)$ is the spectral irradiance of the incident light.

The quantum efficiency (number of electron-hole pairs generated for each incident photon) is given as:

$$\eta = \left[\frac{I_p}{q}\right]\left[\frac{P_{opt}}{h\nu}\right]^{-1} \tag{2.95}$$

where I_p is the photogenerated current from the absorption of incident optical power P_{opt} at a given λ (corresponding to a photon energy $h\nu$) [9].

From Equation (2.94) and Equation (2.95), it follows that

$$\eta = \frac{J_{sc}(\lambda)}{qN_{ph}} = \frac{hc}{q\lambda} R_{I,\lambda} \tag{2.96}$$

hence,

$$\eta \times \lambda = 1.242 \times 10^{-6} R_{I,\lambda} \tag{2.97}$$

where η is the quantum efficiency, q retains its meaning, N_{ph} is the incident photon flux, c is the speed of light hence it can be inferred that the product of the external quantum efficiency (EQE) and wavelength is proportional to the spectral response as shown in Equation (2.97). This strong link of spectral response with wavelength explains the dependence of cell performance on the spectral content of the incident radiation and the "heterojunction window effect" usually observed in heterojunction solar cell spectral response/quantum efficiency curve. The internal quantum efficiency (IQE) is related to

the (EQE) as:

$$IQE = \frac{EQE}{(1-R)} \tag{2.98}$$

where the (1-R) term accounts for reflection [8, 35, 39].

2.7.3 Loss Mechanisms in Solar Cells

The predicted theoretical efficiency of a given solar cell is hardly obtained in practice because of the loss mechanisms inherent in real devices which arises mostly from nature of material or design issues. These includes [40]:

- Photon losses: These include (i) thermalisation of hot carriers for h$\nu > E_g$ in which the excess energy is wasted as heat (ii) transmission losses for h$\nu < E_g$, there is no e-h pair generation and also long wavelength photons are not usefully absorbed (iii) reflection losses; some incident photons undergo reflection and are not absorbed (iv) some photon absorption due to extrinsic process do not produce e-h pairs but also results in heat generation.

- Carrier losses: These include (i) surface recombination (ii) bulk recombination (iii) recombination at the junction (iv) collection efficiency loss arising from the fact that not all the photoexcited carriers are utilised by the internal electric field (vi) energy loss due to thermalisation of carriers over the potential barrier i.e. for E$_g > qV_{oc}$, the energy consumed in free carrier generation (h$\nu > E_g$) is much greater than the open-circuit voltage. All carrier loss processes results in heat generation in the cell.

- Power losses: These are due to the presence of series and parallel resistances in the device. The resistances of the bulk p-type and n-type regions and associated with the resistances of the electrical contacts to these regions [38, 40]. This is shown on Figure 2.25(a)–(b). The short circuit current and fill factor are mostly affected by the presence of a high series resistance (R_s). Ideally R_s should be zero but in practice, it is typically $< 1.3\,\Omega\,\mathrm{cm}^2$ for commercial cells. Series resistance generally depends on the depth of the junction, the doping concentration of the p-type and n-type sides as well as the front contacts [9]. The negative effect of an increasing value of series

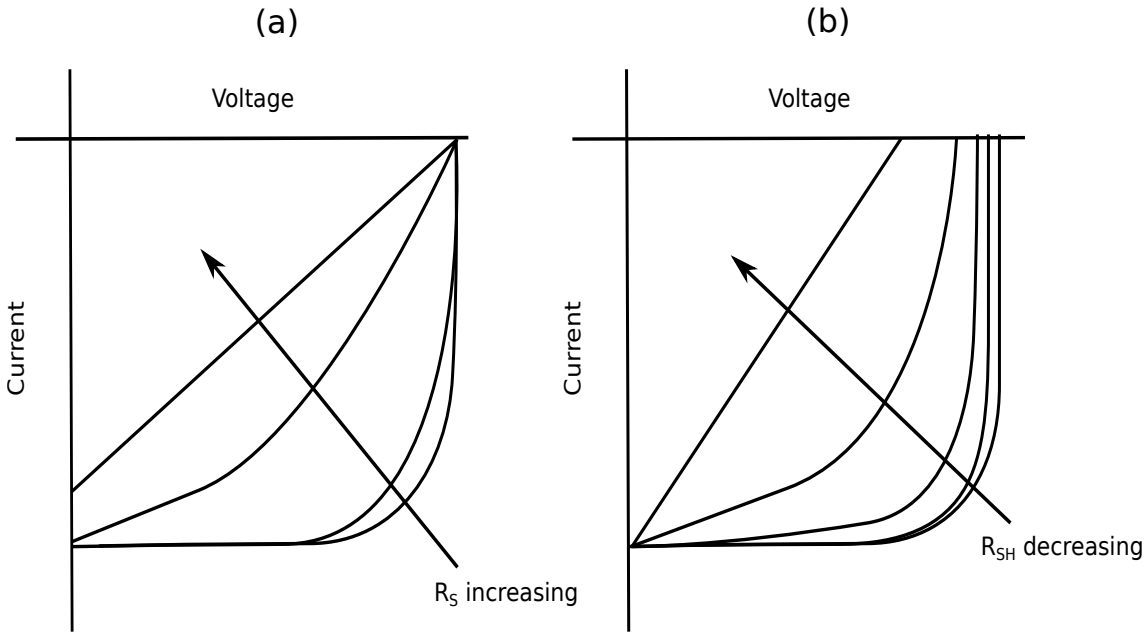

Figure 2.25: The Effects of Resistance on a Silicon Solar Cell (a) Series Resistance (b) Shunt Resistance.

resistance can be seen in the $I - V$ plot of a silicon cell shown in Figure 2.25(a). The shunt resistance (R_{sh}) arises from the shunting or leakage paths between the n- and p-type regions. Ideally, the value of R_{sh} should be infinite but in practice values of $R_{sh} > 100$ ohms are regarded as acceptable. Also the influence of shunt resistance on the open circuit voltage as shown in Figure 2.25(b) clearly illustrate the adverse effect on the device. Power losses result in heat generation in the solar cell device [41]. In general, careful material control and cell design can help minimise some of the aforementioned losses substantially.

2.8 Heterojunction Material Requirements

The fundamental requirements for a material to function either as an absorber or window layers for a heterojunction device are many and varied. This is because material properties depends on a lot of parameters ranging from atomic to bulk scale. For instance, an attempt to characterise a semiconductor fully will require some extensive knowledge of the material, optical and electrical properties which in turn depends on some understanding of other parameters which to mention but a few include:

- Band structure and the nature of bonds holding the atoms together.

- Chemical composition of the pure crystal which will give information on the intrinsic properties (E_g and effective masses of the carriers).
- Native lattice defects (vacancy, interstitials, complexes and dislocations) which introduce energy states within the band gap of the material and some perturbations thereby modifying the intrinsic properties.
- Extrinsic properties (doping) usually done intentionally or unintentionally and has the effect of substantial modification of the intrinsic material property such as bandgap narrowing, band tailing, deformation potential and compressional strain.
- Structural dimensions which arises when the dimension are comparable to de Broglie wavelength of the charge carriers such that quantum size effects dominates.

2.8.1 Absorber Layer Requirements

The fundamental requirements for a material to function as an absorber layer include but are not limited to:

- Bandgap – The material should have a bandgap near to 1.5 eV to ensure maximium absorption of the solar radiation since this is close to the optimum for photovoltaic solar energy conversion. Direct energy bandgap materials are preferred because carriers are generated close to the junction and hence layers of a few microns ($< 3\mu m$) can be used to make devices. This will lead to a reduction in the overall cost.
- Optical absorption coefficients – The optical absorption coefficient, α should be $> 10^4 cm^{-1}$ as this will make for a thin absorber layer (as photons are absorbed close to the junction interface) resulting in reduced material requirement.
- Conductivity type – The absorber layer should be p-type because the minority diffusion length of electrons in a p-type semiconductor is much larger than that of holes in an n-type semiconductor.
- Diffusion voltage –This should be as large as possible to ensure maximum V_{oc} which is proportional to the diffusion voltage.

- Electrical contacts – The external contacts to the absorber layer must be Ohmic so that device performance will not be affected.

- Grain boundaries – These are regions of increased recombination due to structural defects and/or segregated impurities. They impede carrier transport by charge trapping to form potential barriers or as sites for carrier recombination. This could be minimised by ensuring that the absorber layers are polycrystalline material with large columnar grains.

- Material resistivity – A good absorber layer should have low resistivity so as to avoid excessive power drop. This is achieved by doping the layers with suitable materials.

- Film thickness – The absorber layer thickness must be large enough to absorb most of the incident radiation, usually at least twice the optical absorption length, $\frac{1}{\alpha}$ i.e $\frac{2}{\alpha}$ [38]. Also the absorber layer thickness should be large enough to provide substantial grain size which must be several times the average optical absorption length for solar photons in order to reduce loss of photogenerated carriers [42]. It has been established that efficiency of polycrystalline solar cells is enhanced for higher grain sizes [43].

2.8.2 Window Layer Requirements

The general requirements for a material to be used as a window layer include:

- Bandgap –Mostly materials with an energy bandgap $\geq 2\,\text{eV}$ are preferred as this will allow most of the incident sunlight to be transmitted to the absorber layer.

- Material resistivity – Despite being a large energy bandgap material a low value of window layer resistivity (low series resistance) is required to minimise power loss.

- Crystallite size – Grain size has a strong correlation with solar cell efficiency [43]. A good window layer should consist of large crystallites with good crystallinity as this will make for a near defect free junction such that the density of short circuit paths will be substantially reduced.

- Thermal expansion mismatch – Window layers should be chosen in a way to ensure a matching of the thermal expansion coefficient to that of the absorber layer. This is important because of the high temperatures at which most junctions are formed.

- Electron affinities – The window layer should be chosen such that the absence of a potential spike with the absorber layer is ensured at the junction. This is because the presence of band (conduction or valence) spikes will impede the transport of photogenerated carriers thereby reducing device performance.

- Lattice mismatch – The window layer should be chosen in a way that ensures very little mismatch of lattice constants to that of the absorber partner. Low lattice mismatch reduces interface state thereby minimising loss of photogenerated carriers that could have arisen due to recombination effects. The degree of lattice mismatch can be deduced from [44] as:

$$\text{Lattice mismatch} \quad = \quad \frac{2(\lambda_1 - \lambda_2)}{\lambda_1 + \lambda_2} \tag{2.99}$$

  where λ_1 and λ_2 are the lattice constants of the two semiconductors.

2.9 Thin Film Solar Cell Configurations

Thin film solar cell are made using either the superstrate or substrate configurations. With the superstrate configuration the glass substrate serves as the supporting structure, and the window for the illumination, since light is shone on the solar cell through the glass substrate. A schematic diagram of a typical superstrate configuration device for a SnS/CdS solar cell is shown in Figure 2.26. In a substrate configuration device the light enters through the front contact. For this type of configuration, the choice of a suitable metal or semiconductor surface is critical since this layer must form an Ohmic contact with the p-type layer. Figure 2.27 gives a schematic diagram of a typical SnS/CdS substrate configuration solar cell. This configuration offers flexibility in that recrystallisation of the absorber layer is possible. Both configurations are employed in the advanced thin film solar cells based on the use of CdTe and CIGS absorber layers.

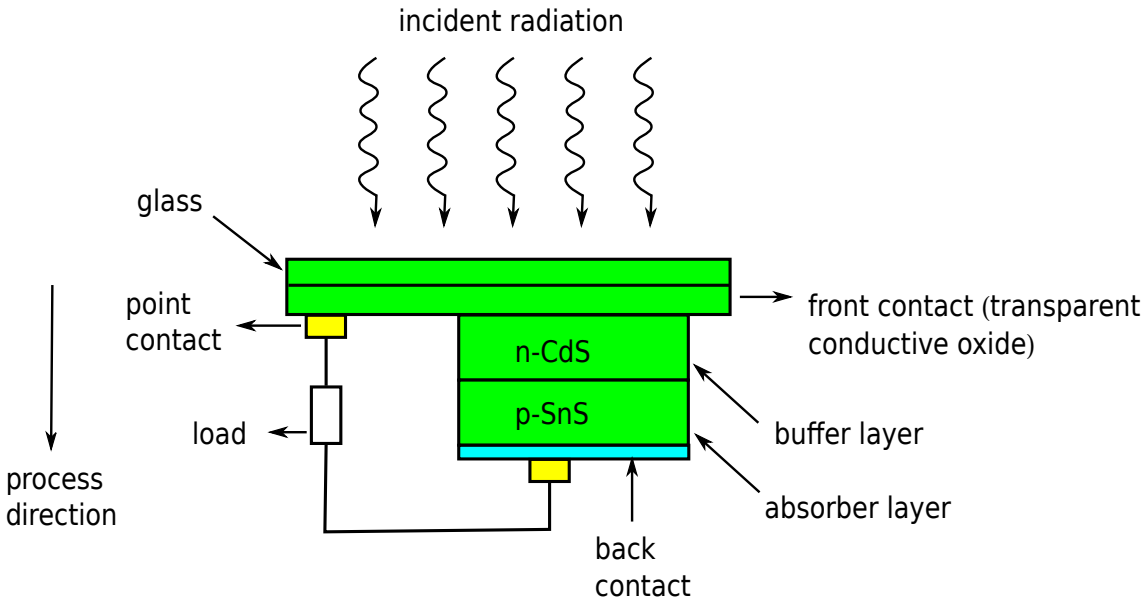

Figure 2.26: Superstrate Configuration of SnS/CdS Thin Film Solar Cell.

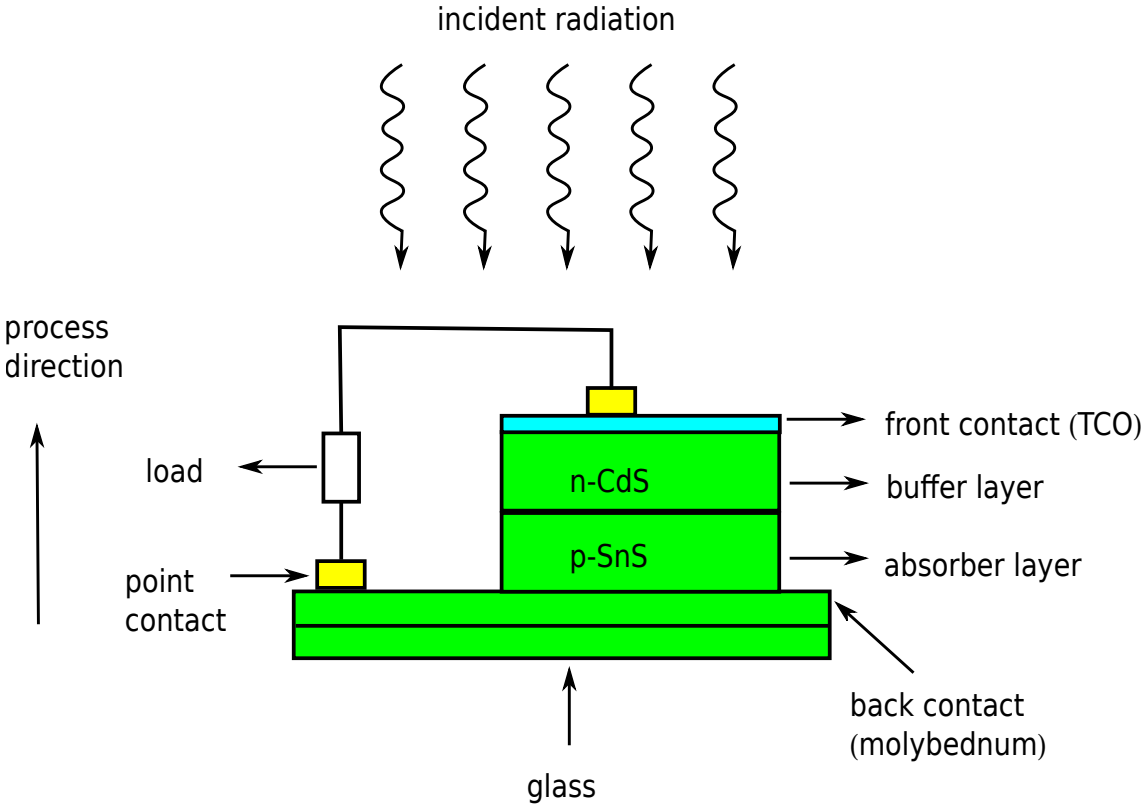

Figure 2.27: Substrate Configuration of SnS/CdS Thin Film Solar Cell.

References

[1] G. N. Tiwari. *Solar Energy: fundamentals, design, modelling and applications*. Narosa Publishing House, New Delhi, 2002 (cit. on pp. 11, 13).

[2] R. C. Willson and H. S. Hudson. "Solar luminosity variations in solar cycle 21". In: *Nature* 332 (1988), pp. 810–812 (cit. on p. 11).

[3] C. Gueymard. "The sun's total and spectral irradiance for solar energy applications and solar radiation models". In: *Solar Energy* 76 (2004), pp. 423–453 (cit. on pp. 11, 12).

[4] R. W. Miles, K. M. Hynes, and I. Forbes. "Photovoltaic solar cells: An overview of state-of-the-art cell development and environmental issues". In: *Progress in Crystal Growth and Characterization of Materials* 51 (2005), pp. 1–42 (cit. on pp. 11, 48).

[5] J. I. Pankove. *Optical Processes in Semiconductors*. Prentice Hall Inc., Englewood Cliffs, New Jersey, 1971 (cit. on pp. 13, 14).

[6] J. Bardeen, F. J. Blatt, and L. H. Hall. "Proceedings of the Conference on Photoconductivity, Atlantic City, November 4-6, 1954". In: (John Wiley & Sons, Inc., New York, 1956) (cit. on p. 14).

[7] C. Hu and R. M. White. *Solar cells: from basic to advanced systems*. Mc Graw-Hill, Inc, New York, 1983 (cit. on pp. 14, 16).

[8] A. L. Fahrenbruch and R. H. Bube. *Fundamentals of Solar Cells: Photovoltaic Solar Energy Conversion*. Academic Press, New York, 1983 (cit. on pp. 14, 53).

[9] S. M. Sze. *Semiconductor Devices: Physics and Technology*. 1st Edition. Wiley, New York, 1985 (cit. on pp. 15, 16, 23, 24, 27, 28, 31, 33, 52, 53).

[10] P. Bhattacharya. *Semiconductor optoelectronic devices*. Prentice-Hall, Inc., Englewood Cliffs, New Jersey, 1994 (cit. on pp. 16, 24, 32).

[11] M. A. Green. *Solar Cells: Operating Principles, Technology, and System Applications*. Prentice Hall Inc., Englewood Cliffs, New Jersey, 1982 (cit. on pp. 16, 48).

[12] G. Parker. *Introductory semiconductor device physics*. Prentice Hall, New York, 1994 (cit. on pp. 18, 20).

[13] A. S. Grove. *Physics and technology of semiconductor devices.* Wiley, New York, 1967 (cit. on pp. 19, 21, 48).

[14] S. M. Sze. *Semiconductor Devices: Physics and Technology.* 2nd Edition. Wiley, New York, 2001 (cit. on pp. 19, 30).

[15] S. M. Sze. *Physics of Semiconductor Device.* Wiley, New York, 1981 (cit. on pp. 20–22, 37, 39).

[16] B. G. Streetman and S. K. Banerjee. *Solid State Electronic Devices.* 6th Edition. Prentice- Hall, Inc, New Jersey, 2006 (cit. on pp. 23, 32, 34, 48).

[17] B. L. Sharma and R. K. Purohit. *Semiconductor Heterojunctions.* Pergamon Press, Oxford, 1974 (cit. on pp. 26, 37, 40, 42, 44).

[18] B. G. Streetman. *Solid State Electronic Devices (4th ed.)* Prentice-Hall, Inc., Upper Saddle River, New Jersey, 1995 (cit. on p. 26).

[19] J. Singh. *Semiconductor Devices.* McGraw-Hill, Inc, New York, 1994 (cit. on pp. 26, 46).

[20] W. Shockley. "The theory of p–n junctions in semiconductors and p–n junction transistors". In: *Bell Systems Technical Journal* 28 (1949), pp. 435–489 (cit. on p. 29).

[21] R. S. Muller and T. I. Kamins. *Device Electronics for Integrated Circuits.* John Wiley & Sons, New York, 1977 (cit. on p. 34).

[22] K. W. Mitchell. *Evaluation of the CdS/CdTe Heterojunction Solar Cell.* Garland Publishing Inc., New York, 1979 (cit. on pp. 34, 35, 39).

[23] R. Anderson. "Experiments on Ge-GaAs heterojunctions". In: *Solid State Electronics* 5 (1962), pp. 341–344 (cit. on p. 37).

[24] A. G. Milnes and D. L. Feucht. *Heterojunctions and Metal-Semiconductor Junctions.* Academic Press, New York, 1972 (cit. on p. 40).

[25] S. S. Perlman and D. L. Feucht. "p-n Heterojunctions". In: *Solid-State Electronics* 7 (1964), pp. 911–923 (cit. on p. 41).

[26] U. Dolega. “Theorie des pn-Kontaktes zwischen Halbleitern mit verschiedenen Kristallgittern”. In: *Zeitschrift Naturforschung Teil A* 18 (1963), p. 653 (cit. on p. 42).

[27] R. Rediker, S. Stopek, and J. H. R. Ward. “Interface-alloy epitaxial heterojunctions”. In: *Solid State Electronics* 7 (1964), pp. 621–622 (cit. on p. 43).

[28] P. J. Price. “Transmission of Bloch waves through crystal interfaces”. In: *Proc. Int. Conf. on Semiconductors*. 1962, p. 99 (cit. on p. 43).

[29] C. J. M. Van Opdorp. PhD thesis. Technische Hodgeschool, Eindhoven, Netherlands, 1963 (cit. on p. 43).

[30] P. C. Newman. “Forward characteristics of heterojunctions”. In: *Electronics Letters* 1 (1965), p. 265 (cit. on p. 44).

[31] J. P. Donnelly and A. G. Milnes. “Current/Voltage characteristics of pn Ge-Si and Ge-As heterojunctions”. In: *Proceedings of the Institution of Electrical Engineers* 113 (1966), pp. 1468–1476 (cit. on p. 44).

[32] C. T. Sah. *Fundamentals of Solid State Electronics*. World Scientific, Singapore, 1991 (cit. on p. 45).

[33] E. F. Schubert. *Physical Foundations of Solid State Devices*. Rensselaer Polytechnic Institute, Troy, New York, 2009 (cit. on p. 45).

[34] R. H. Bube. *Photoconductivity of Solids*. John Wiley, New York, 1960 (cit. on p. 46).

[35] H. J. Hovel. *Semiconductors and Semimetals. Volume II: Solar Cells*. Ed. by R. K. Willardson and A. C. Beer. Academic Press, New York, 1975 (cit. on pp. 50, 53).

[36] J. Nelson. *The Physics of Solar Cells*. Imperial College Press, London, 2003 (cit. on p. 50).

[37] J. Lindmayer. “Theoretical and practical fill factors in solar cells”. In: *COMSAT Technical. Rev* 2 (1972), p. 105 (cit. on p. 51).

[38] Richard H. Bube. *Photovoltaic Materials*. Imperial College Press, London, 1998 (cit. on pp. 51, 53, 56).

[39] S. R. Wenham, M. A. Green, M. E. Watt, and R. Corkish. *Applied Photovoltaics*. Earthscan, UK, 2007 (cit. on p. 53).

[40] A. Rothwarf and K. W. Böer. "Direct conversion of solar energy through photovoltaic cells". In: *Progress in Solid State Chemistry* 10 (1975), pp. 71–102 (cit. on p. 53).

[41] K. L. Chopra and S. R. Das. *Thin Film Solar Cells*. Plenum Press, New York, 1983 (cit. on p. 54).

[42] A. Rothwarf. "Crystallite size considerations in polycrystalline solar cells". In: *12th Photovoltaic Specialists Conference*. Vol. 1. 1976, pp. 488–495 (cit. on p. 56).

[43] A. K. Ghosh, C. Fishman, and T. Feng. "Theory of the electrical and photovoltaic properties of polycrystalline silicon". In: *Journal of Applied Physics* 51 (1980), pp. 446–454 (cit. on p. 56).

[44] M. N. Rudden and J. Wilson. *Elements of Solid State Physics*. John Wiley and Sons, New York, 1993 (cit. on p. 57).

Chapter 3

Literature Review

3.1 Tin sulphide: Historical Perspective

Tin sulfide, SnS belongs to IV-VI group of compound semiconductors. Other phases of Sn_xS_y include SnS_2, Sn_2S_3, Sn_3S_4 and Sn_4S_5 with SnS, SnS_2 and Sn_2S_3 the most stable phases [1–3]. The origin of SnS (herzenbergite) can be traced to the Latvian–German chemist, Prof. Robert Herzenberg who discovered it in 1934 in the Maria-Teresa mine near Huari, between Oruro and Uyuni, Bolivia [4, 5]. The synthesis of single crystals of SnS by reacting stoichiometric tin and sulphur over a temperature range of 600 °C - 750 °C was also reported by Herzenberg. The crystallographic properties of SnS are: crystal structure – orthorhombic, lattice parameters: a = 4.32Å, b = 11.19Å, c = 3.97Å, Ratio of lattice constants: a:b:c = 0.386 : 1 : 0.355, unit cell volume: V = 191.91Å (calculated from unit cell) [5–7]. SnS dimensions belongs to the orthorhombic space group *Pbnm* where six sulphur atoms surround each tin atom with three short Sn-S bonds within the layer and three long bonds connecting two neighbouring SnS layers. The electrical conductivity of SnS is found to be predominantly p-type [8].

3.2 Chronology of Single Crystalline SnS Studies

Pioneering work on SnS was mostly done on single crystal SnS.

- Anderson and Morton [9–11] used the Bridgemann technique to grow the layers of SnS. They established that the conductivity of SnS between room temperature and

400 °C varies as:

$$\sigma(T) = A_1 e^{-E_1/2kT} + A_2 e^{-E_2/2kT} \tag{3.1}$$

and this variation could be correlated directly with small changes in stoichiometric composition brought about by chemical treatments. They also studied the effects of hydrogen, oxygen and hydrogen sulphide treatments on the grown layers and observed a decrease in conductivity for samples treated in hydrogen ambient at temperatures below those at which a reduction to tin can occur. However exposure to oxygen or hydrogen sulphide restores the conductivity of the samples. They attributed the changes in the conductivity to the stoichiometric excess of non-metal in the lattice. Anderson and Ridge [12] noted that the melting point of SnS is 870 °C while Clark and Anderson [13] reported on the conducting properties of the layers.

- Braithwaite [14] reported on the infrared photoconductivity of SnS and observed that signals were detected at a wavelength threshold of 0.9 µm.

- Gorbrecht and Barschat [15] worked on the infrared, transmission, photoconductivity and rectifying properties of layers of SnS, and determined an energy bandgap of 1.25 eV.

- Albers and Haas [8] studied the electrical and optical properties of SnS crystals grown by melting the constituent elements in a quartz tube at 900 °C. They determined that the layers were p-conductivity type with a hole concentration of 10^{17} – 10^{18} cm^{-3} and hole mobility of 65 $\mathrm{cm}^2/\mathrm{V\,s}$ at 25 °C. The conductivity along the c-axis of the crystals was found to be six times smaller than in the perpendicular direction. They determined an energy bandgap of (1.07 ± 0.04) eV and they observed that the melting point of SnS is (880 ± 5) °C.

- Haas and Corbey [16] reported on the optical constants: refractive index, dielectric constants, and also on the effective charge and masses. They also analysed the infrared reflection spectrum of p-conductivity type SnS crystals from 2 µm to 25 µm, and explained the observed dispersion on the basis of the free holes and vibrations in the lattice structure of the crystals.

- Albers et al. [17] presented an extensive report on the equilibrium between the solid, liquid and gaseous phases of SnS. The most significant findings of the work are that there are two compounds (SnS and SnS_2) which melt congruently, that the melting point of tin sulphide in a neutral atmosphere is $(1153 \pm 5)\,K$, the boiling point at normal air pressure is 1503 K and the maximum melting point of SnS to be at sulphur pressure of 3.34×10^3 Pa while for SnS_2(1143 K) is at sulphur pressure of 4×10^6 Pa respectively. Figure 3.1 gives the phase diagram as presented by [17]. Albers also reported on the variation of hole mobility with temperature [18].

- Hans Rau [19] reported on the high temperature equilibrium of atomic disorder in SnS and also observed that the layers are p-conductivity type.

- Feiziev et al. [20] studied the heat capacity(C_p), thermal diffusivity($\varkappa$) and the thermal conductivity(λ) of SnS and determined that $C_p \propto T^3$ where T is the temperature.

- Lambros et al. [21] presented work on the optical absorption edge in SnS grown by melting stoichiometric amounts of the compounds in an evacuated quartz tube and obtained an indirect energy bandgap in the range 1.095 eV to 1.142 eV and the refractive index between 3.6–4.6.

- Goswami and Mitra [22] reported extensively on the optical constants (refractive index, extinction coefficient, optical absorption coefficient) of SnS and its variation with film thickness, wavelength and photon energy for vacuum deposited SnS films. They obtained an energy bandgap of 1.6 eV.

- Chamberlain et al. [23] used far-infrared reflectivity measurements to investigate SnS single crystals grown by the Bridgeman technique. They used polarised radiation in the frequency range 50 cm^{-1} to 350 cm^{-1} and found the lattice constants to be: a = 3.99 Å, b = 4.34 Å and c = 11.20 Å. They observed n- and p-type conductivity with carrier concentrations in the range 10^{17} – 10^{18} cm^{-3}.

- Chamberlain and Merdan [24] obtained an indirect energy gap of 1.13 ± 0.02 eV and 1.22 ± 0.02 eV at 77 K and a direct energy gap of 1.43 ± 0.02 eV. The layers show a p-conductivity type with a carrier concentration N_A-$N_D \approx 10^{17}$ – 10^{18} cm^{-3}.

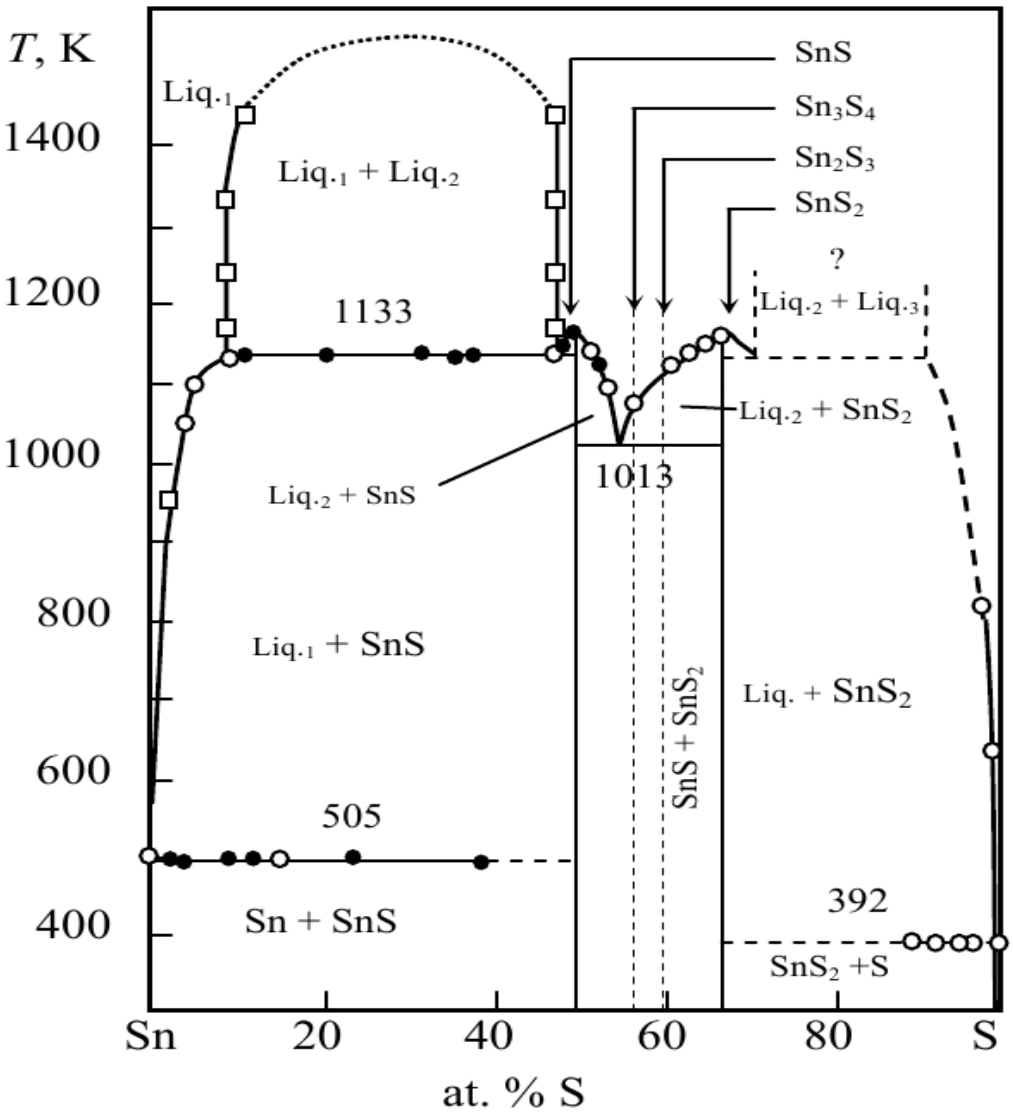

Figure 3.1: Phase Diagram of the SnS System.

Hughes et al. [25] also obtained a p-conductivity type with a carrier concentration of $10^{18}\,\mathrm{cm}^{-3}$.

- Nikolic [26] and Chandrasekhar [27] reported on the Raman modes of SnS grown using the Bridgeman technique. Nikolic and Todorović [28] also used the same technique to grow SnS layers, measured the photo-acoustic response and transmission spectra, and obtained an energy bandgap in the range 0.95 eV to 1.15 eV and a free carrier concentration of $7.5 \times 10^{18}\,\mathrm{cm}^{-3}$. The first research group to fabricate n-p junction photovoltaic detectors with the p-type single crystal SnS using Sb+ ion implantation was Trbojevic et al. [29]. They studied the current-voltage and capacitance-voltage characteristics and obtained a peak quantum efficiency of 44%.

- Chattopadhyay et al. [30] used elastic neutron scattering to study crystal structure of SnS in the temperature range 293 K to 1000 K. They observed that SnS undergoes a second order phase transition from α-phase to the high temperature β-phase at 887 K. Chattopadhyay et al. [31] also studied the structural phase transitions in SnS using neutron diffraction in the temperature range 295 K to 1000 K and also observed second order phase transition from α-phase to β-phase.

- Parenteau and Carlone [32] studied the influence of temperature and pressure on the electronic transitions in SnS and SnSe semiconductors. They obtained a direct and an indirect energy bandgap of 1.296 eV and 1.047 eV respectively for SnS.

- Elkorashy [33] used the Bridgman technique to grow SnS crystals and noted that the samples exhibit p-conductivity type with a hole concentration of $10^{18}\,\mathrm{cm}^{-3}$.

Other authors include Wiedeimeir and Hans Georg von Schnering [34] reported on the "Refinement of the structures of GeS, GeSe, SnS and SnSe", Wiedeimeir and Csillag [35] on the "thermal expansion and high temperature transformation of SnS and SnSe", Wiedeimeir and Csillag [36] on "equilibrium sublimation and thermodynamic properties of SnS" and Schnering and Wiedeimeir [37] on "the high temperature structure of β-SnS and β-SnSe". These authors all observed the orthorhombic structure for SnS. These earlier works have served as a gateway to the current investigation of SnS which is largely dominated by polycrystalline layers.

3.3 Thin Film Deposition Techniques

Thin film deposition techniques can be broadly categorised into physical deposition and chemical deposition methods. Physical deposition includes physical vapour deposition (PVD) techniques such as thermal evaporation, electron beam evaporation, sputtering, closed space vapour transport (CSVT), atomic layer deposition (ALD), brush plating, hot wall deposition (HWD), pulsed laser deposition and molecular beam epitaxy (MBE). A typical schematic diagram of a process flow of physical vapour deposition is shown on Figure 3.2.

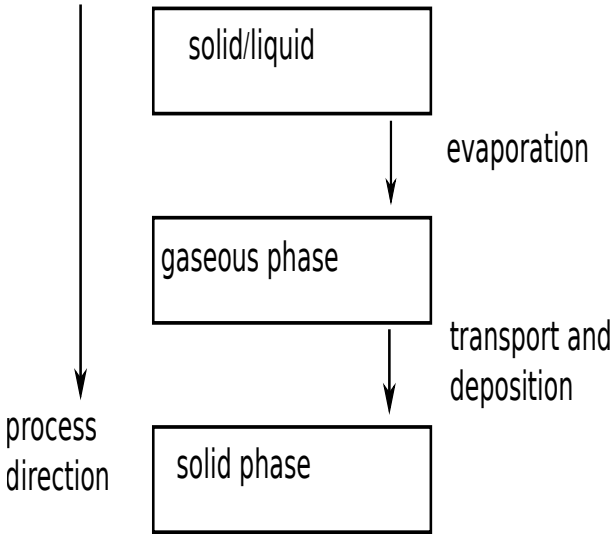

Figure 3.2: Schematic of a PVD Process Flow.

Chemical deposition includes chemical bath deposition (CBD), chemical spray pyrolysis (CSP), successive ionic layer adsorption and reaction (SILAR), chemical vapour deposition (CVD), metal organic chemical vapour deposition (MOCVD), plasma enhanced chemical vapour deposition (PECVD), spin coating, dip technique and the solution dispersion method.

3.3.1 Physical Deposition

3.3.1.1 Conventional Thermal Evaporation Technique

The fundamental steps in vacuum evaporation are as shown on Figure 3.2 i.e.;

- Phase change from solid or liquid into a gaseous state.

- Vapour material travels from the evaporation source to the substrate at a low gas pressure.
- Vapour material condenses when it impinges on the substrate.

However, the general requirement for evaporation of any material is that it should be well heated in order to attain the requisite vapour pressure [38] and then the evaporation rate is governed by the Langmuir-Dushman equation [39]:

$$N_e = \frac{3.513 \times 10^{22} P_e}{\sqrt{MT}} [\text{molecules cm}^{-2}\text{s}^{-1}] \tag{3.2}$$

where P_e is the equilibrium vapour pressure of the evaporated material under saturated vapour conditions at a temperature T, and M is the molecular weight of the material [39]. At sufficiently high temperature under an appreciable vacuum, most solid materials undergo sublimation. The rate of deposition of the vapour on the substrate largely depends on the source geometry, the position of the source relative to the substrate, and condensation coefficient. Another important parameter in this process is the "impingement rate ϕ" of the vapour atoms or molecules which is the number of vapour atoms or molecules that strikes a unit area on the surface per unit time. The expression relating ϕ and the gas pressure is [40]:

$$\phi = 2.64 \times 10^{20} \Big[\frac{P}{\sqrt{MT}}\Big] \tag{3.3}$$

where M and T retain their meanings and P is the pressure in Pa.

Taking into account the scattering events due to interaction with residual gas molecules, the mean free path mfp, is related to the gas pressure as [41]:

$$\lambda = \frac{kT}{P\pi\sigma^2\sqrt{2}} \tag{3.4}$$

where λ is the mfp and σ refers to all molecules with the same diameter.

The typical values for the mean-free path at 25 °C for 1×10^{-7} Torr and 1×10^{-9} Torr are 5.1×10^4 cm and 5.1×10^6 cm respectively [39]. Equation (3.4) implies that λ is inversely proportional to the gas pressure.

Vaporisation of a compound can be achieved through dissociation, association or an amalgam of the two processes. When the constituent elements have equal volatility, the evaporation process is said to be congruent and if otherwise the evaporation is incongruent [41]. Practically, only very few compounds evaporate congruently and hence the composition of the vapour and that of the condensed material are not the same as the source material. SnS is a typical example of this incongruent case and follows the pattern:

$$AB_{(s)} = A_{(g)} + \tfrac{1}{2} B_{2(g)} \tag{3.5}$$

The various degrees of vacuum according to their pressure ranges as contained in [41] are shown in Table 3.1.

Vacuum	Pressure (Torr)
Low vacuum	760 Torr to 25 Torr
Medium vacuum	25 Torr to 10^{-3} Torr
High vacuum	10^{-3} Torr to 10^{-6} Torr
Very high vacuum	10^{-6} Torr to 10^{-9} Torr
Ultra high vacuum	Below 10^{-9} Torr

Table 3.1: Vacuum and Pressure Range.

The merits of employing a vacuum system in thermal evaporation also lies in the fact that since the solid melts at lower temperature in vacuum, the chance of oxide formation is drastically reduced, thus reducing impurities to the barest minimum. Also by virtue of Equation (3.4), the mfp of the vapour atom will be considerably larger at low pressure and this can consequently lead to the formation of films of good uniformity and thickness.

The first attempt to fabricate n-CdS/p-SnS based heterojunction solar cell using the thermal evaporation technique was in 1994 by Hidenori Noguchi and co-workers [42]. They used a substrate temperature in the range 150 °C to 350 °C and observed a change in the most prominent peak from (111) to (040) with an increase of substrate temperature. They also obtained a direct energy bandgap of 1.48 eV. They attributed (the wider energy bandgap than expected) to the presence of Sn_2S_3 and SnS_2 in the films. They also observed p-type electrical conductivity in the SnS films with a resistivity of 13 Ω cm to 20 Ω cm, a carrier density of 6.3×10^{14} cm^{-3} to 1.2×10^{15} cm^{-3} and a Hall mobility of 400 cm^2 V^{-1} s^{-1} to 500 cm^2 V^{-1} s^{-1}. They reported a solar conversion efficiency of 0.29% obtained under

100 mW cm^{-2} illumination. Other cell parameters are shown on Table 3.2. In the same year Deraman et al. [43] reported on the electrical conductivity of thermally evaporated thin films of SnS. They deposited SnS films using a substrate temperature range of 50 °C to 300 °C and observed that the conductivity of the films increased from 0.5 Sm^{-1} to 2.0 Sm^{-1} with an increase in substrate temperature from 50 °C to 250 °C. They also obtained activation energies of 0.12 eV to 0.14 eV at temperatures above 220 K to 250 K for films deposited at 50 °C and 150 °C respectively. In another report, a post-deposition heat treatment of the as-deposited layer of thickness of 7 nm in an argon environment for 36 hours yielded an optical absorption coefficient of the order of 10^5 cm^{-1} for both cases [44]. Badachhape and Goswami [45] carried out an electron diffraction study of evaporated films of tin sulphide. The layers were polycrystalline in nature and they also observed a structural transformation from orthorhombic to cubic between 250 °C to 425 °C.

Johnson et al. [46] worked on the optimisation of photoconductivity in SnS thin films grown by vacuum evaporation. They reported on the effect of different annealing environments, contacts, and film thicknesses on the photconductivity of the grown films. They also observed a conversion of SnS to SnO_2 at higher annealing temperatures. El-Nahass et al. [47] reported on the optical properties of thermally evaporated amorphous SnS thin films. They observed that the energy band gap varied from 1.4 eV to 2.18 eV. This was interpreted as due to the presence of other phases of tin sulphide e.g. SnS_2. A structural transformation after annealing resulted in a change of the energy bandgap from 1.38 eV to 2.33 eV for the crystalline layers. The variation of the optical constants; i.e. refractive index, extinction coefficient, the optical absorption coefficient and the dispersion properties with the annealing parameters were also presented.

Abou Shama and Zeyada [48] reported on the electronic dielectric constants of thermally evaporated SnS layers deposited using substrate temperature in the range 300 K to 423 K using the thermal evaporation technique. They reported a dispersion energy of 6.67 eV to 20.28 eV for the amorphous and thermally treated films respectively and obtained an indirect forbidden and a direct allowed transition with an energy gap of 1.4 eV and 2.18 eV in the former, and 1.38 eV and 2.33 eV in the latter.

Devika et al. [49] reported the formation of a low resistivity single phase SnS when thermally evaporated using a substrate temperature of 275 °C. They also reported a direct

energy bandgap of 1.35 eV with an optical absorption coefficient of $10^5\,cm^{-1}$. Other reports from the same group include an investigation of the effect of substrate surface on the physical properties [50], annealing effects on the physical properties [51] and substrate temperature effects on the surface structure and electrical resistivity of thermally evaporated layers [52]. Devika and co-workers [53] also used the rapid thermal processing technique and noticed that films treated at 400 °C for 1 min in N_2 atmosphere exhibited a low electrical resistivity of $5\,\Omega\,cm$ with a high Hall mobility and carrier density of $99\,cm^2\,V^{-1}\,s^{-1}$ and $1.3 \times 10^{16}\,cm^{-3}$ respectively. Qiu et al. [54] deposited SnS thin films using the vacuum evaporation method. They observed that the films were stoichiometric with a strong (111) preferred orientation, and a grain size between 0.2 µm to 0.3 µm. They obtained a direct energy band gap of 1.35 eV with an optical absorption coefficient of $10^5\,cm^{-1}$, a p-conductivity type with a resistivity of $2.4 \times 10^2\,\Omega\,cm$. They also fabricated a p-SnS/n-Si heterojunction device that yielded a fill factor of 0.51 and a solar conversion efficiency of 0.71%.

Biswajit Ghosh et al. [55] reported on the fabrication of vacuum evaporated SnS/CdS heterojunctions with a photoconversion efficiency of 0.08% under $100\,W\,m^{-2}$. Other cell parameters are contained in Table 3.2. They did a post-deposition heat operation after a $CdCl_2$ treatment and this enhanced the photovoltaic parameters. However they observed a large series resistance which they noted as the cause of the low conversion efficiency. Other reports by these authors are given in [56, 57].

Ogah et al. [58, 59] reported on the structural, optical, electrical and air annealing of thermally evaporated layers of SnS. They also reported on the properties of n-CdS/p-SnS based heterojunction solar cell. Yuying et al. [60] worked on the effect of different annealing environments on the properties of thermally evaporated SnS thin films. The dopant sources were Sb, Sb_2O_3, Se, Te, In, In_2O_3, Se and In_2O_3. They observed that the resistivity of the Sb-doped layers are reduced by four orders of magnitude while the value of G_{photo}/G_{dark} is double that of the as-deposited layers. Cheng et al. [61, 62] also used the thermal evaporation technique and reported mostly on the variation of some physical, structural and optical properties of the deposited layers.

Using the thermal evaporation technique, Reddy [63] and Reddy et al. [64, 65] have reported on the influence of growth temperature, and on the impact of chemical treatment

on the properties of the deposited layer. They observed that the chemical composition of the SnS films changed gradually from sulphur-rich to tin-rich with the increase of growth-temperature, a change of orientation from <111> to <040> direction with an increase of growth temperatures from 275 °C to 350 °C and that Raman studies confirmed the films to be single phase. The authors showed that the optical bandgap was direct and decreased with an increase of growth temperature while the electrical resistivity decreased from 335 Ω cm to 97 Ω cm between growth temperatures of 275 °C to 350 °C. The authors also showed that the films treated with chloroform exhibited a low electrical resistivity of 5 Ω cm [65].

Schneikart et al. [66] used the thermal evaporation technique to fabricate a CdS/SnS solar cell in the superstrate configuration. They obtained a solar conversion efficiency of 1.6%, a short circuit current density of 19 mA cm^{-2} and an open circuit voltage of 217 mV. They also reported on the band alignments of the CdS/SnS junction and noted that Fermi level pinning in SnS may be responsible for the inadequate energy band alignments observed in their work. Selim et al. [67] reported on the effect of film thickness on the structure and optical properties of thermally evaporated SnS films. They observed that the crystallinity of the films improved with an increase of film thickness. The energy bandgap decreased from 1.68 eV to 1.36 eV with an increase of film thickness from 152 nm to 585 nm and the optical absorption coefficient was of the order of 10^4 cm^{-1}. The refractive index of the films was found to increase with increasing film thicknesses.

Wu and co-workers [68] worked on the influence of heat treatment on the microstruture of SnS/ZnS films prepared by vacuum evaporation. They observed a strong (111) diffraction peak from XRD studies and an average grain size of 50 nm from SEM analysis. They annealed the films between 300 °C to 500 °C in a N_2 atmosphere and observed an increase in the grain size, and change in the electrical properties of the layers due to annealing effects.

Jakhar et al. [69] deposited thin films of tin sulphide with the thermal evaporation technique. Using a constant deposition rate of 2.7 Å/s, they obtained films that were uniform and dark in colour, with film thicknesses of 270, 480, 600, 630 and 900 nm respectively. They observed that annealing at 373 K to 473 K for 30 min under vacuum of 10^{-3} Torr did not change the colour of the films but increased the grain size and

the refractive index and thus attributed the increasing trend of refractive index to the improvement in crystal ordering due to an increase in the grain size.

3.3.1.2 Other Evaporation Methods

Cifuentes et al. [70] used the co-evaporation of the elements to deposit SnS layers. They used substrate temperature in the range 200 °C to 400 °C and investigated the formation of SnS and SnS_2 films with energy band gaps of 1.3 eV and 1.6 eV respectively. They also observed a decrease of optical transmittance with increasing film thickness as indicated in Table 3.4 and Table 3.5. Reddy et al. [71] also reported on the synthesis and characterisation of co-evaporated SnS thin films. They observed single-phase SnS films that showed the orthorhombic crystal structure and a strong (040) orientation and had grain size of 0.12 µm. The authors noted that the films exhibited a direct energy band gap of 1.37 eV and had a high optical absorption coefficient ($> 10^4\,\mathrm{cm}^{-1}$), an electrical resistivity of 6.1 Ω cm with an activation energy of 0.26 eV.

Tanuševski and Poelman [72] reported on SnS layers using the electron beam evaporation technique and observed an indirect optical bandgap of 1.23 eV and direct energy bandgap of 1.38 eV. They also reported on the photoconductivity and activation energy of the layers. Henry et al. [73] also reported on the effect of annealing temperature on the structural and optical properties of SnS films grown by electron beam evaporation. They used annealing temperatures in the range 100 °C to 300 °C and observed that the energy bandgap values decreased from 1.77 eV to 1.57 eV due to the heat treatments.

Using hot-wall deposition technique, Bashkirov et al. [74] reported the fabrication of a Mo/p-SnS/n-CdS/ZnO heterojunction solar cell. The thickness of the SnS layer was varied from 1.5 µm to 5.5 µm while that of the CdS buffer layer was 500 nm. The best cells were obtained with SnS films deposited at a substrate temperature of 350 °C and a thickness of 5 µm. Leith-C conductive glue was used as the contact to the ZnO layer. They obtained a solar conversion efficiency of 0.5%. Other cell parameters are contained in Table 3.2.

Hedge et al. [75] deposited SnS films by physical vapour deposition technique. They reported on the structural, optical and electrical properties and observed that the Sn-to-S atomic ratio was 1.02 from EDS studies, that the layers had an orthorhombic structure with (040) orientation from XRD analysis and the optical measurements revealed an

indirect optical band gap of 1.06 eV and direct energy band gap of 1.21 eV. They also observed a p-conductivity type and obtained an electrical resistivity of 120.35 Ω cm, a carrier concentration of 1.52×10^{15} cm^{-3}, a Hall coefficient of 4108.9 cm^3 C^{-1} and a carrier mobility of 34.14 $cm^2/V\,s$.

3.3.1.3 Sputtering

Sputtering is the kinetic ejection of vapour species from the surface of a material known as the target or cathode by bombardment with energetic and non-reactive ions [76, 77]. A film is formed when these ejected atoms condenses on the substrate surface. A common method of sputtering is the glow discharge sputtering which uses a direct current electric field. In this case the sample is placed on the anode and with the application of an electric potential of a few kV, the ejected ions are accelerated from the cathode thereby condensing on the surface of the substrate. Magnetron sputtering is one method which employs radio frequencies in the sputtering process. This allows non-metallic target materials to be used. The efficiency of ionisation is enhanced by the presence of magnets in the configuration. Figure 3.3 gives a schematic block diagram of a sputtering system.

Guang-Pu et al. [78] were the first to report on RF sputtered SnS thin films. They deposited amorphous and crystalline layers whose structural properties varied with the sputtering conditions. They obtained a direct energy bandgap of 1.46 eV and a type conversion of the p-type layers to n-type layers by incorporating an antimony dopant and annealing at a temperature range of 350 °C to 450 °C. The electrical resistivity also reduced from 20 Ω cm to 2 Ω cm.

Hartman et al. [79] showed that the resistivity, stoichiometry, phase, grain size and shape, bandgap, and optical absorption coefficient can be varied by the modifying argon pressure for a fixed deposition time for RF sputtered SnS layers. They reported indirect band gaps ranging from 1.08 eV to 1.18 eV. Stadler et al. [80] worked on RF sputtered SnS layers and analysed them with respect to space–time dependencies of the sputtering process.

Banai et al. [81, 82] deposited SnS thin films by RF magnetron sputtering and noticed that the films are stoichiometric and exhibits the herzenbergite phase. They obtained an indirect energy bandgap in the range 1.2 eV to 1.3 eV, forbidden gap in the range 1.3 eV to 1.34 eV and direct energy bandgap in the range 1.47 eV to 1.55 eV, and an optical absorption

coefficient in the range $10^5\,\mathrm{cm}^{-1}$ to $10^6\,\mathrm{cm}^{-1}$.

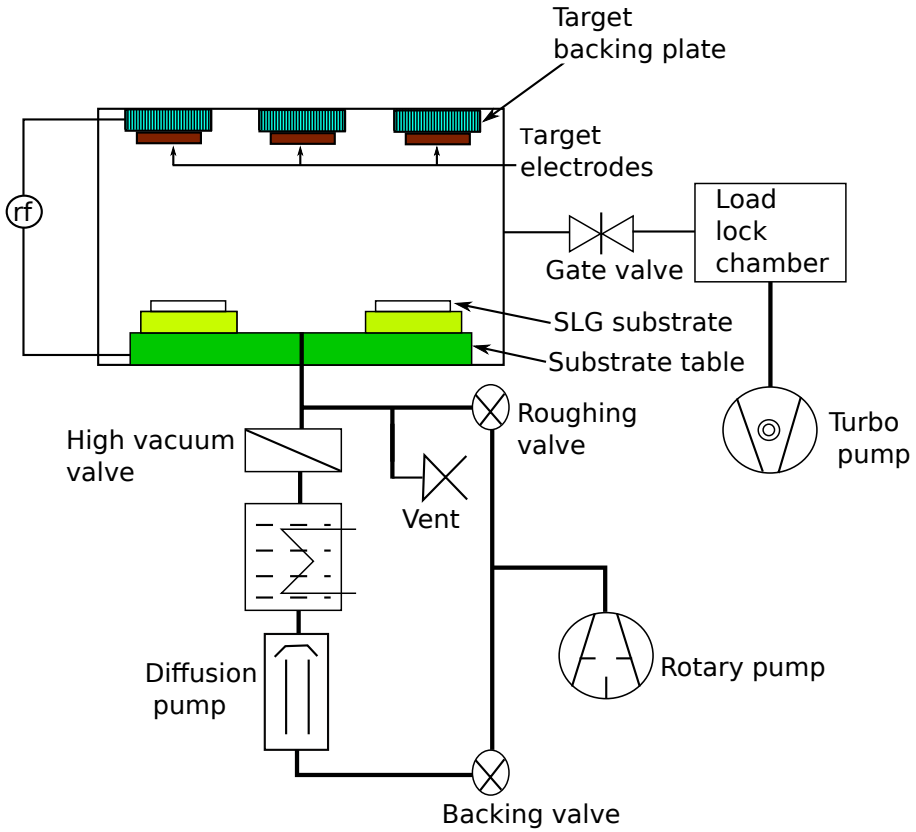

Figure 3.3: Schematic Diagram of a RF Sputtering System.

3.3.1.4 Sulphurisation (2-step Process)

This is a two-stage process that involves depositing the "Sn" precursors on the substrate using thermal evaporation or sputtering then followed by annealing in the presence of elemental sulphur to form SnS thin films. Ramakrishna Reddy et al. [83, 84] were the first workers to use this technique to deposit high quality single phase SnS layers. Ramakrishna Reddy et al. [85] also reported on the energy band discontinuities in SnS/ZnMgO thin film heterojunction devices. Zaret and co-workers [86] used the two-step process and obtained single phase SnS films of orthorhombic structure that had the (040) preferred orientation for films formed at temperatures between 250 °C to 350 °C. They obtained a direct energy bandgap in the range 1.15 eV to 1.24 eV and an optical absorption coefficient greater than $10^4\,\mathrm{cm}^{-1}$, and the SnS films were of p-conductivity type with electrical resistivity in the range $40\,\Omega\,\mathrm{cm}$ to $200\,\Omega\,\mathrm{cm}$. Cheng at al. [87] in their study, observed that SnS films that exhibited near stoichiometric composition, showed (111) preferred orientation, and had

the orthorhombic crystal structure can be obtained for sulphurisation temperatures in the range 573 K to 673 K. They observed a p-type electrical conductivity and a resistivity of the order of $10^2\,\Omega\,\text{cm}$.

Jiang et al. [88] deposited SnS layers using the 2-step process and observed that the layers had the orthorhombic structure and a (040) preferential growth that increased with an increase of sulphurisation time. They obtained a direct energy bandgap of 1.3 eV and an optical absorption coefficient $> 10^4\,\text{cm}^{-1}$, a p-conductivity type and a decrease of the photo and dark resistivities of the layers with different sulphurisation time. Jiang et al. [89] also used the 2-step process to fabricate a SnS/α-Si heterojunction solar cell. They found a direct energy bandgap of 1.35 eV and observed that the junction exhibits a typical rectifying diode behaviour in the dark with a diode factor of 2.34 while under illumination the open circuit voltage was 289 mV and the short circuit current density was $1.55\,\text{mA}\,\text{cm}^{-2}$.

Sugiyama and co-workers [90] used the 2-step process to deposit SnS layers to fabricate CdS/SnS and SnS/SnO_2 heterojunction devices. They obtained a valence band offset of 1.5 eV for CdS/SnS and 3.5 eV for SnS/SnO_2 interface and a conduction band discontinuity of 0.4 eV and 1.0 eV for the CdS/SnS and SnS/SnO_2 junctions respectively. Botero et al. [91] used the sulphurisation method and observed predominantly SnS phase with an orthorhombic structure, a direct energy bandgap of 1.3 eV, an optical absorption coefficient greater than $10^4\,\text{cm}^{-1}$, and that the layers were p-conductivity type. They also observed similar properties with a direct energy bandgap of 1.37 eV in a separate report [92].

Leach et al. [93] and Hirano et al. [94] also used the sulphurisation method and both groups observed a (111) preferred orientation in the layers. Qiang et al. [95] deposited SnS layers with the 2-stage process and obtained films that were uniform and had an orthorhombic structure, a (040) preferred orientation, a direct energy band gap of 1.23 eV, a high optical absorption coefficient of $5 \times 10^4\,\text{cm}^{-1}$ and showed a persistent photoconductivity effect.

3.3.1.5 Molecular Beam Epitaxy

Pioneering work on the use of molecular beam epitaxy to deposit SnS is by Cho and co-workers [96]. Molecular beam epitaxy occurs when the condensation of a directed beam of atoms or molecules onto a crystalline surface resulted in epitaxial growth under ultra-high vacuum ($\geq 10^{-8}$Pa) conditions [97]. MBE is largely controlled by surface-kinetic

processes under non-equilibrium conditions.

Nozaki et al. [98] reported on the variation of lattice parameters of SnS thin films grown by MBE method. They obtained a direct energy bandgap in the range 1.7 eV to 2 eV and indirect energy bandgap between 1.06 eV to 1.09 eV. Wang et al. [99–104] also reported on SnS thin films deposited by MBE method and obtained a direct energy bandgap of 1.25 eV and an optical absorption coefficient of $10^4\,\mathrm{cm}^{-1}$.

3.3.1.6 Closed Space Vapour Transport

Closed space vapour transport method is a low cost technique and the set-up can easily be assembled locally. The earliest work that utilised closed space vapour transport for SnS thin films can be traced to the works of Yanuar et al. [105, 106]. These authors reported a direct energy bandgap of 1.32 eV, an optical absorption coefficient of $10^4\,\mathrm{cm}^{-1}$, p-type conductivity layers with a hole concentration of $10^{17}\,\mathrm{cm}^{-3}$, a resistivity of $14.5\,\Omega\,\mathrm{cm}$ and a hole mobility of $3.8\,\mathrm{cm}^2/\mathrm{V\,s}$.

Other physical deposition methods used to deposit SnS by various authors are; brush plating by Jayachandran et al. [107], atomic layer deposition by Kim et al. [108] and Sinsermsuksakul et al. [109], pulsed layer deposition by Vidal et al. [110] and physical vapour deposition by Hegde et al. [75]. SnS layers that showed a (111) preferred orientation were observed by [107, 109], a (040) preferred orientation in [75], and an orthorhombic structure with p-conductivity type layers in [75, 107, 109, 110].

3.3.2 Chemical Deposition

3.3.2.1 Chemical Bath Deposition

Chemical bath deposition is believed to have originated from the work of Gerhard Brückman in 1933 [111], when he produced thin films of lead sulphide from a solution of lead acetate, thiourea and sodium hydroxide. The general principle of CBD involves the dissolution of a soluble salt of the required metal in an aqueous solution to release cations while the anions are generated from a suitable compound of the non-metallic element that can decompose in the presence of hydroxide ions. The compound is then formed by the reaction of the anions and cations. It is generally known that film deposition on a substrate occurs in two steps;

nucleation and particle growth. However nucleation and film growth is achieved by any of, combination of, or all of the processes of a simple ion-ion mechanism, a simple hydroxide cluster mechanism, a complex ion-by-ion decomposition mechanism and a complex cluster decomposition mechanism [112]. In growing the CdS layers used as a buffer layer, an alkaline solution of a cadmium salt (in this case cadmium acetate) and a thiourea solution are prepared and the film growth takes place through ion-by-ion condensation of Cd^{2+} and S^{2-} ions on the substrate when Cd^{2+} and S^{2-} ions exist over the solubility limit [113]. The typical process reaction steps involving cadmium acetate are as follows:

$$(NH_2)_2CS + 2\,OH^- \longrightarrow S^{2-} + CN_2H_2 + 2\,H_2O \tag{3.6}$$

$$Cd(NH_3)_4^{2+} \longrightarrow Cd^{2+} + 4\,NH_3 \tag{3.7}$$

$$Cd^{2+} + S^{2+} \longrightarrow CdS \tag{3.8}$$

The sulphide ions are released by the hydrolysis of thiourea. The Cd^{2+} ions form tetraaminecadmium(II)complex ions by combining with NH_3 in the pH range of 10–11 [114]. These $Cd(NH_3)_4^{2+}$ complexes adsorb on the glass and a heterogenous nucleation and growth then takes place through an ionic exchange reaction with S^{2-} [115].

Chemically bath deposited SnS thin films were first reported by Pramanik et al. [116] using a Sn^{2+} salt solution ($SnCl_2 \cdot 2\,H_2O$), triethanolamine (TEA), ammonia and thioacetamide as reagents. They indicated that the films were amorphous with an optical energy bandgap of 1.51 eV and n-type electrical conductivity and the films were found to be photoconductive. Nair and Nair [117] used the CBD method to grow SnS layers with thicknesses up to 1.2 µm. They reported that the films showed p-type dark conductivity in the range $10^{-5}\,\Omega^{-1}\,cm^{-1}$ to $10^{-4}\,\Omega^{-1}\,cm^{-1}$ and a photo-current to dark-current ratio of 5-10 under $500\,W\,m^{-2}$ tungsten halogen illumination (for a film thickness of $\approx 1\mu m$). They also reported a conversion of SnS to SnO_2 [118–120]. Ristov et al. [121] deposited SnS films of p-type conductivity using aqueous solutions of $SnCl_2$ and $(NH_4)_2S$ and observed changes on the conductivity and stoichiometry due to annealing. Annealing the layers above 280 °C for a short duration changed the conductivity of the films to n-type without altering the stoichiometry of the SnS layers. However longer period of annealing changed the films

to SnS_2 while oxidation of the films by annealing in open air between 300 °C to 400 °C resulted in the emergence of SnO_2. In a separate report, the authors also reported on the photovoltaic properties of chemically deposited SnS layers [122].

Tanuševski [123] reported on the optical and photoelectric properties of SnS deposited by the CBD method. He observed that the (111) preferred orientation increased with thermal annealing. A direct energy bandgap of 1.38 eV was obtained for the layers independent of the thermal treatment. Using chemical bath deposition, David Avellaneda and co-workers reported on the fabrication of heterojunctions with the superstrate structure: SnO_2:F/CdS/SnS/CuS/silver print [124]. The SnS absorber layer was deposited using a bath temperature between 293 K to 303 K with a thickness of 450 nm, CuS was deposited using the same conditions with a thickness of 80 nm while the CdS was grown at 333 K with a thickness of 80 nm. The cell parameters are contained in Table 3.2. Sreedevi and Ramakrishna Reddy [125], and Gopinath and Ramakrishna Reddy [126] used the CBD technique to deposit SnS layers and obtained a direct energy bandgap in the range 1.30 eV to 1.35 eV with a high optical absorption coefficient ($> 10^4\,cm^{-1}$) in the former and energy bandgap in the range 2.87 eV to 3.32 eV in the latter. They fabricated a SnS/In_2S_3/ZnO:Al heterojunction solar cell that showed a solar conversion efficiency of 0.6% [126].

Other investigations [127–134] obtained SnS layers that showed zincblende and orthorhombic structures while only an orthorhombic structure was found in [112, 133, 135–139].

3.3.2.2 Spray Pyrolysis

The first spray pyrolysis process was probably that of Foex in 1944 [140]. However Chamberlin and Skarman extended it to sulfide and selenide films two decades later when they used the technique to fabricate CdS/$Cu_{2-x}S$ heterojunction solar cells [141]. One of the merits of this technique is that the equipment can easily be assembled and hence different spray pyrolysis set-ups can be found in the literature. Spray pyrolysis involves spraying an aqueous solution containing soluble salts of the constituent atoms/vapour of the required compound onto a substrate at very high temperatures, such that pyrolytic (endothermic) decomposition is achieved, resulting in the formation of a single crystal or an aggregate of crystallite of the required product. Hence the energy needed for the thermal

decomposition and subsequent recombination of the constituent atoms/vapours followed by sintering and recrystallisation of the aggregates of the crystallites to form a coherent film is provided by the thermal energy of the substrate [39]. A typical spray pyrolysis set up is shown on Figure 3.4.

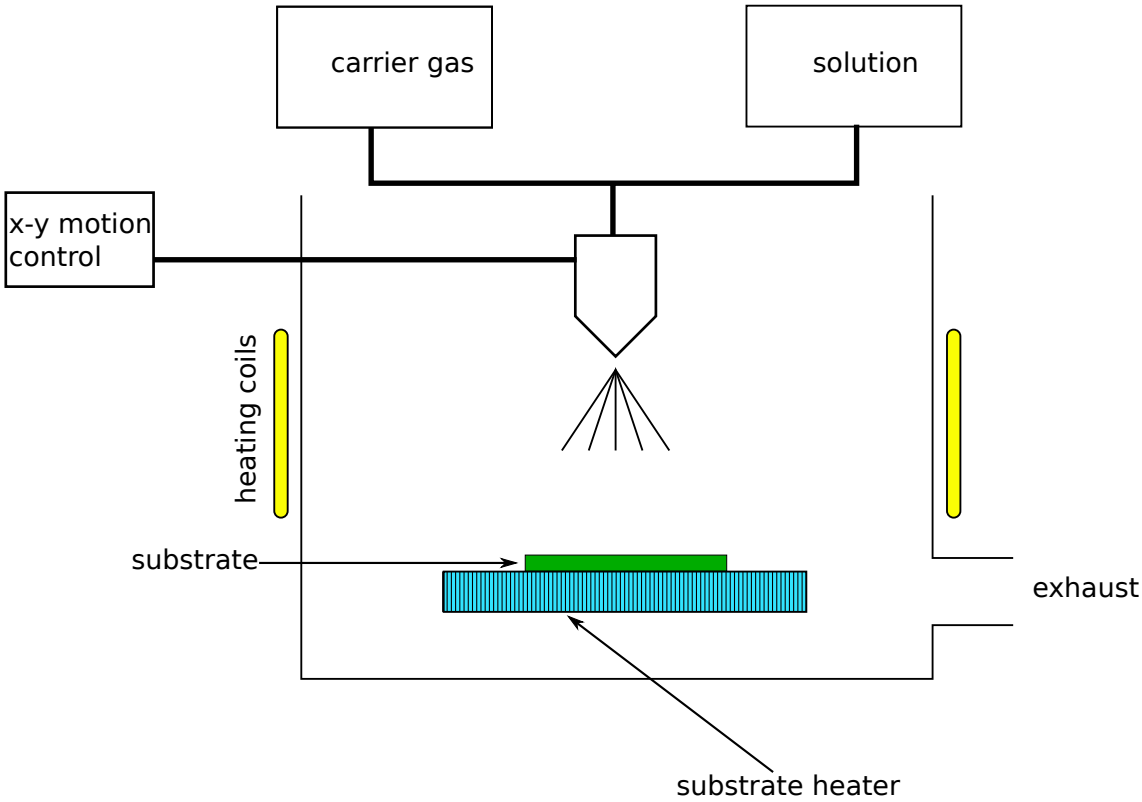

Figure 3.4: Schematic Diagram of a Spray Pyrolysis System.

Reddy, Reddy and Miles [142] were the first worker to report on a spray pyrolysed tin sulphide heterojunction solar cell. The absorber layer thickness was 0.6 µm at 350 °C and the optical energy band gap was found to be 1.32 eV. The layer had a resistivity of 30 Ω cm which reduced to 5 Ω cm after annealing. The solar cell had a solar conversion efficiency of 1.3%. Other solar cell parameters are contained in Table 3.2.

Other research groups [143–149] have used spray pyrolysis to deposit SnS thin films. These authors all observed the presence of other phases of SnS such as SnS_2 and Sn_2S_3. However Jeyaprakash et al. [150] observed only the SnS phase with an orthorhombic structure and a (111) preferred orientation. They noted that the intensity of the XRD peaks increased with an increase of substrate temperature and attributed it to better crystallinity at the higher growth temperatures. They obtained a direct energy bandgap of 1.35 eV at a substrate

temperature of 300 °C. They observed that the energy bandgap decreased from 1.40 eV to 1.30 eV with an increase of growth temperature and this was explained as due to lesser grain size and quantum confinement at the lower growth temperatures.

3.3.2.3 Successive Ionic Layer Adsorption and Reaction

This is a variant of the chemical bath deposition which requires immersing the substrates alternately in cationic and anionic precursor solutions and rinsing between every two consecutive immersions with deionised water to avoid homogeneous precipitation in the solution. This ensures that only the tightly adsorbed layers are retained on the substrate. SILAR method has been widely used in SnS thin film deposition by Gao et al. [132, 151–153] and Gosh et al. [154–156]. Ristov et al. [122] also used successive immersion in hot and cold precursor solutions to obtain SnS films with thicknesses up to 3 µm after 200–300 immersions. They also reported on the effect of different contacts on the photovoltaic properties of the devices made using these layers.

3.3.2.4 Chemical Vapour Deposition

The CVD method dates back to that of Mellor [157]. This technique involves the exposure of a substrate material to one or several compounds in the vapour phase, some or all of which contain constituents of the desired material to be deposited. The exposure leads to the initiation of a chemical reaction at or near the substrate surface resulting in the condensation of the desired material on the substrate [39]. Chemical reactions in CVD can also be initiated by heat, radio frequency, light or catalytic action and the reaction can be broadly grouped into:

- polymerisation,
- transport reactions,
- decomposition reactions, and
- hydrogen or metal reduction of halogens.

Sinsermsuksakul et al. [158] reported an efficiency of 2.04% for a substrate configuration device with the structure; glass/Mo/SnS/Zn(O,S)/ZnO/ITO. The SnS was deposited using

CVD process and the other layers using sputtering. The cell parameters are indicated in Table 3.2. The report of Price et al. [159] showed it was possible to obtain single phase SnS layers using the CVD technique. Other authors have reported on SnS thin films grown using the CVD method [160–164]. These authors observed similar peaks corresponding to SnS from Raman studies [160–163] while layers that had an orthorhombic structure with the (101) preferred orientation were also observed [161, 164].

3.3.2.5 Metal Organic Chemical Vapour Deposition (MOCVD)

Metal organic chemical vapour deposition is a branch of chemical vapour deposition in which the starting materials are metallo-organic compounds. The gaseous mixture is then passed over a heated substrate and this makes the precursor molecules pyrolyse, leaving the atoms on the surface of the substrate where they undergo bonding to form a crystalline layer [39, 165]. Park et al. [166, 167] reported on SnS thin films deposited with the MOCVD process. They worked in a temperature range of 300 °C to 400 °C and obtained films that had the orthorhombic structure with an average grain size of 50 nm. They observed XRD peaks corresponding to PDF 01-984 with strong preferential orientation in the (013) plane. The films had an optical energy bandgap of 1.31 eV.

3.3.2.6 Plasma Enhanced Chemical Vapour Deposition (PECVD)

PECVD is CVD carried out in a "plasma". The plasma is usually created by AC frequency or DC discharge at pressures between mTorr and Torr range [39, 168]. Ortiz and co-workers [169] deposited SnS thin films with the PECVD method and observed that the layers had the orthorhombic structure, an indirect energy bandgap of 1.16 eV, a p-conductivity type and an activation energy of 0.3 eV. Sánchez-Juárez et al. [170] first reported on SnS-based heterojunction deposited by PECVD method. They used SnS_2 as the buffer layer and obtained an open circuit voltage of 0.35 V and a short circuit current density of 1.5 mA cm^{-2}. Cheng et al. [171, 172] also deposited SnS films using the PECVD technique. They obtained single phase layers confirmed with Raman studies, a direct energy bandgap of 1.5 eV and an optical absorption coefficient greater than 10^4 cm^{-1}.

Other chemical deposition techniques used by various authors to deposit SnS thin films include; a modified solution dispersion method by Zhao et al. [173], a dip technique by

Ray et al. [174], a multi-layer based solid state reaction by Xu and Chen [175], a spin coating by Liu et al. [176] and by a wet chemical route by Sohila et al. [177]. Most of these research groups obtained SnS layers that had the orthorhombic structure with the (040) preferred orientation [173–176] and a (111) preferred orientation [177].

3.3.3 Electrodeposition

Electrodeposition occurs when a substance is deposited on an electrode as the result of electrolysis. The principle is based on Faraday's laws of electrolysis [178] summed up as:

$$W = \frac{IEt}{F} \tag{3.9}$$

where W is the mass of the substance deposited in grams, I is the current in amperes, E is the electrochemical equivalent, t is the time in second and F is a constant equal to the amount of charge needed to deposit the equivalent weight of any ion from a solution. This constant is numerically equal to 96,500C (1 Faraday).

The electrodeposition of SnS can be obtained from an aqueous solution containing $SnCl_2$, $Na_2S_2O_3 \cdot 5\,H_2O$. The reaction steps involved are [179]:

$$S_2O_3^{2-} \longrightarrow S^{2-} + SO_3^{2-} \tag{3.10}$$

The Sn^{2+} and S^{2-} ions are reduced at the cathode to form SnS

$$Sn^{2+} + S^{2-} + 2\,e^- \longrightarrow SnS \tag{3.11}$$

Electrodeposition is relatively inexpensive and can easily be scaled up for commercial production.

Engelken and co-workers [180] used a chemical precipitation method (electroless deposition) employing an organic acid-H_2O baths of $SnCl_2$(0.1 mol to 1.0 mol) and S and Sn(II) complexing agents (potassium gluconate or tartaric acid) to deposit films ($\geq 10\,\mu m$) of gray-black $Sn_{1\text{-}x}S$ ($E_g \sim 1.0$ eV to 1.3 eV), brown $Sn_{2\text{-}x}S_3$ ($E_g \sim 1.6$ eV to 1.9 eV) and $SnS_{2\text{-}x}$ ($E_g \sim 2.1$ eV to 2.3 eV). They observed that films containing less than 10% by volume of water were mostly grey $Sn_{1\text{-}x}S$ with $E_g \sim 1.0$ eV to 1.3 eV while films grown without water

were mostly brown SnS_{2-x} with $E_g \sim 2.1\,eV$ to $2.3\,eV$. Sharon and Basavaswaran [181] were the first to fabricate an electrodeposited SnS solar cell. However it should be noted that in their solar cell the SnS layer was n-type conductivity with a bandgap of $1.29\,eV$. They obtained a photoconversion efficiency of 0.63% and fill factor of 0.44. Mishra et al. [182] reported on the electrodeposition and characterisation of SnS thin films. They used a novel room-temperature electrodeposition technique and reported on the morphology, composition and photoactivity of the SnS layers. Adachi et al. [183] worked on the electrodeposition of SnS thin films. The film thickness was varied between $0.25\,\mu m$ to $0.75\,\mu m$ and they noted that the film growth depended on the stirring of the electrolyte solution. The optical absorption coefficient of the layers were found to be $10^5\,cm^{-1}$.

Zainal et al. [184] reported on the cathodic electrodeposition of SnS, employing the principle of co-depositing a higher valent metal and chalcogenide ions on metal or any conducting substrate as shown;

$$M^{n+} + ne^- \longleftrightarrow M^0 \tag{3.12}$$

$$S_2O_3^{2-} \longrightarrow S^0 + SO_3^{2-} \tag{3.13}$$

$$M^0 + S^0 \longleftrightarrow MS \text{ (where M is the metal ion)} \tag{3.14}$$

Structural analysis of the films revealed stoichiometric layers while optical studies indicated an indirect bandgap in the range $0.9\,eV$ to $1.1\,eV$. In a separate report [185], they used EDTA (ethylenediaminetetraacetic acid) as a chelating agent in the bath and reported better adhesion, improved crystallinity, better uniformity and more thorough surface coverage in the films. Strong photoactivity and p-conductivity type were observed in the SnS layers. Ghazali et al. [186] also reported on the cathodic electrodeposition of SnS in the presence of EDTA and observed herzenbergite SnS structure with an energy bandgap of $\approx 1.1\,eV$.

Subramanian et al. [187] used electrodeposition method to deposit SnS layers and found that the layers were stoichiometric and had the orthorhombic structure. Annealing was found to significantly increase the grain sizes of the films. They also reported an efficiency of 0.54% for a solar cell made using electrochemically deposited SnS layers. Other cell

parameters are shown on Table 3.2.

Ichimura et al. [188] utilised a unique approach with electrochemical deposition of SnS on In_2O_3 coated glass substrates using an aqueous bath of $SnSO_4$[1 mmol to 7.5 mmol] and $Na_2S_2O_3$[100 mmol] with the pH of the solution varied between 3 and 4 by the addition of sulphuric acid. They reported on the structural and optical properties of the layers. Structural analysis indicated that the SnS layers were tin rich and had the orthorhombic crystal structure. The energy band gap of the films was determined to be 1.3 eV. They also noted that the composition of the films was not crucially dependent on the deposition conditions unless the deposition potential was more cathodic than −1.1 V. For these conditions the SnS films were highly tin rich, with low transmittances.

Gunasekaran and Ichimura [189] used pulsed electrochemically deposited SnS and photochemically deposited CdS and $Cd_{1-x}Zn_xS$ to fabricate heterojunction devices. They obtained an open circuit voltage of 340 mV, short circuit current of 2.36 mA cm^{-2}, fill factor of 0.35 and conversion efficiency of 0.22%. They noted that photovoltaic parameters were better for the $Cd_{1-x}Zn_xS$ based cells and observed that for $x = 0.13$, the best cells were obtained with an open circuit volatge of 288 mV, short circuit current value of 9.16 mA cm^{-2} and a solar conversion efficiency of 0.71%. Vequizo and Ichimura [190] fabricated an electrodeposited SnS/SnO_2 superstrate heterojunction device and obtained an open circuit voltage in the range 40 mV to 90 mV, short circuit current density between 1.5 mA cm^{-2} to 9.7 mA cm^{-2} and a valence band offset of 1.85 eV. Miyawaki and Ichimura [191] used electrochemical deposition method to deposit SnS layers that were nearly stoichiometric, showed p-conductivity type and photosensitivity. They fabricated a ZnS/SnS heterojunction solar cell and obtained a short-circuit current density of 0.95 µA cm^{-2} and an open-circuit voltage of 135 mV when illuminated by a Xenon lamp of 100 mW cm^{-2}.

Other investigations [192–198] observed that the stoichiometry of Sn:S ratio in the films varied with the deposition potential and that the layers all had the orthorhombic crystal structure. Also a (021) preferred orientation was reported in [179, 199], a (111) preferred orientation in [200–202], and single phase layers with a direct energy bandgap of 1.37 eV [203], an indirect energy bandgap of 1.17 eV [204] and an optical absorption coefficient greater than 10^4 cm^{-1} in both cases.

The progressive trend of SnS based heterojunction devices, independent of the deposition

technique is shown on Table 3.2.

3.3.4 Review of Theoretical Analysis of SnS and Selected Characterisation Techniques

SnS is a novel material and hence not much has been done in investigating the intrinsic and extrinsic properties using modern theoretical/simulation packages compared to other advanced thin films such as CdTe and CIGS. The first attempt on this was probably that of Ettema and co-workers using Ab-initio band-structure calculations [205]. They observed that the charge distribution in the α (low temperature) and β (high temperature) phase are relatively the same but the energy bandgap of the α phase was greater.

Martinez et al. [206] used ab-initio Hartree-Fock program CRYSTAL to investigate the bulk and surface electronic structure of α-SnS. They reported similar charge distribution with [205] but observed higher energy bandgap (4 eV) compared to their experimental values (1.2 eV). The work of Nabi et al. [207] reported extensively on the electronic band structure, density of states and some important optical constant. They utilised the local density approximation (LDA) using the full potential linearised augmented plane wave method (FP-LAPW) in their investigations and the results compared relatively well with experiments. Vidal et al. [110] carried out total-energy defect and effective mass calculations by utilising projected augmented wave (PAW) implementation of the Vienna ab-initio simulation package (VASP) code and obtained an indirect bandgap of 1.07 eV. They also reported on the effective mass and other parameters. To date there are few reports on important characterisation techniques such as photoluminescence, Raman spectroscopy and X-ray photoelectron spectroscopy. Table 3.3 gives a summary of the reports in the literature of SnS for photoluminescence, Raman spectroscopy and band alignment studies.

3.3.5 Review of Transmittance of SnS Films

The strong link between the solar conversion efficiency and film thickness has been earlier indicated in subsection 2.8.1. Studies on SnS indicates that the transmittance strongly depends on the film thickness. At higher thickness, the transmittance is drastically reduced. Table 3.4 and Table 3.5 gives a summary of the variation of film thickness with the optical transmittance based on the literature at the time of submission of this thesis.

Technique	Thickness (SnS)	Band gap	V_{oc}	J_{sc}/I_{sc}	Cell area	FF	Efficiency	Ref
Thermal evaporation	–	1.48 eV	120 mV	$7\ mA/cm^2$	–	0.35	0.29%	[42]
Thermal evaporation	$1\,\mu m$	–	274 mV	$301\,\mu A$	–	0.40	0.08%	[55]
CBD	$0.5\,\mu m$	1.2 eV	370 mV	$1.23\,mA/cm^2$	–	0.44	0.2%	[208]
Spray pyrolysis	$0.6\,\mu m$	1.3 eV	260 mV	$9.6\,mA/cm^2$	$0.3cm^2$	0.53	1.3%	[142]
PECD	–	–	270 mV	$2.36\,mA/cm^2$	$1mm^2$	0.35	0.22%	[189]
CBD	$2-3\,\mu m$	–	230 mV	$39\,\mu A$	–	–	–	[122]
Thermal evaporation	$1\,\mu m$	–	120 mV	$39.91\,\mu A$	$0.4cm^2$	0.33	0.003%	[56]
PECD	–	1.3 eV	110 mV	$0.72\,mA/cm^2$	–	0.32	–	[200]
Electrodeposition	–	–	60 mV	$9.74\,mA/cm^2$	–	–	$10^{-2}-10^{-1}$%	[190]
PECVD	$0.35\,\mu m$	1.255 eV	350 mV	$1.5\,mA/cm^2$	–	–	–	[170]
Low temperature organometallic synthesis	–	1.52 eV/1.45 eV	200 mV	$4.2\,mA/cm^2$	–	0.29	0.27%	[209]
Sputtering	–	1.35 eV	289 mV	$1.55\,mA/cm^2$	–	–	–	[89]
PECD	–	–	280 mV	$4.8\,mA/cm^2$	–	0.34	–	[210]
Thermal evaporation	$1.8\,\mu m$	–	217 mV	$19\,mA/cm^2$	–	0.392	1.6%	[66]
CED	$1\,\mu m$	1.15 eV	320 mV	$0.65\,mA/cm^2$	$0.5\,cm^2$	0.65	0.54%	[211]
PEC	$1.0-1.1\,\mu m$	1.12 eV	230 mV	$1.63\,mA/cm^2$	–	–	<1%	[212]
PEC	$1.0-2.5\,\mu m$	1.18 eV	370 mV	–	–	55	0.63%	[213]
Hot wall deposition	$5\,\mu m$	–	132 mV	$3.68\,mA/cm^2$	$0.2cm^2$	0.29	0.5%	[74]
Homojunction	–	–	650 mV	$7.64\,mA/cm^2$	–	39	1.95%	[214]
Inorganic/organic	–	–	850 mV	$7.35\,mA/cm^2$	–	45	2.81%	[215]
CVD	$1.5\,\mu m$	–	0.244 V	$19.42\,mA/cm^2$	$0.71cm^2$	42.97%	2.04%	[158]
RF	50 nm	1.3 eV	270 mV	$12.1\,mA/cm^2$	–	64	2.1%	[216]

Table 3.2: Progressive Trend of SnS Based Heterojunction Devices.

Technique	Photoluminescence	Raman modes (cm^{-1})	XPS	Alignment	Ref
Sulfurisation	–	–	CdS/SnS	Type II	[90]
Evaporation and Sulfurisation	–	–	CdS/SnS	Type II	[217]
Theoretical	–	–	CdS/SnS	Type I	[218]
ECD	–	–	CdS/SnS	Type II	[219]
CBD	–	–	CdS/SnS	Type II	[219]
ECD	–	–	InS_xO_y/SnS	Type I	[219]
CBD	–	–	InS_xO_y/SnS	Type I	[219]
EDM	–	–	SnO_2/SnS	Type I	[190]
Bridgeman technique	–	47, 50, 58, 78, 111, 160, 170, 194, 216, 264 = SnS	–	–	[26]
CD	–	40, 49, 70, 85, 95, 164, 192, 208, 218, 290 = SnS, 160 = ?	–	–	[27]
CBD	–	64, 106, 269 = SnS, 304 = SnS_2 or Sn_2S_3	–	–	[137]
Solvothermal	–	38, 47, 93, 162, 191, 218 = SnS	–	–	[220]
ALD	–	68, 94, 162, 191, 219, 288 = SnS	–	–	[109]
Thermal evaporation	–	173, 181, 219, 286 = SnS, 153 = Sn_2S_3	–	–	[61]
Thermal evaporation	–	173, 181, 219, 286 = SnS	–	–	[62]
CBD	–	162, 193, 223 = SnS, 316 = SnS_2, 237, 254 = Sn_2S_3	–	–	[221]
CVD	–	190.4, 223, 273.7 = SnS	–	–	[161]
Wet chemical route	–	46, 52, 57, 77, 109, 154, 170, 182, 229, 260 = SnS	–	–	[177]
Microwave-assisted polyol synthetic method	–	229, 312 = SnS_2	–	–	[222]
CBD	–	189, 220 = SnS, 313 = SnS_2	–	–	[223]
CBD	–	219, 221 = SnS, 303 = Sn_2S_3	–	–	[138]
SILAR	825nm	–	–	–	[154]
Solution dispersion method	415 and 480nm	–	–	–	[173]
SILAR	680 and 825nm	–	–	–	[155]
Hydrothermal	553.05nm	–	–	–	[224]

Table 3.3: Photoluminescence, Raman and XPS Survey of SnS.

Technique	Thickness	Band gap	Polycrystalline	Single phase	Transmittance	Ref
Bridgman technique	216 µm	1.30 eV	No	–	35%	[33]
CBD	1.2 µm	≈ 1.3 eV	Yes	–	≈ 70%	[117]
CBD	0.35 − 0.45 µm	–	Yes	–	≈ 90%	[117]
Spray pyrolysis	1.0 µm	1.27 eV	Yes	–	≈ 45%	[145]
Dip technique	0.5 µm	1.4 eV	Yes	–	≈ 50%	[174]
ECD	< 1 − 2.5 µm	1.0–1.3 eV	Yes	–	< 2%	[188]
CSVT	3 µm	1.32 eV	Yes	–	≈ 40%	[106]
CSVT	3 µm	1.32 eV	Yes	–	≈ 40%	[105]
Brush plated	2 µm	1.1 eV	Yes	–	≈ 65%	[107]
ECD	1 µm	1.15 eV	Yes	–	50%	[211]
Thermal evaporation	55 − 365nm	1.38 –2 eV and 2.18–2.33 eV	–	–	95%	[47]
CBD	< 1 µm	1.38 eV	Yes	–	50%	[123]
PECD	2.5 µm	1.67 eV	Yes	–	15%	[192]
PECVD	0.35 µm	1.25^{I} eV	Yes	–	90%	[170]
Co-evaporation	< 1 µm	1.3 eV	Yes	–	85%	[91]
Co-evaporation	1.2 µm	1.3 eV	Yes	–	48%	[70]
Co-evaporation	1.02 µm	–	Yes	–	80%	[70]
Co-evaporation	296nm	–	Yes	–	80%	[70]
Thermal evaporation	0.5 µm	1.35 eV	Yes	Yes	90%	[51]
Thermal evaporation	0.5 µm	1.35 eV	Yes	–	80%	[50]
CCEDM	< 1 µm	1.21–1.42 eV	Yes	–	80%	[194]
PED	966nm	1.32 eV	Yes	–	42%	[225]
PED	960nm	1.30 eV	Yes	–	30%	[225]
PED	946nm	1.23 eV	Yes	–	42%	[225]
Spray pyrolysis	0.6 µm	1.32 eV	Yes	yes	80%	[226]
CBD	450nm	1.7 eV	Yes	–	65%	[124]
Thermal evaporation	1.8 µm	0.94 eV	Yes	–	≈ 40%	[227]
Thermal evaporation	1.2 µm	≈ 1.15 eV	Yes	–	≈ 98%	[227]
Thermal evaporation	0.6 µm	1.36 eV	Yes	–	≈ 70%	[227]
Thermal evaporation	0.3 µm	≈ 1.32 eV	Yes	–	≈ 60%	[227]
Thermal evaporation	0.25 µm	≈ 1.26 eV	Yes	–	≈ 65%	[227]
EDM	980nm	1.16 eV	Yes	–	18%	[196]

Table 3.4: Transmittance of SnS Thin Films with Thickness.

Technique	Thickness	Band gap	Polycrystalline	Single phase	Transmittance	Ref
SILAR	0.20 µm	1.43 eV	Yes	–	80%	[154]
SILAR	0.20 µm	1.43 eV	Yes	–	80%	[155]
ECD	$<$ 1 µm	1.37 eV	Yes	Yes	80%	[203]
CBD	290nm	1.31 eV	Yes	–	65%	[127]
Thermal evaporation	3 µm	1.45 eV	Yes	–	$\approx$ 80%	[228]
Thermal evaporation	0.6 µm	1.9 eV	Yes	–	$\approx$ 70%	[58]
SILAR	150nm	1.71 eV	Yes	–	80%	[152]
SILAR	150nm	1.71 eV	Yes	–	80%	[151]
GECD	400nm	$\approx$ 1.56 eV	Yes	–	60%	[198]
CBD	$\approx 100 - 434$nm	$\approx 1.7 - 1.76$ eV	Yes	–	$\approx 40 - 80$%	[128]
Spray pyrolysis	2 µm	1.21 eV	Yes	–	$<$ 1%	[147]
Sulfurisation	200nm	1.3 eV	Yes	–	80%	[85]
PVDT	170 µm	1.21 eV	No	–	16%	[75]
ECD	$<$ 1.4 µm	1.1 eV	poly	–	reflectance given	[199]
Thermal evaporation	65nm	2.28 eV	Yes	–	40%	[62]
Thermal evaporation	185nm	2.15 eV	Yes	–	80%	[62]
Thermal evaporation	350nm	1.68 eV	Yes	–	70%	[62]
Thermal evaporation	580nm	1.55 eV	Yes	–	68%	[62]
HWD	1.5 µm	1.07 eV	Yes	yes	18%	[229]
HWD	1 µm	1.27 eV	Yes	yes	60%	[229]
Sulfurisation	800nm	1.27 eV	Yes	yes	55%	[230]
Sputtering/sulfurisation	280nm	0.9 eV	Yes	yes	18%	[88]
Sputtering/sulfurisation	385nm	1.16 eV	Yes	yes	28%	[88]
Sputtering/sulfurisation	409nm	1.22 eV	Yes	yes	46%	[88]
Sputtering/sulfurisation	420nm	1.30 eV	Yes	yes	56%	[88]
Thermal evaporation	20nm	2.15 eV	Yes	–	80%	[61]
Thermal evaporation	40nm	2.28 eV	Yes	–	70%	[61]
Thermal evaporation	65nm	2.28 eV	Yes	–	45%	[61]
CBD	375 – 450nm	1.06–1.13 eV	Yes	–	60–78%	[133]
Thermal evaporation	300nm	1.45 eV	Yes	–	$<$ 10%	[175]
Sputtering/sulfurisation	193 – 208nm	1.31–1.36 eV	Yes	–	reflectance given	[93]
Thermal evaporation	0.75 – 1.14 µm	1.32–1.06 eV	Yes	–	32–25%	[231]
Vacuum deposited	561 – 1127 Å	1.62-1.67 eV	not given	–	80–60%	[22]

Table 3.5: Transmittance of SnS Thin Films with Thickness – contd.

References

[1] P. Woulffe. “Experiments to show the nature of aurum mosaicum”. In: *Philosophical Transactions* 61 (1771), pp. 114–130 (cit. on p. 63).

[2] T. Jiang and G. A. Ozin. “New directions in tin sulfide materials chemistry”. In: *Journal of Materials Chemistry* 8 (1998), pp. 1099–1108 (cit. on p. 63).

[3] G. Barone, T. G. Hibbert, M. F. Mahon, K. C. Molloy, L. S. Price, I. P. Parkin, A. M. E. Hardy, and M. N. Field. “Deposition of tin sulfide thin films from tin(IV) thiolate precursors”. In: *Journal of Materials Chemistry* 11 (2001), pp. 464–468 (cit. on p. 63).

[4] R. Herzenberg. “Kolbeckin, Sn_2S_3, ein neues Zinnmineral”. In: *Zentralblatt für Mineralogie A* (1932), pp. 345–355 (cit. on p. 63).

[5] P. Ramdohr. “Vorkommen und Eigenschaften des Herzenbergits”. In: *Zeitschrift für Kristallographie* 92 (1935), pp. 186–189 (cit. on p. 63).

[6] C. Palache, H. Berman, and C. Frondel. *The System of Mineralogy of J. D. Dana and E. S. Dana*. 7th Edition. John Wiley & Sons, Inc., New York, 1944 (cit. on p. 63).

[7] A. Sugaki, A. Kitakaze, and H. Kitazawa. “Synthesized tin and tin-sulfide minerals; Synthetic sulfide minerals (XIII)”. In: *Science Reports of the Tohoku University* 16(3) (1985), pp. 199–211 (cit. on p. 63).

[8] W. Albers, C. Haas, and F. van der Maesen. “The preparation and the electrical and optical properties of SnS crystals”. In: *Journal of Physics and Chemistry of Solids* 15 (1960), pp. 306–310 (cit. on pp. 63, 64).

[9] J. S. Anderson and M. C. Morton. “The electrical conductivity of stannous sulphide”. In: *Proceedings of the Royal Society of London. Series A. Mathematical and Physical Sciences* 184 (1945), pp. 83–101 (cit. on p. 63).

[10] J. S. Anderson and M. C. Morton. “Semi-conducting Properties of Stannous Sulphide”. In: *Nature* 155 (1945), p. 112 (cit. on p. 63).

[11] J. S. Anderson and M. C. Morton. “Semi–conducting properties of stannous sulphide. Part II.—Thermoelectric effect”. In: *Transactions of the Faraday Society* 43 (1947), pp. 185–194 (cit. on p. 63).

[12] J. S. Anderson and M. J. Ridge. “Distribution equilibria in the system tin-stannous sulphide”. In: *Transactions of the Faraday Society* 39 (1943), pp. 93–98 (cit. on p. 64).

[13] M. C. Clark and J. S. Anderson. “Semi-conducting Properties of Stannous Sulphide”. In: *Nature* 152 (1943), pp. 75–76 (cit. on p. 64).

[14] J. G. M. Braithwaite. “Infra-red photoconductivity of certain valence intermetallic compounds”. In: *Proceedings of the Physical Society B* B64 (1951), pp. 274–275 (cit. on p. 64).

[15] H. Gobrecht and A. Bartschat. “Über die Halbleitereigenschaften von synthetischen Herzenbergit-(SnS-) Kristallen”. In: *Zeitschrift für Physik A Hadrons and Nuclei* 149 (1957), pp. 511–522 (cit. on p. 64).

[16] C. Haas and M. M. G. Corbey. “Measurement and analysis of the infrared reflection spectrum of semiconducting SnS”. In: *Journal of Physics and Chemistry of Solids* 20 (1961), pp. 197–203 (cit. on p. 64).

[17] W. Albers, C. Haas, H. J. Vink, and J. D. Wasscher. “Investigations on SnS”. In: *Journal of Applied Physics* 32 (1961), pp. 2220–2225 (cit. on p. 65).

[18] W. Albers, C. Haas, H. Ober, G. R. Schodder, and J. D. Wasscher. “Preparation and properties of mixed crystals $SnS_{(1-x)}Se_x$”. In: *Journal of Physics and Chemistry of Solids* 23 (1962), pp. 215–220 (cit. on p. 65).

[19] H. Rau. “High temperature equilibrium of atomic disorder in SnS”. In: *Journal of Physics and Chemistry of Solids* 27 (1966), pp. 761–769 (cit. on p. 65).

[20] Ya. S. Feiziev, Ya. N. Nasirov, and O. N. Novuroz. “Thermal properties of tin sulphide single crystals”. In: *Physica Status Solidi* 28 (1968), K113–K115 (cit. on p. 65).

[21] A. P. Lambros, D. Geraleas, and N. A. Economou. “Optical absorption edge in SnS”. In: *Journal of Physics and Chemistry of Solids* 35 (1974), pp. 537–541 (cit. on p. 65).

[22] A. Goswami and A. Mitra. “Optical properties of vacuum-deposited SnS films”. In: *Indian Journal of Pure and Applied Physics* 13 (1975), pp. 508–511 (cit. on pp. 65, 91).

[23] J. M. Chamberlain, P. M. Nikolic, M. Merdan, and P. Mihailovic. “Far-infrared optical properties of SnS”. In: *Journal of Physics C Solid State Physics* 9 (1976), pp. L637–L642 (cit. on p. 65).

[24] J. M. Chamberlain and M. Merdan. “Infrared photoconductivity in p-SnS”. In: *Journal of Physics C: Solid State Physics* 10 (1977), pp. L571–L574 (cit. on p. 65).

[25] O. H. Hughes, P. M. Nikolic, J. M. Chamberlain, C. J. Doran, and M. Merdan. “Coupled Plasmon-Phonon Effects in IV-VI Semiconductors”. In: *Phonon Scattering in Solids*. Springer, 1976, pp. 312–314 (cit. on p. 67).

[26] P. M. Nikolic, P. Mihajlovic, and B. Lavrencic. “Splitting and coupling of lattice modes in the layer compound SnS”. In: *Journal of Physics C: Solid State Physics* 10 (1977), pp. L289–L292 (cit. on pp. 67, 89).

[27] H. R. Chandrasekhar, R. G. Humphreys, U. Zwick, and M. Cardona. “Infrared and Raman spectra of the IV-VI compounds SnS and SnSe”. In: *Physical Review B* 15 (1977), pp. 2177–2183 (cit. on pp. 67, 89).

[28] P. M. Nikolic and D. M. Todorovic. “Photo-acoustic and thermo-acoustic properties of single-crystal SnS compared with its near-infrared optical and transport measurements”. In: *Journal of Physics C: Solid State Physics* 20 (1987), pp. 39–46 (cit. on p. 67).

[29] D. Trbojevic, P. M. Nikolic, B. Perovic, and V. Cvekic. “Photovoltaic detectors in SnS produced by Sb ion implantation”. In: *Applied Physics Letters* 38 (1981), pp. 362–364 (cit. on p. 67).

[30] T. Chattopadhyay, A. Werner, H. G. Von Schnering, and J. Pannetier. "Temperature and pressure induced phase transition in IV-VI compounds". In: *Revue de Physique Appliquée* 19 (1984), pp. 807–813 (cit. on p. 67).

[31] T. Chattopadhyay, J. Pannetier, and H. G. Von Schnering. "Neutron diffraction study of the structural phase transition in SnS and SnSe". In: *Journal of Physics and Chemistry of Solids* 47 (1986), pp. 879–885 (cit. on p. 67).

[32] M. Parenteau and C. Carlone. "Influence of temperature and pressure on the electronic transitions in SnS and SnSe semiconductors". In: *Physical Review B* 41 (1990), pp. 5227–5234 (cit. on p. 67).

[33] A. M. Elkorashy. "Photoconductivity in tin sulphide single crystals". In: *Physica B* 168 (1991), pp. 257–267 (cit. on pp. 67, 90).

[34] H. Wiedemeier and Hans Georg von Schnering. "Refinement of the structures of GeS, GeSe, SnS and SnSe". In: *Zeitschrift für Kristallographie* 148 (1978), pp. 295–303 (cit. on p. 67).

[35] H. Wiedemeier and F. J. Csillag. "The thermal expansion and high temperature transformation of SnS and SnSe*". In: *Zeitschrift für Kristallographie* 149 (1979), pp. 17–29 (cit. on p. 67).

[36] H. Wiedemeier and F. J. Csillag. "Equilibrium sublimation and thermodynamic properties of SnS". In: *Thermochimica Acta* 34 (1979), pp. 257–265 (cit. on p. 67).

[37] Hans Georg von Schnering and H. Wiedemeier. "The high temperature structure of β-SnS and β-SnSe and the B16-to-B33 type λ-transition path". In: *Zeitschrift für Kristallographie* 156 (1981), pp. 143–150 (cit. on p. 67).

[38] K. L. Chopra. *Thin Film Phenomena.* McGraw-Hill, New York, 1969 (cit. on p. 69).

[39] K. L. Chopra and S. R. Das. *Thin Film Solar Cells.* Plenum Press, New York, 1983 (cit. on pp. 69, 81–83).

[40] S. M. Sze. *Semiconductor Devices: Physics and Technology.* 2nd Edition. Wiley, New York, 2001 (cit. on p. 69).

[41] L. I. Maissel and R. Glang. *Handbook of Thin Film Technology.* McGraw-Hill, New York, 1970 (cit. on pp. 69, 70).

[42] H. Noguchi, A. Setiyadi, H. Tanamura, T. Nagatomo, and O. Omoto. "Characterization of vacuum-evaporated tin sulfide film for solar cell materials". In: *Solar Energy Materials and Solar Cells* 35 (1994), pp. 325–331 (cit. on pp. 70, 88).

[43] K. Deraman, S. Sakrani, B. B. Ismail, and Y. Wahab. "Electrical conductivity measurements in evaporated tin sulphide thin films". In: *International Journal of Electronics* 76 (1994), pp. 917–922 (cit. on p. 71).

[44] K. Deraman, S. Sakrani, and B. Ismail. "Evaporated SnS semiconducting thin films [2364-59]". In: *Proceedings–SPIE The International Society for Optical Engineering* (1994), p. 357 (cit. on p. 71).

[45] S. B. Badachhape and A. Goswami. "Electron diffraction study of evaporated films of tin sulphide". In: *Indian Journal of Pure and Applied Physics* 2 (1964), pp. 250–53 (cit. on p. 71).

[46] J. B. Johnson, H. Jones, B. S. Latham, J. D. Parker, R. D. Engelken, and C. Barber. "Optimization of photoconductivity in vacuum-evaporated tin sulfide thin films". In: *Semiconductor Science and Technology* 14 (1999), pp. 501–507 (cit. on p. 71).

[47] M. M. El-Nahass, H. M. Zeyada, M. S. Aziz, and N. A. El-Ghamaz. "Optical properties of thermally evaporated SnS thin films". In: *Optical Materials* 20 (2002), pp. 159–170 (cit. on pp. 71, 90).

[48] A. Abou Shama and H. M. Zeyada. "Electronic dielectric constants of thermally evaporated SnS thin films". In: *Optical Materials* 24 (2003), pp. 555–561 (cit. on p. 71).

[49] M. Devika, K. T. Ramakrishna Reddy, N. Koteeswara Reddy, K. Ramesh, R. Ganesan, E. S. R. Gopal, and K. R. Gunasekhar. "Microstructure dependent physical properties of evaporated tin sulfide films". In: *Journal of Applied Physics* 100 (2006), p. 23518 (cit. on p. 71).

[50] M. Devika, N. Koteeswara Reddy, K. Ramesh, H. R. Sumana, K. R. Gunasekhar, E. S. R. Gopal, and K. T. Ramakrishna Reddy. "The effect of substrate surface on the physical properties of SnS films". In: *Semiconductor Science and Technology* 21 (2006), pp. 1495–1501 (cit. on pp. 72, 90).

[51] M. Devika, N. K. Reddy, K. Ramesh, K. R. Gunasekhar, E. S. R. Gopal, and K. T. Ramakrishna Reddy. “Influence of annealing on physical properties of evaporated SnS films”. In: *Semiconductor Science and Technology* 21 (2006), pp. 1125–1131 (cit. on pp. 72, 90).

[52] M. Devika, N. K. Reddy, K. Ramesh, V. Ganesan, E. S. R. Gopal, and K. T. Ramakrishna Reddy. “Influence of substrate temperature on surface structure and electrical resistivity of the evaporated tin sulphide films”. In: *Applied Surface Science* 253 (2006), pp. 1673–1676 (cit. on p. 72).

[53] M. Devika, N. Koteeswara Reddy, S. Venkatramana Reddy, K. Ramesh, and K. R. Gunasekhar. “Influence of rapid thermal annealing (RTA) on the structural and electrical properties of SnS films”. In: *Journal of Materials Science: Materials in Electronics* 20 (2009), pp. 1129–1134 (cit. on p. 72).

[54] Y. Qiu, W. Shi, G. Wei, H. XU, and F. LIN. “Characterization of the SnS thin films deposited by vacuum evaporation”. In: *Journal of Optoelectronics Laser* 17 (2006), p. 817 (cit. on p. 72).

[55] B. Ghosh, M. Das, P. Banerjee, and S. Das. “Fabrication of vacuum-evaporated SnS/CdS heterojunction for PV applications”. In: *Solar Energy Materials and Solar Cells* 92 (2008), pp. 1099–1104 (cit. on pp. 72, 88).

[56] B. Ghosh, M. Das, P. Banerjee, and S. Das. “Fabrication of the SnS/ZnO heterojunction for PV applications using electrodeposited ZnO films”. In: *Semiconductor Science and Technology* 24 (2009), p. 025024 (cit. on pp. 72, 88).

[57] B. Ghosh, R. Bhattacharjee, P. Banerjee, and S. Das. “Structural and optoelectronic properties of vacuum evaporated SnS thin films annealed in argon ambient”. In: *Applied Surface Science* 257 (2011), pp. 3670–3676 (cit. on p. 72).

[58] O. E. Ogah, G. Zoppi, I. Forbes, and R. W. Miles. “Thin films of tin sulphide for use in thin film solar cell devices”. In: *Thin Solid Films* 517 (2009), pp. 2485–2488 (cit. on pp. 72, 91).

[59] O. E. Ogah, K. R. Reddy, G. Zoppi, I. Forbes, and R. W. Miles. "Annealing studies and electrical properties of SnS-based solar cells". In: *Thin Solid Films* 519 (2011), pp. 7425–7428 (cit. on p. 72).

[60] G. Yuying, S. Weimin, and W. Guangpu. "Electrical Properties of Doped Sns Thin Films Prepared by Vacuum Evaporation". In: *Proceedings of ISES World Congress 2007 (Vol. I–Vol. V)*. Springer. 2009, pp. 1337–1340 (cit. on p. 72).

[61] S. Cheng and G. Conibeer. "Physical properties of very thin SnS films deposited by thermal evaporation". In: *Thin Solid Films* 520 (2011), pp. 837–841 (cit. on pp. 72, 89, 91).

[62] S. Cheng and H. Zhang. "Influence of thickness on structural and optical properties of evaporated tin sulphide films". In: *Micro & Nano Letters, IET* 6 (2011), pp. 473–475 (cit. on pp. 72, 89, 91).

[63] N. K. Reddy. "Growth-Temperature Dependent Physical Properties of SnS Nanocrystalline Thin Films". In: *ECS Journal of Solid State Science and Technology* 2 (2013), P259–P263 (cit. on p. 72).

[64] N. Koteeswara Reddy, Y. B. Hahn, M. Devika, H. R. Sumana, and K. R. Gunasekhar. "Temperature-dependent structural and optical properties of SnS films". In: *Journal of Applied Physics* 101 (2007), p. 093522 (cit. on p. 72).

[65] N. K. Reddy, M. Devika, Y. Hahn, and K. R. Gunasekhar. "Impact of chemical treatment on the surface, structure, optical and electrical properties of SnS thin films". In: *Applied Surface Science* 268 (2013), pp. 317–322 (cit. on pp. 72, 73).

[66] A. Schneikart, H. J. Schimper, A. Klein, and W. Jaegermann. "Efficiency limitations of thermally evaporated thin-film SnS solar cells". In: *Journal of Physics D: Applied Physics* 46 (2013), p. 305109 (cit. on pp. 73, 88).

[67] M. S. Selim, M. E. Gouda, M. G. El-Shaarawy, A. M. Salem, and W. A. Abd El-Ghany. "Effect of thickness on optical properties of thermally evaporated SnS films". In: *Thin Solid Films* 527 (2012), 164–169 (cit. on p. 73).

[68] W. Wu, W. Shi, Z. Hu, S. Liu, W. Yang, and G. Wei. "Influence of heat treatment on the microstruture of SnS/ZnS film prepared by vacuum evaporation". In: *Seventh International Conference on Thin Film Physics and Applications*. International Society for Optics and Photonics. 2010, pp. 79952D–79952D. DOI: http://dx.doi.org/10.1117/12.888226 (cit. on p. 73).

[69] A. Jakhar, A. Jamdagni, A. Bakshi, T. Verma, V. Shukla, P. Jain, N. Sinha, and P. Arun. "Refractive Index of SnS Thin Nano-crystalline Films". In: *Solid State Communications* 168 (2013), pp. 31–35 (cit. on p. 73).

[70] C. Cifuentes, M. Botero, E. Romero, C. Caldern, and G. Gordillo. "Optical and structural studies on SnS films grown by co-evaporation". In: *Brazilian Journal of Physics* 36 (2006), pp. 1046–1049 (cit. on pp. 74, 90).

[71] N. Koteeswara Reddy, K. Ramesh, R. Ganesan, K. T. Ramakrishna Reddy, K. R. Gunasekhar, and E. S. R. Gopal. "Synthesis and characterisation of co-evaporated tin sulphide thin films". In: *Applied Physics A: Materials Science & Processing* 83 (2006), pp. 133–138 (cit. on p. 74).

[72] A. Tanuševski and D. Poelman. "Optical and photoconductive properties of SnS thin films prepared by electron beam evaporation". In: *Solar Energy Materials and Solar Cells* 80 (2003), pp. 297–303 (cit. on p. 74).

[73] J. Henry, K. Mohanraj, S. Kannan, S. Barathan, and G. Sivakumar. "Structural and optical properties of SnS nanoparticles and electron-beam-evaporated SnS thin films". In: *Journal of Experimental Nanoscience* (2013), pp. 1–8. DOI: DOI: 10.1080/17458080.2013.788226 (cit. on p. 74).

[74] S. A. Bashkirov, V. F. Gremenok, V. A. Ivanov, V. V. Lazenka, and K. Bente. "Tin sulfide thin films and Mo/p-SnS/n-CdS/ZnO heterojunctions for photovoltaic applications". In: *Thin Solid Films* 520 (2012), pp. 5807–5810 (cit. on pp. 74, 88).

[75] S. S. Hegde, A. G. Kunjomana, K. A. Chandrasekharan, K. Ramesh, and M. Prashantha. "Optical and electrical properties of SnS semiconductor crystals grown by physical vapor deposition technique". In: *Physica B: Condensed Matter* 406 (2011), pp. 1143–1148 (cit. on pp. 74, 78, 91).

[76] J. A. Thornton. “Influence of apparatus geometry and deposition conditions on the structure and topography of thick sputtered coatings”. In: *Journal of Vacuum Science and Technology* 11 (1974), pp. 666–670 (cit. on p. 75).

[77] R. Behrisch. *Physical Sputtering of Single-Element Solids*. Springer, Berlin, 1979 (cit. on p. 75).

[78] W. Guang-Pu, Z. Zhi-Lin, Z. Wei-Ming, G. Xiang-Hong, C. Wei-Qun, H. Tanamura, M. Yamaguchi, H. Noguchi, T. Nagatomo, and O. Omoto. “Investigation on SnS film by RF sputtering for photovoltaic application.” In: *IEEE First World Conference on Photovoltaic Energy Conversion, Waikoloa, Hawaii*. 1994, pp. 365–368. DOI: doi:10.1109/WCPEC.1994.519977 (cit. on p. 75).

[79] K. Hartman, J.L. Johnson, M.I. Bertoni, D. Recht, M.J. Aziz, M.A. Scarpulla, and T. Buonassisi. “SnS thin-films by RF sputtering at room temperature”. In: *Thin Solid Films* 519 (2011), pp. 7421–7424 (cit. on p. 75).

[80] A. Stadler, H.J. Schimper, U. Brendel, D. Topa, A. Basch, and H. Dittrich. “Analyzing UV/Vis/NIR spectra with the single-layer model—sputtered SnS thin films I: space–time dependencies”. In: *Thin Solid Films* 519 (2011), pp. 7951–7958 (cit. on p. 75).

[81] R. E. Banai, H. Lee, M. A. Motyka, R. Chandrasekharan, N. J. Podraza, J. R. S. Brownson, and M. W. Horn. “Optical Properties of Sputtered SnS Thin Films for Photovoltaic Absorbers”. In: *IEEE Journal of Photovoltaics* 3 (2013), pp. 1084–1089 (cit. on p. 75).

[82] R. E. Banai, H. Lee, M. Lewinsohn, M. A. Motyka, R. Chandrasekharan, N. J. Podraza, J. R. S. Brownson, and M. W. Horn. “Investigation of the absorption properties of sputtered tin sulfide thin films for photovoltaic applications”. In: *Photovoltaic Specialists Conference (PVSC), 2012 38th IEEE*. 2012, pp. 000164–000169. DOI: doi:10.1109/PVSC.2012.6317592 (cit. on p. 75).

[83] K. T. Ramakrishna Reddy, P. Purandhra Reddy, P. K. Datta, and R. W. Miles. “Formation of polycrystalline SnS layers by a two-step process”. In: *Thin Solid Films* 403 (2002), pp. 116–119 (cit. on p. 76).

[84] K. T. Ramakrishna Reddy and P. Purandhra Reddy. “Structural studies on SnS films grown by a two-stage process”. In: *Materials Letters* 56 (2002), pp. 108–111 (cit. on p. 76).

[85] K. T. Ramakrishna Reddy, K. Ramya, G. Sreedevi, T. Shimizu, Y. Murata, and M. Sugiyama. “Studies on the energy band discontinuities in SnS/ZnMgO thin film heterojunction”. In: *Energy Procedia* 10 (2011), pp. 172–176 (cit. on pp. 76, 91).

[86] E. P. Zaretskaya, V. F. Gremenok, V. A. Ivanov, S. A. Bashkirov, V. B. Zalesski, and B. I. Kovalevski. “Physical Properties of Polycrystalline SnS Thin Films for Solar Cells”. In: *EU-PVSEC Proceedings*. 2009, pp. 262–265. DOI: doi:10.4229/24thEUPVSEC2009-1CV.3.10 (cit. on p. 76).

[87] S. Cheng, N Zhong, C. Huang, and G. Chen. “SnS films prepared by sulfuration of Sn precursor layers”. In: *SPIE Proceedings*. Vol. 5633. 2005. DOI: doi:http://dx.doi.org/10.1117/12.568466 (cit. on p. 76).

[88] F. Jiang, H. Shen, C. Gao, B. Liu, L. Lin, and Z. Shen. “Preparation and properties of SnS film grown by two-stage process”. In: *Applied Surface Science* 257 (2011), pp. 4901–4905 (cit. on pp. 77, 91).

[89] F. Jiang, H. Shen, W. Wang, and L. Zhang. “Preparation of SnS Film by Sulfurization and SnS/a-Si Heterojunction Solar Cells”. In: *Journal of The Electrochemical Society* 159 (2012), H235–H238 (cit. on pp. 77, 88).

[90] M. Sugiyama, Y. Murata, T. Shimizu, K. Ramya, C. Venkataiah, T. Sato, and K. T. Ramakrishna Reddy. “Sulfurization Growth of SnS Thin Films and Experimental Determination of Valence Band Discontinuity for SnS-Related Solar Cells”. In: *Japanese Journal of Applied Physics* 50 (2011), 05FH03 (cit. on pp. 77, 89).

[91] M. Botero, C. Cifuentes, E. Romero, J. Clavijo, and G. Gordillo. “Properties of SnS thin films grown by a two-step process”. In: *Photovoltaic Energy Conversion, Conference Record of the 2006 IEEE 4th World Conference on*. Vol. 1. 2006, pp. 79–82. DOI: doi:10.1109/WCPEC.2006.279351 (cit. on pp. 77, 90).

[92] M. Botero, P. Bartolo Perez, C. Calderon, E. Romero, and G. Gordillo. “Study of SnS: Bi thin films prepared by sulfurization”. In: *Photovoltaic Specialists Conference*

(PVSC), 2009 34th IEEE. 2009, pp. 000852–000856. DOI: doi:10.1109/PVSC.2009.5411154 (cit. on p. 77).

[93] M. Leach, K.T. Reddy, M.V. Reddy, J.K. Tan, D.Y. Jang, and R.W. Miles. "Tin Sulphide Thin Films Synthesised using a Two Step Process". In: *Energy Procedia* 15 (2012), pp. 371–378 (cit. on pp. 77, 91).

[94] T. Hirano, T. Shimizu, K. Yoshida, and M. Sugiyama. "Sulfurization growth of SnS films and fabrication of ZnO/SnS heterojunction for solar cells". In: *Photovoltaic Specialists Conference (PVSC), 2011 37th IEEE*. 2011, pp. 001280–001282. DOI: doi:10.1109/PVSC.2011.6186191 (cit. on p. 77).

[95] Ji. Qiang, S. Hong-lie, J. Feng, W. Wei, and Z. You-hong. "Research on the Optoelectronic Properties of SnS Thin Films Prepared by Two-Stage Process". In: *Imaging Science and Photochemistry* 31 (2013), pp. 150–156 (cit. on p. 77).

[96] A. Y. Cho and J. R. Arthur. "Molecular beam epitaxy". In: *Progress in Solid State Chemistry* 10 (1975), pp. 157–192 (cit. on p. 77).

[97] P. Bhattacharya. *Semiconductor optoelectronic devices*. Prentice-Hall, Inc., Englewood Cliffs, New Jersey, 1994 (cit. on p. 77).

[98] H. Nozaki, M. Onoda, M. Sekita, K. Kosuda, and T. Wada. "Variation of lattice dimensions in epitaxial SnS films on MgO (001)". In: *Journal of Solid State Chemistry* 178 (2005), pp. 245–252 (cit. on p. 78).

[99] W. Wang, K.K. Leung, W.K. Fong, S.F. Wang, Y.Y. Hui, S.P. Lau, Z. Chen, L.J. Shi, C.B. Cao, and C. Surya. "Molecular beam epitaxy growth of high quality p-doped SnS van der Waals epitaxy on a graphene buffer layer". In: *Journal of Applied Physics* 111 (2012), p. 093520 (cit. on p. 78).

[100] W. Wang, K. K. Leung, W. K. Fong, S. F. Wang, Y. Y. Hui, S. P. Lau, and C. Surya. "Growth of epitaxial quality SnS thin films on graphene". In: *Electron Devices and Solid State Circuit (EDSSC), 2012 IEEE International Conference on*. IEEE. 2012, pp. 1–3. DOI: doi:10.1109/EDSSC.2012.6482879 (cit. on p. 78).

[101] S. F. Wang, W. K. Fong, W. Wang, K. K. Leung, and C. Surya. "Growth of SnS van der Waals Epitaxies on Layered Substrates". In: *MRS Proceedings*. Vol. 1493. Cambridge Univ Press. 2013, mrsf12–1493. DOI: doi:http://dx.doi.org/10.1557/opl.2013.234 (cit. on p. 78).

[102] W. Wang, K. K. Leung, W. K. Fong, S. F. Wang, Y. Y. Hui, S. P. Lau, and C. Surya. "Application of a graphene buffer layer for the growth of high quality SnS films on GaAs (100) substrate". In: *Photovoltaic Specialists Conference (PVSC), 2012 38th IEEE*. IEEE. 2012, pp. 002614–002616. DOI: doi:10.1109/PVSC.2012.6318130 (cit. on p. 78).

[103] W. Wang, K. K. Leung, W. K. Fong, S. F. Wang, Y. Y. Y. Hui, S. P. P. Lau, and C. Surya. "High quality SnS van der Waals Epitaxies on graphene buffer layer". In: *SPIE Solar Energy+ Technology*. International Society for Optics and Photonics. 2012, 84700E–84700E. DOI: doi:10.1117/12.930946;http://dx.doi.org/10.1117/12.930946 (cit. on p. 78).

[104] W. Wang, K. K. Leung, W. K. Fong, S. F. Wang, Y. Y. Hui, S. P. Lau, and C. Surya. "Growth of high quality SnS van der Waals epitaxies on graphene buffer layer for photovoltaic applications". In: *Solid-State and Integrated Circuit Technology (ICSICT), 2012 IEEE 11th International Conference on*. IEEE. 2012, pp. 1–4. DOI: doi:10.1109/ICSICT.2012.6467666 (cit. on p. 78).

[105] Yanuar, G. Moussa, F. Guastavino, and C. LIinares. "Preparation and Characterization of SnS Thin Films Obtained by Close-Spaced Vapor Transport for Solar Cell Application". In: *IEEE Proceedings* (2000), pp. 66–68. DOI: doi:10.1109/CMPLES.2000.939863 (cit. on pp. 78, 90).

[106] Yanuar, F. Guastavino, C. LIinares, and G. E. Moussa. "SnS thin films grown by close-spaced vapor transport". In: *Journal of Materials Science Letters* 19 (2000), pp. 2135–2137 (cit. on pp. 78, 90).

[107] M. Jayachandran, S. Mohan, B. Subramanian, C. Sanjeeviraja, and V. Ganesan. "Studies on the brush plated SnS thin films". In: *Journal of Materials Science Letters* 20 (2000), pp. 381–383 (cit. on pp. 78, 90).

[108] J.Y. Kim and S.M. George. “Tin monosulfide thin films grown by atomic layer deposition using tin 2, 4-pentanedionate and hydrogen sulfide”. In: *Journal of Physical Chemistry C* 100 (2010), pp. 17597–17603 (cit. on p. 78).

[109] P. Sinsermsuksakul, J. Heo, W. Noh, A. S. Hock, and R. G. Gordon. “Atomic layer deposition of tin monosulfide thin films”. In: *Advanced Energy Materials* 1 (2011), pp. 1116–1125 (cit. on pp. 78, 89).

[110] J. Vidal, S. Lany, M. dAvezac, A. Zunger, A. Zakutayev, J. Francis, and J. Tate. “Band-structure, optical properties, and defect physics of the photovoltaic semiconductor SnS”. In: *Applied Physics Letters* 100 (2012), p. 032104 (cit. on pp. 78, 87).

[111] G. Brückmann. “Darstellung und Eigenschaften dünner Bleisulfid-Schichten unter besonderer Berücksichtigung ihrer Detektorwirkung, II”. In: *Colloid & Polymer Science* 65 (1933), pp. 148–161 (cit. on p. 78).

[112] E. Guneri, C. Ulutas, F. Kirmizigul, G. Altindemir, F. Gode, and C. Gumus. “Effect of deposition time on structural, electrical, and optical properties of SnS thin films deposited by chemical bath deposition”. In: *Applied Surface Science* 257 (2010), pp. 1189–1195 (cit. on pp. 79, 80).

[113] D. Lincot and R. Ortega. “Chemical bath deposition of cadmium sulfide thin films. In situ growth and structural studies by combined quartz crystal microbalance and electrochemical impedance techniques.” In: *Journal of the Electrochemical Society* 139 (1992), pp. 1880–1889 (cit. on p. 79).

[114] P. C. Rieke and S. B. Bentjen. “Deposition of cadmium sulfide films by decomposition of thiourea in basic solution”. In: *Chemistry of Materials* 5 (1993), pp. 43–53 (cit. on p. 79).

[115] N. R. Pavaskar, C. A. Menezes, and A. P. B. Sinha. “Photoconductive CdS films by a chemical bath deposition process”. In: *Journal of the Electrochemical Society* 124 (1977), pp. 743–748 (cit. on p. 79).

[116] P. Pramanik, P. K. Basu, and S. Biswas. “Preparation and characterization of chemically deposited tin(II) sulphide thin films”. In: *Thin Solid Films* 150 (1987), pp. 269–276 (cit. on p. 79).

[117] M. T. S. Nair and P. K. Nair. “Simplified chemical deposition technique for good quality SnS thin films”. In: *Semiconductor Science and Technology* 6 (1991), pp. 132–134 (cit. on pp. 79, 90).

[118] P. K. Nair, M. T. S. Nair, J. Campos, and A. Sanchez. “SnS–SnO_2 conversion of chemically deposited SnS thin films”. In: *Advanced Materials for Optics and Electronics* 1 (1992), pp. 117–121 (cit. on p. 79).

[119] P. K. Nair, M. T. S. Nair, and J. Campos. “Photoconductive SnO_2 Thin Films from Thermal Decomposition of Chemically Deposited SnS Thin Films”. In: *Journal of The Electrochemical Society* 140 (1993), pp. 539–541 (cit. on p. 79).

[120] P. K. Nair, M. T. S. Nair, R. A. Zingaro, and E. A. Meyers. “XRD, XPS, optical and electrical studies on the conversion of SnS thin films to SnO_2”. In: *Thin Solid Films* 239.1 (1994), pp. 85–92 (cit. on p. 79).

[121] M. Ristov, G. Sinadinovski, I. Grozdanov, and M. Mitreski. “Chemical deposition of tin (II) sulphide thin films”. In: *Thin Solid Films* 173 (1989), pp. 53–58 (cit. on p. 79).

[122] M. Ristov, G. Sinadinovski, M. Mitreski, and M. Ristova. “Photovoltaic cells based on chemically deposited p-type SnS”. In: *Solar Energy Materials and Solar Cells* 69 (2001), pp. 17–24 (cit. on pp. 80, 82, 88).

[123] A. Tanuševski. “Optical and photoelectric properties of SnS thin films prepared by chemical bath deposition”. In: *Semiconductor Science and Technology* 18 (2003), pp. 501–505 (cit. on pp. 80, 90).

[124] D. Avellaneda, G. Delgado, M. T. S. Nair, and P. K. Nair. “Structural and chemical transformations in SnS thin films used in chemically deposited photovoltaic cells”. In: *Thin Solid Films* 515 (2007), pp. 5771–5776 (cit. on pp. 80, 90).

[125] G. Sreedevi and K. Tulasi Ramakrishna Reddy. “Properties of Tin Monosulphide Films Grown by Chemical Bath Deposition”. In: *Conference Papers in Energy*. Vol. 2013. Hindawi Publishing Corporation. 2013. DOI: doi:http://dx.doi.org/10.1155/2013/528724 (cit. on p. 80).

[126] G. R. Gopinath and K. T. Ramakrishna Reddy. “Growth of Polycrystalline In_2S_3 Thin Films by Chemical Bath Deposition Using Acetic Acid as Complexing Agent for Solar Cell Application”. In: *ISRN Condensed Matter Physics* 2013 (2013), pp. 1–6 (cit. on p. 80).

[127] E. Turan, M. Kul, A. S. Aybek, and M. Zor. “Structural and optical properties of SnS semiconductor films produced by chemical bath deposition”. In: *Journal of Physics D: Applied Physics* 42 (2009), p. 245408 (cit. on pp. 80, 91).

[128] A. Akkari, C. Guasch, and N. Kamoun-Turki. “Chemically deposited tin sulphide”. In: *Journal of Alloys and Compounds* 490 (2010), pp. 180–183 (cit. on pp. 80, 91).

[129] A. Akkari, C. Guasch, M. Castagne, and N. Kamoun-Turki. “Optical study of zinc blend SnS and cubic In_2S_3: Al thin films prepared by chemical bath deposition”. In: *Journal of Materials Science* 46 (2011), pp. 6285–6292 (cit. on p. 80).

[130] A. Akkari, M. Reghima, C. Guasch, and N. Kamoun-Turki. “Effect of copper doping on physical properties of nanocrystallized SnS zinc blend thin films grown by chemical bath deposition”. In: *Journal of Materials Science* 47 (2012), pp. 1365–1371 (cit. on p. 80).

[131] C. Gao, H. Shen, L. Sun, and Z. Shen. “Chemical bath deposition of SnS films with different crystal structures”. In: *Materials Letters* 65 (2011), pp. 1413–1415 (cit. on p. 80).

[132] C. Gao, H. Shen, and L. Sun. “Preparation and properties of zinc blende and orthorhombic SnS films by chemical bath deposition”. In: *Applied Surface Science* 257 (2011), pp. 6750–6755 (cit. on pp. 80, 82).

[133] C. Gao and H. Shen. “Influence of the deposition parameters on the properties of orthorhombic SnS films by chemical bath deposition”. In: *Thin Solid Films* 520 (2012), pp. 3523–3527 (cit. on pp. 80, 91).

[134] M. Reghima, A. Akkari, C. Guasch, and N. Kamoun-Turki. “Effect of indium doping on physical properties of nanocrystallized SnS zinc blend thin films grown by chemical bath deposition”. In: *Journal of Renewable and Sustainable Energy* 4 (2012), p. 011602 (cit. on p. 80).

[135] P. P. Hankare, A. V. Jadhav, P. A. Chate, K. C. Rathod, P. A. Chavan, and S. A. Ingole. “Synthesis and characterisation of tin sulphide thin films grown by chemical bath deposition technique”. In: *Journal of Alloys and Compounds* 463 (2008), pp. 581–584 (cit. on p. 80).

[136] Y. Wang, Y. B. Reddy, and H. Gong. “Large-surface-area nanowall SnS films prepared by chemical bath deposition”. In: *Journal of the Electrochemical Society* 156 (2009), H157–H160 (cit. on p. 80).

[137] S. Aksay, T. Ozer, and M. Zor. “Vibrational and X-ray diffraction spectra of SnS film deposited by chemical bath deposition method”. In: *European Physical Journal - Applied Physics* 47 (2009), p. 30502 (cit. on pp. 80, 89).

[138] Y. Jayasree, U. Chalapathi, P. Uday Bhaskar, and V. Sundara Raja. “Effect of precursor concentration and bath temperature on the growth of chemical bath deposited tin sulphide thin films”. In: *Applied Surface Science* 258 (2012), pp. 2732–2740 (cit. on pp. 80, 89).

[139] A. Gómez, H. Martınez, M. Calixto-Rodrıguez, D. Avellaneda, P. G. Reyes, and O. Flores. “Modification of optical and electrical properties of chemical bath deposited SnS using O_2 plasma treatments”. In: *Applied Surface Science* 275 (2013), pp. 273–277 (cit. on p. 80).

[140] M. Foex. In: *Bull. Soc. Chim. France* 11.6 (1944) (cit. on p. 80).

[141] R. R. Chamberlin and J. S. Skarman. “Chemical spray deposition process for inorganic films”. In: *Journal of the Electrochemical Society* 113 (1966), pp. 86–89 (cit. on p. 80).

[142] K. T. Ramakrishna Reddy, N. Koteswara Reddy, and R. W. Miles. “Photovoltaic properties of SnS based solar cells”. In: *Solar Energy Materials and Solar Cells* 90 (2006), pp. 3041–3046 (cit. on pp. 81, 88).

[143] T.H. Sajeesh, A.R. Warrier, C.S. Kartha, and K.P. Vijayakumar. “Optimization of parameters of chemical spray pyrolysis technique to get n and p-type layers of SnS”. In: *Thin Solid Films* 518 (2010), pp. 4370–4374 (cit. on p. 81).

[144] T.H. Sajeesh, C.S. Kartha, C. Sanjeeviraja, T. Abe, Y. Kashiwaba, and K.P. Vijayakumar. “Ex situ Sn diffusion: a well-suited technique for enhancing the photovoltaic properties of a SnS absorber layer”. In: *Journal of Physics D: Applied Physics* 43 (2010), p. 445102 (cit. on p. 81).

[145] S. Lopez and A. Ortiz. “Spray pyrolysis deposition of SnxSy thin films”. In: *Semiconductor Science and Technology* 9 (1994), pp. 2130–2133 (cit. on pp. 81, 90).

[146] B. Thangaraju and P. Kaliannan. “Spray pyrolytic deposition and characterization of SnS and SnS_2 thin films”. In: *Journal of Physics D: Applied Physics* 33 (2000), pp. 1054–1059 (cit. on p. 81).

[147] M. Peker, D. Peker, and M. Selami Kılıçkaya. “Structural and optical properties of $Cd_{1-x}Sn_xS$ semiconductor films produced by the ultrasonic spray pyrolysis method”. In: *Physica B: Condensed Matter* 405 (2010), pp. 4831–4837 (cit. on pp. 81, 91).

[148] M. Calixto-Rodriguez, H. Martinez, A. Sanchez-Juarez, J. Campos-Alvarez, A. Tiburcio-Silver, and M. E. Calixto. “Structural, optical, and electrical properties of tin sulfide thin films grown by spray pyrolysis”. In: *Thin Solid Films* 517 (2009), pp. 2497–2499 (cit. on p. 81).

[149] H. B. Haj Salah, H. Bouzouita, and B. Rezig. “Preparation and characterization of tin sulphide thin films by a spray pyrolysis technique”. In: *Thin Solid Films* 480 (2005), pp. 439–442 (cit. on p. 81).

[150] B. G. Jeyaprakash, R. Ashok Kumar, K. Kesavan, and A. Amalarani. “STRUCTURAL AND OPTICAL CHARACTERISATION OF SPRAY DEPOSITED SnS THIN FILM”. In: *Journal of American Science* 6 (2010), pp. 22–26 (cit. on p. 81).

[151] C. Gao, H. Shen, L. Sun, H. Huang, L. Lu, and H. Cai. “Preparation of SnS films with zinc blende structure by successive ionic layer adsorption and reaction method”. In: *Materials Letters* 64 (2010), pp. 2177–2179 (cit. on pp. 82, 91).

[152] C. Gao, H. Shen, T. Wu, L. Zhang, and F. Jiang. "Preparation and the growth mechanism of zinc blende structure tin sulfide films by successive ionic layer adsorption and reaction". In: *Journal of Crystal Growth* 312 (2010), pp. 3009–3013 (cit. on pp. 82, 91).

[153] C. Gao, H. Shen, Z. Shen, and L. Sun. "Influence of SnS buffer layers on the growth and properties of nanostructured Bi_2S_3 films by chemical bath deposition". In: *Applied Surface Science* 257 (2011), pp. 4439–4442 (cit. on p. 82).

[154] B. Ghosh, M. Das, P. Banerjee, and S. Das. "Fabrication of SnS thin films by the successive ionic layer adsorption and reaction (SILAR) method". In: *Semiconductor Science and Technology* 23 (2008), p. 125013 (cit. on pp. 82, 89, 91).

[155] B. Ghosh, M. Das, P. Banerjee, and S. Das. "Fabrication and optical properties of SnS thin films by SILAR method". In: *Applied Surface Science* 254 (2008), pp. 6436–6440 (cit. on pp. 82, 89, 91).

[156] B. Ghosh, S. Chowdhury, P. Banerjee, and S. Das. "Fabrication of CdS/SnS heterostructured device using successive ionic layer adsorption and reaction deposited SnS". In: *Thin Solid Films* 519 (2011), pp. 3368–3372 (cit. on p. 82).

[157] J. W. Mellor. *A Comprehensive Treatise on Inorganic and Theoretical Chemistry*. Vol. 6. Longmans-Green, New York, 1957 (cit. on p. 82).

[158] P. Sinsermsuksakul, K. Hartman, S. D. Kim, J. Heo, L. Sun, H. H. Park, R. Chakraborty, T. Buonassisi, and R. G. Gordon. "Enhancing the efficiency of SnS solar cells via band-offset engineering with a zinc oxysufide buffer layer". In: *Applied Physics Letters* 102 (2013), p. 053901 (cit. on pp. 82, 88).

[159] L. S. Price, I. P. Parkin, M. N. Field, A. M. E. Hardy, R. J. H. Clark, T. G. Hibbert, and K. C. Molloy. "Atmospheric pressure chemical vapour deposition of tin (II) sulfide films on glass substrates from $Bu_3SnO_2CCF_3$ with hydrogen sulfide". In: *Journal of Materials Chemistry* 10 (2000), pp. 527–530 (cit. on p. 83).

[160] I. P. Parkin, L. S. Price, A. M. E. Hardy, R. J. H. Clark, T. G. Hibbert, and K. C. Molloy. "Atmospheric pressure chemical vapour deposition of tin sulfide thin films". In: *Journal de Physique IV* 9 (1999), Pr8–403 (cit. on p. 83).

[161] G. H. Yue, Y. D. Lin, X. Wen, L. S. Wang, Z. Y. Chen, and D. L. Peng. "Synthesis and characterisation of the SnS nanowires via chemical vapour deposition". In: *Applied Physics A* 106 (2012), pp. 87–91 (cit. on pp. 83, 89).

[162] T. G. Hibbert, M. F. Mahon, K. C. Molloy, L. S. Price, and I. V. Parkin. "Deposition of tin sulphide thin films from novel, volatile (uoroalkythiolato)tin(IV) precursors". In: *Journal of Materials Chemistry* 11 (2000), pp. 469–473 (cit. on p. 83).

[163] K. Ramasamy, V. L. Kuznetsov, K. Gopal, M. A. Malik, J. Raftery, P. P. Edwards, and P. O'Brien. "Organotin Dithiocarbamates: Single-Source Precursors for Tin Sulfide Thin Films by Aerosol-Assisted Chemical Vapor Deposition (AACVD)". In: *Chemistry of Materials* 25 (2013), pp. 266–276 (cit. on p. 83).

[164] M. X. Wang, G. H. Yue1, Y. D. Lin, X. Wen, D. L. Peng, and Z. R. Geng. "Synthesis, Optical Properties and Photovoltaic Application of the SnS Quasi-one-dimensional Nanostructures". In: *Nano-Micro Letters* 5 (2013), pp. 1–6 (cit. on p. 83).

[165] T. L. Chu and S. S. Chu. "Thin film II–VI photovoltaics". In: *Solid-State Electronics* 38 (1995), pp. 533–549 (cit. on p. 83).

[166] J. Park, M. Song, W.M. Jung, W.Y. Lee, J. Lee, H. Kim, and I.W. Shim. "Supplementary material preparation of SnS thin films by MOCVD method using single source precursor, bis (3-mercapto-1-propanethiolato) Sn (II)". In: *Bulletin of the Korean Chemical Society* 33 (2012), p. 1 (cit. on p. 83).

[167] J. Park, M. Song, W. Jung, W. Lee, J. Lee, H. Kim, and I. Shim. "Preparation of SnS Thin Films by MOCVD Method Using Single Source Precursor, Bis (3-mercapto-1-propanethiolato) Sn (II)". In: *Bulletin of the Korean Chemical Society* 33 (2012), pp. 3383–3386 (cit. on p. 83).

[168] A. Luque and S. Hegedus. *Handbook of Photovoltaic Science and Engineering.* Ed. by A. Luque and S. Hegedus. Wiley, New York, 2003 (cit. on p. 83).

[169] A. Ortiz, J. C. Alonso, M. Garcia, and J. Toriz. "Tin sulphide films deposited by plasma-enhanced chemical vapour deposition". In: *Semiconductor Science and Technology* 11 (1996), pp. 243–247 (cit. on p. 83).

[170] A. Sánchez-Juárez, A. Tiburcio-Silver, and A. Ortiz. "Fabrication of SnS_2/SnS heterojunction thin film diodes by plasma-enhanced chemical vapor deposition". In: *Thin Solid Films* 480 (2005), pp. 452–456 (cit. on pp. 83, 88, 90).

[171] L. L. Cheng, M. H. Liu, M. X. Wang, S. C. Wang, G. D. Wang, Q. Y. Zhou, and Z. Q. Chen. "Preparation of SnS films using solid sources deposited by the PECVD method with controllable film characters". In: *Journal of Alloys and Compounds* 545 (2012), pp. 122–129 (cit. on p. 83).

[172] L. Cheng, M. Liu, S. Wang, and M. Wang. "Fabrication and characterization of SnS films deposited on different substrates by modified versition of PECVD". In: *Plasma Science (ICOPS), 2012 Abstracts IEEE International Conference on*. IEEE. 2012, 1P–160. DOI: doi:10.1109/PLASMA.2012.6383488 (cit. on p. 83).

[173] Y. Zhao, Z. Zhang, H. Dang, and W. Liu. "Synthesis of tin sulfide nanoparticles by a modified solution dispersion method". In: *Materials Science and Engineering: B* 113 (2004), pp. 175–178 (cit. on pp. 83, 84, 89).

[174] S. C. Ray, M. K. Karanjai, and D. DasGupta. "Structure and photoconductive properties of dip-deposited SnS and SnS_2 thin films and their conversion to tin dioxide by annealing in air". In: *Thin Solid Films* 350 (1999), pp. 72–78 (cit. on pp. 84, 90).

[175] Z. Xu and Y. Chen. "Fabrication of SnS thin films by a novel multilayer-based solid-state reaction method". In: *Semiconductor Science and Technology* 27 (2012), p. 035007 (cit. on pp. 84, 91).

[176] H. Liu, Y. Liu, Z. Wang, and P. He. "Facile synthesis of monodisperse, size-tunable SnS nanoparticles potentially for solar cell energy conversion". In: *Nanotechnology* 21 (2010), p. 105707 (cit. on p. 84).

[177] S. Sohila, M. Rajalakshmi, C. Gosh, A. K. Arora, and C. Muthamizhchelvan. "Optical and Raman scattering on SnS nanoparticles". In: *Journal of Alloys and Compounds* 509 (2011), pp. 5843–5847 (cit. on pp. 84, 89).

[178] F. Michael. *On Electro-chemical Decomposition*. Royal Society, UK, 1833 (cit. on p. 84).

[179] R. Mariappan, M. Ragavendar, and V. Ponnuswamy. “Structural and optical characterization of SnS thin films by electrodeposition technique”. In: *Optica Applicata* 41 (2011), pp. 989–997 (cit. on pp. 84, 86).

[180] R. D. Engelken, H. E. McCloud, C. Lee, M. Slayton, and H. Ghoreishi. “Low temperature chemical precipitation and vapor deposition of Sn_xS thin films”. In: *Journal of the Electrochemical Society* 134 (1987), pp. 2696–2707 (cit. on p. 84).

[181] M. Sharon and K. Basavaswaran. “Photoelectrochemical behaviour of tin monosulphide”. In: *Solar Cells* 25 (1988), pp. 97–107 (cit. on p. 85).

[182] K. Mishra, K. Rajeshwar, A. Weiss, M. Murley, R. D. Engelken, M. Slayton, and H. E. McCloud. “Electrodeposition and characterization of SnS thin films”. In: *Journal of the Electrochemical Society* 136 (1989), pp. 1915–1923 (cit. on p. 85).

[183] A. Adachi, A. Kudo, and T. Sakata. “The optical and photoelectrochemical properties of electrodeposited CdS and SnS thin films”. In: *Bulletin of the Chemical Society of Japan* 68 (1995), pp. 3283–3288 (cit. on p. 85).

[184] Z. Zainal, M. Z. Hussein, and A. Ghazali. “Cathodic electrodeposition of SnS thin films from aqueous solution”. In: *Solar Energy Materials and Solar Cells* 40 (1996), pp. 347–357 (cit. on p. 85).

[185] Z. Zainal, M. Z. Hussein, A. Kassim, and A. Ghazali. “Electrodeposited SnS thin films from aqueous solution”. In: *Journal of Materials Science Letters* 16 (1997), pp. 1446–1449 (cit. on p. 85).

[186] A. Ghazali, Z. Zainal, M. Zobir Hussein, and A. Kassim. “Cathodic electrodeposition of SnS in the presence of EDTA in aqueous media”. In: *Solar Energy Materials and Solar Cells* 55 (1998), pp. 237–249 (cit. on p. 85).

[187] B. Subramanian, C. Sanjeeviraja, and M. Jayachandran. “Cathodic electrodeposition and analysis of SnS films for photoelectrochemical cells”. In: *Materials Chemistry and Physics* 71 (2001), pp. 40–46 (cit. on p. 85).

[188] M. Ichimura, K. Takeuchi, Y. Ono, and E. Arai. “Electrochemical deposition of SnS thin films”. In: *Thin Solid Films* 361 (2000), pp. 98–101 (cit. on pp. 86, 90).

[189] M. Gunasekaran and M. Ichimura. “Photovoltaic cells based on pulsed electrochemically deposited SnS and photochemically deposited CdS and $Cd_{1-x}Zn_xS$”. In: *Solar Energy Materials and Solar Cells* 91 (2007), pp. 774–778 (cit. on pp. 86, 88).

[190] J. J. M. Vequizo and M. Ichimura. “Fabrication of electrodeposited SnS/SnO_2 heterojunction solar cells”. In: *Japanese Journal of Applied Physics* 51 (2012), 10NC38 (cit. on pp. 86, 88, 89).

[191] T. Miyawaki and M. Ichimura. “Fabrication of ZnS thin films by an improved photochemical deposition method and application to ZnS/SnS heterojunction cells”. In: *Materials Letters* 61 (2007), pp. 4683–4686 (cit. on p. 86).

[192] K. Takeuchi, M. Ichimura, E. Arai, and Y. Yamazaki. “SnS thin films fabricated by pulsed and normal electrochemical deposition”. In: *Solar Energy Materials and Solar Cells* 75 (2003), pp. 427–432 (cit. on pp. 86, 90).

[193] N. Sato, M. Ichimura, E. Arai, and Y. Yamazaki. “Characterization of electrical properties and photosensitivity of SnS thin films prepared by the electrochemical depositon method”. In: *Solar Energy Materials and Solar Cells* 85 (2005), pp. 153–165 (cit. on p. 86).

[194] S. Cheng, Y. Chen, C. Huang, and G. Chen. “Characterization of SnS films prepared by constant-current electro-deposition”. In: *Thin Solid Films* 500 (2006), pp. 96–100 (cit. on pp. 86, 90).

[195] S. Cheng, G. Chen, Y. Chen, and C. Huang. “Effect of deposition potential and bath temperature on the electrodeposition of SnS film”. In: *Optical Materials* 29 (2006), pp. 439–444 (cit. on p. 86).

[196] S. Cheng, Y. He, and C. Chen. “Structure and properties of SnS films prepared by electro-deposition in presence of EDTA”. In: *Materials Chemistry and Physics* 110 (2008), pp. 449–453 (cit. on pp. 86, 90).

[197] G. H. Yue, D. L. Peng, P. X. Yan, L. S. Wang, W. Wang, and X. H. Luo. “Structure and optical properties of SnS thin film prepared by pulse electrodeposition”. In: *Journal of Alloys and Compounds* 468 (2009), pp. 254–257 (cit. on p. 86).

[198] B. Ghosh, R. Roy, S. Chowdhury, P. Banerjee, and S. Das. “Synthesis of SnS thin films via galvanostatic electrodeposition and fabrication of CdS/SnS heterostructure for photovoltaic applications”. In: *Applied Surface Science* 256 (2010), pp. 4328–4333 (cit. on pp. 86, 91).

[199] R. Mariappan, T. Mahalingam, and V. Ponnuswamy. “Preparation and characterization of electrodeposited SnS thin films”. In: *Optik-International Journal for Light and Electron Optics* 122 (2011), pp. 2216–2219 (cit. on pp. 86, 91).

[200] N. R. Mathews. “Chemically and electrochemically deposited thin films of tin sulfide for photovoltaic structures”. In: *MRS Proceedings*. Cambridge Univ Press. 2009. DOI: DOI:http://dx.doi.org/10.1557/PROC-1165-M08-35 (cit. on pp. 86, 88).

[201] N. R. Mathews, H. B. M. Anaya, M. A. Cortes-Jacome, C. Angeles-Chavez, and J. A. Toledo-Antonio. “Tin sulfide thin films by pulse electrodeposition: structural, morphological, and optical properties”. In: *Journal of the Electrochemical Society* 157 (2010), H337–H341 (cit. on p. 86).

[202] N. R. Mathews, C. Colın Garcıa, and I. Z. Torres. “Effect of annealing on structural, optical and electrical properties of pulse electrodeposited tin sulfide films”. In: *Materials Science in Semiconductor Processing* 16 (2013), pp. 29–37 (cit. on p. 86).

[203] G. H. Yue, W. Wang, L. S. Wang, X. Wang, P. X. Yan, Y. Chen, and D. L. Peng. “The effect of anneal temperature on physical properties of SnS films”. In: *Journal of Alloys and Compounds* 474 (2009), pp. 445–449 (cit. on pp. 86, 91).

[204] M. Steichen, R. Djemour, L. Gtay, J. Gulliot, S. Siebentritt, and P. J. Dale. “Direct synthesis of single-phase p-type SnS by electrodeposition from a dicyanamide ionic liquid at high temperature for thin film solar cells”. In: *Journal of Physical Chemistry C* 117 (2013), pp. 4383–4393 (cit. on p. 86).

[205] A. R. H. F. Ettema, R. A. de Groot, C. Haas, and T. S. Turner. “Electronic structure of SnS deduced from photoelectron spectra and band-structure calculations”. In: *Physical Review B* 46 (1992), pp. 7363–7373 (cit. on p. 87).

[206] H. Martinez, C. Auriel, M. Loudet, and G. Pfister-Guillouzo. “Electronic structure (XPS and ab-initio band structure calculation) and scanning probe microscopy

images of α-tin sulfide". In: *Applied Surface Science* 103 (1996), pp. 149–158 (cit. on p. 87).

[207] Z. Nabi, A. Kellou, S. Mecabih, A. Khalfi, and N. Benosman. "Opto-electronic properties of rutile SnO_2 and orthorhombic SnS and SnSe compounds". In: *Materials Science and Engineering B* 98 (2003), pp. 104–115 (cit. on p. 87).

[208] D. Avellaneda, M. T. S. Nair, and P. K. Nair. "Photovoltaic structures using chemically deposited tin sulfide thin films". In: *Thin Solid Films* 517 (2009), pp. 2500–2502 (cit. on p. 88).

[209] A. Stavrinadis, J.M. Smith, C.A. Cattley, A.G. Cook, P.S. Grant, and A.A.R. Watt. "SnS/PbS nanocrystal heterojunction photovoltaics". In: *Nanotechnology* 21 (2010), p. 185202 (cit. on p. 88).

[210] M. Gunasekaran, P. Ramasamy, and M. Ichimura. "Preparation of ternary $Cd_{1-x}Zn_xS$ alloy by photochemical deposition (PCD) and its application to photovoltaic devices". In: *Physica Status Solidi (C)* 3 (2006), pp. 2656–2660 (cit. on p. 88).

[211] B. Subramanian, C. Sanjeeviraja, M. Jayachandran, and M. J. Chockalingam. "Electrochemical synthesis of SnS thin films for photoelectrochemical cells". In: *Proceedings of SPIE*. 1999. DOI: doi:http://dx.doi.org/10.1117/12.370350 (cit. on pp. 88, 90).

[212] B. Subramanian, C. Sanjeeviraja, and M. Jayachandran. "Materials poroperties of electrodeposited $SnS_{0.5}Se_{0.5}$ films and characterisation of photoelectrochemical solar cells". In: *Materials Research Bulletin* 38 (2003), pp. 899–908 (cit. on p. 88).

[213] B. Subramanian, C. Sanjeeviraja, and M. Jayachandran. "Photoelectrochemical characteristics of brush plated tin sulfide thin films". In: *Solar Energy Materials and Solar Cells* 79 (2003), pp. 57–65 (cit. on p. 88).

[214] G. Yue, Y. Lin, X. Wen, L. Wang, and D. Peng. "SnS homojunction nanowire-based solar cells". In: *Journal of Materials Chemistry* 22 (2012), pp. 16437–16441 (cit. on p. 88).

[215] W. Guo, Y. Shen, M. Wu, and T. Ma. “Highly efficient inorganic-organic heterojunction solar cells based on SnS-senitized spherical TiO_2 electrodes”. In: *Chemical Communications* 48 (2012), pp. 6133–6135 (cit. on p. 88).

[216] T. Ikuno, R. Suzuki, K. Kitazumi, N. Takahashi, N. Kato, and K. Higuchi. “SnS thin film solar cells with $Zn_{1-x}Mg_xO$ buffer layers”. In: *Applied Physics Letters* 102 (2013), p. 193901 (cit. on p. 88).

[217] M. Sugiyama, K. T. R. Reddy, N. Revathi, Y. Shimamoto, and Y. Murata. “Band offset of SnS solar cell structure measured by X-ray photoelectron spectroscopy”. In: *Thin Solid Films* 519 (2011), pp. 7429–7431 (cit. on p. 89).

[218] M. Ichimura. “Calculation of band offsets at the CdS/SnS heterojunction”. In: *Solar Energy Materials and Solar Cells* 93 (2009), pp. 375–378 (cit. on p. 89).

[219] A. M. Abdel Haleem and M. Ichimura. “Experimental determination of band offsets at the SnS/CdS and SnS/InSxOy heterojunctions”. In: *Journal of Applied Physics* 107 (2010), p. 034507 (cit. on p. 89).

[220] C. An, K. Tang, G. Shen, C. Wang, Q. Yang, B. Hai, and Y. Qian. “Growth of belt-like SnS crystals from ethylenediamine solution”. In: *Journal of Crystal Growth* 244 (2002), pp. 333–338 (cit. on p. 89).

[221] J. Malaquias, P.A. Fernandes, P.M.P. Salomé, and A.F. da Cunha. “Assessment of the potential of tin sulphide thin films prepared by sulphurization of metallic precursors as cell absorbers”. In: *Thin Solid Films* 519 (2011), pp. 7416–7420 (cit. on p. 89).

[222] D. Chen, G. Shen, K. Tang, S. Lei, H. Zheng, and Y. Qian. “Microwave-assisted polyol synthesis of nanoscale SnS_x(x = 1, 2) flakes”. In: *Journal of Crystal Growth* 260 (2004), pp. 469–474 (cit. on p. 89).

[223] X. Gou, J. Chen, and P. Shen. “Synthesis, characterization and application of SnS_x(x = 1, 2) nanoparticles”. In: *Materials Chemistry and Physics* 93 (2005), pp. 557–566 (cit. on p. 89).

[224] M. Salvati-Nasiri, D. Ghanbari, and F. Davar. “Shape selective hydrothermal synthesis of tin sulfide nanoflowers based on nanosheets in the presence of thioglycolic acid”. In: *Journal of Alloys and Compounds* 492 (2010), pp. 570–575 (cit. on p. 89).

[225] S. Cheng, Y. Chen, Y. He, and G. Chen. “The structure and properties of SnS thin films prepared by pulse electro-deposition”. In: *Materials Letters* 61 (2007), pp. 1408–1412 (cit. on p. 90).

[226] N. Koteeswara Reddy and K. T. Ramakrishna Reddy. “Preparation and characterisation of sprayed tin sulphide films grown at different precursor concentrations”. In: *Materials Chemistry and Physics* 102 (2007), pp. 13–18 (cit. on p. 90).

[227] M. Devika, N. K. Reddy, D. S. Reddy, S. V. Reddy, K . Ramesh, E. S. R. Gopal, K. R. Gunasekhar, V. Ganesan, and Y. B. Hahn. “Optimization of the distance between source and substrate for device-grade SnS films grown by the thermal evaporation technique”. In: *Journal of Physics: Condensed Matter* 19 (2007), p. 306003 (cit. on p. 90).

[228] R. W. Miles, O. E. Ogah, G. Zoppi, and I. Forbes. “Thermally evaporated thin films of SnS for application in solar cell devices”. In: *Thin Solid Films* 517 (2009), pp. 4702–4705 (cit. on p. 91).

[229] S. A. Bashkirov, V. F. Gremenok, and V. A. Ivanov. “Physical properties of SnS thin films fabricated by hot wall deposition”. In: *Semiconductors* 45 (2011), pp. 749–752 (cit. on p. 91).

[230] C. L. C. Triana, E. Banguero, P. Bartolo-Perez, and G. Gordillo. “Preparation and Characterization of SnS:Bi Thin Films”. In: *Brazilian Journal of Physics* 41 (2011), pp. 15–20 (cit. on p. 91).

[231] A. E. Abdelhrahman, W. M. M. Yunus, and A. K. Arof. “Optical properties of tin sulphide (SnS) thin film estimated from transmission spectra”. In: *Journal of Non-Crystalline Solids* 358 (2012), pp. 1447–1451 (cit. on p. 91).

Chapter 4

Experimental Procedure

4.1 Pre-deposition Process

4.1.1 Substrate Cleaning

The soda–lime glass slides used as substrate were cleaned ultrasonically with the DAWE SONICLEANER TYPE 6443BE using DECON–90 obtained from SIGMA–ALDRICH and further cleaned with propan-2-ol obtained from the same company. The substrates were then dried using nitrogen gas. All the water used in the cleaning process was de-mineralised using the ELGA PURELAB demineraliser.

4.1.2 Source Preparation

The source materials (SnS, CdS, ZnS, ZnTe and ZIS, $ZnInSe_4$) used were all solids either in powdered or lump form. For the lumps (SnS), a suitable mortar and pestle were used to crush them into a powdery form before putting them into the quartz crucible. The high grade SuperVac SnS with purity of 99.999% was obtained from Testbourne Limited, UK. Others were sourced from SIGMA–ALDRICH, UK.

4.2 Deposition Process

4.2.1 Thermal Evaporation System

The merits of vacuum evaporation over other deposition techniques and the range of obtainable vacuum in relation to the available vacuum pressure has been earlier highlighted

in 3.3.1.1. A crucial step to obtaining high quality films includes creating a conducive environment that has little or no interference with the film formation process. Interactions between residual gases and surface of the growing films can be significantly reduced through low pressure (high vacuum) in a closed chamber. The major components of the deposition plant are:

- Edwards rotary vane pump – high pressure (low vacuum stage),
- Leybold Hereaus oil diffusion pump – low pressure (high vacuum stage),
- Pirani gauge and Penning gauge.

A typical process control diagram of the deposition plant is shown on Figure 4.1 [1] and the picture of the deposition plant on Figure 4.2.

4.2.1.1 High Pressure (Low-Vacuum Stage)

The rotary pump removes gases from the enclosed chamber and exhausts the gas load externally. The rotary pump consists of a rotor, stator, oil discharge valve and a spring. A schematic diagram of a rotary vane pump is shown on Figure 4.3. The vane in conjunction with the spring, provides the requisite centripetal force needed for the operation of the rotor. The movement of the vane and the rotor compresses the gas molecules that enters the inlet from the chamber, thus forcing the discharge valve open and emptying the gas [2]. The oil serves as a lubricant, a seal and for cooling purposes (removing the heat that arises from the gas compression).

4.2.1.2 Low Pressure (High-Vacuum Stage)

Figure 4.4 gives a schematic of the diffusion pump in operation [3, 4]. As shown in Figure 4.4, the electrical connection to the heater, supplies the required current that heats up the heater, thus heating the oil. The heated oil results in a fluid vapour which streams at a supersonic speed from the nozzle to form a supersonic jet as indicated in Figure 4.4. Gaseous molecules that encounters the jets are suppressed down and expelled through the backing pump. Any fluid on touching the pump wall undergoes condensation to form a liquid condensate that drifts from the wall to the boiler, thus setting up a continuous

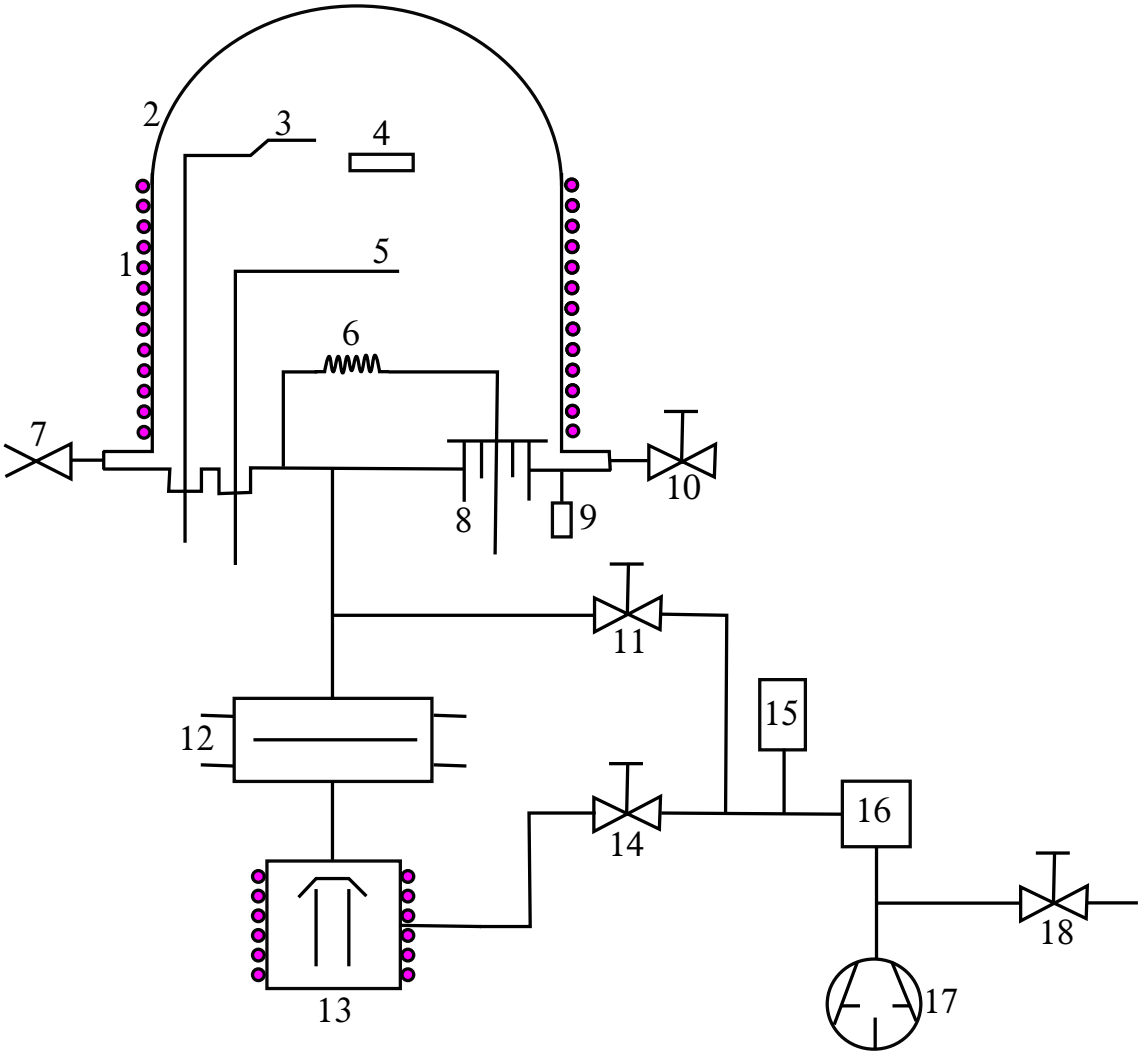

Figure 4.1: Process Control Diagram of the Deposition Plant: (1) Water Cooling Coils (2) Bell Jar (3) Thickness Monitor (4) Substrate (5) Source Shutter (6) Resistive Heater (7) Air Admittance (Vent) Valve (8) Current Feed Through (9) Penning Gauge (10) Inert Gas Valve (11) Roughing Valve (12) Baffle Valve (13) Diffusion Pump (14) Backing Valve (15) Pirani Gauge (16) Fore-line Trap (17) Sliding Vane Rotary Vacuum Pump (18) Isolation Valve.

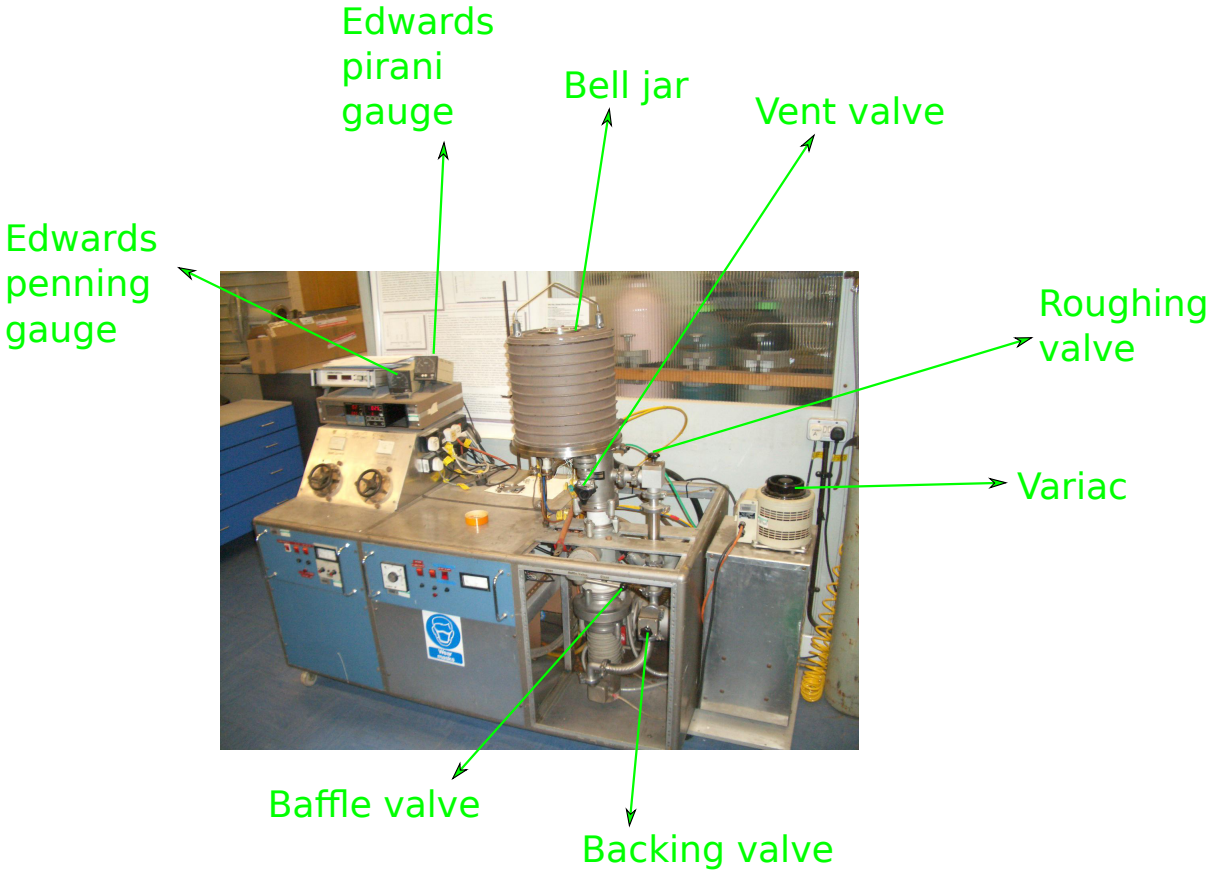

Figure 4.2: Picture of the Thermal Evaporation Deposition System.

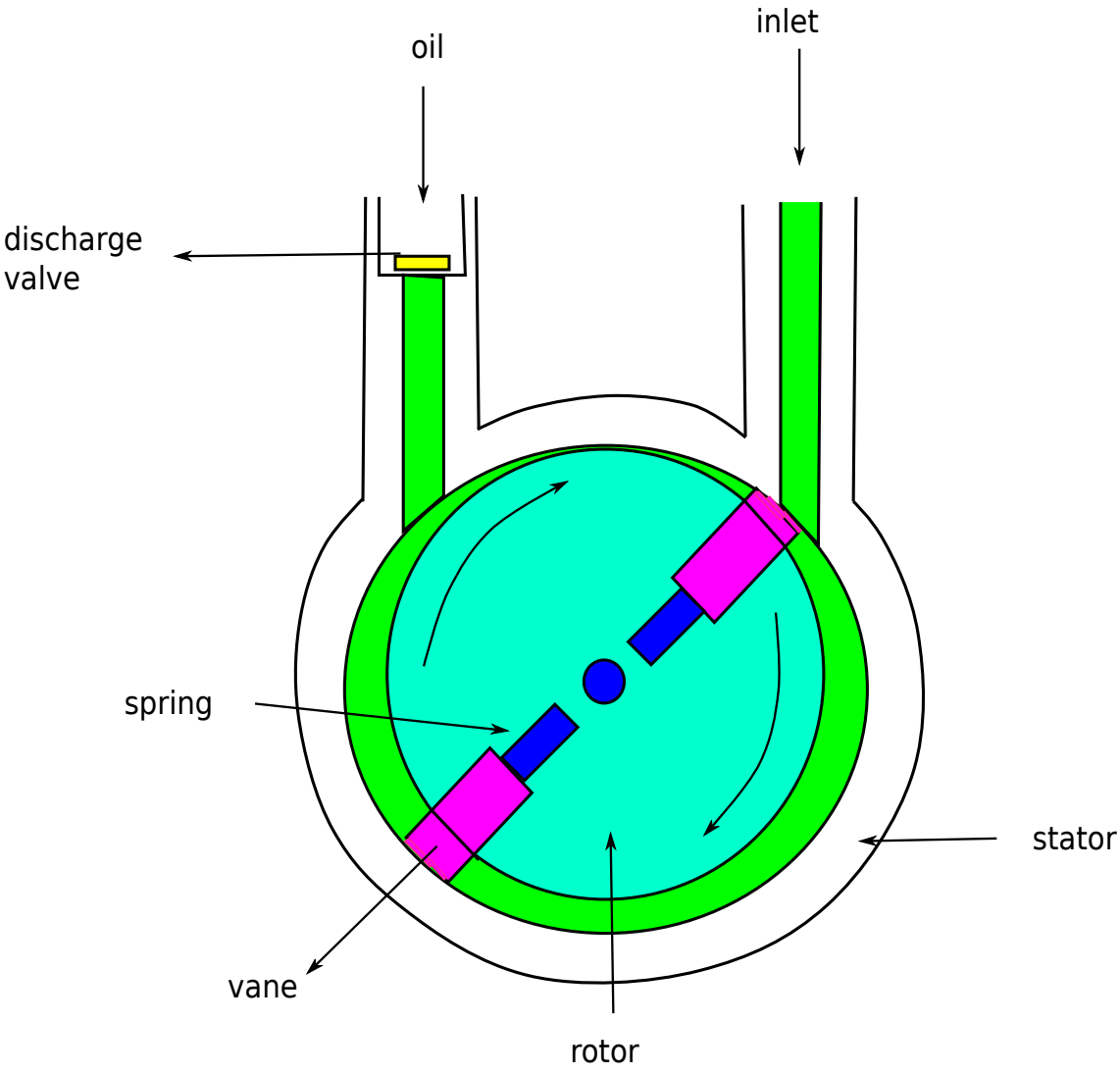

Figure 4.3: Schematic Diagram of a Rotary Vane Pump.

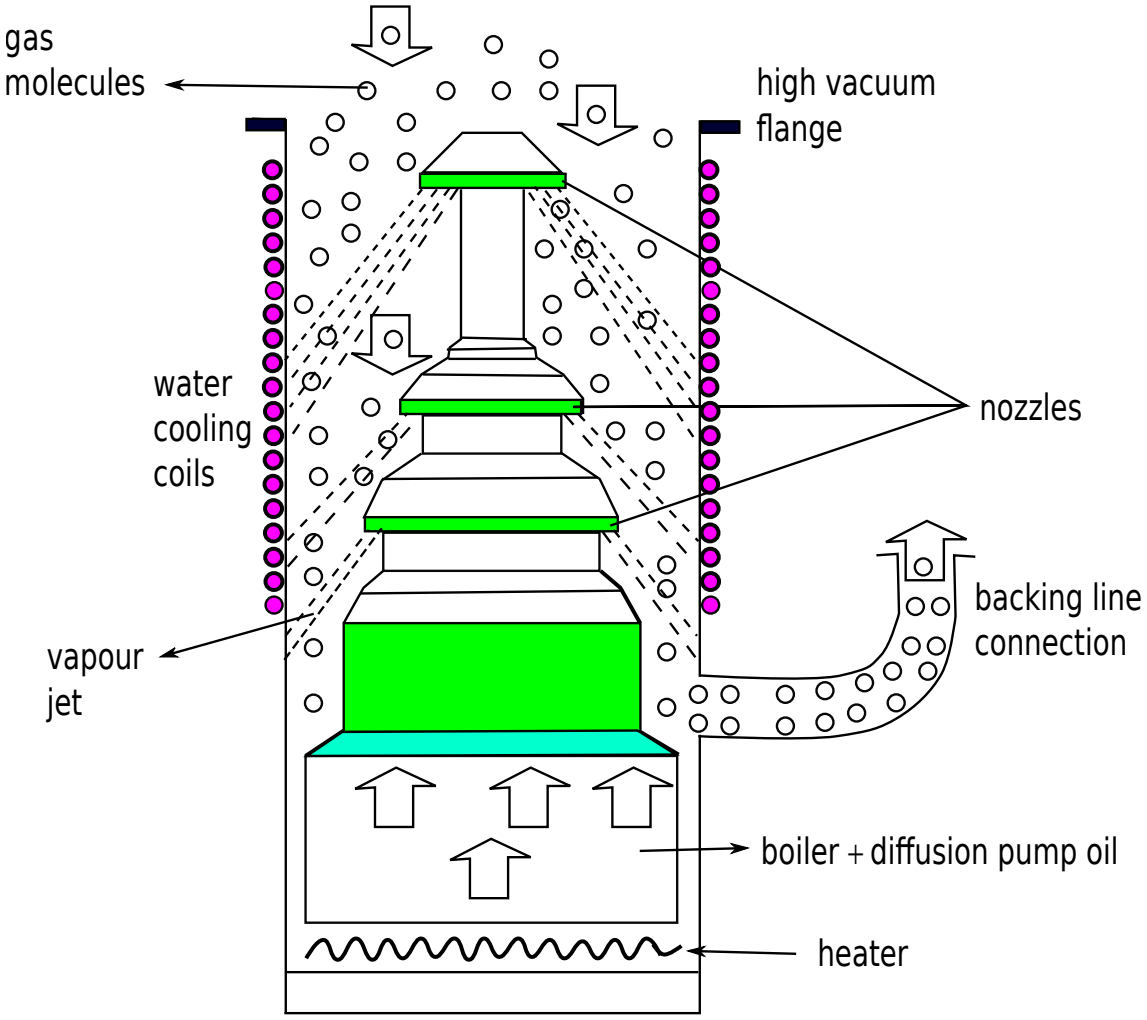

Figure 4.4: Schematic of Diffusion Pump in Operation.

cycle. However, it must be mentioned that the degassing section (not shown in Figure 4.4) ensures that the returning liquid condensate are liberated from impurities and adsorbed gases before re-entry into the boiler.

4.2.1.3 Pirani Gauge (Thermal Conductivity Gauge) and Penning Gauge (Cold Cathode Ionisation Gauge)

An Edwards Pirani Gauge Model 502 was used to measure the vacuum pressure. It works on the principle that the rate of heat transfer through the gas is a function of the gas pressure, thus any change of pressure in the vacuum system will introduce a change in the number of gas molecules present and consequently a change in the thermal conductivity of the gas. The configuration (not shown) is such that the filament within the gauge head constitutes an arm of the Wheatstone bridge. Measurement of the voltage across the bridge gives the pressure because the heat transfer from the filament to the gas increases with an increase of pressure. The quick response usually observed during pump down is due to the constant temperature of the filament arising from the controlled heating voltage applied to the bridge.

An Edwards Penning Gauge Model 505 was also used in the measurements. Its operation depends on the fact that electrons emitted from a cold cathode are accelerated by an electric field leading to ionisation and the rate of ionisation per electron can be increased by increasing the electrons mean free path through the presence of a magnetic field. With this in mind, a gas discharge kept at low pressure, with the help of a magnet, is produced when a high voltage is applied. The pressure is measured through the gas discharge within a gauge head and this pressure is proportional to the signal indicated in the meter as output of the resulting ion current.

4.2.1.4 Loading and Unloading the Chamber

With the baffle valve (12) and the backing valve (14) closed, the vent valve (7) is opened and the bell jar (2) removed. The samples (source and substrate material) are then loaded appropriately as shown in Figure 4.5 and the shutter (5) closed. With the shutter closed, the bell jar is quickly closed and the vent valve also closed. The roughing valve (11) is then opened and after the pressure reading on the Pirani gauge (15) is of the order of

10^{-1} mbar, it is closed and (14) opened, followed by a gradual opening of (12). The quartz

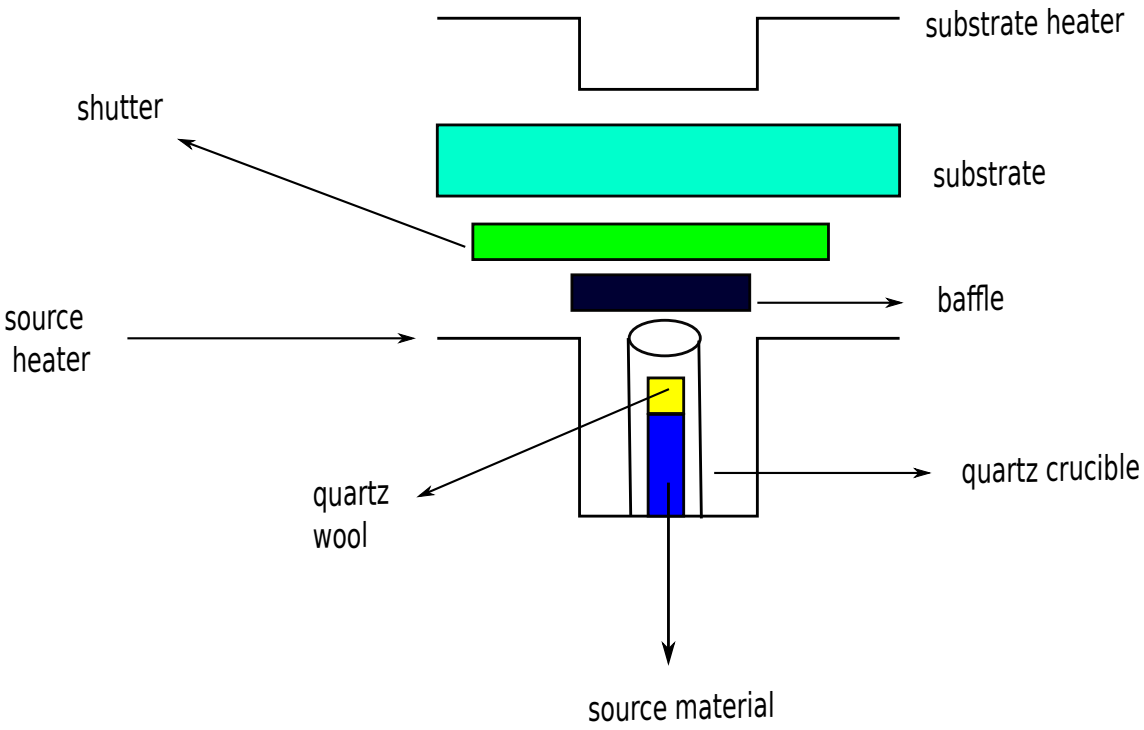

Figure 4.5: Schematic Diagram of a R.D. Mathis CH-8 Heat Shielded Crucible Heater with a Multi-Lab Quartz Crucible.

crucible were purchased from Multi-Lab QuartzTec Ltd. The evaporant (source materials) were carefully included inside the quartz crucible and then covered with a quartz wool to prevent spattering effects (Figure 4.5).

Further, the crucible was then inserted in the CH-8 shielded heat crucible connected to cylindrical tantalum heating elements obtained from the R.D. Mathis company and the temperature measured from the thermocouple connected to the CH-8 crucible.

To unload, (12) and (14) must be closed before opening (7).

4.3 Post-deposition Process and Device Fabrication

4.3.1 Thickness Measurement

The film thickness was measured using a surface profilometer (Rank Taylor–Hobson Talystep 112/1037 M17 Model). The Talystep gives a simple and direct accurate measurement of the thickness of the deposited films by producing a graphic recording of the step height (the difference in level between the surface of the substrate and the film) as the stylus

transverses from the substrate to the film. The step height corresponds to the film thickness and is then read off on the graph in line with the applied magnification. Film thickness of very few angstroms up to 12.5 µm can be measured. A typical block diagram of the Talystep is shown on Fig 4.6 while Fig 4.7 gives a picture of the Rank Taylor-Hobson Talystep.

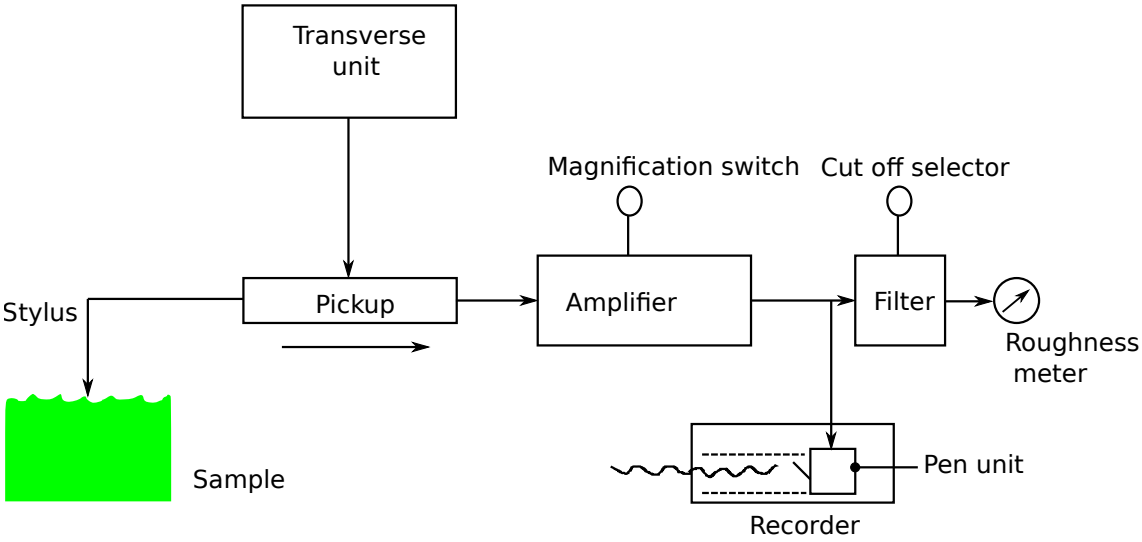

Figure 4.6: Block Diagram of the Rank Taylor-Hobson Talystep.

4.3.2 Post Deposition Heat Treatments

The post deposition heat treatments was done in the environments: air, elemental sulphur, 5% hydrogen sulphide in argon (H_2S/Ar), and air annealing after a dip in a saturated solution of tin (iv) chloride in methanol ($SnCl_4/CH_3OH$). The annealing time was varied between 15 min and 180 min while the annealing temperature was between 250 °C to 500 °C. The heating rate was fixed at 15 °C/min in all cases.

For air annealing, the equipment used was a Carbolite annealing system fitted with a Eurotherm 2132 temperature controller. For annealing with elemental sulphur, a fixed mass of S was included in a graphite box, which contained the sample, and the annealing done using a Carbolite annealing system fitted with a Eurotherm 2132 temperature controller. The system was evacuated to a base pressure of 10^{-3} mbar and the annealing carried out using a temperature of 300 °C and for annealing times in the range 15 min to 90 min. Fig 4.8 gives the picture of the system used for air annealing while that of sulphur annealing is shown on Fig 4.9. Annealing in (H_2S/Ar) was performed in an evacuated closed quartz

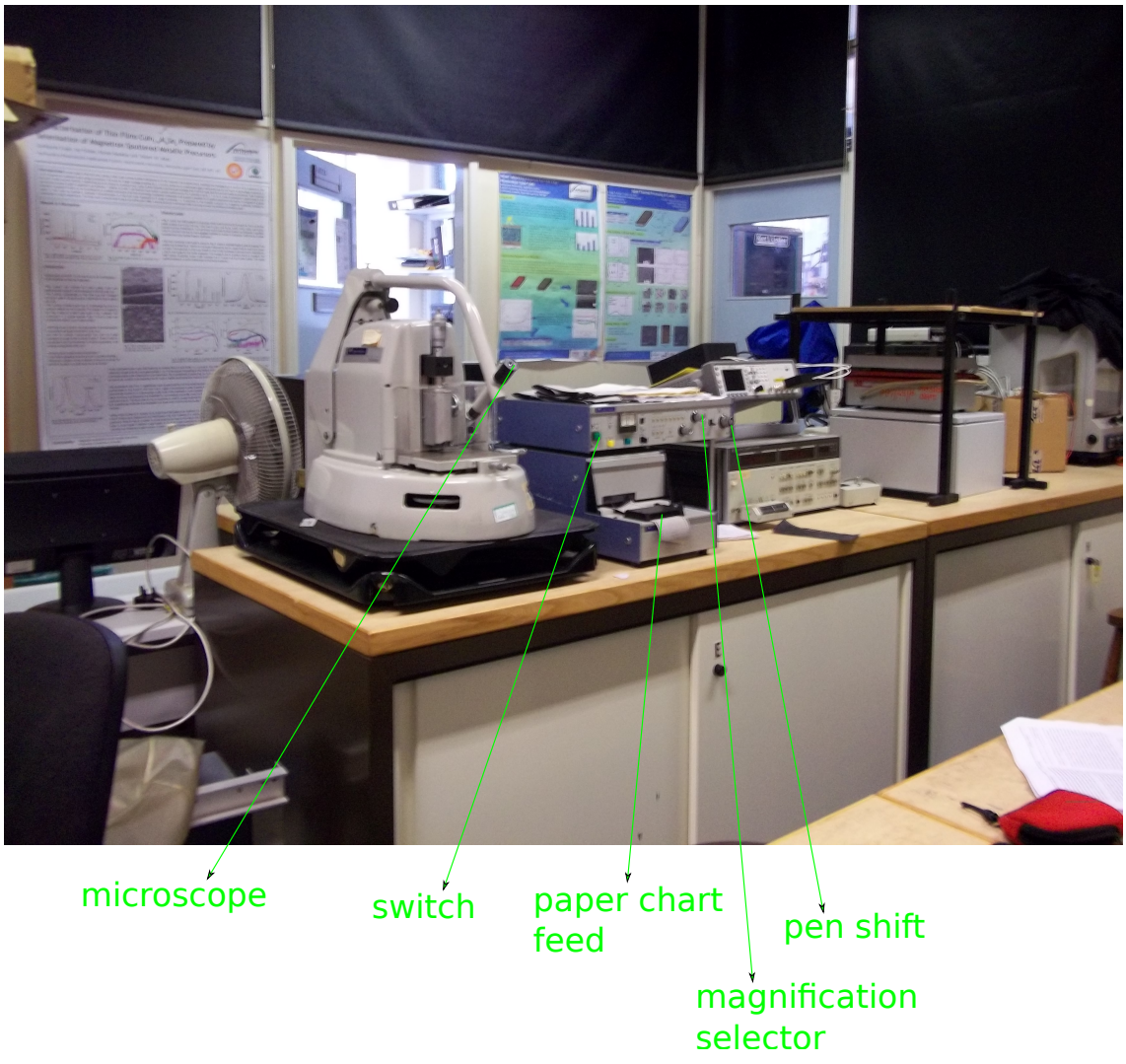

Figure 4.7: Picture of the Rank Taylor-Hobson Talystep.

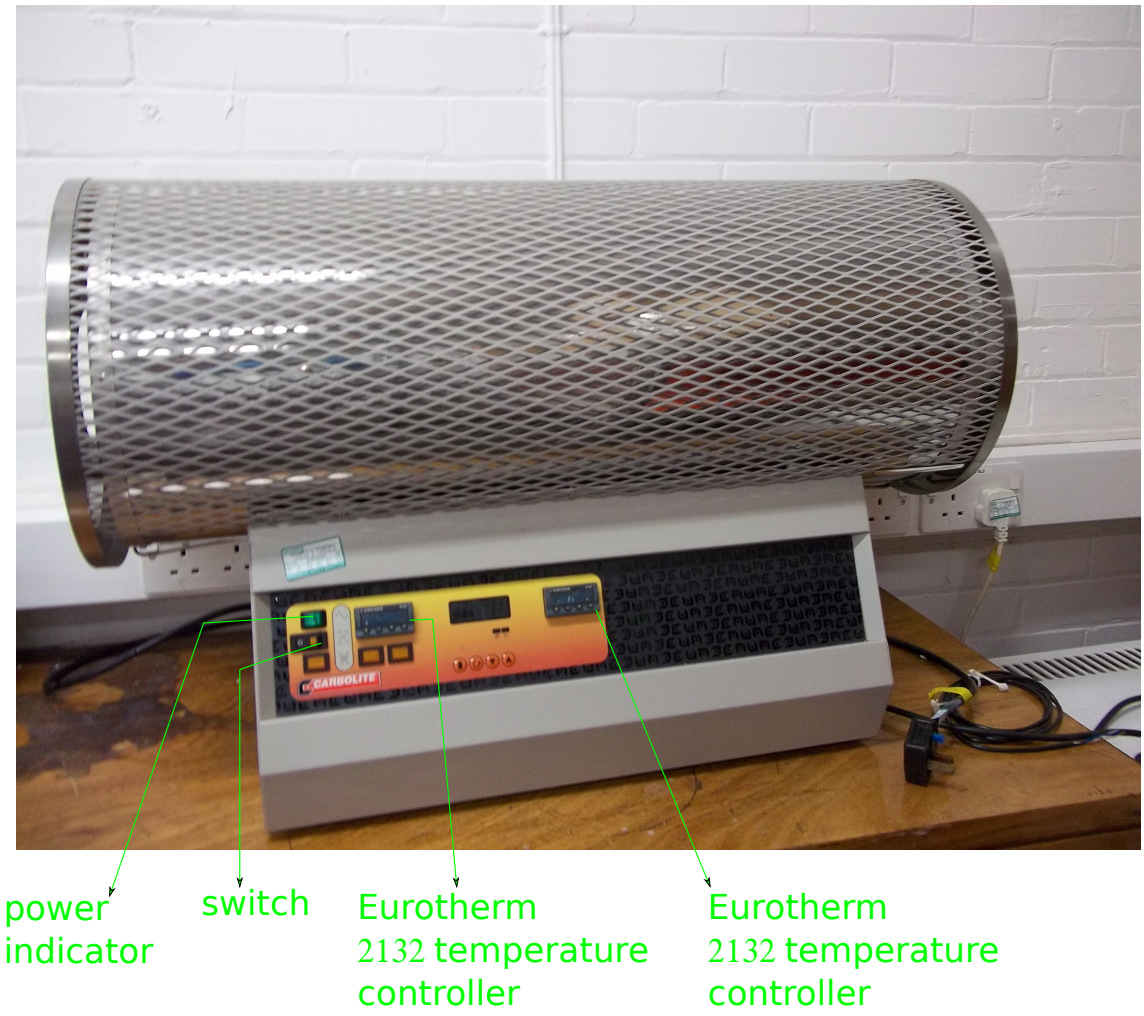

Figure 4.8: Picture of the Air Annealing System.

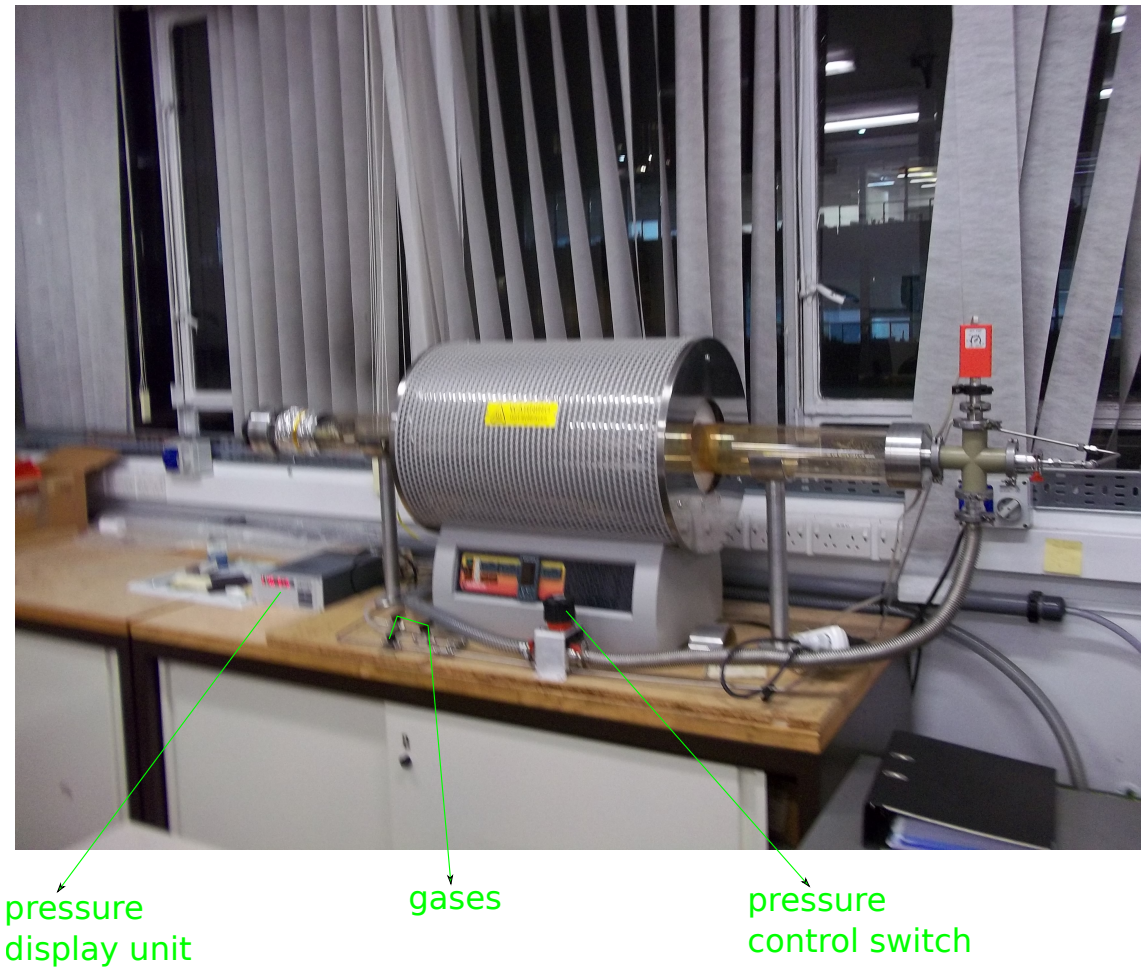

Figure 4.9: Picture of the Sulphur Annealing System.

tube into which a mixture of 5% (H_2S/Ar) was admitted and the tube then sealed at a vacuum pressure of $1.013\,25 \times 10^{-3}$ mbar. The samples were then annealed at an annealing temperature in the range 250 °C to 450 °C and a time of 15-90 min. The furnace used was a Thermal CVD System from the Sun Han Korean Company. After the desired annealing time and temperature, the furnace was then filled with argon and flushed twice and finally allowed to cool before vacuum was broken and the sample removed. Annealing in (H_2S/Ar) ambient was done at Seoul National University of Science and Technology, South Korea.

For the $SnCl_4/CH_3OH$ ambient, the samples were dipped into a saturated solution of 0.1M $SnCl_4/CH_3OH$ and then annealed in air using the same equipment as in the air annealing.

4.3.3 Device Fabrication

The devices were made in both superstrate and substrate configurations. For the "superstrate configuration" devices, the substrates used were indium tin oxide (ITO) coated glass slides, produced by RF magnetron sputtering of the ITO onto the soda lime glass substrates. Prior to thermally evaporating the SnS absorber layers, a n-conductivity type buffer layer of either CdS/ZnS/ZnO/ZIS was formed on the ITO surface. This was typically 50 nm to 100 nm thick. This layer was annealed in forming gas at 400 °C for 20 min prior to the deposition of the SnS. The devices were then completed by evaporating a metallic contact onto the SnS surface, taking care not to short out the junction. For "substrate configuration" devices, Mo was initially sputtered onto glass as the bottom contact of the device. Onto this layer the p-type SnS absorber layer was deposited, followed by the buffer layer, then the transparent (TCO) window layer and then finally a top metallic contact as grid.

The contact fabrication were done using either solid or liquid targets. For the solid targets (copper or indium), the metallisation plant and RF sputtering was used. The metallisation plant is very similar in structure and in operating principle to the thermal evaporation deposition plant except that the bell jar is a transparent high temperature resistant glass and the source crucible is an Alumina Coated Tungsten Boat S2B-AO-W also obtained from the R.D. Mathis company. Fig 4.10 gives a picture of the metallisation plant. The liquid contacts used are; wire glue purchased from www.andersproducts.com,

Leith-C, conducting glue bought from SIGMA ALDRICH, UK and silver DAG conductive paste obtained from Agar Scientific, UK. The liquid contacts all have the property of rapid solidification on exposure to air.

4.4 Characterisation Techniques

The characterisation done will be discussed under four major headings: material, optical, electrical and device characterisation. Material characterisation will include structural studies made using Scanning Electron Microscopy SEM, Energy Dispersive X-ray Spectroscopy EDS, X-ray Diffractometery XRD, Raman Spectroscopy, Secondary Ion Mass Spectroscopy (SIMS), optical characterisation (transmittance and reflectance versus wavelength measurements), electrical characterisation (electrical conductivity type and film resistivity measurements) while device characterisation included current-voltage (I-V), capacitance-voltage (C-V), spectral response measurements and X-ray photoelectron spectroscopy (XPS) studies.

4.4.1 Material Characterisation

4.4.1.1 Scanning Electron Microscopy and Energy Dispersive X-ray Spectroscopy

A FEI Quanta 200 Oxford Instrument Environmental Scanning Electron Microscope (typically operating 20 kV/97 µA) was used to investigate the surface topology and topography of the deposited films. The working principle of the SEM is based on the fact that photons and electrons signals are emitted when electron beam strikes the sample. For SEM to provide a controlled electron beam, the electron column must be under vacuum at a pressure $< 10^{-5}$ Torr [5]. Amongst the emitted signals, the most commonly used are the secondary electrons which gives information on the morphology of the specimen, backscattered electrons which provides information on the atomic number and topography, and X-ray (energy dispersive x-ray spectroscopy) which gives information on the elemental/atomic composition of the sample. Figure 4.11 shows a schematic illustration of the zones from which signals may be detected and formation of the secondary electrons [6]. They are mostly formed due to the interaction of the energetic electron beam and the

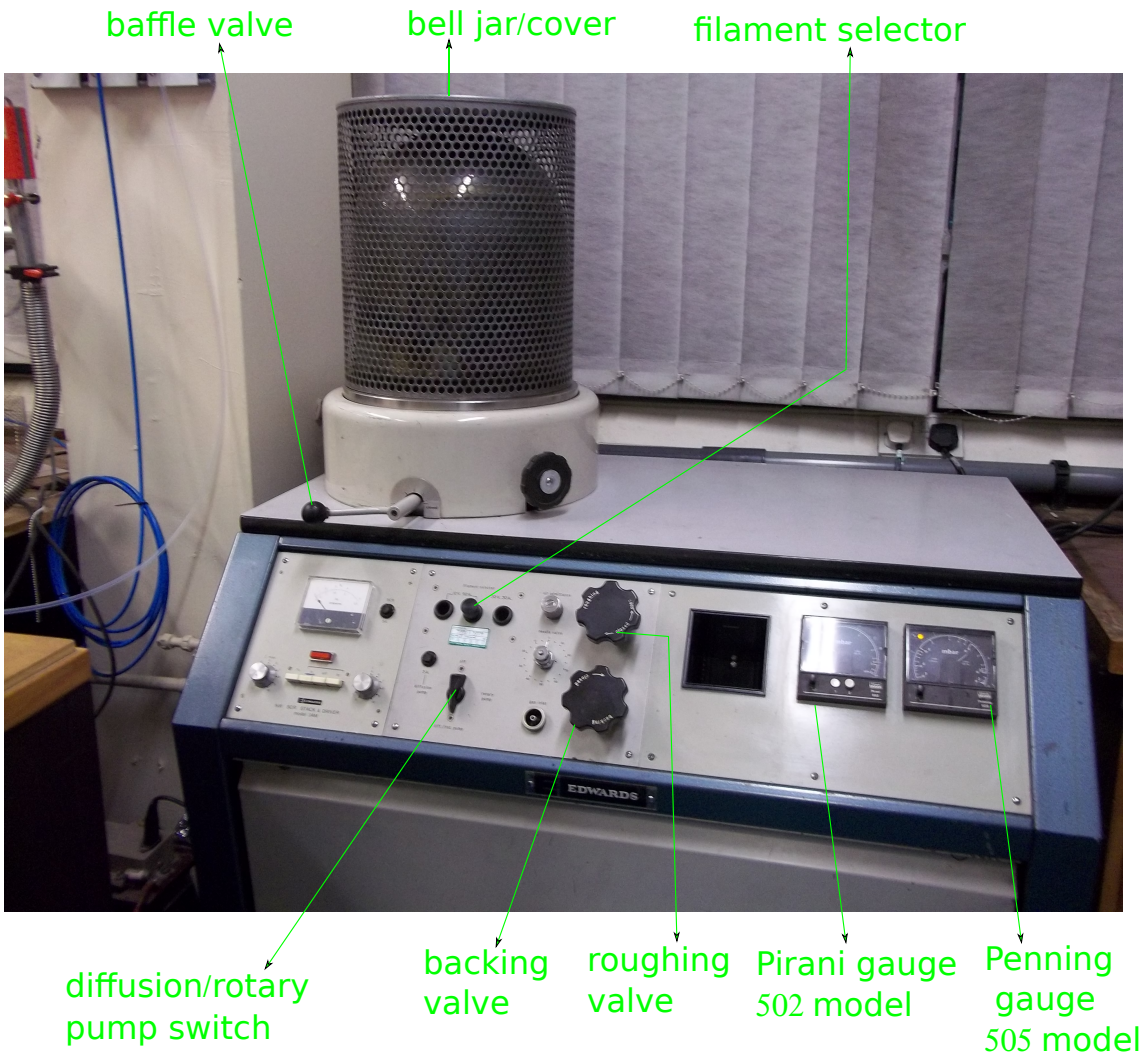

Figure 4.10: Picture of the Metallisation Plant.

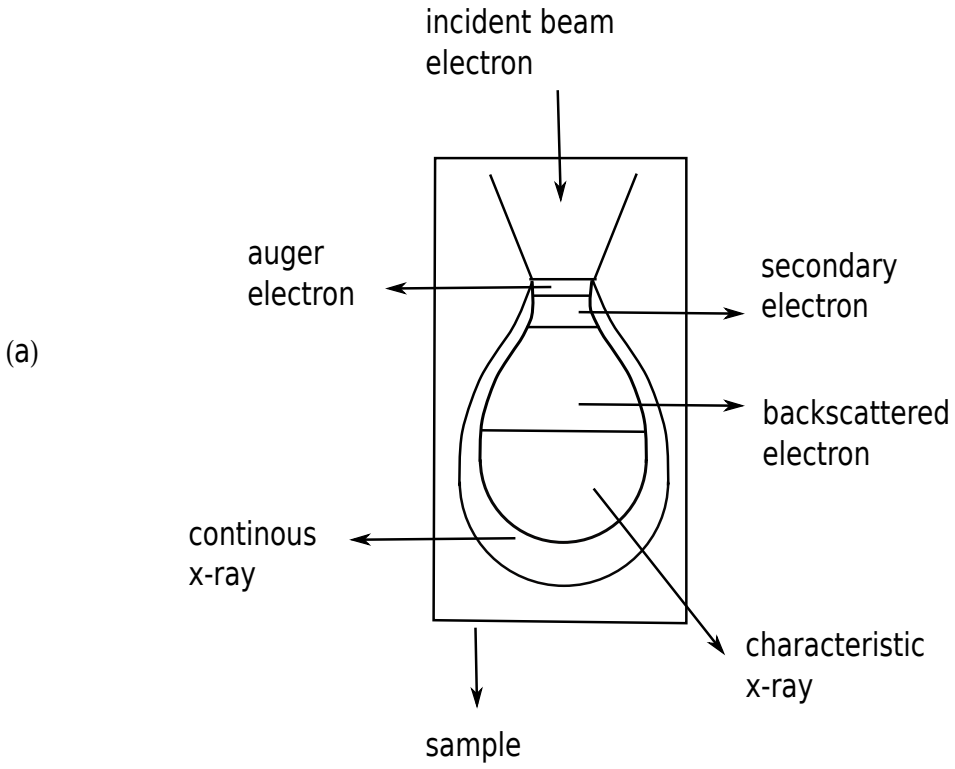

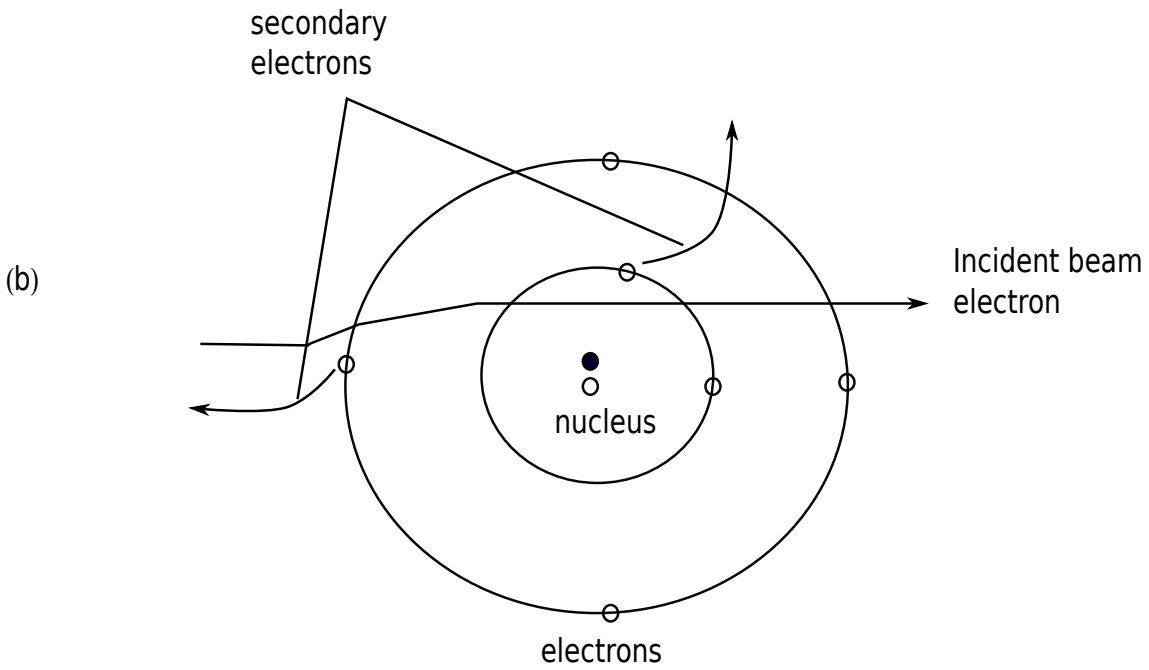

Figure 4.11: Schematic of (a) SEM Signal Sources (b) Formation of Secondary Electrons.

valence or core electrons, thus only a small amount of kinetic energy is transferred to the secondary electrons owing to the large difference in energy between the electron beam and the specimen electrons. Secondary electrons are mostly characterised by energies $<$ 50 eV [6].

The backscattered electrons arises from the effect of elastic collision and scattering between the specimen atomic nuclei and the electron beam. For the EDS, interaction between the electron beam and the specimen electron could result in the ejection of a core electron within the specimen to subsequently produce a characteristic X-ray signal that is detected by the EDS detector. The picture of the FEI Quanta 200 Oxford Instrument Environmental Scanning Electron Microscope is shown in Figure 4.12.

4.4.1.2 X-ray Diffractometry

X-ray diffraction technique is a non-contact and non-destructive method generally used in the analysis of thin film coatings or alloys to:

- identify crystalline/polycrystalline phases of material,
- determine the strain, crystallite orientation and size,
- determine the atomic arrangement in the material,
- reveal defect imaging and characterisation,
- determine concentration profile with depth,
- determine film thickness measurement,
- and to perform an in-situ measurement of crystalline phases under influence of heat.

XRD can be operated in different mode such as:

- Locked couple mode – In this, the X-ray source (tube) moves in sequence with the detector during operation. A graph of intensity in counts against the diffraction angle (2θ) is produced and the reference database (JCPDS PDF–Joint Committee on Powder and Diffraction Standard Powder Diffraction File) is then used to identify the structural phases of the diffraction pattern shown on the graph for the corresponding test sample.

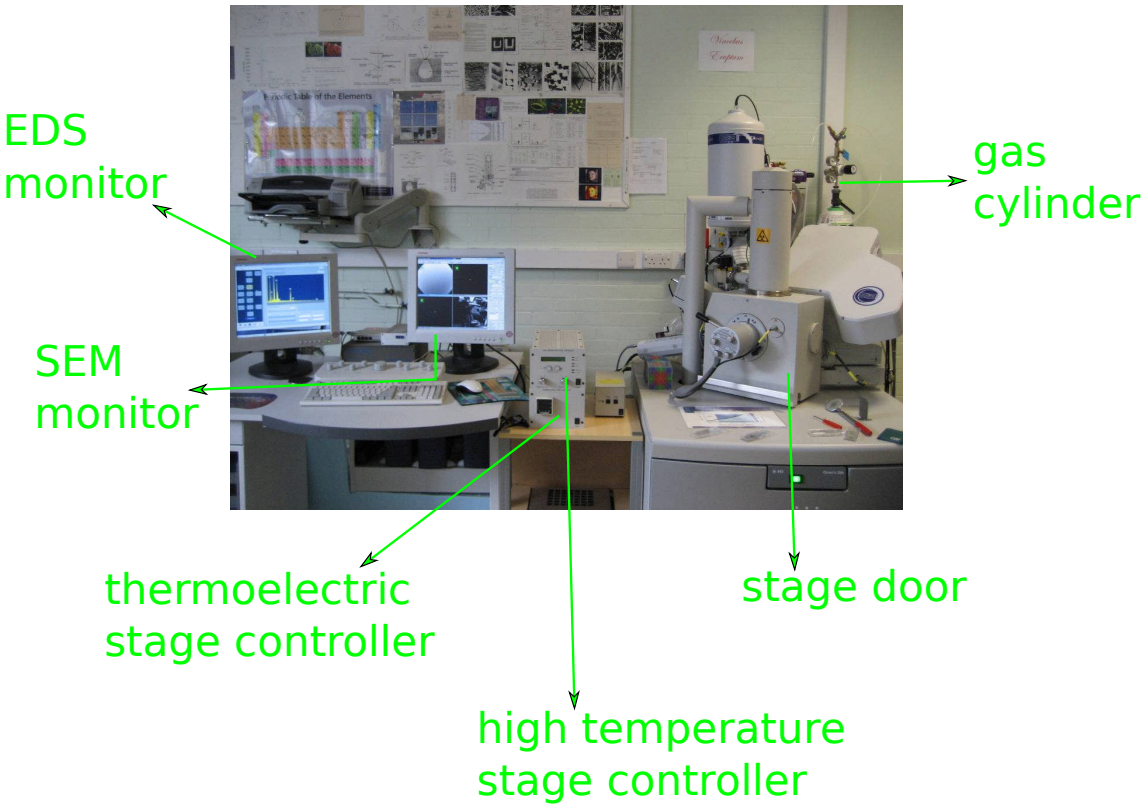

Figure 4.12: Picture of the FEI Quanta 200 Oxford Instrument Environmental Scanning Electron Microscope.

- Depth profile mode – This refers to when the tube is locked at a small angle to reduce the amount of x-ray penetration and a glancing angle is then incorporated thus producing the intensity pattern as a function of 2θ.
- Diffraction pattern analysis – This applies when individual diffraction graphs are incorporated into the same graph which can then be used to show trends and speed up analysis.
- Rocking curve mode (double diffraction method) – In this mode, it can be used to determine the layer thickness and also to reveal a pseudo-topographical information.

A Siemens D5000 X-Ray Diffractometer with a CuK_{α} radiation source with wavelength of 1.5406 Å operated in the locked-coupled mode was used in the investigation. Independent of the mode it is operated, XRD basically works on the principle of Bragg's law of diffraction given as [7, 8]:

$$2dsin\theta \ = n\lambda \tag{4.1}$$

where d is the inter planar spacing, θ is the angle between the incident and the diffracted x-rays, n is an integer (usually 1 for XRD) and λ is the wavelength of the radiation. A typical schematic of the XRD is shown on Figure 4.13. As shown in Figure 4.13, the planes of the atoms are spaced by d from each other but because several atomic planes could arise with different d-spacing, a coordinate system whose unit vectors a, b, and c are edges or axes of the unit cell is introduced, thus the atomic planes can be uniquely defined by its Miller indices (the three (hkl) reciprocal intercepts of the plane with the a, b, and c axes reduced to the smallest whole number ratio) such that a (hkl) plane intercepts the crystallographic axes at a/h, b/k, and c/l [2]. SnS shows an orthorhombic structure hence the interplanar spacing d_{hkl} between neighbouring (hkl) planes is given as

$$d_{hkl} \ = \ \left[\frac{a^2}{h^2} + \frac{b^2}{k^2} + \frac{c^2}{l^2}\right]^{0.5} \tag{4.2}$$

where $a \neq b \neq c$ as earlier indicated in subsection 3.1. A picture of the Siemens D-5000 X-ray Diffractometer is given in Figure 4.14.

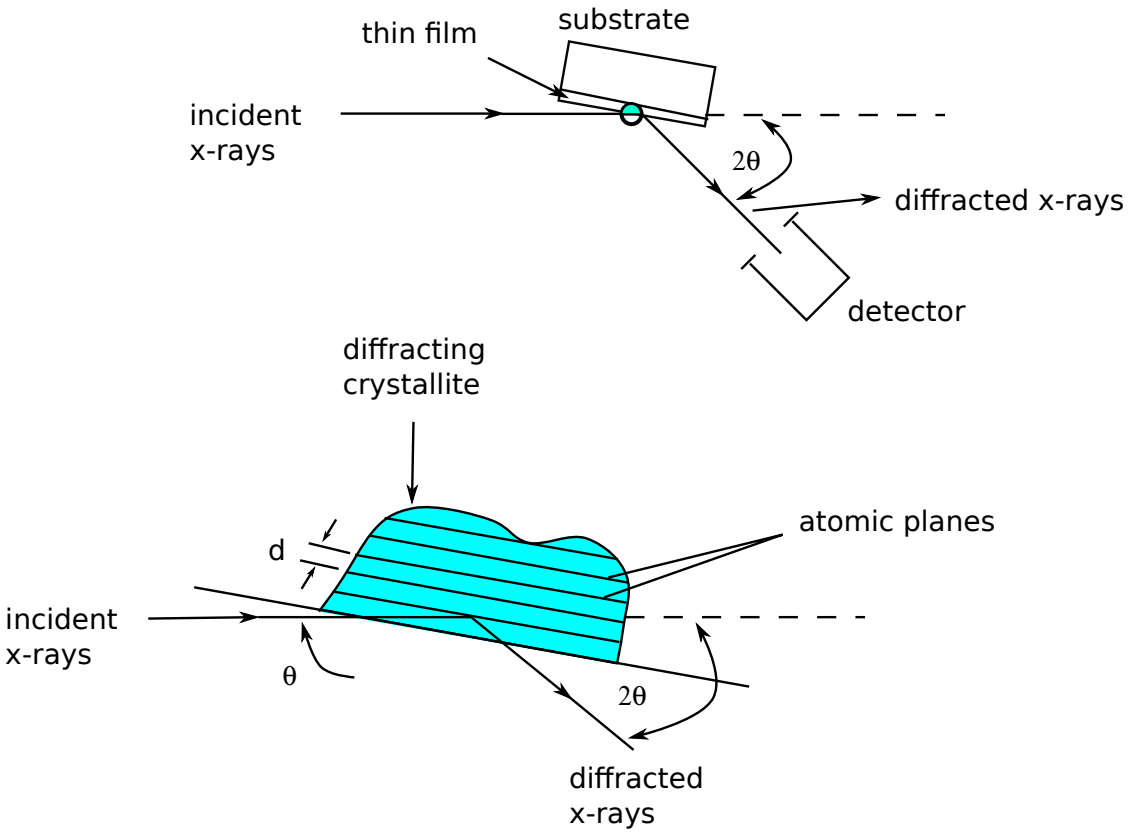

Figure 4.13: Schematic Diagram of a Typical XRD Experiment.

4.4.1.3 Raman Spectroscopy

Raman spectroscopy is primarily a non-destructive structural characterisation tool generally used in thin film analysis. Raman spectroscopy has proved to be successful in the identification of crystalline or molecular phases, for obtaining structural information on non-crystalline solids, for identifying molecular species in aqueous solutions, and for characterising solid-liquid interfaces. Raman measurement is a vibrational spectroscopy whose principle is based on the inelastic scattering of a monochromatic excitation source. This is because phonons in crystals or molecular vibrational modes have frequencies which are characteristic of the particular crystal or molecular structure. In this work the uniformity and phases of the SnS films were further verified using a Micro Raman spectrometer. The Raman measurements were taken at Sri Venkateswara University, Tirupati in India.

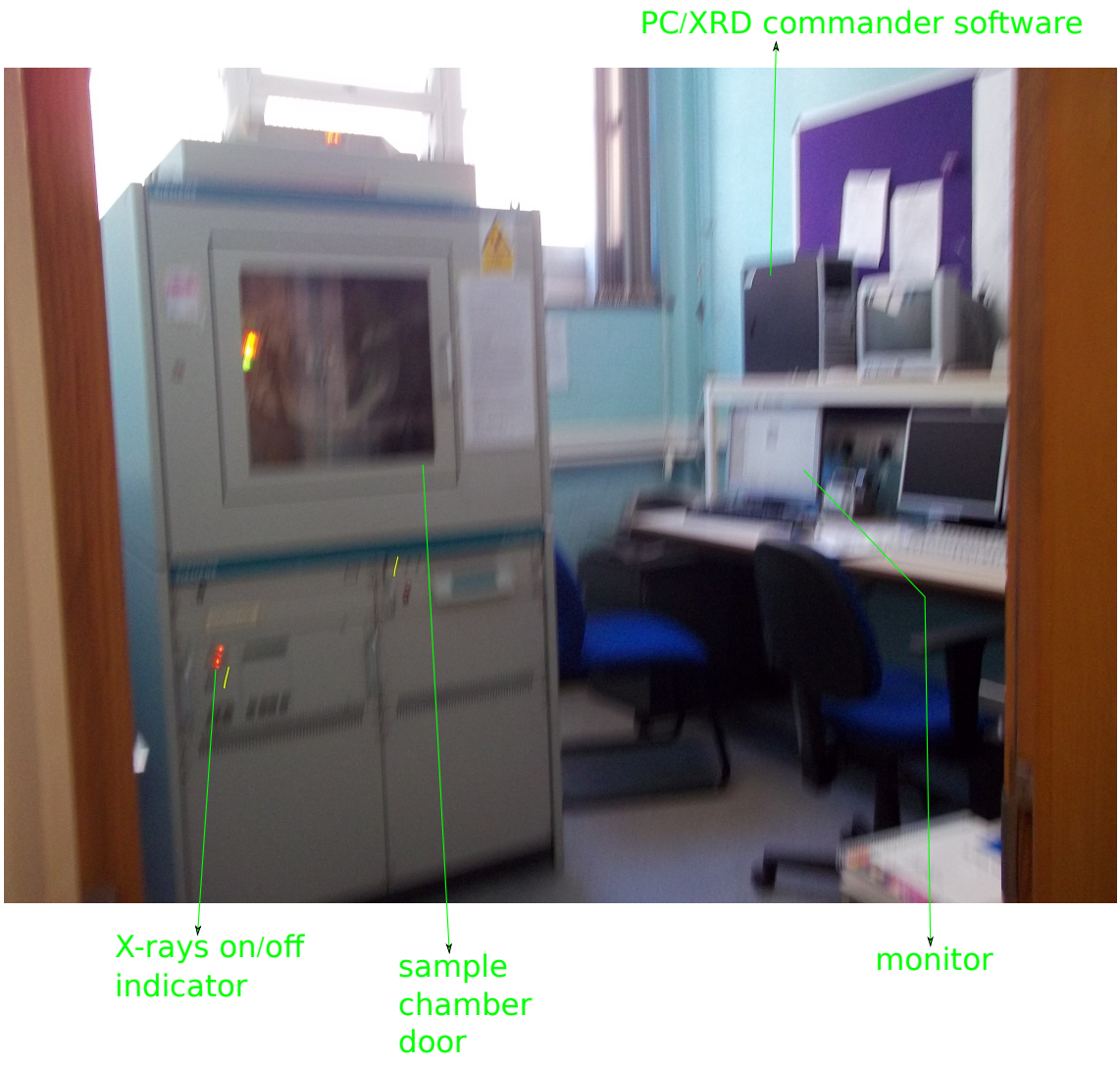

Figure 4.14: Picture of the Siemens D5000 X-Ray Diffractometer.

4.4.1.4 Secondary Ion Mass Spectroscopy (SIMS)

Secondary ion mass spectrometry is a technique generally used to analyse the composition of solid surfaces and thin films by sputtering the surface of the test sample with a focused primary ion beam and collecting and analysing ejected secondary ions with the mass spectrometer, enabling the elemental, isotopic, or molecular composition of the surface to be determined up to a depth of few nanometres. The Secondary Ion Mass Spectroscopy measurements was done using a Hiden Analytical SIMS to further determine the elemental, isotopic, or molecular composition of the surface of the as-grown and annealed films. Figure 4.15 gives the picture of the equipment. The system is equipped with two primary ion guns, the IG20 Gas Ion Gun for oxygen and argon bombardment during SIMS and SNMS (sputtered neutral mass spectroscopy) and IG5C Caesium Ion Gun for sensitive detection of electronegative ions. The action of both ion guns are controlled from the computer interface. Samples are carefully mounted from the underside of the standard sample mounting plate and loaded into the chamber via a load-lock system. After evacuation, the samples are transferred to the chamber where it is positively locked to the manipulator. The maxim spectrometer in the equipment detects the positive and negative ions while the SNMS electron impact ioniser detects the neutral species. The MASsoft software suite is used to control the analytical parameters and the normal incidence camera in the device enables a clear view of the sample for accurate targeting of features for analysis.

4.4.2 Optical Characterisation

4.4.2.1 Transmittance and Reflectance Measurements

The transmittance (T) and reflectance (R) versus wavelength measurements were made using a Shimadzu SolidSpec 3700 UV–VIS–NIR spectrophotometer. The wavelength range used for the absorber was between 300 nm to 2600 nm while for the buffer, a range of 190 nm to 2600 nm was used. The Shimazu can be operated in different modes: direct transmittance, specular reflectance and diffuse reflectance. Before taking measurement, it is important to run an initialisation test to ensure that all the active components of the equipment are ready. A baseline test with plane sodalime glass inserted at the appropriate column to ensure that the desired response is at 100% transmittance or reflectance and

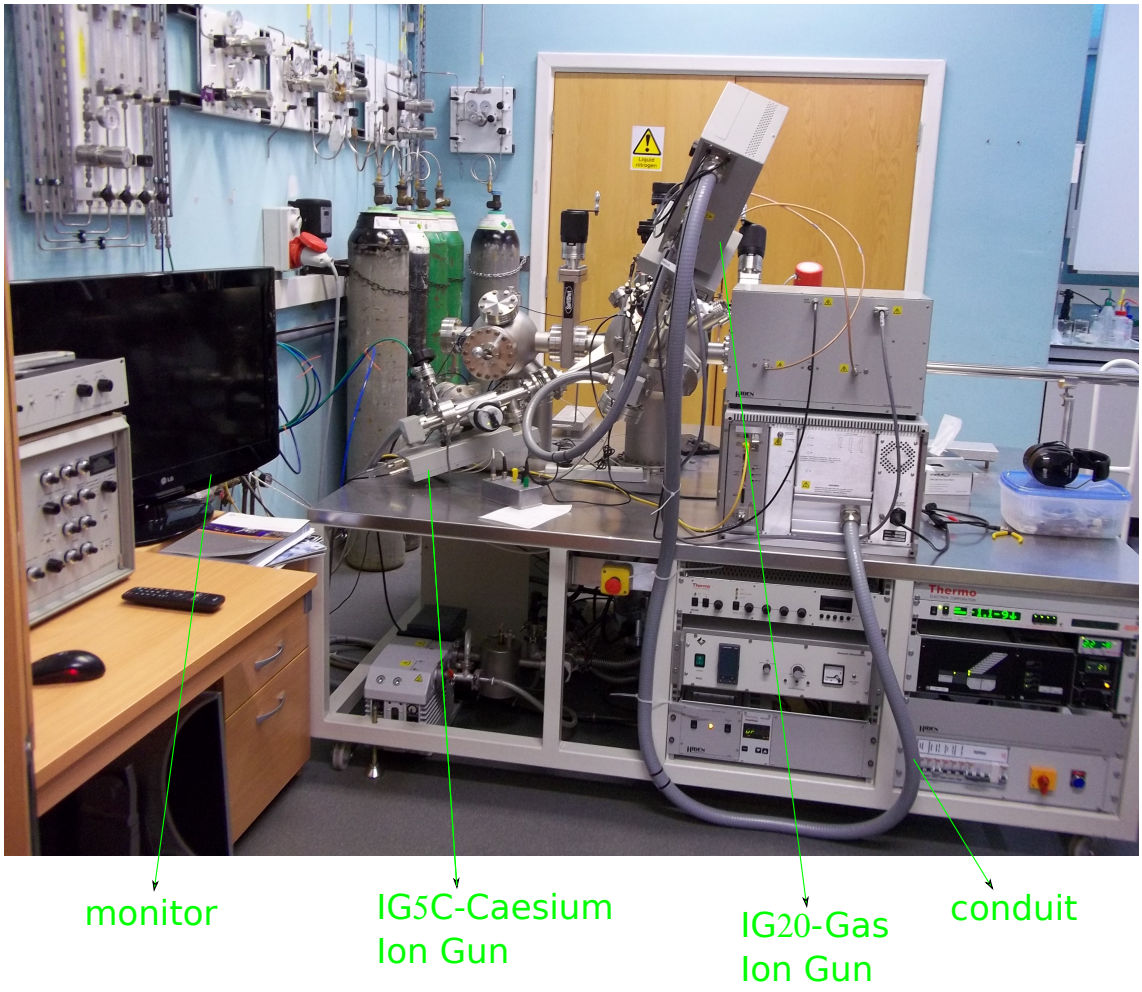

Figure 4.15: Picture of the Hiden Analytical SIMS.

also that the wavelength is at the range of interest is done after the initialisation test. A picture of the spectrophotometer is shown on Figure 4.16.

4.4.3 Electrical Characterisation

4.4.3.1 Electrical Conductivity Type

The hot probe method was used to investigate the electrical conductivity type because of its simplicity and straightforward approach in revealing whether a film is p-type or n-type conductivity. The probes (hot and cold) are wired to a sensitive multimeter, voltmeter or ammeter with the hot probe connected to the positive terminal of the meter while the cold probe is connected to the negative terminal. This technique requires that the probes will make contact with the film surface, thus needs a special caution. On making contact (usually in seconds), carriers diffuse away from the contact point with the effect that the charge of the dominant carrier (electrons or holes) determines the direction of the net current flow [9, 10]. For an n-type material, a positive current reading/deflection on the meter is observed while p-type material yields a negative current/deflection. Figure 4.17 gives a typical set-up of the hot probe.

4.4.3.2 Resistivity Measurement

The four point probe and Van der Pauw technique was used to measure the resistivity (sheet and bulk) of the samples. The four point probe is a destructive technique in that contact is made between the probes and the surface (layer of atoms over which the effect of termination of the solid decays until the bulk properties are reached [11]) of the films.

As indicated in Figure 4.18, current is made to flow between the outer probes while the voltage is measured between the two inner probes and then read off from a Keithely sourcemeter 2602 model. The picture of the set-up is shown on Figure 4.19. An extensive treatment of this technique can be found in [12, 13], thus the sheet resistivity is given as:

$$\rho_s = 4.532\frac{V}{I} \tag{4.3}$$

The bulk resistivity ρ_b is then obtained by the product of the ρ_s and the film thickness (t).

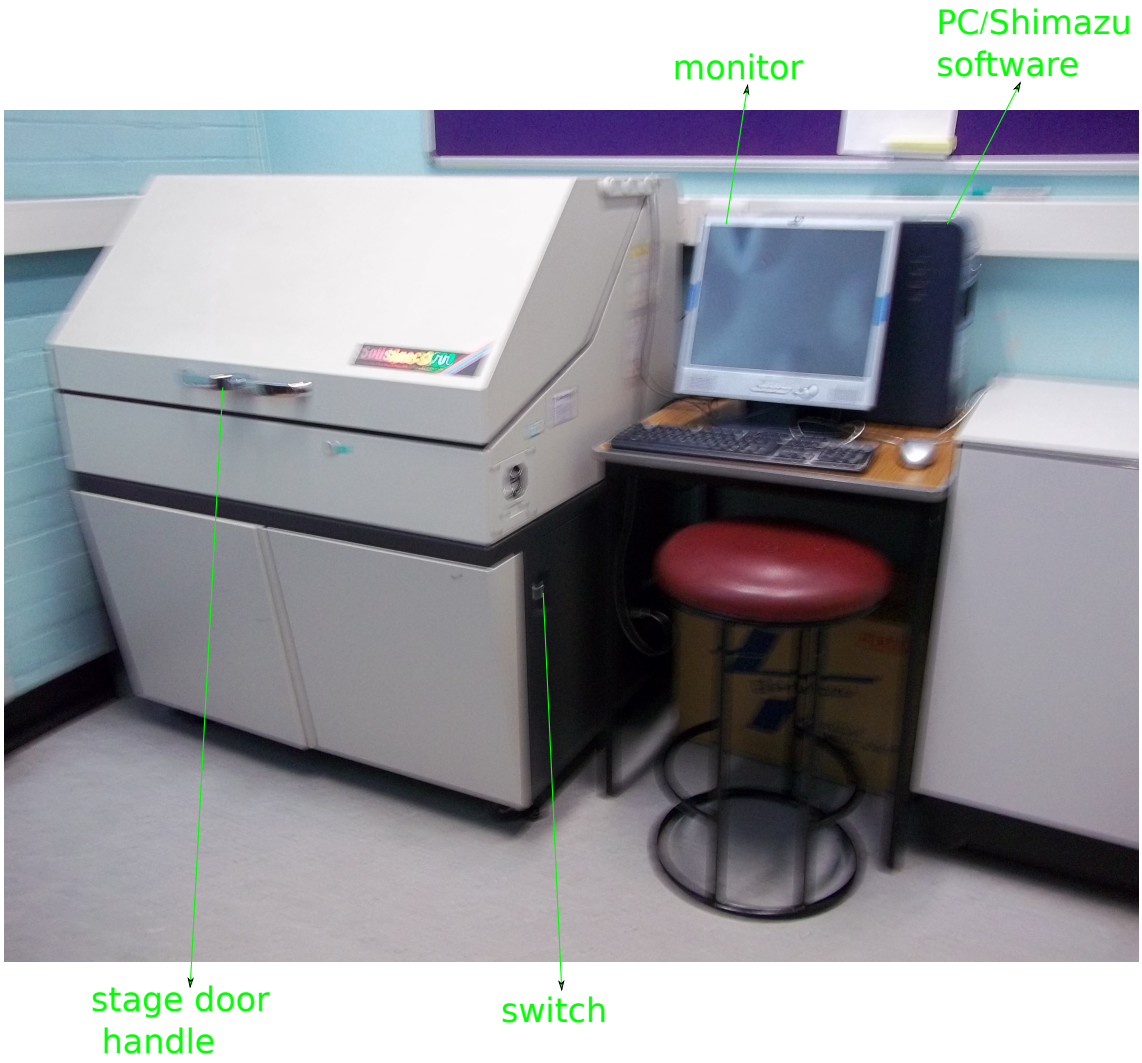

Figure 4.16: Picture of the Shimadzu SolidSpec 3700 UV–VIS–NIR Spectrophotometer.

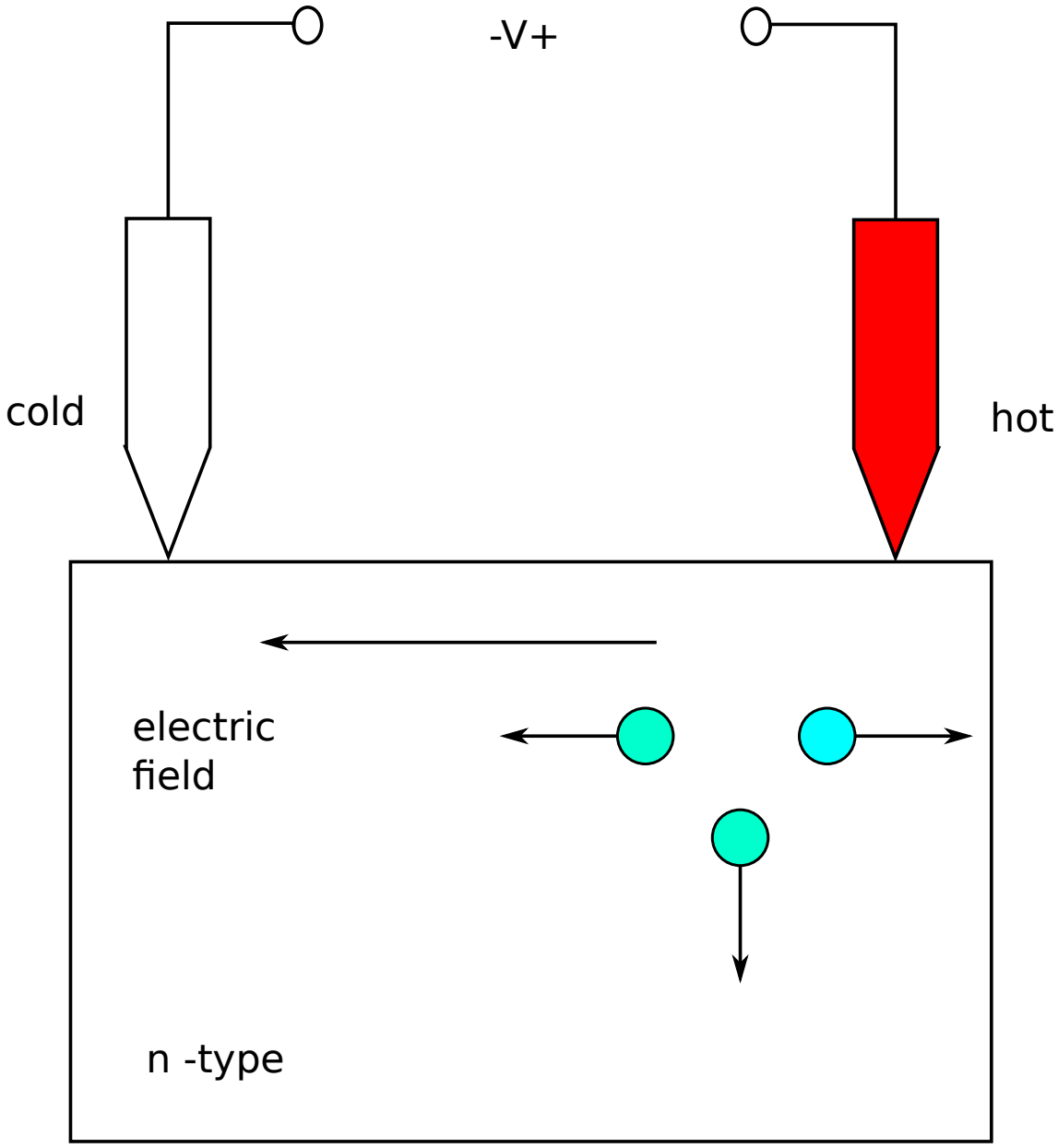

Figure 4.17: Schematic Diagram of a Hot Probe Set-up.

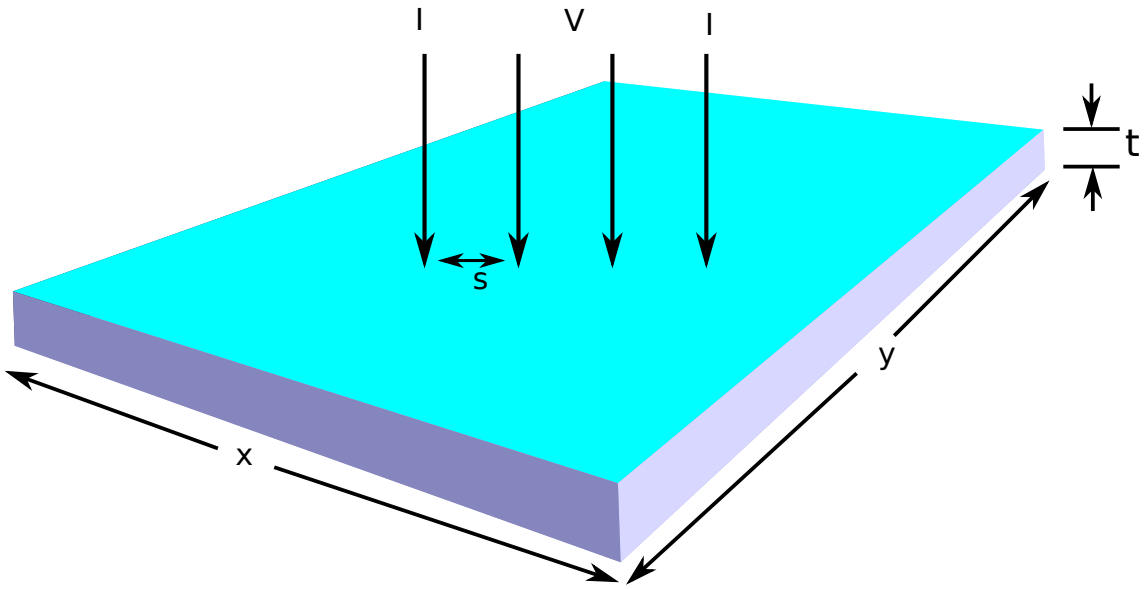

Figure 4.18: Schematic Diagram of a Four Point Probe.

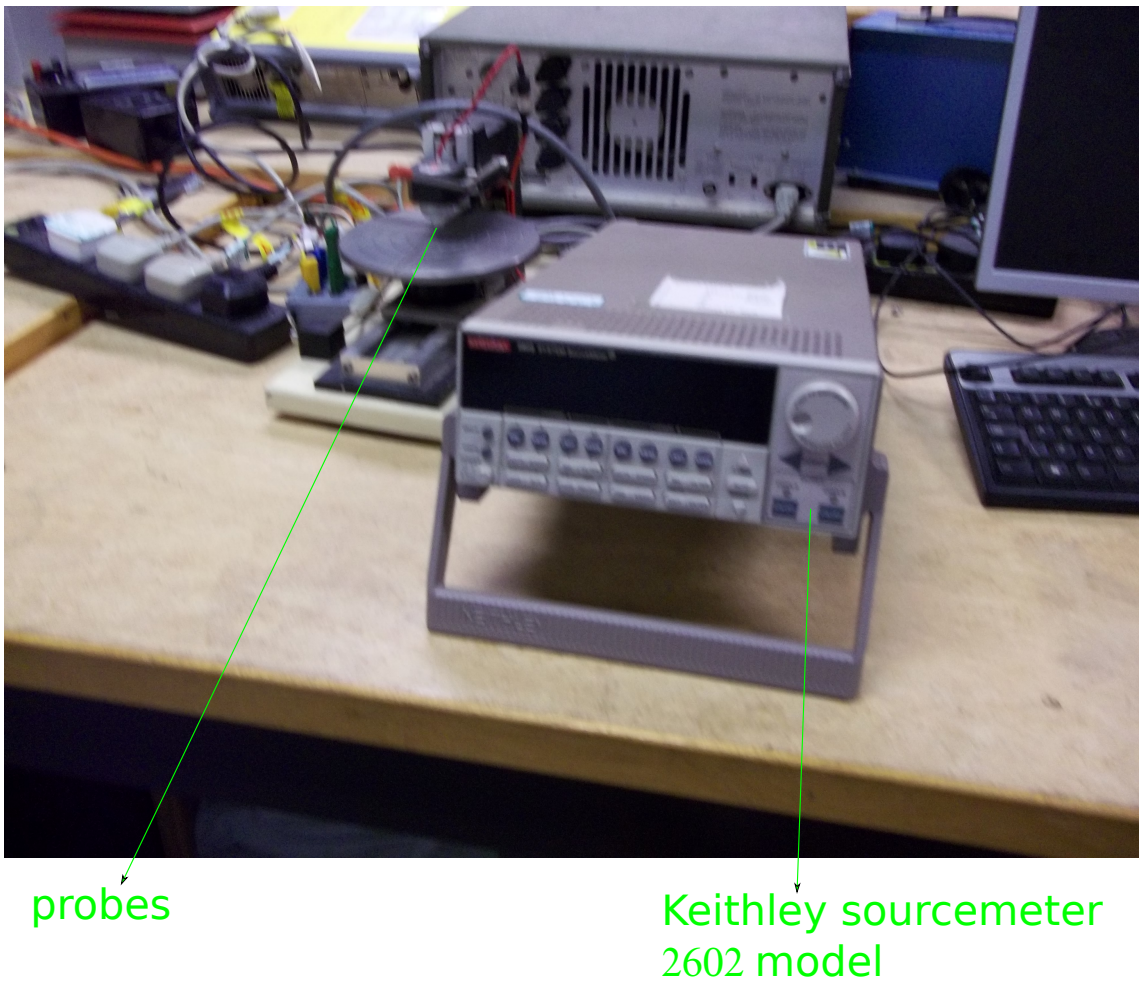

Figure 4.19: Picture of the Four Point Probe Set-up.

4.4.3.3 Van der Pauw Technique

The Van der Pauw technique can be used to measure the resistivity of any arbitrary shaped sample with four contacts based on the following assumptions:

- the contacts are at the periphery of the sample,
- the contacts are sufficiently small,
- and the sample is of uniform thickness.

For a flat sample of an arbitrary shape that satisfies the above criteria and the contacts are labelled as a, b, c and d, if current is made to enter through contact "a" and leave through "b" or otherwise, the resistance is given by:

$$R_{ab,cd} = \frac{V_{cd}}{I_{ab}} \tag{4.4}$$

$$R_{bc,ad} = \frac{V_{ad}}{I_{bc}} \tag{4.5}$$

$$R_{cd,ab} = \frac{V_{ab}}{I_{cd}} \tag{4.6}$$

$$R_{da,bc} = \frac{V_{da}}{I_{bc}} \tag{4.7}$$

hence

$$\rho_s = 4.532 \frac{V_{av}}{I_{av}} \tag{4.8}$$

where V_{av}/I_{av} is obtained from the average of Equation (4.4), Equation (4.5), Equation (4.6), and Equation (4.7) and $\rho_b = \rho_s$ t.

4.4.4 Device Characterisation

4.4.4.1 Current-Voltage Measurement

The I-V measurements were done using a Keithley sourcemeter 2400 model incorporated with a Labtracer software, and the ABET TECNOLOGIES Sun 2000 Solar Simulator model was used to generate a simulated AM1.5 spectrum, set to 1000 $\mathrm{W\,m^{-2}}$. The operation of the solar simulator is simple and easy to use, and has a long working distance optics that gives room for sample positioning or testing equipment to be varied accordingly. A schematic diagram of the solar simulator set up is shown on Figure 4.20 while a picture of the experimental set-up is shown on Figure 4.21.

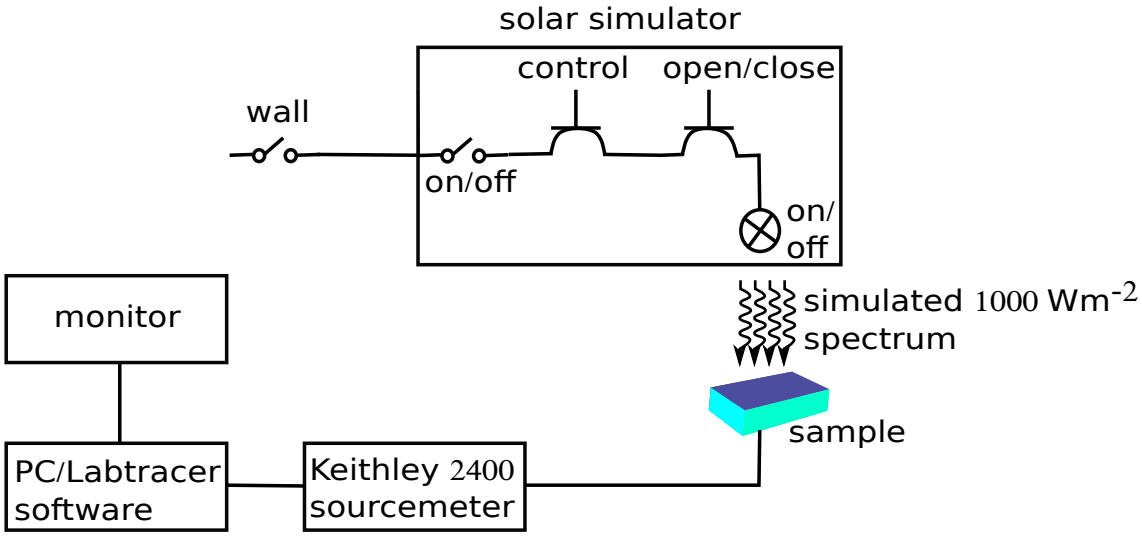

Figure 4.20: Schematic Diagram of the Solar Simulator Set-up.

4.4.4.2 Capacitance-Voltage Measurement

The C-V measurements were made in the dark using a Hewlett Packard 4274A Multifrequency LCR Meter regulated by the 16023B Bias controller such that the capacitance could be recorded at each voltage and frequency selected. A more advanced Agilent E4980A Precision LCR Meter operating in the 20 Hz – 2 MHz was also used in the studies. Figure 4.22 and Figure 4.23 give the pictures of both meters. The basic theory underlying capacitance-voltage measurements has been discussed in subsection 2.3.1. Further reading can be obtained in [14–16] and other relevant literature.

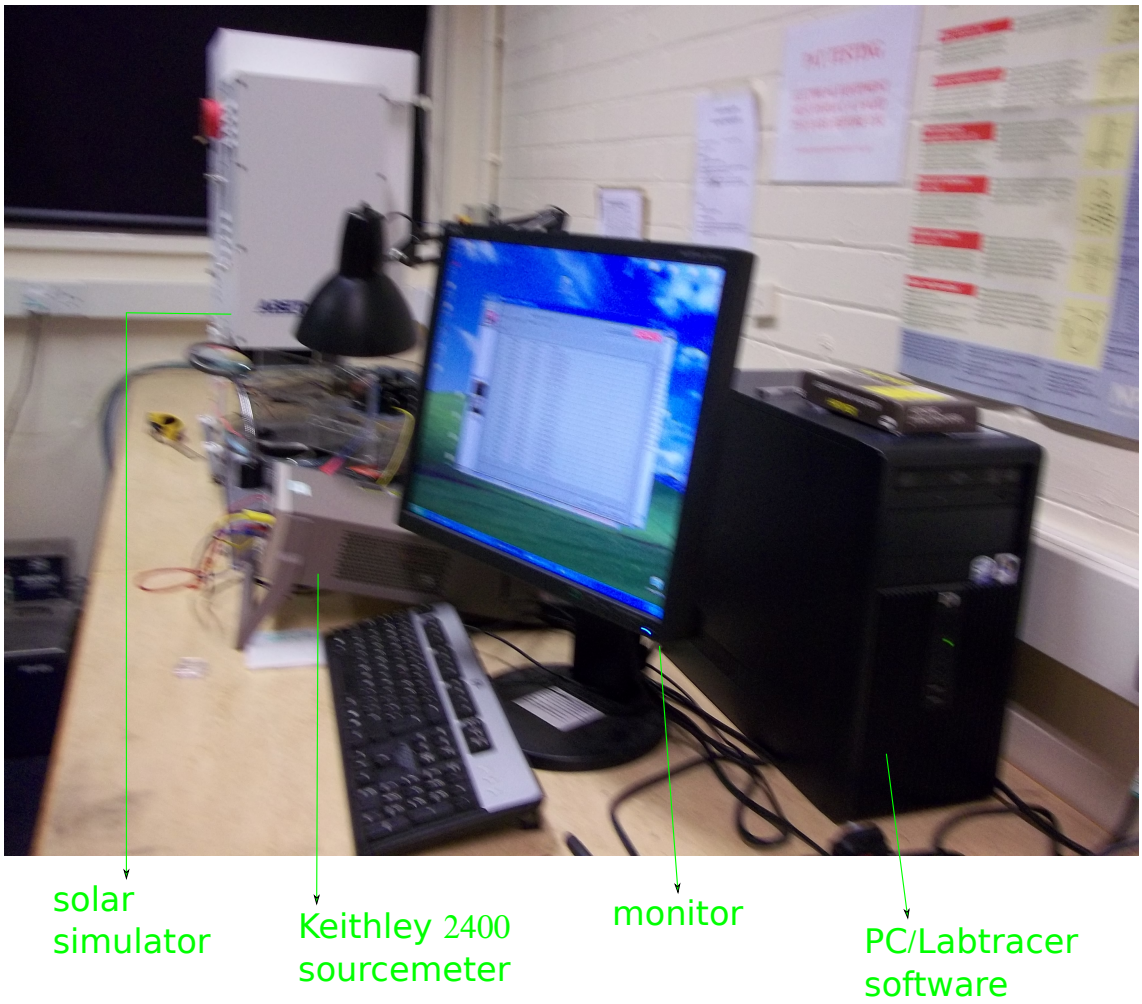

Figure 4.21: Picture of the Solar Simulator Set-up.

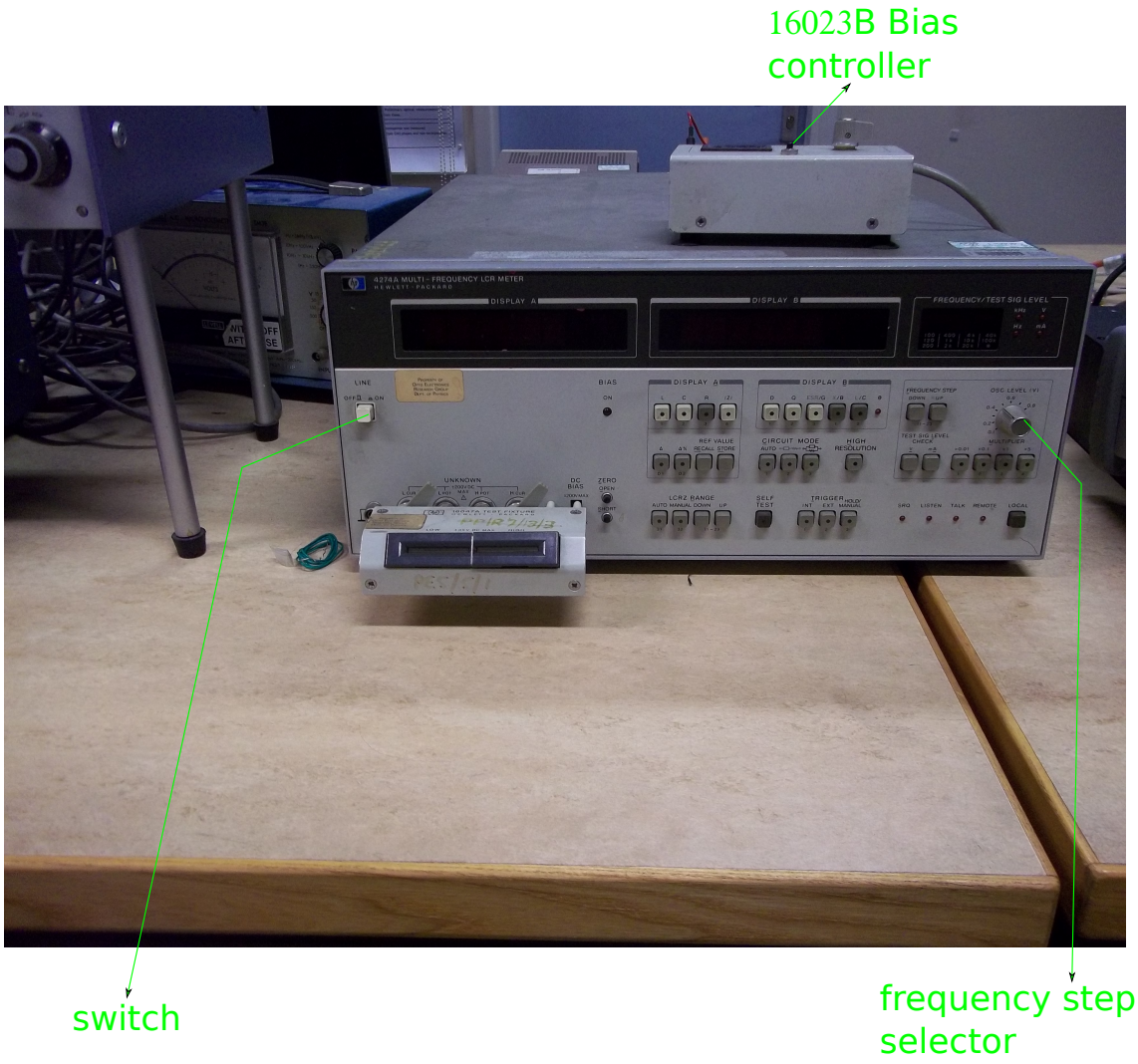

Figure 4.22: Picture of the Hewlett Packard Meter.

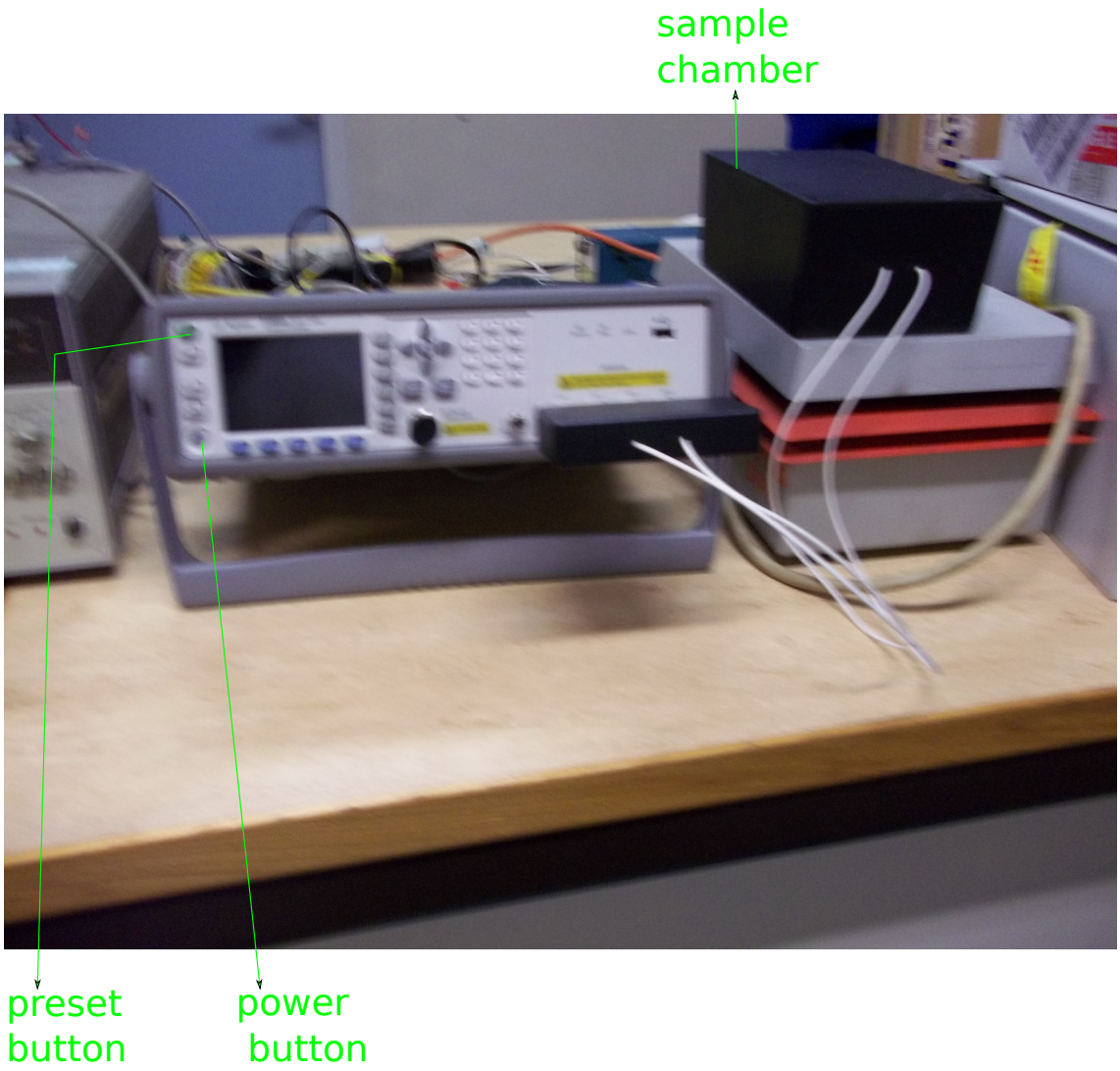

Figure 4.23: Picture of the Agilent E4908A Precision LCR Meter.

4.4.4.3 Spectral Response Measurement

The spectral response measurements were made using a commercially obtainable Bentham 605 spectral response system. The photocurrent was measured as a function of wavelength on each device and on a calibrated standard Si solar cell (with known spectral response) used as reference. The quantum efficiency was then derived by sequence of analysis from a program with Excel using a standard silicon solar cell of a known spectral response and the response of the device under test. The basic principles underlying spectral response measurement has been earlier highlighted in subsection 2.7.2. A typical generic schematic diagram of the spectral response system is shown on Figure 4.24 while the picture of the experimental set-up is shown on Figure 4.25.

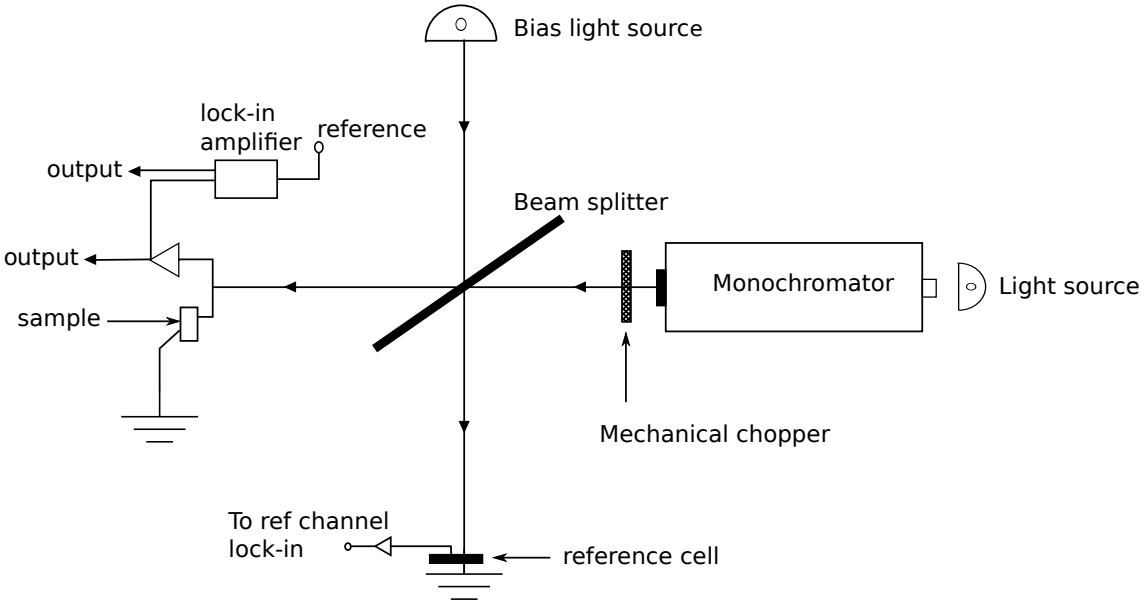

Figure 4.24: Schematic of a Generic Diagram of a Spectral Response System.

4.4.4.4 X-ray Photoelectron Spectroscopy (XPS)

Characterisation of materials using the X-ray photoelectron spectroscopy is a standard quantitative spectroscopic technique which measures the elemental composition, empirical formula, chemical state and electronic state of the elements that exist within the sample under study. It utilises photo-ionisation and analysis of the kinetic energy distribution of the emitted photoelectrons to examine the composition and electronic state of the surface region of the sample using soft x-rays (with a photon energy of 200–2000 eV) to examine

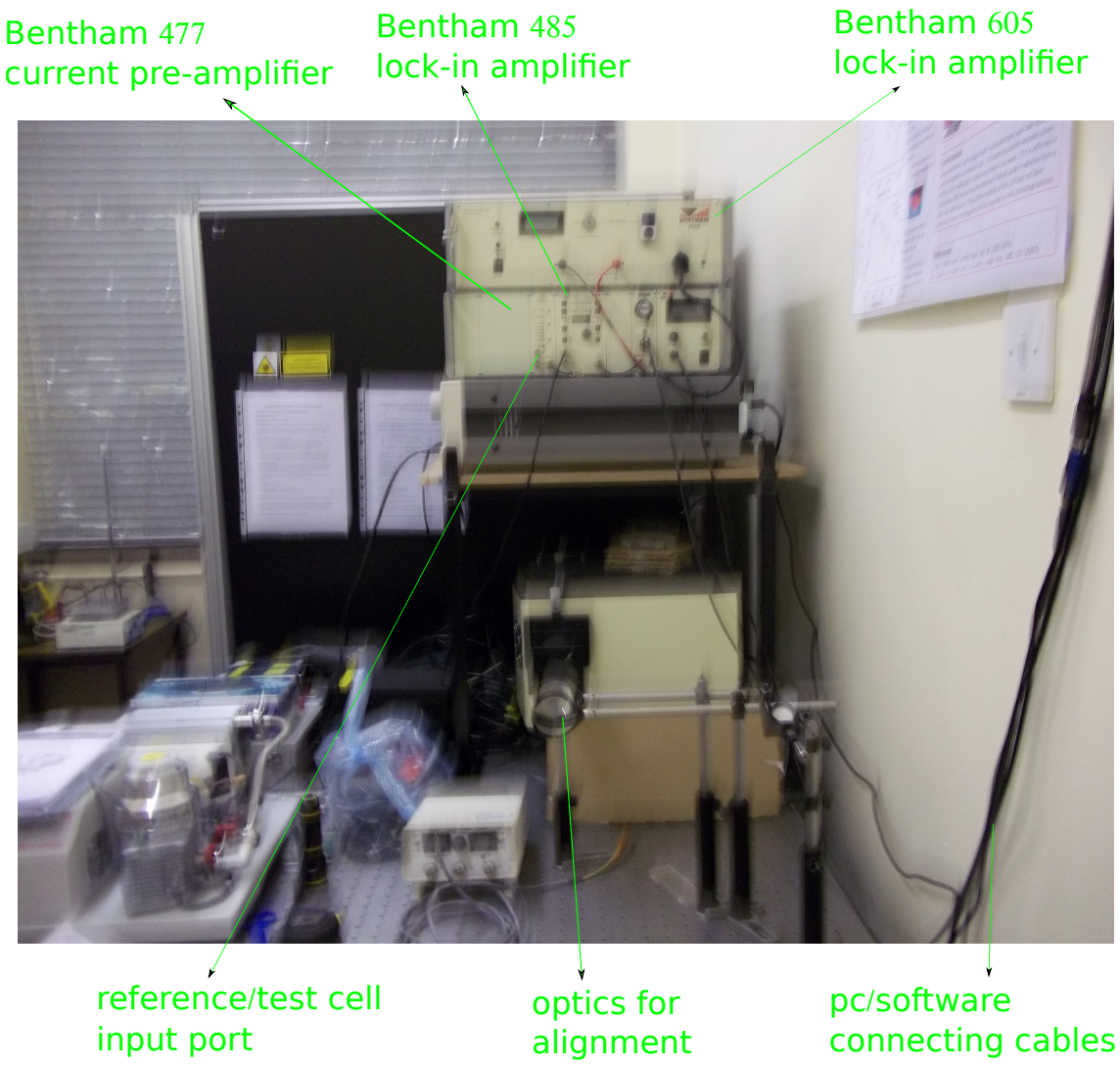

Figure 4.25: Picture of the Spectral Response Set-up.

the core-level. In general, the photon is absorbed by an atom in a molecule or solid, resulting in ionisation and emission of a core (inner shell) electron of the test sample. It is understood that for each element, there will be a characteristic binding energy associated with each core atomic orbital i.e. each element will give rise to a characteristic set of peaks in the photoelectron spectrum at kinetic energies determined by the photon energy and the respective binding energies. This implies that the emergence of peaks at particular energies indicates the presence of a specific element in the sample under study. The XPS measurements were done at Sri Venkateswara University, Tirupati, India.

References

[1] American Vacuum Society. *Graphical Symbols in Vacuum Technology*. American Vacuum Society, 1967 (cit. on p. 119).

[2] L. I. Maissel and R. Glang. *Handbook of Thin Film Technology*. McGraw-Hill, New York, 1970 (cit. on pp. 119, 136).

[3] W. Umrath. *Fundamentals of Vacuum Technology*. Oerlikon Leybold Vacuum, 2007 (cit. on p. 119).

[4] H. G. Tompkins and F. R. Shepherd. *The Fundamentals of Vacuum Technology*. American Vacuum Society, 1991 (cit. on p. 119).

[5] C. E. Lyman. *Scanning electron microscopy, x-ray microanalysis, and analytical electron microscopy: a laboratory workbook*. Plenum Publishing Corporation, 1990 (cit. on p. 131).

[6] M. T. Postek, K. S. Howard, A. H. Johnson, and K. L. McMichael. "Scanning electron microscopy: A student's handbook. Ladd Research Industries". In: *Inc, Burlington, VT* (1980) (cit. on pp. 131, 134).

[7] B. D. Cullity. *Elements of X-Ray Diffraction*. 2nd Edition. Addison Wesley, Massachusetts, 1978 (cit. on p. 136).

[8] H. P. Klug and L. E. Alexander. *X-Ray Diffraction Procedures for Polycrystalline and Amorphous Materials*. 2nd Edition. John Wiley & Sons, New York, 1974 (cit. on p. 136).

[9] J. S. Laird, B. C. Johnson, K. Ganesan, S. Kandasamy, G. Davidson, S. Borg, and C. G. Ryan. "Impurity mapping in sulphide minerals using Time-resolved Ion Beam Induced Current imaging". In: *Nuclear Instruments and Methods in Physics Research Section B: Beam Interactions with Materials and Atoms* 268 (2010), pp. 1903–1910 (cit. on p. 141).

[10] G. Golan, A. Axelevitch, B. Gorenstein, and V. Manevych. "Hot-Probe method for evaluation of impurities concentration in semiconductors". In: *Microelectronics Journal* 37 (2006), pp. 910–915 (cit. on p. 141).

[11] H. Bubert and H. Jenett, eds. *Surface and Thin Film Analysis: Principles, Instrumentation, Applications*. Wiley-VCH Verlag GmbH, 2002 (cit. on p. 141).

[12] L. B. Valdes. "Resistivity measurements on germanium for transistors". In: *Proceedings of the IRE* 42 (1954), pp. 420–427 (cit. on p. 141).

[13] D. R. Zrudsky, H. D. Bush, and J. R. Fassett. "Four Point Sheet Resistivity Techniques". In: *Review of Scientific Instruments* 37 (1966), pp. 885–890 (cit. on p. 141).

[14] R. F. Pierret. *Semiconductor device fundamentals*. Addison-Wesley Reading, MA, 1996 (cit. on p. 146).

[15] S. M. Sze and K. Ng. Kwok. *Physics of Semiconductor devices*. 3rd Edition. Wiley & Sons, New Jersey, 2007 (cit. on p. 146).

[16] L. C. Kimerling. "Influence of deep traps on the measurement of free-carrier distributions in semiconductors by junction capacitance techniques". In: *Journal of Applied Physics* 45 (1974), pp. 1839–1845 (cit. on p. 146).

Chapter 5

Results

5.1 Results and Analysis

Most of the films were deposited using a source to substrate distance of 31 mm, vacuum pressure in the range 10^{-5} Torr to 10^{-6} Torr, substrate temperature in the range 280 °C to 360 °C, source temperature in the range 300 °C to 350 °C, film thickness between 20 nm to 4.3 µm, and the deposition time varied between 10 sec to 3 min.

5.1.1 Morphological Properties

Physical observations of the films showed that the colour of the films was closely related to the deposition conditions. Films deposited for lower deposition times ($<$ 20 sec) with film thicknesses ($\leq$ 20 nm) appeared brownish black while for higher deposition times/film thicknesses, the layers were predominantly a bluish-black colour. All films deposited were pinhole free and adhered strongly to the substrate.

Figure 5.1 and Figure 5.2 show SEM micrographs of SnS thin films. From SEM studies, the shape of the grains in the films were not the same as sometimes large leaf-like grains [1] or rice-like grains [2, 3] were observed depending on the deposition conditions. Figure 5.1 shows typical SEM micrographs of large leaf-like grains at different substrate temperatures while Figure 5.2 shows rice-like grains for different deposition time. Other relevant data are contained in [4, 5]. Different/similar grain shapes for SnS films grown either by the thermal evaporation technique or other methods have been reported by other authors [6–16].

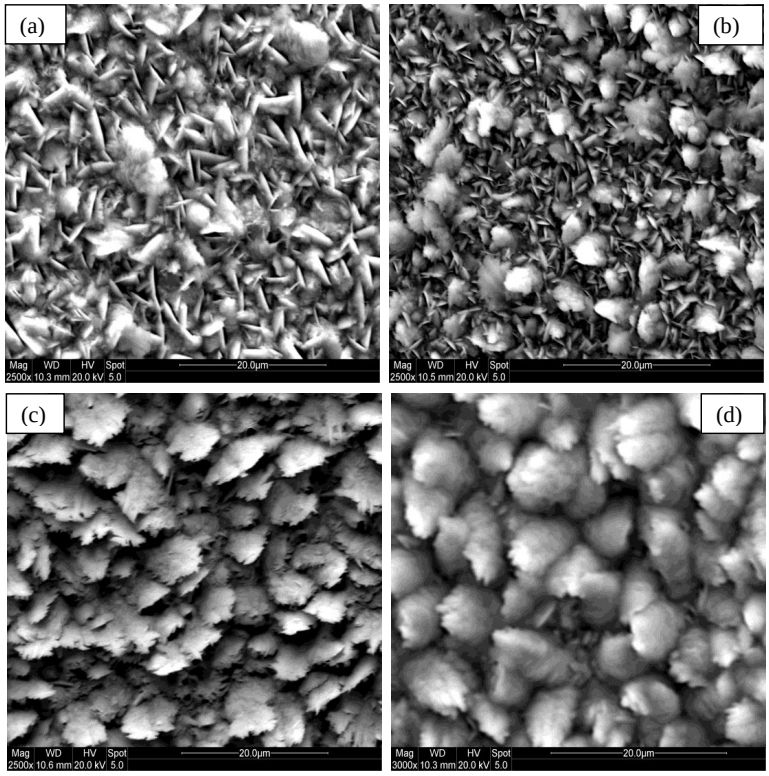

Figure 5.1: SEM Micrographs of SnS Layers Deposited at Different Substrate Temperatures; (a) 300 °C (b) 322 °C (c) 335 °C (d) 350 °C with Constant Source Temperature (300 °C) and Deposition Time (3 min) [1].

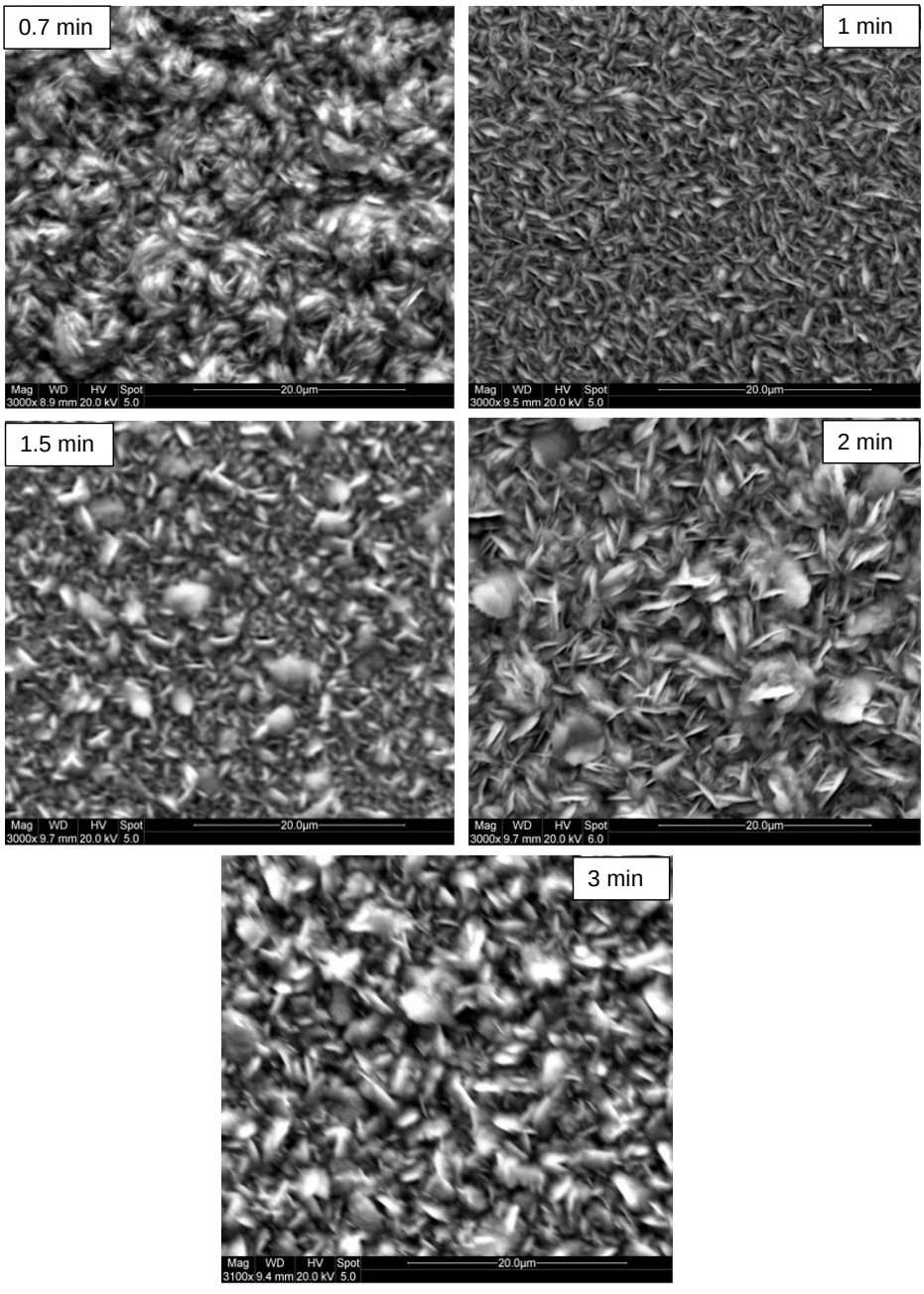

Figure 5.2: SEM Micrographs of SnS Layers Deposited at Constant Substrate Temperature of 350 °C, Constant Source Temperature of 300 °C and Deposition Time between (0.7–3 min) [3].

5.1.2 Compositional Properties

Figure 5.3 and Figure 5.4 give the variation of Sn/S atomic ratio with substrate temperature and deposition time respectively. Compositional analysis plays a role in understanding the stoichiometry of the constituent elements in thin films irrespective of the deposition technique. EDS studies indicated that the films were slightly Sn-rich when deposited using substrate temperatures $\geq 300\,^{\circ}\mathrm{C}$. The slight Sn-rich behaviour was found to increase with an increase of substrate temperature or deposition time as evidenced in [1, 3]. The Sn/S atomic ratio varied between 1.02–1.23. This was mostly attributed to the difference in vapour pressure between the Sn and S atoms. Similar behaviour for same or other deposition variables have been reported by other authors in the literature [6–8, 17–22].

5.1.3 Structural Properties

The XRD spectra at different substrate temperature, deposition time and film thickness are shown in Figure 5.5, Figure 5.6, Figure 5.7 and Figure 5.8. From XRD studies, the films were found to have the orthorhombic crystal structure consistent with the Powder Diffraction File: 00-039-0354 [23]. The layers were mostly single phase with the (111)/(040) planes giving rise to the most prominent peak. The (040) reflections are more likely associated to higher values of film thickness, substrate temperature or deposition time as indicated in [1, 3–5] while the (111) are more likely at lower values of the deposition variables as shown in [2, 24] and by other authors [6, 25–27]. Variation of the (111)/(040) peaks with different deposition conditions has been widely observed by various research groups independent of the deposition technique as contained in [7, 10, 21, 22, 28–32]. Other Bragg peaks were observed alongside the most prominent peaks in the films. These include the (110), (120), (021), (101), (131), (141), (002), (211), (151), (231), (042), (251) and the (171) diffraction peaks consistent with Powder Diffraction File: 00-039-0354. The results obtained indicate that the nature of the films depends to a large extent on the deposition variables i.e. the substrate temperature, film thickness, deposition time, source to substrate distance and the deposition rate. The narrow structured XRD peaks depend on better crystallinity and larger grain size which are strong functions of the deposition conditions

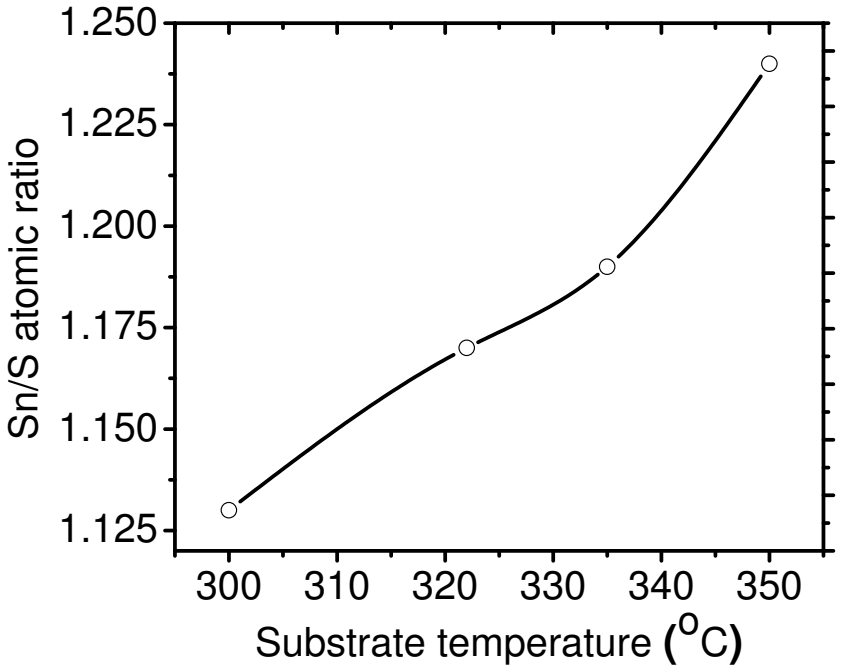

Figure 5.3: Variation of Sn/S Atomic Ratio with Different Substrate Temperatures at Constant Source Temperature (300 °C) and Deposition Time (3 min) [1].

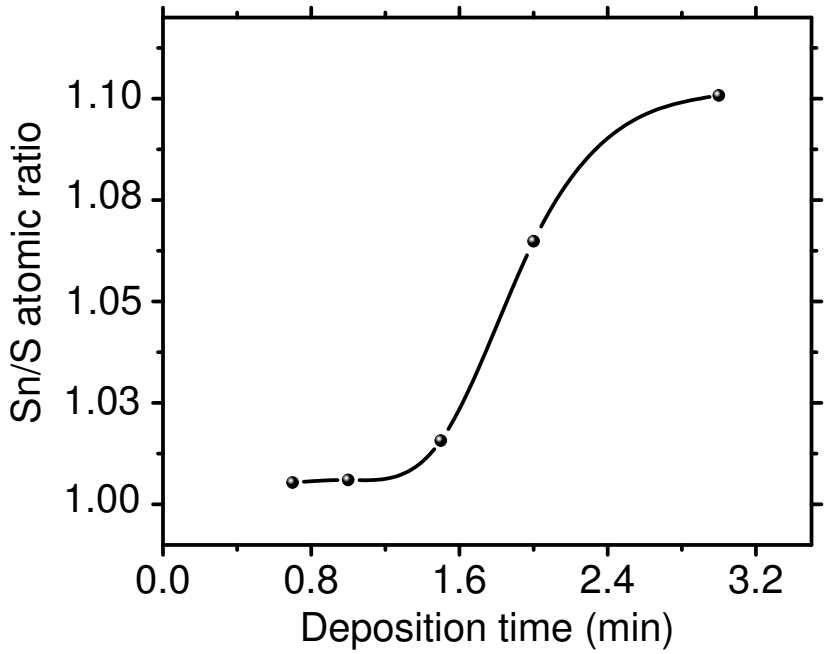

Figure 5.4: Variation of Sn/S Atomic Ratio with Different Deposition Times at Constant Source and Substrate Temperature of 300 °C and 350 °C.

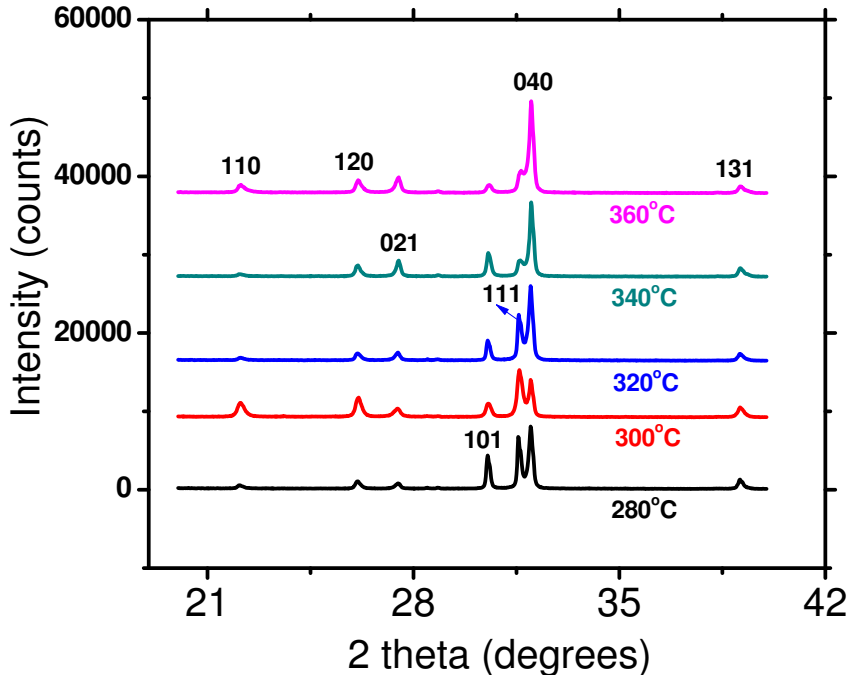

Figure 5.5: XRD Spectra of SnS Films at Different Substrate Temperatures with Constant Source Temperature (300 °C) and Deposition Time (3 min) [5].

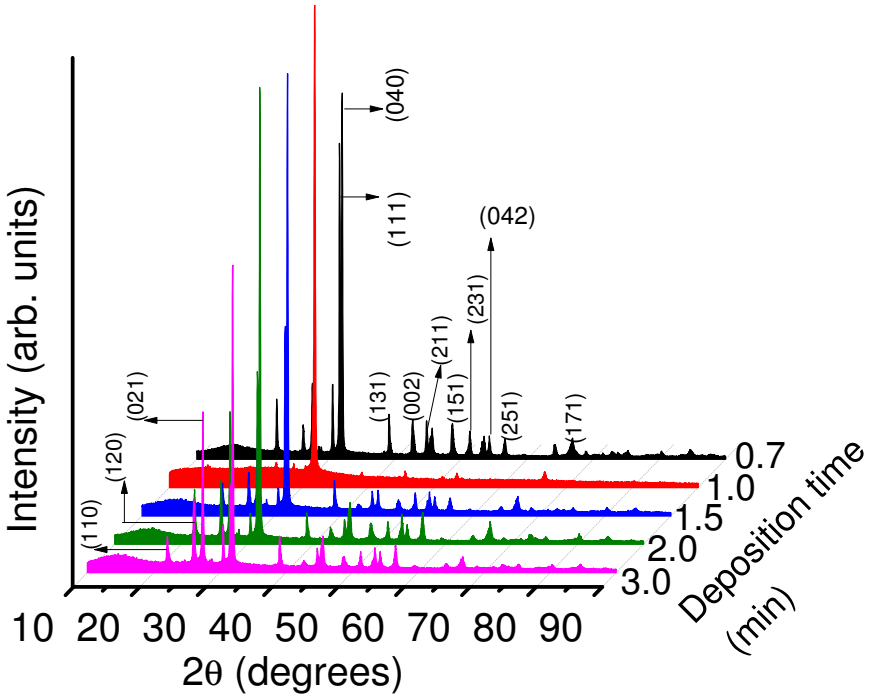

Figure 5.6: XRD Spectra of SnS Films with Different Deposition Times at Constant Source and Substrate Temperature of 300 °C and 350 °C [3].

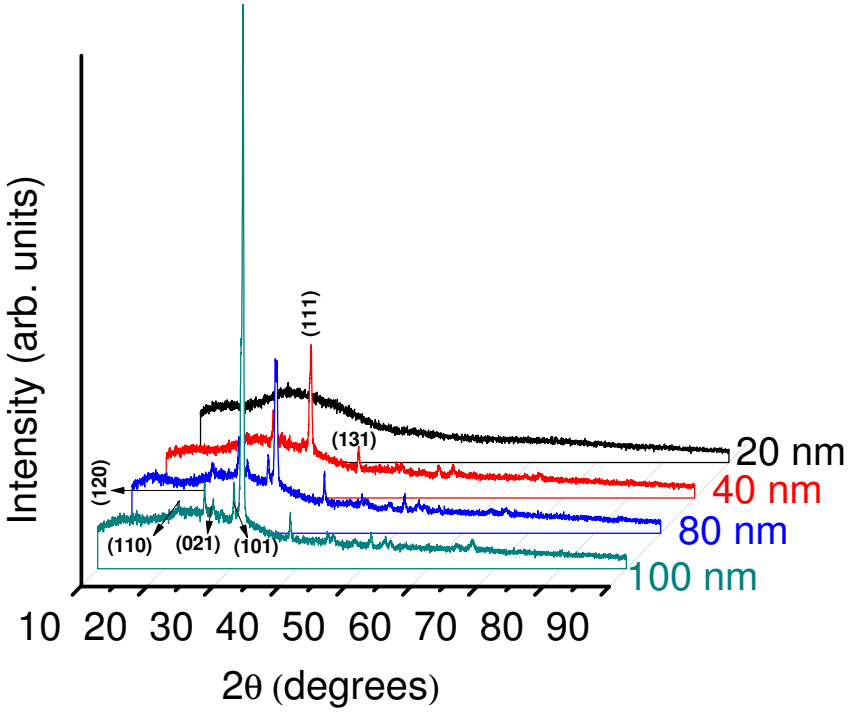

Figure 5.7: XRD Spectra of SnS Films with Different Film Thicknesses (nm) at Constant Source and Substrate Temperature of 300 °C and 350 °C with Deposition Time between 10 sec to 1 min [33].

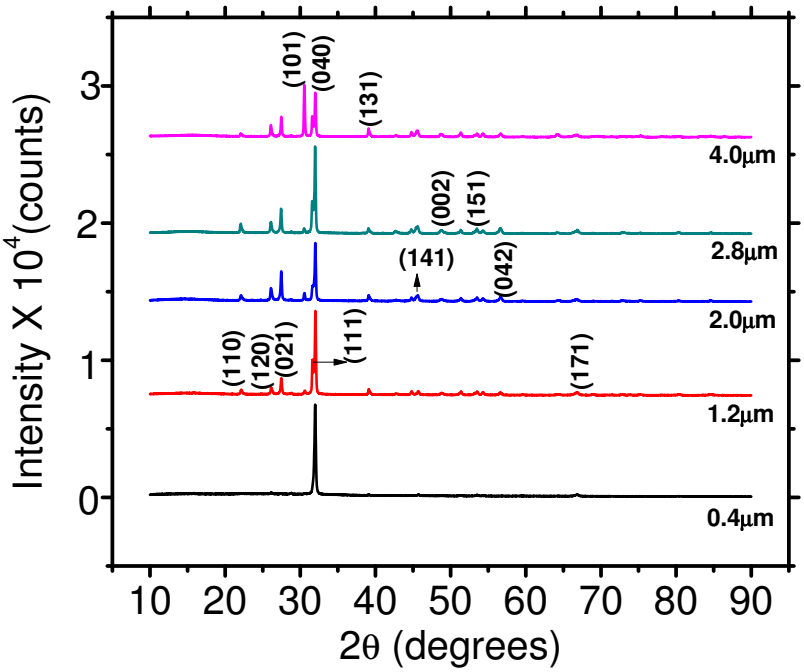

Figure 5.8: XRD Spectra of SnS Films with Different Film Thicknesses (μm) at Constant Source and Substrate Temperature of 300 °C and 350 °C with Deposition Time between (0.7–3 min).

as indicated in [1–5, 34, 35]. This behaviour has been commonly observed by other research groups according to the literature [6, 36–40]. It was also observed that the reflections (211), (111), (310) and (440) of the Sn_2S_3 phase (belonging to the Powder Diffraction File: 00-014-0619 [41]) do occur simultaneously with the reflections (111)/(040), (120), (101) and (211) of the SnS phase (belonging to the Powder Diffraction File: 00-039-0354 [23]). A typical XRD diffractogram that illustrates such a pattern is shown in Figure 5.9. This behaviour was attributed to the proximity of the d-spacing of these (hkl) reflections. Ghosh et al. [42], Ogah et al. [7] and Miles et al. [43] have also made similar observations. However in order to ascertain if the films contain other phases of SnS Raman measurements were used for further investigations.

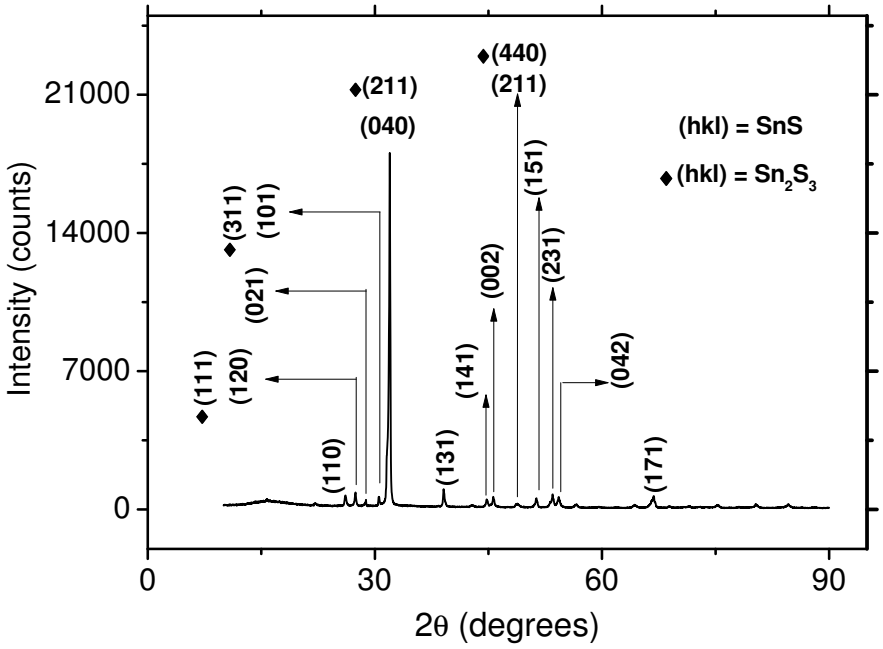

Figure 5.9: XRD Diffractogram of SnS Layer Deposited at Substrate Temperature of 350 °C, Source Temperature of 300 °C and Deposition Time of 3 min.

Figure (5.10)a–b gives the Raman spectra of SnS films deposited at different substrate temperatures and film thicknesses. Raman data for the layers are also given in Figure (5.10)a–b respectively. All the films showed a dominant peak at a wave number of 190.54 cm^{-1}, with the other peaks present at 219.63 cm^{-1}, 161.33 cm^{-1}, 95.63 cm^{-1}, 67.75 cm^{-1} for increasing substrate temperatures while for varying film thicknesses, the Raman peaks at a wave number of 95 cm^{-1}, 162 cm^{-1}, 187 cm^{-1} and 218 cm^{-1} were

observed. These peaks are in good agreement with the data reported for SnS by other authors independent of the deposition method as contained in [44–49], indicating that the layers are single phase SnS.

5.1.3.1 Crystallite Size (C), Grain Size and the Number of Crystallites (N_c)

Figure 5.11, Figure 5.12 and Figure 5.13 give the variation of the crystallite size with film thicknesses, substrate temperatures and the deposition times. Based on the information extracted from the XRD analysis, the crystallite size was deduced from the Debye-Scherrer's formula given as [50–52]:

$$C = \frac{k\lambda}{\beta \cos\theta} \tag{5.1}$$

where C is the crystallite size, k is a constant (0.94), λ is the wavelength of the X-ray (1.5406Å), β is the full width at half maximum of the most prominent peak and θ is the Bragg angle. The crystallite size was observed to increase with increase of film thickness, substrate temperature [1] and the deposition time [3].

Figure 5.14 gives the variation of grain size with substrate temperature. The grain sizes were measured directly using the FEI Quanta 200 Environmental Scanning Electron Microscope. Enlargement of grain size during film growth is very crucial, considering the relationship between grain size and solar cell efficiency as earlier highlighted in subsections 2.8.1 and 2.8.2 respectively. Grain size depends strongly on the deposition conditions. The presence of the grain boundaries reduces the important photovoltaic indicators such as short-circuit current density J_{SC}, open-circuit voltage V_{OC} and the fill factor through recombination effects [53]. As expected, the grain size increased with an increase of substrate temperature [4]. This was attributed to the higher surface mobility of the films at higher substrate temperature which allows the film to decrease its total energy by growing larger grains thereby decreasing the grain boundary area. Increase in grain size/crystallite size with deposition conditions has been widely observed by others in the literature for SnS films grown by same/different techniques [6, 12, 14, 17, 38, 39, 54–56].

Figure 5.15 and Figure 5.16 give the variation of the number of crystallites per unit area N_c with substrate temperatures and deposition times. The number of crystallites per unit

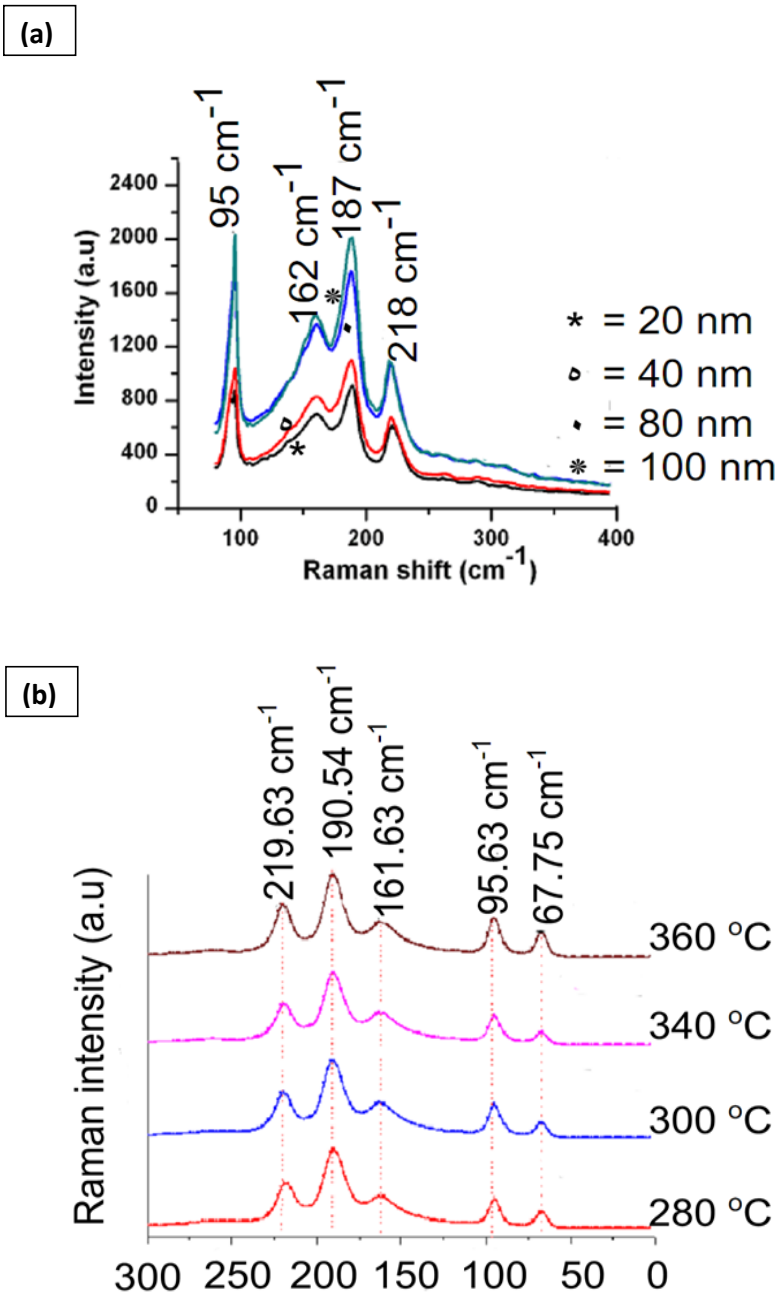

Figure 5.10: Raman Spectra of SnS Films Formed at; (a) Different Film Thicknesses at Constant Source and Substrate Temperature of 300 °C and 350 °C with Deposition Time between 10 sec to 1 min [33]. (b) Different Substrate Temperatures at Constant Source Temperature of 300 °C and Deposition Time of 3 min.

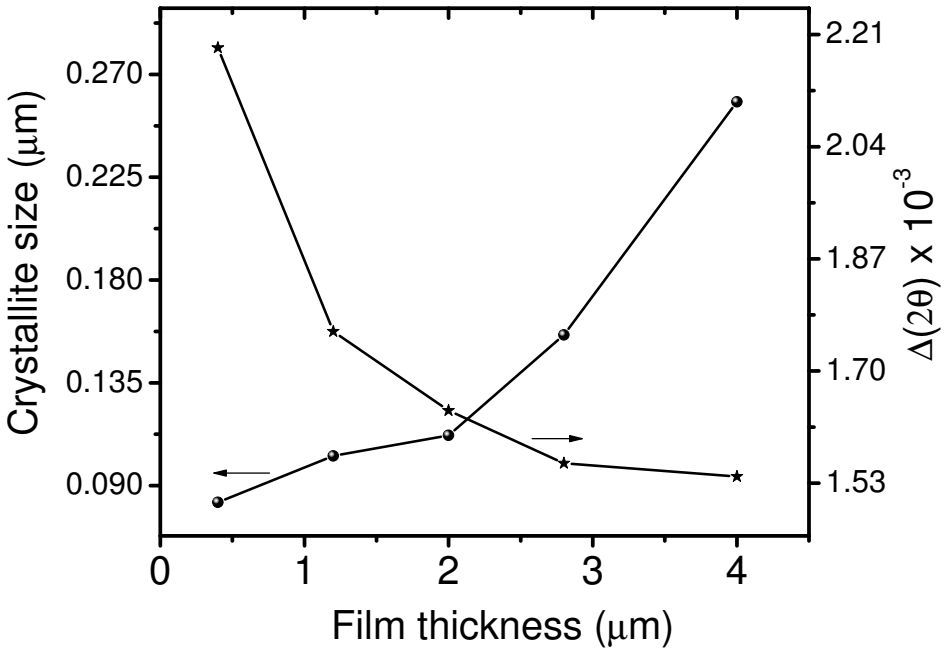

Figure 5.11: Variation of Crystallite Size and Angular Broadening with Film Thicknesses at Constant Source and Substrate Temperature of 300 °C and 350 °C with Deposition Time between (0.7–3 min).

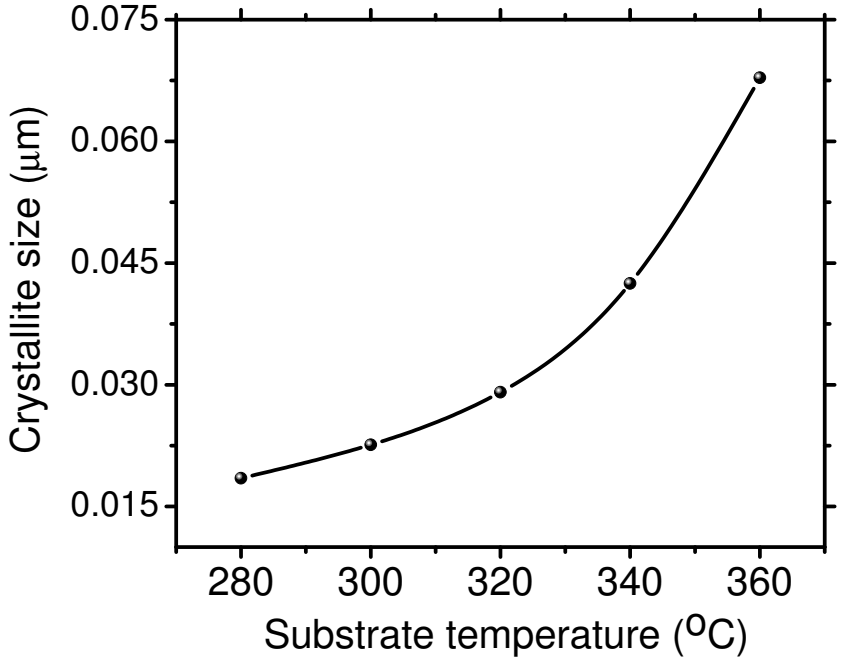

Figure 5.12: Variation of Crystallite Size with Substrate Temperatures at Constant Source Temperature of 300 °C and Deposition Time of 3 min [4].

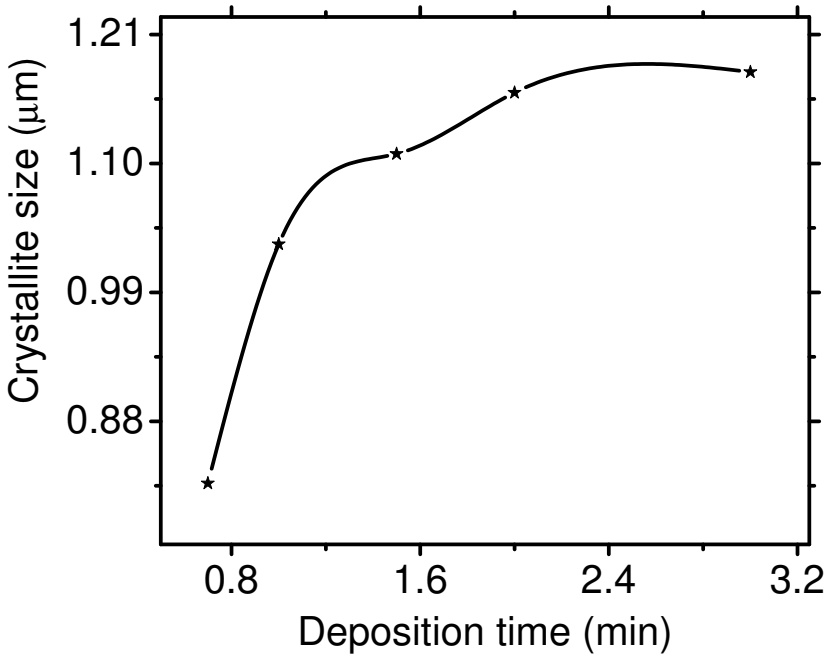

Figure 5.13: Change of Crystallite Size with Deposition Times at Constant Source and Substrate Temperature of 300 °C and 350 °C [3].

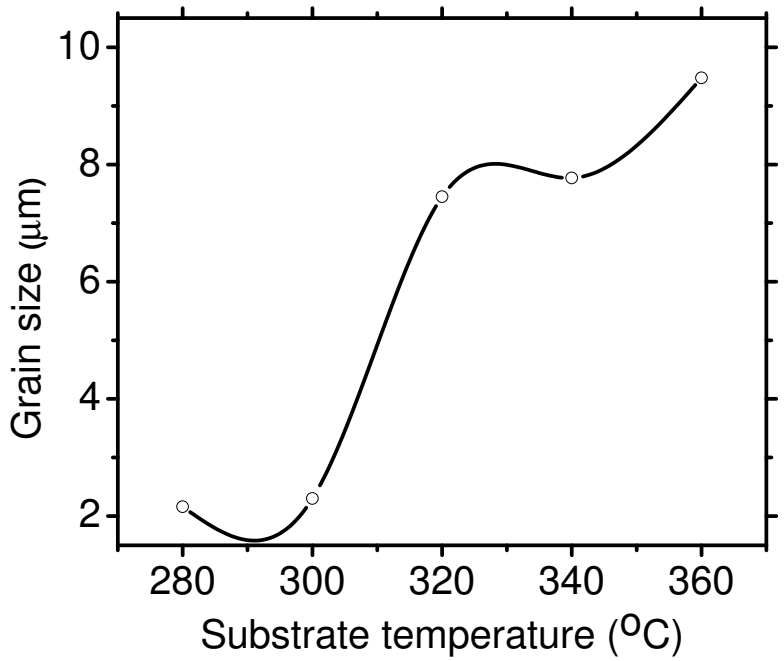

Figure 5.14: Variation of Grain Size with Substrate Temperatures at Constant Source Temperature of 300 °C and Deposition Time of 3 min [4].

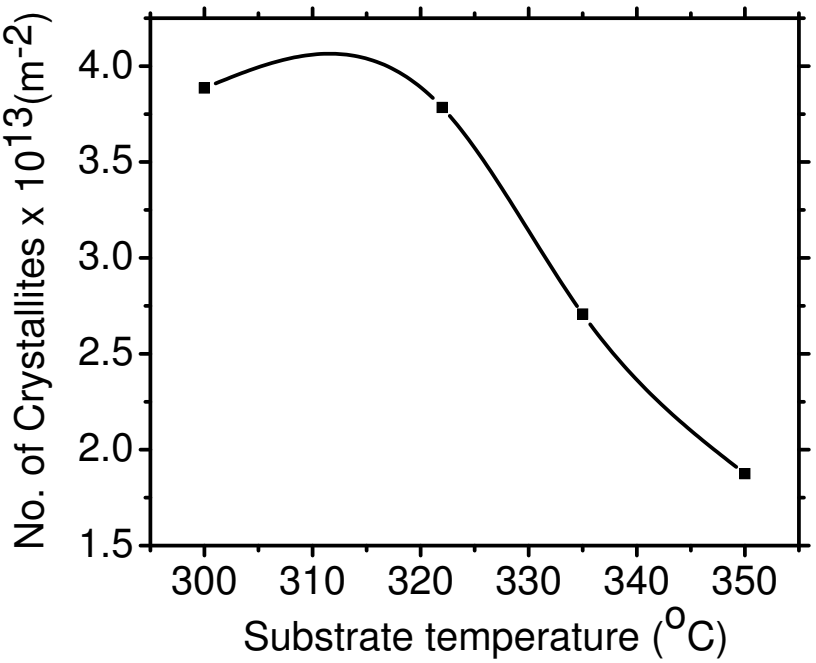

Figure 5.15: Variation of the Number of Crystallites with Substrate Temperatures at Constant Source Temperature of 300 °C and Deposition Time of 3 min [1].

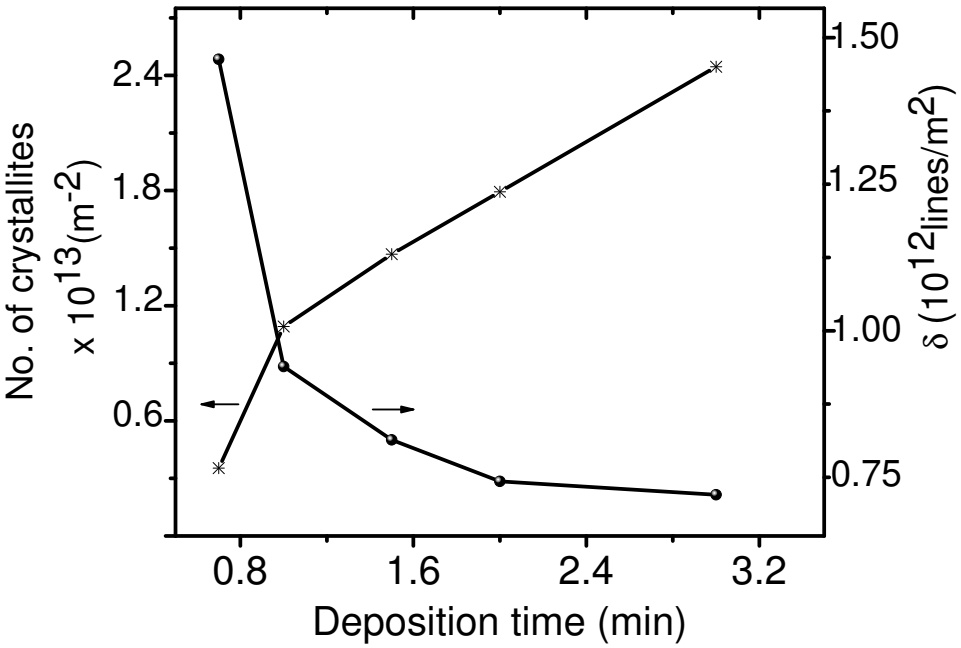

Figure 5.16: Change of δ (Dislocation Density) and Number of Crystallites with Deposition Times at Constant Source and Substrate Temperature of 300 °C and 350 °C [3].

area N_c was investigated at different deposition conditions using the relation [14, 57]:

$$N_c = \left[\frac{t}{C^3}\right]\left[unit\ \ area\right]^{-1} \tag{5.2}$$

where t is the film thickness and C retains its meaning. The results show that N_c varied with the change of deposition conditions as contained in [1, 3]. The result indicate a decrease of N_c with increasing substrate temperatures. This was attributed to an increase in the crystallinity of the layers. The variation of N_c with the deposition conditions is consistent with the reports of other authors [14, 58].

5.1.3.2 Texture Coefficient and Degree of Preferred Orientation

Figure 5.17 shows the variation of $T_{C(hkl)}$ with substrate temperatures while Figure 5.18 and Table 5.1–Table 5.6 give the variation of $T_{C(hkl)}$ with film thickness. According to Lotgering [59] and Moutinho et al. [60], in oriented polycrystalline material, the texture can be defined by a distribution function which gives the fraction of the material with crystals having some particular axes that make a certain angle with the direction of orientation. The texture coefficient $T_{C(hkl)}$, gives a measure of the orientation of each reflection (hkl values) in comparison to a completely randomly oriented sample (the Powder Diffraction File). A value of 1 represents a random orientation while a value above 1 implies the utmost case of non-random distribution of the crystallites (preferred orientation) in that direction *i.e.* an abundance of grains orientated in a given <hkl> direction. The $T_{C(hkl)}$ was calculated using the relation [60–64]:

$$T_{C(hkl)} = \left[\frac{I_{(hkl)}}{I_{0(hkl)}}\right]\left[\frac{1}{N}\Sigma_N \frac{I_{(hkl)}}{I_{0(hkl)}}\right]^{-1} \tag{5.3}$$

where $I_{(hkl)}$ is the measured intensity for the (hkl) plane, $I_{0(hkl)}$ is the standard intensity from the Powder Diffraction File for the corresponding powder, N is the number of reflections considered in the analysis. The films exhibited a high degree of uniformity and good crystallinity such that the $T_{C(hkl)}$ was > 1 in most cases as evidenced in [1, 2, 33, 35]. Figure 5.17 shows an increase of texture coefficient with substrate temperature and this was attributed to the increase of crystallinity in the films.

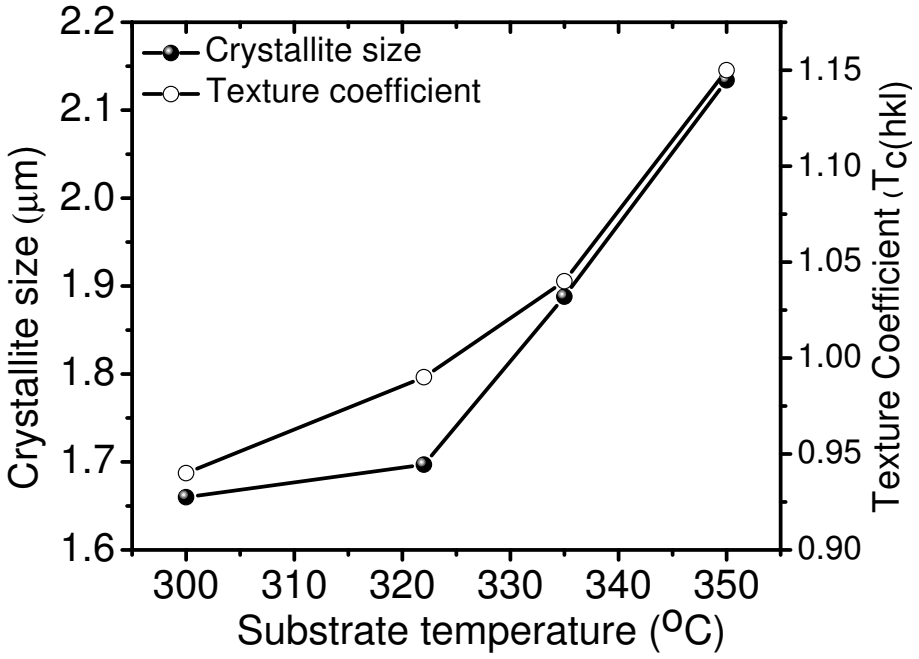

Figure 5.17: Variation of $T_{C(hkl)}$ with Substrate Temperatures at Constant Source Temperature of 300 °C and Deposition Time of 3 min [1].

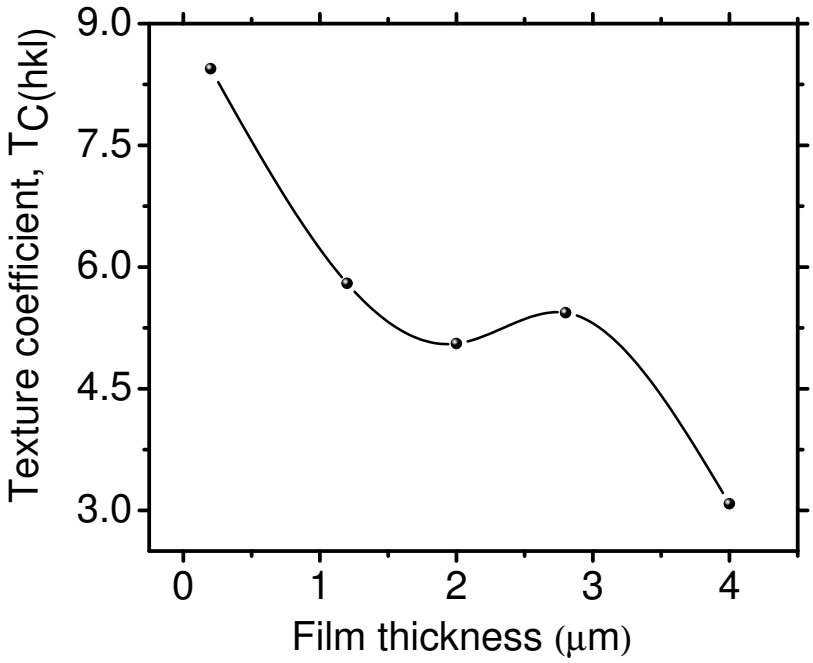

Figure 5.18: Change of $T_{C(hkl)}$ with Film Thicknesses at Constant Source and Substrate Temperature of 300 °C and 350 °C with Deposition Time between (0.7–3 min).

For film thicknesses $\leq 0.1\,\mu m$, the results show an increase of $T_{C(hkl)}$ with an increase of film thickness [33]. This is clearly evident from the XRD spectra shown on Figure 5.7 as only the (111) peaks are quite visible while the other reflections are very low indicating that the crystallites are predominantly orientated in the (111) plane. However, for film thicknesses $> 0.1\,\mu m$, a decrease of texture coefficient was observed with increasing film thicknesses with the highest value appearing for the layer, that exhibited the (040) as the most prominent peak, at the thickness of $0.4\,\mu m$. This is because at that thickness, other Bragg peaks as indicated in Table 5.1–Table 5.6 all showed $T_{C(hkl)} < 1$, indicating loss of preferred orientation in those (hkl) reflections. In general the texture coefficient for the (040) reflections were all $\gg 1$ for thicknesses $> 0.1\,\mu m$. The decrease in the $T_{C(hkl)}$ for the values of the (040) peak at the highest thickness was because there are other Bragg peaks that had values of $T_{C(hkl)} > 1$ as shown in Table 5.1. This is also evident from the XRD spectra shown on Figure 5.8 as the (101) reflection increased dramatically while the (040) peak decreased. This suggests that although more crystallites were oriented in the <040> direction, there was a more random distribution of crystallites to other (hkl) reflections at the higher thicknesses. These changes observed herein can be attributed to the change in the stoichiometry arising from the difference in vapour pressure of Sn and S respectively. To the best of my knowledge at the time of submission of this thesis, there is no detailed report on $T_{C(hkl)}$ for SnS thin films in the literature. However for other inorganic thin-film PV material, Zoppi et al. [65] reported on the variation of $T_{C(hkl)}$ with film thickness and annealing time for CdTe absorber layers grown using metal-organic chemical vapour deposition method. Moutinho et al. [60, 61] studied the impact of post deposition annealing and different deposition techniques on the $T_{C(hkl)}$ for CdTe polycrystalline thin films while Kim and Chun [63] reported on the effects of film thickness on the $T_{C(hkl)}$ for SnO_2 polycrystalline thin films.

Table 5.1–Table 5.6 also gives the variation of the degree of preferred orientation σ for different film thicknesses. The degree of preferred orientation (an utmost case of non-random distribution of crystallites in the layers) of the films were deduced by analysis from the standard deviation of the $T_{C(hkl)}$ by considering the same number of (hkl) reflections used to deduce the $T_{C(hkl)}$ i.e. by calculating the standard deviation of the $T_{C(hkl)}$ values of each diffracting crystal plane from the powder diffraction condition as a whole instead of

using the $T_{C(hkl)}$ of a particular (hkl) peak. The standard deviation was calculated using the relation [60, 63]:

$$\sigma = \left[\frac{1}{N}\Sigma(T_{C(hkl)} - 1)^2\right]^{0.5} \tag{5.4}$$

where N and $T_{C(hkl)}$ retain their usual meanings and σ is the standard deviation used to compare the degree of preferred orientation in the as-grown films. Equation 5.4 implies that σ is zero when $T_{C(hkl)}$ is 1; hence higher value of σ indicate less randomly oriented samples while a lower value of σ indicates more randomly oriented samples. From the viewpoint of Kim and Chun [63], preferred orientation in polycrystalline thin films is strongly influenced by the mode of the film growth depending on the deposition technique and hence noted such modes to include:

- an initial nucleation on the substrate and growth of nuclei arising from the surface diffusion of the impinging flux,
- an oriented overgrowth due to preferred nucleation on the growing crystal surface,
- a sticking of homogeneous nuclei from the gas phase on the growing surface and their growth.

It is pertinent to note that in the literature, some authors do interchange peak intensity ratio with preferred orientation [6, 21, 22, 29, 39, 66] while peak intensity ratio is clearly presented in some [5, 67]. For clarity, the steps taken to calculate the $T_{C(hkl)}$ and σ are:

- The intensity (counts) I, of the (hkl) peaks is recorded, say N (hkl) peaks where N is an integer > 3.
- The intensity (counts) I_{max}, of the most prominent (hkl) peak is recorded.
- $I_{(hkl)}$ is calculated using:

$$I_{(hkl)} = \frac{I}{I_{max}} \times \frac{100}{1} \tag{5.5}$$

- $I_{(hkl)}$ and $I_{0(hkl)}$ are substituted in Equation 5.3 to determine the $T_{C(hkl)}$.

- As a litmus test the sum of all $T_{C(hkl)}$ must equal N and the average of $T_{C(hkl)}$ must equal 1.
- $T_{C(hkl)}$ is substituted into Equation 5.4 to determine σ.
- Values of $\sigma > 0$ imply preferred orientation in the film and hence the greater the value of σ, the higher the degree of preferred orientation of the crystallites.

The variation of the texture coefficient and degree of preferred orientation for different film thicknesses given in Table 5.1–Table 5.6 indicate clearly that $T_{C(hkl)}$ and σ depend strongly on the number of (hkl) peaks used in the analysis. This is also a function of polycrystalline nature of the films. It also indicates that σ has a strong link with the number of peaks whose $T_{C(hkl)}$ values are > 1 i.e. films that showed less randomisation of the crystallites. The values obtained herein are in line with Figure 5.8 which indicate a high crystallinity of the films and a slight randomisation of crystallites for higher film thicknesses. As mentioned before, to the best of my knowledge, there is also no detailed report on the change of the degree of preferred orientation with film thickness for SnS thin films in the literature at the time of this thesis submission hence for other inorganic thin film materials, Kim and Chun [63] observed an increase of σ with film thickness for SnO_2 films grown by the chemical vapour deposition method. However Tanuševski and Poelmman [68] reported a preferred orientation of the (111) peaks induced by nucleation effects for SnS thin films prepared by electron beam evaporation while Mathews et al. [69] observed a decrease in the degree of preferred orientation caused by a recrystallisation effect in electro-deposited SnS films. For the most efficient polycrystalline thin film absorbers $Cu(In,Ga)Se_2$, Contreras et al. [70] has reported on the impact of preferred orientation on the optical and photovoltaic properties in such solar cell devices.

5.1.3.3 Strain and Dislocation Density

Strain in thin films mostly arises from:

(i) A mismatch of thermal expansion coefficients of the film and the substrate.

(ii) Crystal defects.

(iii) Stoichiometric deviation. This is a strong function of the deposition conditions.

Thickness (μm)	(hkl) reflections (110)	(120)	(021)	(101)	(111)	(040)
0.4	0.369	0.331	0.270	0.252	0.258	8.456
1.2	0.459	0.527	0.864	0.238	1.321	5.799
2.0	0.633	1.130	0.193	0.559	0.654	5.057
2.8	0.686	0.656	1.110	0.253	0.972	5.437
4.0	0.320	0.774	1.005	2.845	0.752	3.082

Table 5.1: Variation of Texture Coefficient $T_{C(hkl)}$, and Degree of Preferred Orientation σ, at Different Film Thicknesses for N = 12 (contd.),

Thickness (μm)	(hkl) reflections (131)	(141)	(002)	(151)	(042)	(171)	σ
0.4	0.256	0.277	0.281	0.278	0.185	0.787	2.25
1.2	0.447	0.456	0.334	0.431	0.317	0.807	1.48
2.0	0.618	0.587	0.565	0.496	0.594	0.914	1.24
2.8	0.375	0.413	0.462	0.379	0.502	0.755	1.36
4.0	0.650	0.573	0.433	0.512	0.368	0.686	0.90

Table 5.2: Variation of Texture Coefficient $T_{C(hkl)}$, and Degree of Preferred Orientation σ, at Different Film Thicknesses for N = 12.

Thickness (μm)	(hkl) reflections (110)	(120)	(021)	(101)	(111)	(040)	(131)	(141)	(002)	σ
0.4	0.308	0.277	0.226	0.211	0.216	7.077	0.215	0.234	0.236	2.15
1.2	0.395	0.454	0.744	0.205	1.138	4.997	0.386	0.393	0.288	1.44
2.0	0.570	1.016	0.174	0.503	0.588	4.553	0.558	0.529	0.509	1.27
2.8	0.596	0.570	0.964	0.220	0.844	4.720	0.326	0.359	0.401	1.34
4.0	0.276	0.668	0.867	2.454	0.648	2.658	0.561	0.494	0.374	0.85

Table 5.3: Variation of Texture Coefficient $T_{C(hkl)}$, and Degree of Preferred Orientation σ, at Different Film Thicknesses with N = 9.

Thickness (μm)	(hkl) reflections							σ
	(120)	(021)	(101)	(111)	(040)	(131)	(141)	
0.4	0.230	0.187	0.175	0.179	5.858	0.178	0.193	1.98
1.2	0.383	0.626	0.172	0.958	4.205	0.325	0.331	1.33
2.0	0.899	0.153	0.445	0.520	4.023	0.493	0.467	1.25
2.8	0.498	0.843	0.192	0.738	4.130	0.285	0.314	1.30
4.0	0.560	0.727	2.057	0.544	2.228	0.470	0.414	0.73

Table 5.4: Variation of Texture Coefficient $T_{C(hkl)}$, and Degree of Preferred Orientation σ, at Different Film Thicknesses with N = 7.

Thickness (μm)	(hkl) reflections					σ
	(021)	(101)	(111)	(040)	(131)	
0.4	0.142	0.133	0.136	4.454	0.135	1.73
1.2	0.498	0.137	0.762	3.345	0.258	1.19
2.0	0.136	0.395	0.462	3.571	0.436	1.29
2.8	0.681	0.155	0.597	3.337	0.230	1.19
4.0	0.603	1.707	0.451	1.849	0.390	0.64

Table 5.5: Variation of Texture Coefficient $T_{C(hkl)}$, and Degree of Preferred Orientation σ, at Different Film Thicknesses with N = 5.

Thickness (μm)	(hkl) reflections			σ
	(101)	(111)	(040)	
0.4	0.084	0.086	2.830	1.29
1.2	0.097	0.539	2.364	0.98
2.0	0.268	0.312	2.420	1.00
2.8	0.114	0.437	2.449	1.03
4.0	1.278	0.338	1.384	0.47

Table 5.6: Variation of Texture Coefficient $T_{C(hkl)}$, and Degree of Preferred Orientation σ, at Different Film Thicknesses with N = 3.

(iv) Any combination or all of the above effects.

Figure 5.19 shows the change of strain with substrate temperature. Strain could affect the film growth or the optoelectronic properties of the grown layers because of the distortion of the lattice [71]. Strain can be compressional (negative values) or tensile (positive values). The strain ε was calculated using the relation [50]:

$$\varepsilon = \frac{\Delta\theta}{2(\tan\theta)} \tag{5.6}$$

where θ is the diffraction angle and $\Delta\theta$ is the shift in the X-ray peaks. The strain was observed to decrease with an increase of substrate temperature [5]. This was attributed to the increase of crystallite size with substrate temperature which led to a reduction in the inter-crystalline barriers or grain boundary area in the layers. Other authors [25, 27, 72–74] have reported on the decrease of strain with same/other deposition conditions for SnS films grown with similar/different deposition techniques.

Figure 5.20, Figure 5.21 and Figure 5.16 give the variation of the dislocation density δ with substrate temperature, film thickness and deposition time. Dislocation density δ can be defined as the length of dislocation lines per unit volume of the crystal and gives a

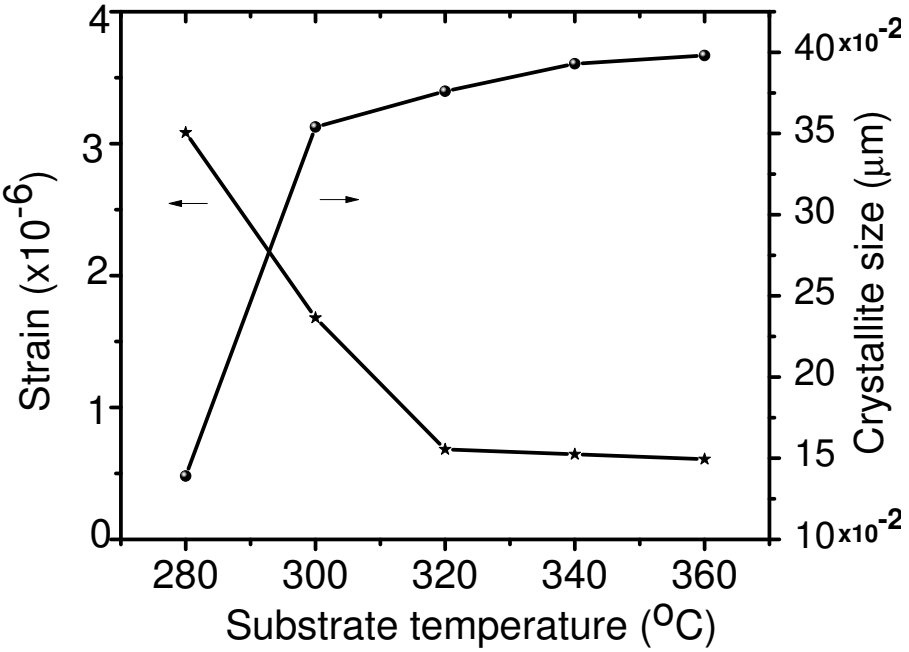

Figure 5.19: Variation of ε with Substrate Temperatures at Constant Source Temperature (300 °C) and Deposition Time (3 min) [5].

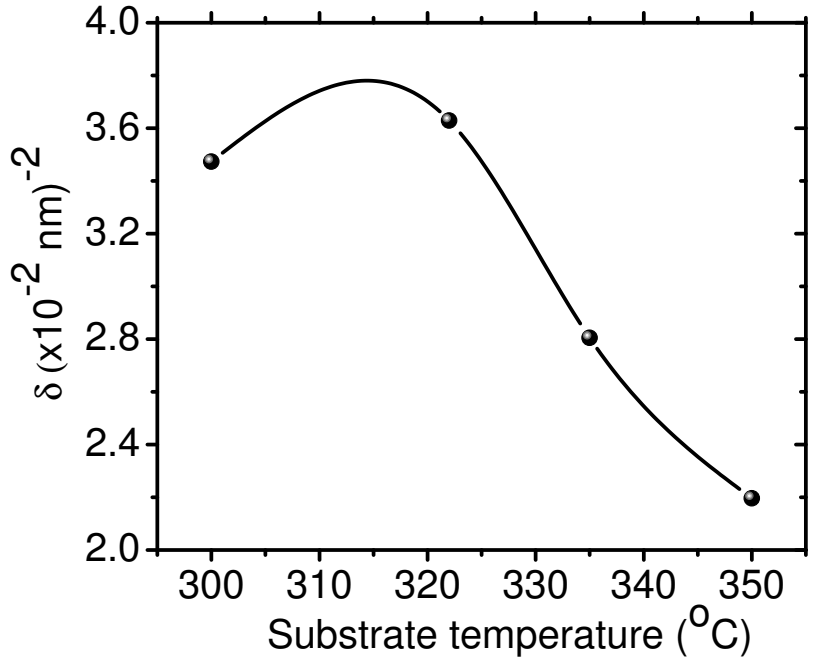

Figure 5.20: Change of δ with Substrate Temperatures at Constant Source Temperature (300 °C) and Deposition Time (3 min) [1].

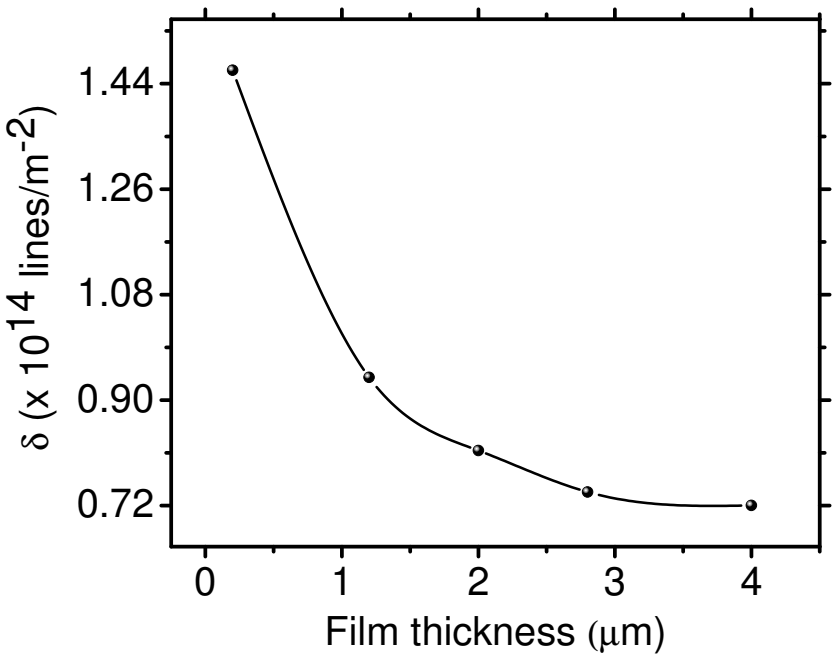

Figure 5.21: Variation of δ with Film Thicknesses at Constant Source and Substrate Temperature of 300 °C and 350 °C with Deposition Time between (0.7–3 min).

measure of the degree of defects in the film. The crystallite size was used to estimate the value of δ using the standard formula given as [75]:

$$\delta = \frac{n}{D^2} \tag{5.7}$$

where n = 1 implies a case of minimum dislocation density, and D is the crystallite size. For cubic and hexagonal crystal structure [76, 77], δ is given as:

$$\delta = \frac{15\varepsilon}{aD} \tag{5.8}$$

where a is the lattice parameter, D and ε retains their meanings. Results obtained indicated that δ varied with the deposition conditions, decreasing with increase of substrate temperature, film thickness and deposition time. This decrease was attributed to the increase in crystallinty of the layers. Similar findings due to change of deposition conditions or other associated effects have been reported by other research groups in SnS in the literature [25, 58, 73].

Figure 5.11 shows the effect of angular broadening on the as-grown films. It is generally understood that broadening of diffracted peaks are usually caused by lattice microstrain and smaller crystallite size. The angular broadening of the diffraction pattern was calculated using the relation given in [50]:

$$\Delta(2\theta) = \frac{\lambda}{\mathrm{C}\,\cos\theta} \tag{5.9}$$

where C, λ and θ retains their meanings. It is observed that the angular broadening decreased with an increase of film thickness. This is clearly due to the increase of the crystallite size as shown in Figure 5.11. From the discussion so far, it can be inferred that an increase of crystallite size or grain size leads to a corresponding decrease of the strain, dislocation density and angular broadening in the films.

5.1.4 Optical Properties

Results of the optical measurements indicated that the transmittance and reflectance of the films varied with the deposition conditions. The variation of the optical transmittance

with film thickness and substrate temperature are shown in Figure 5.22 and Figure 5.23. The cut-off wavelength was found to decrease with an increase of film thickness and was attributed to the progressive increase of the grain size at the higher film thicknesses. The transmittance were very high for lower film thicknesses and tended to reduce for higher film thicknesses. This behaviour has been explained on the basis that for the thicker films, the corresponding larger grain size leaves behind a large unfilled intergranullar volume thereby reducing the absorption per unit thickness [78]. For wide range of substrate temperatures and film thicknesses, the transmittance spectra exhibited interference fringes which is an indication of good surface homogeneity and uniformity of the grown films. Cifuentes et al. [79] also observed a blue shift with wavelength for decreasing film thickness and explained it on the basis of the band structure and the degree of superposition of electron clouds of neighbouring atoms. The optical absorption coefficient α was deduced from the transmittance and reflectance data using the relations [80, 81]:

$$\alpha = \frac{-1}{\mathrm{d}} \ln\left[\frac{\mathrm{T}}{(1-R)^2}\right] \tag{5.10}$$

or

$$\alpha = \left[\mathrm{d}\right]^{-1} \ln\left[\frac{100}{\mathrm{T}\%}\right] \tag{5.11}$$

where d is the film thickness, R and T are reflectance and transmittance respectively. The optical absorption coefficient α was $> 10^5 \mathrm{cm}^{-1}$ while the energy bandgap deduced using Equation (2.3) was found to be direct and varied between 2.0 eV to 1.30 eV with the higher values obtained for film thicknesses $< 0.5\,\mu\mathrm{m}$. The widening of the energy bandgap for film thicknesses $< 200\,\mathrm{nm}$ was due to a "quantum size effect" [14, 27, 47, 82, 83]. The thinner layers grown with thickness $< 0.5\,\mu\mathrm{m}$ in some cases exhibited different behaviour in that they were found to contain small amounts of carbon and oxygen, and secondary phases of binary compounds e.g. SnS_2 and Sn_2S_3 and to have a higher energy bandgap than single phase SnS [2]. The variation of energy bandgap in SnS thin films induced by similar or other associated effects are commonly observed irrespective of the deposition technique employed. Calixto-Rodriguez et al. [84] observed a similar effect for

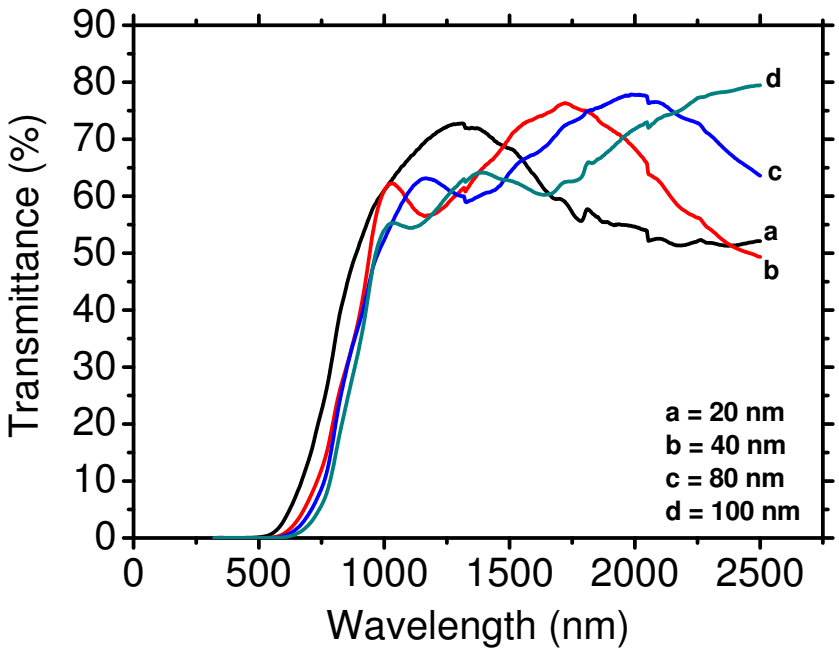

Figure 5.22: Transmittance as a Function of Wavelength at Different Film Thicknesses at Constant Source and Substrate Temperature of 300 °C and 350 °C with Deposition Time between 10 sec to 1 min [33].

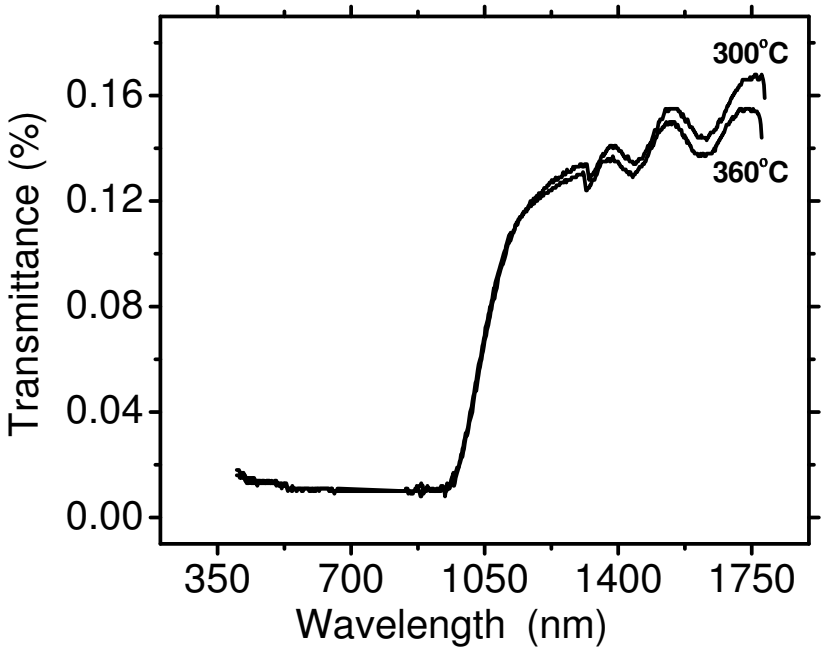

Figure 5.23: Transmittance as a Function of Wavelength for Different Substrate Temperatures at Constant Source Temperature (300 °C) and Deposition Time (3 min) [5].

increasing substrate temperatures in SnS films grown by spray pyrolysis and attributed it to the change of phase from a mixture of SnS to SnS_2. Sajeesh et al. [85] observed bandgap dependence on composition while Reddy and Reddy [86] noted that the variation in the energy bandgap was caused by the presence of SnS_2 and Sn_2S_3 and possibly Sn-O-S induced by changes in the chemical stoichiometry of the layers (for SnS films grown by spray pyrolysis). Significant findings on the variation of the optical properties with the deposition conditions are reported in [3, 5, 87]. The decrease of the transmittance at higher film thickness or other associated effects have been observed by other authors independent of the deposition method as summarised in Table 3.4 – Table 3.5.

5.1.5 Electrical Properties

Figure 5.24 gives the variation of the resistivity with film thickness. The results of the electrical properties (electrical resistivity and conductivity type) showed that the bulk resistivity varied with the deposition conditions. The bulk resistivity varied between 3 Ω cm to 40 Ω cm for film thicknesses ≤ 3 µm and also changed from 210 Ω cm to 98.5 Ω cm between 20 nm to 100 nm [33], decreasing with increase in thickness for both ranges. This

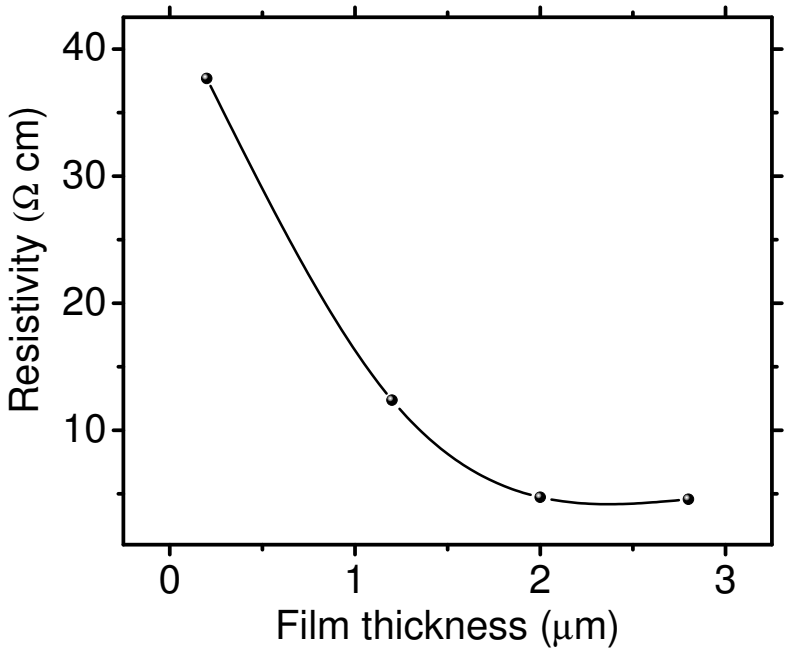

Figure 5.24: Dependence of Electrical Resistivity on Film Thickness at Constant Source and Substrate Temperature of 300 °C and 350 °C with Deposition Time between (0.7–3 min).

was attributed to an improvement in the crystallinty of the layers. The layers all exhibited p-conductivity type and this has been generally accepted to be due to the presence of Sn-vacancies. The observed reduction in resistivity as indicated in Figure 5.24 could be due to the increase of crystallite size with increasing film thickness as evidenced in Figure 5.11. An increase in crystallite size could lead to a substantial decrease in the intercrystalline barrier size to consequently reduce the resistance posed by the barriers to the charge carriers, leading to the observed effect. This trend is commonly observed in SnS thin films for different deposition parameters and/or post-deposition heat treatments, irrespective of the deposition method [20, 38].

5.1.6 Optimisation (Post-deposition Heat Treatments)

Optimisation of the conditions used for the depositions as indicated earlier, showed that the best layers were formed at a substrate temperature of 350 °C, source temperature of 300 °C and a deposition time of 3 min. Further optimisation of the layers were done through a post-deposition annealing as discussed in subsection 4.3.2. The effects of the treatments on the layers are discussed.

5.1.6.1 Effects of Annealing on the Morphological, Compositional and Structural Properties

Figure 5.25 and Figure 5.26 contains typical SEM micrographs of annealed SnS layers. For film thicknesses < 1 µm, the SEM micrograph shows that the layers consisted of randomly orientated elongated grains, each of which was several microns long and less than 0.5 µm wide as shown on Figure 5.25. A substantial increase of the grain size was recorded after annealing in air or a sulphur environment. As shown on Figure 5.26, the morphology looks approximately similar, but the layers annealed in sulphur had higher grain size 5 µm than the as-deposited films. SEM micrographs of SnS films grown with a deposition time of 1.5 min and then annealed in the respective ambients revealed that annealing in elemental sulphur and in the 5% H_2S in argon mixture resulted in uniform, densely packed grains with a grain size of up to 10 µm obtained for the H_2S/argon ambient [35]. For air annealing, after the $SnCl_4$/methanol treatment, sharper more faceted grains are observed [35].

Figure 5.27(a)–(c) show the EDS profiles of annealed SnS films. For layers grown with

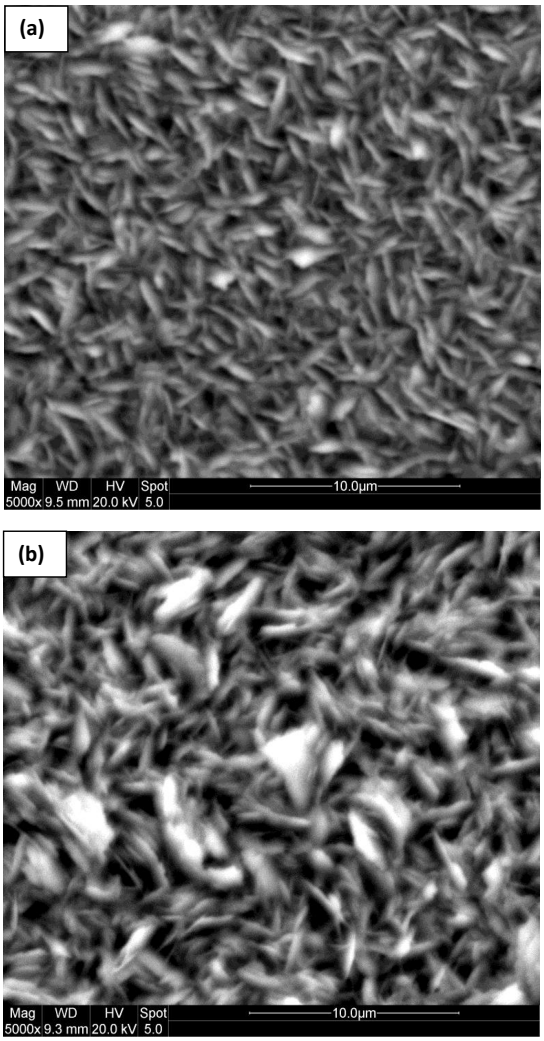

Figure 5.25: (a) SEM Micrograph of SnS Layer Deposited at Substrate Temperature of 350 °C, Source Temperature of 300 °C and Deposition Time at 1 min (b) the Layer Annealed in Air at 300 °C for 30 min [2].

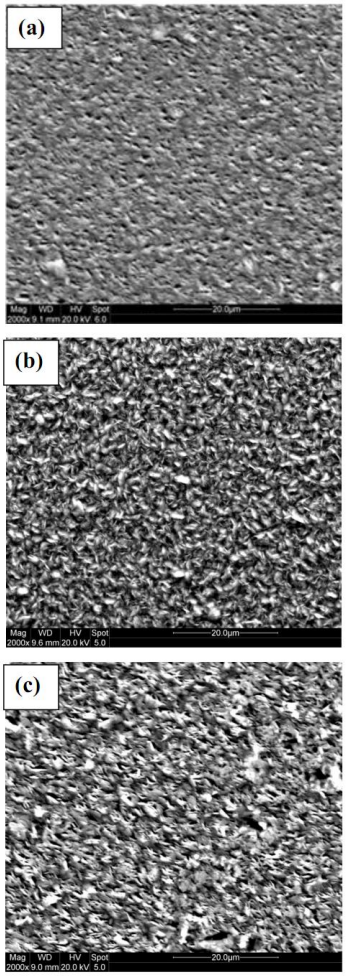

Figure 5.26: SEM Pictures of; (a) SnS Layer Deposited at Substrate Temperature of 350 °C, Source Temperature of 300 °C and Deposition Time at 1.5 min (b) the Layer Annealed in Air at 300 °C for 30 min (c) the Layer Annealed in Sulphur at 300 °C for 30 min [34].

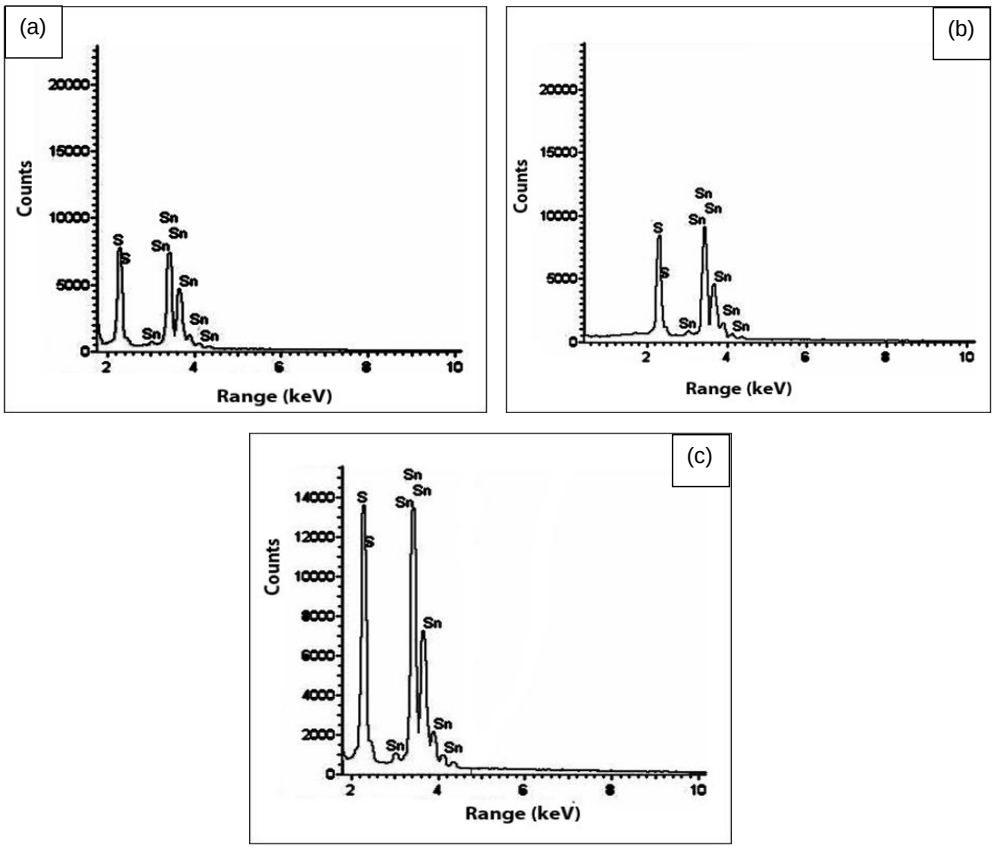

Figure 5.27: EDS Spectrum of SnS Layer Deposited at Substrate Temperature of 350 °C, Source Temperature of 300 °C and Film Thickness of 2 µm (b) the Layer Annealed in Air at 400 °C for 30 min (c) the Layer Annealed in Sulphur at 400 °C for 30 min [2].

thicknesses $> 2\,\mu m$, the EDS compositional analysis data indicated that the as–grown layers were slightly sulphur–deficient. For annealing in air and sulphur environments, post deposition annealing in air led to a further increase in sulphur deficiency where-as annealing in a sulphur environment acted to restore the chemical stoichiometry of the layers, tending to move the ratio of Sn:S toward unity.

Figure 5.28(a)–(c) give the SIMS profiles of as-grown, air and sulphur annealed layers which indicate uniform doping in all the layers. The air annealed layer exhibits sulphur loss with some sodium and oxygen impurities present in the layers. The presence of sodium and oxygen was less significant in the sulphur annealed layer.

The effects of the post deposition heat treatments on the XRD spectra are given in Figure 5.29. For layers $< 1\,\mu m$, it was observed that annealing the samples in air or in an environment containing excess sulphur brought about a reduction in the intensity of these reflections. Using an annealing temperature of $300\,^{\circ}C$ for 30 min for layers $< 1\,\mu m$, it was observed that sulphur annealing also lowered the intensity of the most prominent reflection (111/040) relative to the air annealed layers. This was attributed to a loss of preferred orientation during the sulphur annealing to produce more randomly orientated crystallites [34]. This is also evident from the XRD spectra (Figure 5.30) where an increase in intensity of the other orientations, e.g., (120) and (021) peaks, were observed after the heat treatments. A similar behaviour of a reduction in the intensity of the most prominent peak/s compared to the as-grown layers after annealing has been observed in the literature [37]. However, annealing in a sulphur environment for annealing time longer than 30 min introduced other phases of SnS e.g. SnS_2 was observed and was indexed with the Powder Diffraction File: 01-083-1706 [88]. The figure associated to this change is shown in Figure 5.31. For all the annealed samples, the full width half maximum (FWHM) of each peak was found to be decreased, corresponding to an improvement of the crystallinity of the layers. Also for the H_2S/argon annealed samples, additional peaks corresponding to Sn_2S_3 were observed and indexed with the Powder Diffraction File: 00-014-0619 [41]. This is also shown in Figure 5.32. The Sn_2S_3 phase is orthorhombic with lattice parameters a = 8.86400, b = 14.02000 and c = 3.74700. The intensity of the most prominent reflection (111)/(040) was also slightly reduced in the H_2S/argon environment. Annealing in air after a dip in $SnCl_4$/methanol solution resulted in the most dramatic change in the diffraction

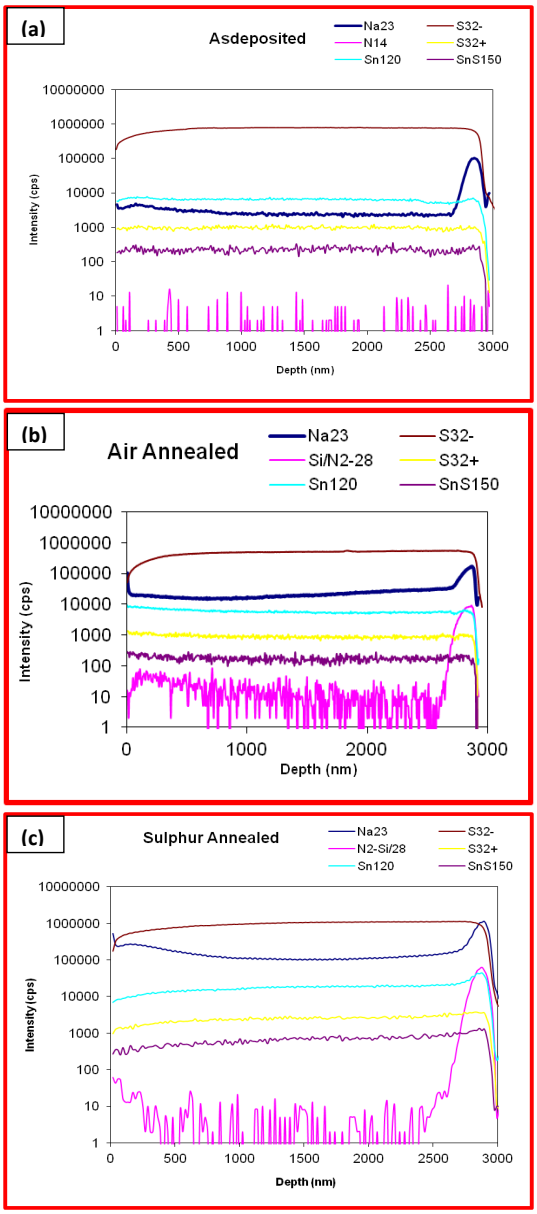

Figure 5.28: (a) SIMS Profiles of SnS Layer Deposited at Substrate Temperature of 350 °C, Source Temperature of 300 °C and Film Thickness of 2 µm (b) the Layer Annealed in Air at 400 °C for 30 min (c) the Layer Annealed in Sulphur at 400 °C for 30 min.

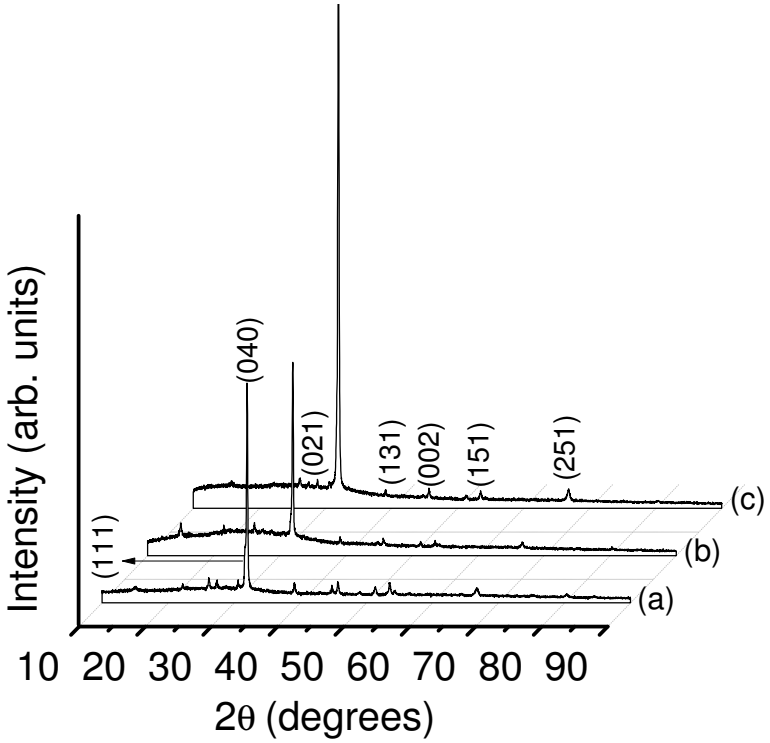

Figure 5.29: XRD Spectra for SnS Films: (a) the Layer Annealed in Air at 400 °C for 30 min (b) the Layer Annealed in Sulphur at 400 °C for 30 min (c) As-deposited Layer at Substrate Temperature of 350 °C, Source Temperature of 300 °C and Deposition Time at 1 min [2].

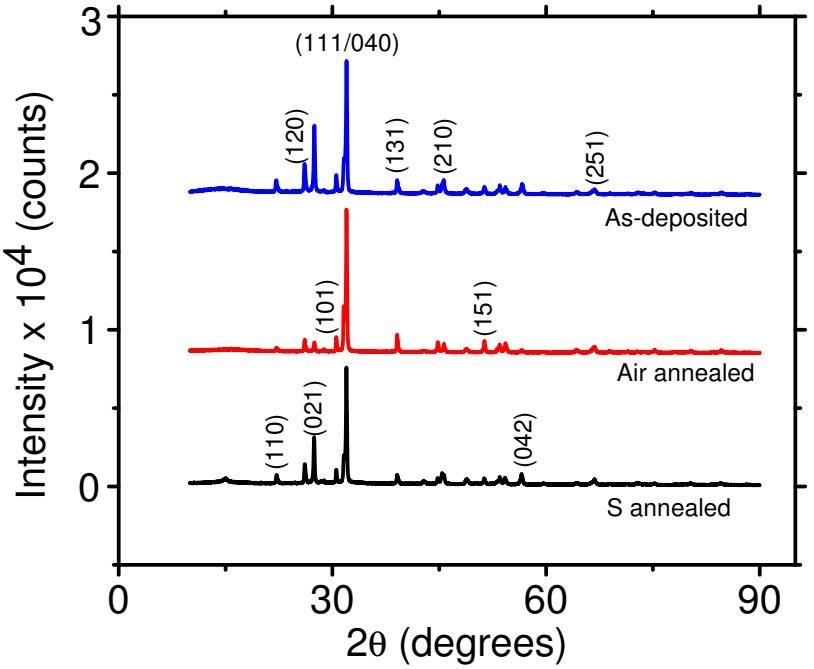

Figure 5.30: XRD Spectrum for SnS Layer Deposited at Substrate Temperature of 350 °C, Source Temperature of 300 °C and Deposition Time at 1.5 min, the Layer Annealed in Air at 300 °C for 30 min, and the Layer Annealed in Sulphur at 300 °C for 30 min [34].

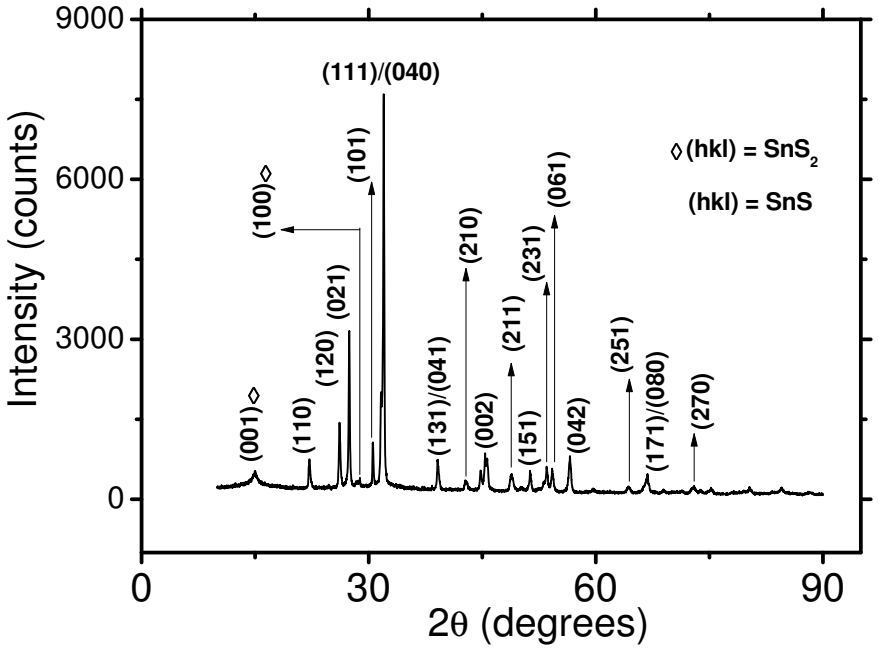

Figure 5.31: XRD Spectrum of a Sulphur Annealed Layer Using Annealing Temperature and Time of 300 °C and 60 min.

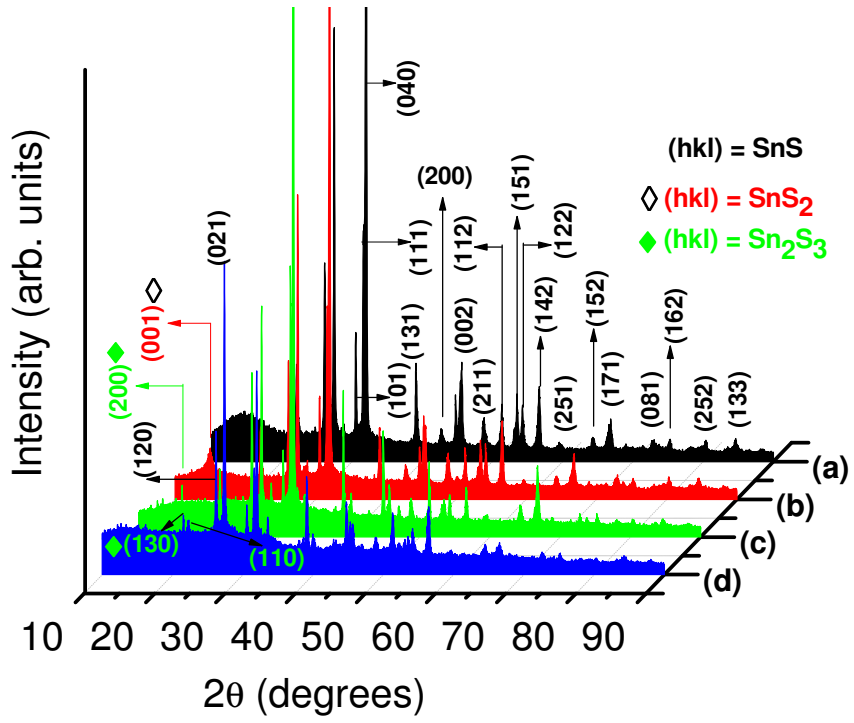

Figure 5.32: Variation of XRD Spectra in Different Ambients: (a) As-deposited Layer (b) the Layer Annealed in Elemental Sulphur (c) Annealed in a 5% H_2S in Argon Mixture (d) Annealed in Air After $SnCl_4$/methanol Treatments.

pattern in that the height of the (040) peak reduced drastically while that of the (021) peak increased markedly as shown in Figure 5.32. This could be due to changes in the stoichiometry of the Sn and S in the layers.

Figure (5.33) and Figure (5.34) give the changes induced by annealing time on the crystallite size and the texture coefficient $T_{C(hkl)}$ for the layers annealed in the H_2S/argon environments. Information gleaned from the XRD data was used to evaluate the effects of annealing on the crystallite size and the texture coefficient. The crystallite size and texture coefficient as functions of annealing time were calculated using the previously defined relations (Equation (5.1) and Equation (5.3)). It was observed that the crystallite size increased with an increase of annealing time, indicating an improvement in the crystallinity of the layers due to annealing. An increase in the crystallite or grain size induced by a post deposition heat treatments of as-grown SnS layers has been reported by other research groups [20, 21, 89, 90]. The texture coefficients calculated for the samples annealed in the different environments, calculated along three different orientations were observed to increase marginally for annealing in sulphur environments with a significant increase for those layers annealed in H_2S/argon. However, there was a drastic reduction in the $T_{C(hkl)}$ value for the samples dipped into $SnCl_4$/methanol and then annealed in air. The observed

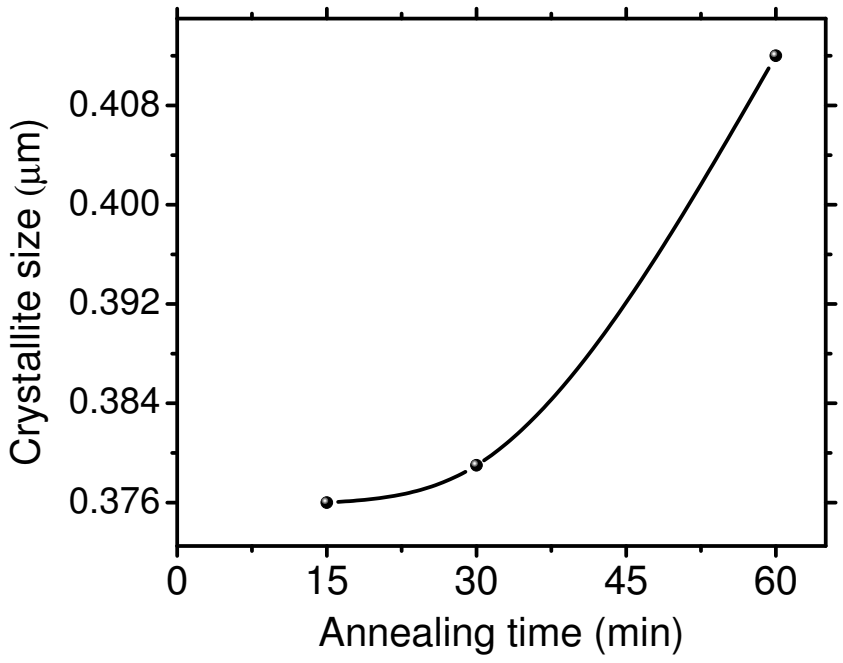

Figure 5.33: Crystallite Size Versus Annealing Time.

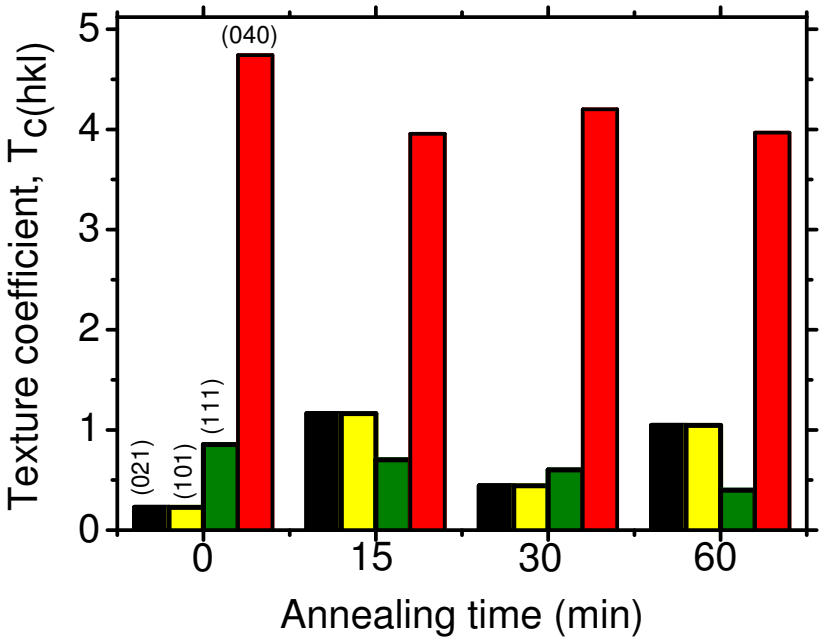

Figure 5.34: Variation of Texture Coefficient with Annealing Time.

decrease of $T_{C(hkl)}$ can be attributed to the change of orientation as observed from the XRD spectra. Despite the observed reduction, the texture coefficient values are quite high implying that the layers are improved by the heat treatments. The changes induced by the post deposition treatments on the texture coefficients in the respective media are shown in Figure 5.35. Such a change in structural parameters induced by annealing effect on SnS thin films has been reported in the literature [6, 20].

Figure (5.36) shows the effect of annealing time on the strain ε for SnS layers annealed in the H_2S/argon environments. Strain can be deduced by indirect measurements of the change in the lattice parameters which can cause a corresponding change in the position of the diffraction peaks in the annealed layers. The strain developed in the annealed films was deduced using the relative d-spacing variation defined by the relation [50, 91]:

$$\varepsilon = \frac{d_{exp} - d_o}{d_o} \tag{5.12}$$

where d_{exp} is the calculated d-values while d_o was extracted from the XRD profiles and ε retains its meaning.

The results revealed that the residual strain changed from tensile for lower annealing time to compressive for longer annealing time. This clearly suggests that annealing in

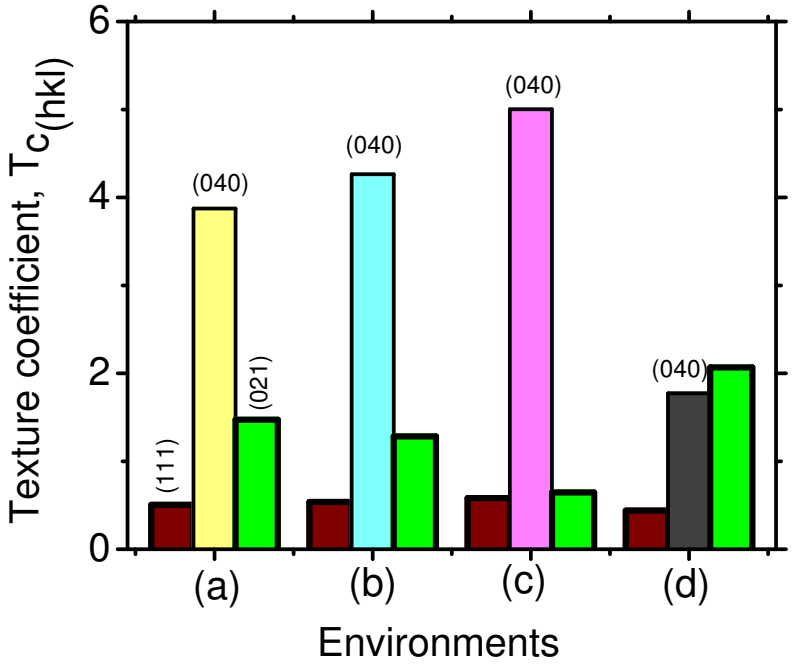

Figure 5.35: Texture Coefficient Versus Environments: (a) As-deposited Layer (b) the Layer Annealed in Elemental Sulphur (c) Annealed in a 5% H_2S in Argon Mixture (d) Annealed in Air After $SnCl_4$/methanol Treatments [35].

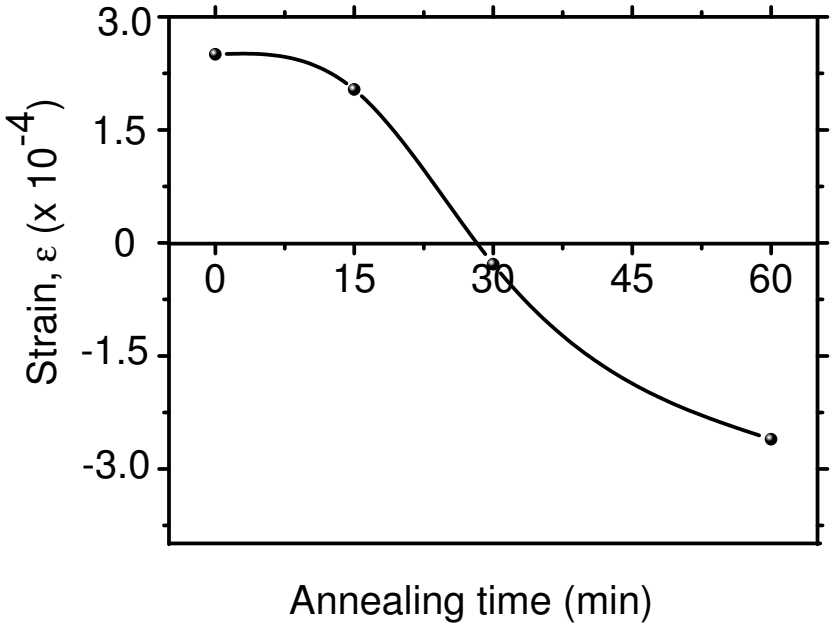

Figure 5.36: Strain Versus Annealing Time.

H_2S/argon environments led to further improvement in crystallinity of the layers. Reddy et al. [90] reported on the influence of chemical treatment with selected organic solvents on the surface morphology, surface topology and other physical properties of SnS thin films and observed a decrease in the strain for SnS layers treated in chloroform.

5.1.6.2 Effects of Annealing on the Optical and Electrical Properties

The optical transmittance versus wavelength spectra of as-grown and annealed SnS layers, that indicated the significance of post deposition annealing in air and sulphur ambient, are shown on Figure (5.37). The transmittance spectra give a clear interference pattern indicating a uniform thickness and good surface homogeneity induced by the annealing process. The appearance of the interference fringes indicates a significant improvement on the uniformity and crystallinity of the grown films making it possible to deduce the important optical constants such as the refractive index and extinction coefficient from the spectra.

Figure (5.38) shows the changes arising from the effect of the post deposition heat treatments on the optical absorption coefficient and energy bandgap. The effect of heat treatments on the layers showed that the optical constants; optical absorption coefficient and energy bandgap are relatively independent of annealing environment probably due to the short duration of the annealing and the high crystallinity of the layers in as-deposited form [2, 35]. Tanuševski [81] also reported on the independence of the optical constant on the thermal treatment for SnS films grown by electron beam evaporation method. For longer annealing times, there was a shift in the cut-off wavelength toward the infra-red region as shown in Figure (5.38). Plots of $(\alpha h\nu)^2$ versus hν given in Figure (5.38) are straight lines indicating that the transition is direct and the intercept on the hν axis gives a value of energy bandgap that varied in the range 1.3 eV to 1.4 eV, with the as-deposited layers showing a higher energy bandgap. This was attributed to a deviation of Sn/S ratio from the stoichiometric value because of the difference in vapour pressure of Sn and S. A shift in the energy band gap towards lower values after annealing has been reported in the literature [42]. Figure (5.38), exhibits "Urbach tails " for energies $< E_g$ rather than showing $(\alpha h\nu)^2 = 0$ for energies $< E_g$. Such behaviour is commonly observed in polycrystalline thin films due to the effect of "bandgap tailing". This could lead to an extension of the

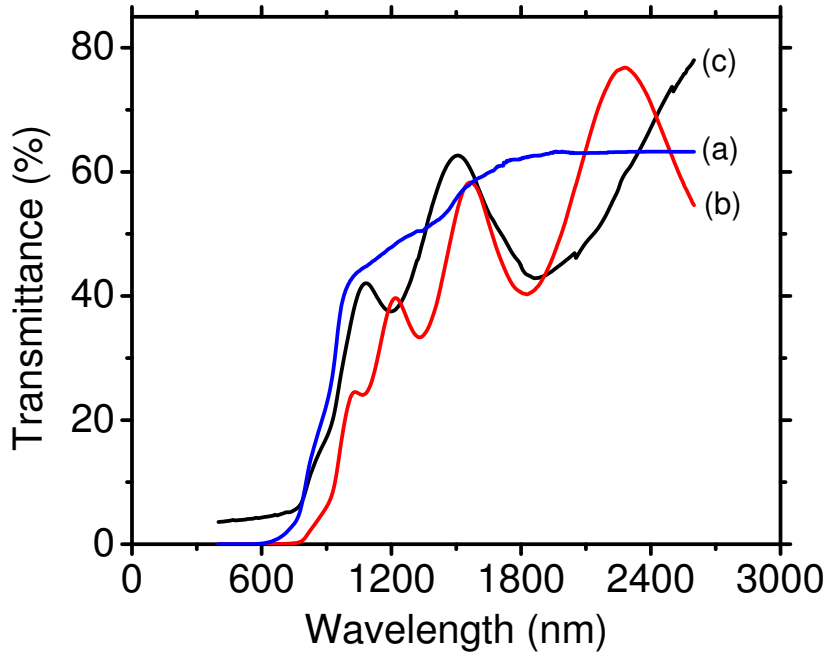

Figure 5.37: Transmittance Versus Wavelength Spectra; (a) SnS Layer Deposited at Substrate Temperature of 350 °C, Source Temperature of 300 °C and Deposition Time at 1.5 min (b) the Layer Annealed in Air at 300 °C for 30 min (c) the Layer Annealed in Sulphur at 300 °C for 30 min [34].

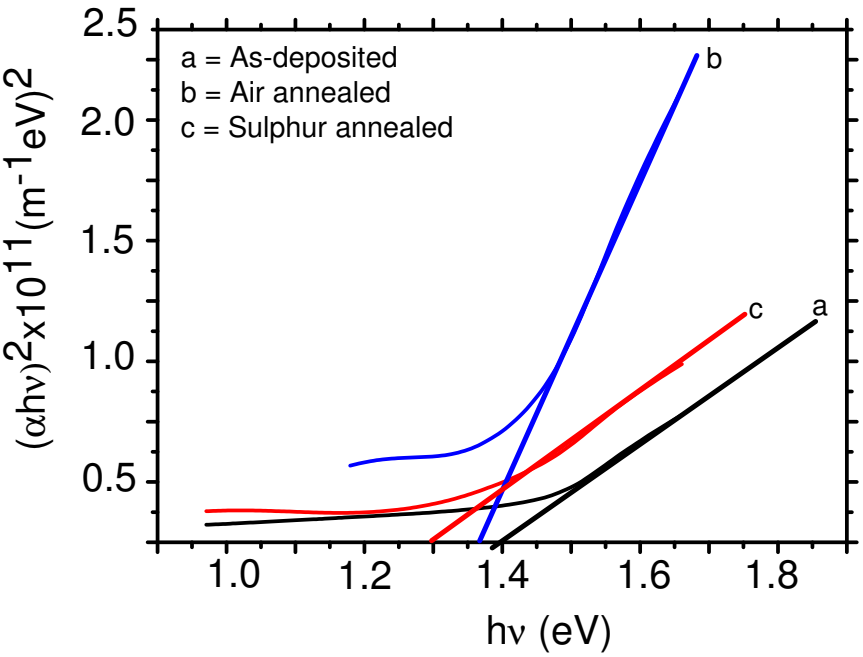

Figure 5.38: Plots of $(\alpha h\nu)^2$ Versus hν for SnS Layer Deposited at Substrate Temperature of 350 °C, Source Temperature of 300 °C and Deposition Time at 1.5 min, the Layer Annealed in Air at 300 °C for 30 min, and the Layer Annealed in Sulphur at 300 °C for 30 min [34].

long wavelength spectral response of SnS-based devices. Such behaviour has been reported by different researchers in the literature for SnS thin films [39, 49, 92].

Figure (5.39) gives the changes induced on the refractive index of the films by the annealing ambients. The refractive index was calculated using the Manifacier's theory given as [93]:

$$n = \left[N + \left\{N^2 + {n_0}^2 {n_1}^2\right\}^{0.5}\right]^{0.5} \tag{5.13}$$

where

$$N = \frac{{n_0}^2 + {n_1}^2}{2} + 2{n_0}^2{n_1}^2 \left\{\frac{T_{max} - T_{min}}{T_{max}T_{min}}\right\} \tag{5.14}$$

T_{max} and T_{min} are the transmittance maxima and minima while n, n_o and n_1 are the refractive indices of the film, air and glass (substrate) respectively at the same wavelength for corresponding values of T_{max} and T_{min}.

The refractive index varied in the range, 1.53 - 1.59 and exhibited the normal trend expected in that it fell sharply from the onset (around the fundamental edge) and decreased gradually at lower photon energies (longer wavelengths). This was attributed to the effect of free carrier absorption at longer wavelengths. The observed trend is in line with the reports of other authors independent of the deposition technique or annealing environment [25, 79, 94–97]. The refractive index could not be calculated for the as-deposited film due to the absence of an interference pattern (used to estimate the transmittance maximum and minimum). Also the refractive index for the air annealed case was relatively higher than that of the sulphur annealed film and this was attributed to the deviation in stoichiometry of the layers.

The change in extinction coefficient due to the annealing effect is shown on Figure (5.40). The extinction coefficient k, was calculated using the relation given in [98]:

$$k = \frac{\alpha\lambda}{4\pi} \tag{5.15}$$

where α retains its meaning and λ is the wavelength. The evaluated extinction coefficient, k changed marginally in the range, 0.035–0.11 for the as-deposited and annealed films. The

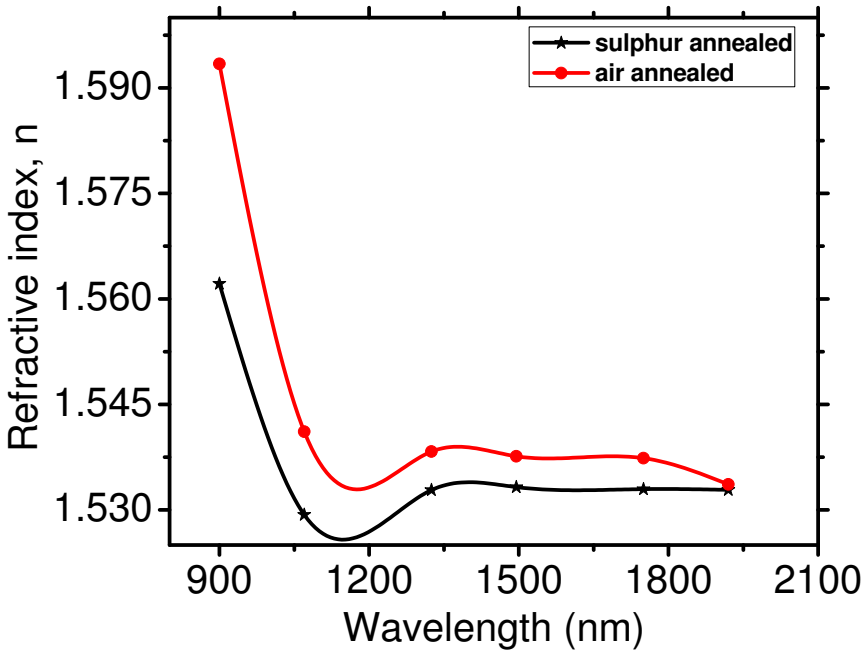

Figure 5.39: Variation of Refractive Index Versus Wavelength for SnS Layer Deposited at Substrate Temperature of 350 °C, Source Temperature of 300 °C and Deposition Time at 1.5 min, Annealed in Air at 300 °C for 30 min, and the Layer Annealed in Sulphur at 300 °C for 30 min.

extinction coefficient decreased gradually up to a "critical wavelength in each case and then increased. The observed decrease of extinction coefficient with wavelength has been reported by other authors [25, 80, 95, 96, 99].

Figure (5.41) gives the change on the optical density of the films due to the post deposition heat treatments. The optical density was deduced using the formula contained in [79]:

$$\rho_{opt} = \alpha d \tag{5.16}$$

where α retains its meaning and d is the film thickness. The evaluated optical density varied in the range 0.01–0.03. An increasing trend of optical density with the annealing environments was also observed with the increase appearing more pronounced in the air annealed layer.

The effects of post-deposition annealing on the electrical properties (electrical conductivity type and bulk resistivity) indicated that the layers retained their p-conductivity in the respective environment of annealing except for air annealing after dipping the samples in a saturated solution of $SnCl_4$/methanol. In this case the samples changed from p-conductivity

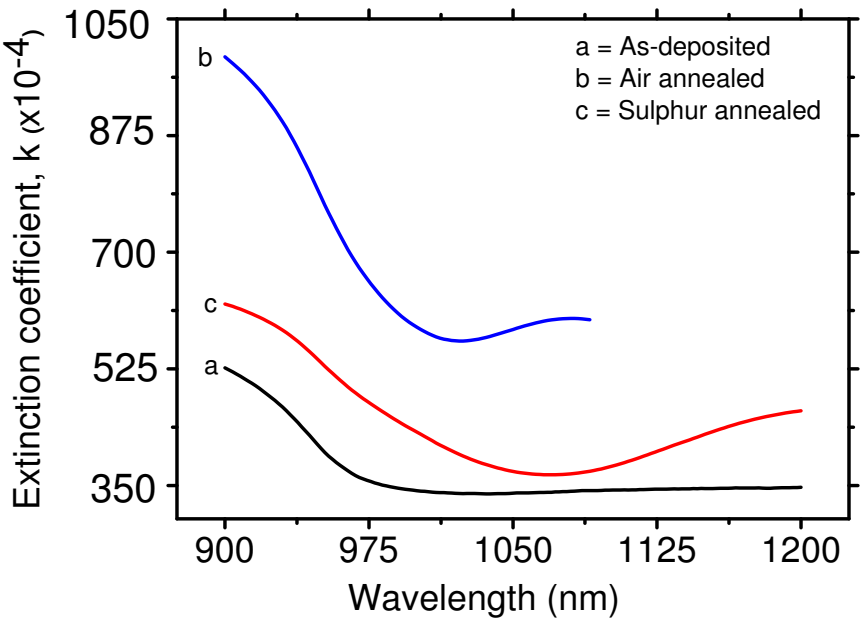

Figure 5.40: Variation of SnS Layer Deposited at Substrate Temperature of 350 °C, Source Temperature of 300 °C and Deposition Time at 1.5 min, the Layer Annealed in Air at 300 °C for 30 min, and the Layer Annealed in Sulphur at 300 °C for 30 min.

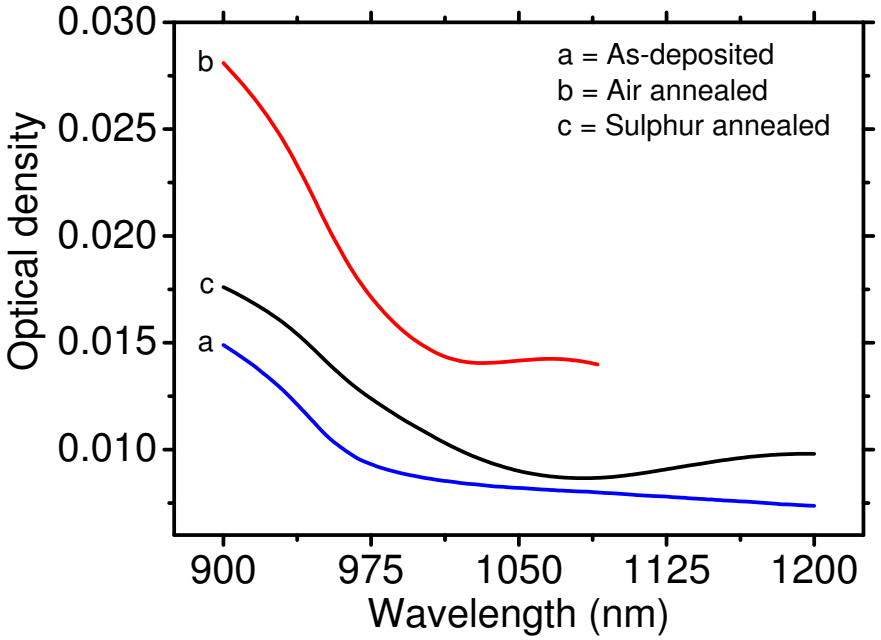

Figure 5.41: Variation of Optical Density Versus Wavelength for SnS Layer Deposited at Substrate Temperature of 350 °C, Source Temperature of 300 °C and Deposition Time at 1.5 min, the Layer Annealed in Air at 300 °C for 30 min, and the Layer Annealed in Sulphur at 300 °C for 30 min [34].

type to n-conductivity type, with a more substantial reduction in the conductivity of the samples. The effects of annealing in the different environments on the electrical properties of the films are summarised in Table 5.7 for a sample with an as-grown resistivity of 13.9 Ω cm.

Environments	Conductivity type	Resistivity Ωcm
As-deposited	p-type	13.9
Air	p-type	13.7
Sulphur	p-type	11.8
H_2S/argon	p-type	10.3
$SnCl_4$/methanol	n-type	6.8

Table 5.7: Effect of Annealing in Different Ambients and Chemical Treatments on the Electrical Properties of SnS Layers.

5.1.7 Device Properties

SnS-based photovoltaic cells were developed using CdS and $ZnIn_2Se_4$ as the buffer layers mainly in the substrate configuration. Figure (5.42) gives a schematic cross-sectional view of the configuration of the best solar cell devices fabricated in this work. For both structures in Figure (5.42), SnS films were formed by thermal evaporation at Northumbria Photovoltaics Applications Centre, Northumbria University, United Kingdom while the $ZnIn_2Se_4$ was grown by a novel chemical bath deposition process and ZnO/ZnO:Al (AZO) by magnetron sputtering at the Thin Films Laboratory, Department of Physics, Sri Venkateswara University, Tirupati, India. Devices made with CdS are completed at Northumbria University. The thickness of the various layers used for device fabrication are also given in Figure (5.42).

5.1.7.1 Current-Voltage Properties (Dark Current-Voltage Analysis)

Dark current density-voltage (J-V) measurements were made to evaluate the quality of the hetero-interface, the dominant current transport across the junction and other junction parameters for the diodes fabricated. The temperature dependence of the dark-current voltage gives an insight into the nature of current transport across the junction. For all the dark current-voltage measurements, the forward and reverse bias mode were performed at a temperature range of 180 K to 370 K. The dark forward and reverse J-V characteristics

of the junctions indicated that the forward characteristics were approximately exponential. The data extracted from the J-V studies of the various junctions were fitted to the following equations [100]:

$$\mathbf{J} = \mathbf{J}_o \left[e^{(qV/AkT)} - 1 \right] \tag{5.17}$$

where A is the ideality factor, q is the electronic charge and J_o is the saturation current density defined as:

$$\mathbf{J_o} = \mathbf{J}_{oo} \left[e^{(-E_a/AkT)} \right] \tag{5.18}$$

J_{oo} is the pre-exponential factor that is constant and E_a is the activation energy. From the recombination analysis given in [101], Equation (5.17) and Equation (5.18) yields:

$$V_{\mathrm{OC}} \approx \frac{E_a}{q} - \frac{AkT}{q} \ln \left[\frac{J_{\mathrm{OO}}}{J_{\mathrm{SC}}} \right] \tag{5.19}$$

From Equation (5.18) values of J_{oo} and A can be obtained from slope of a graph of $\ln(J_o)$ against $10^3/\mathrm{T(K)}$. The value of J_{oo} and A were obtained as $9.4 \times 10^{-7}\,\mathrm{A\,cm^{-2}}$ and 1.85 respectively for the SnS/ZIS/AZO heterojunction device. Results obtained indicated that the saturation current density varied between $0.5 \times 10^{-7}\,\mathrm{A\,cm^{-2}}$ and $4.6 \times 10^{-7}\,\mathrm{A\,cm^{-2}}$ for temperatures < 268 K. Based on these values of the saturation current density and the relative independence of J_o with temperature indicate that the current transport across the junction is largely dominated by a tunnelling mechanism. A schematic of the possible tunnelling-recombination mechanisms taking place at the junction and in the entire device are shown on Figure (5.43). The tunnelling-recombination currents observed here are analogous to those discussed in subsection 2.6 and are commonly observed in heterojunctions due to the presence of bulk and interface defects. Current transport via tunnelling is common in highly doped materials with doping concentration in the range 10^{19} – $10^{20} cm^{-3}$. For this work, the acceptor concentration in the SnS films was determined to be in the range 10^{15} – $10^{16} cm^{-3}$. Since this value is less than the required condition for a single step tunnelling to occur, it is possible that the current transport across the interface/junction was largely dominated by multi-step tunnelling process. It was also

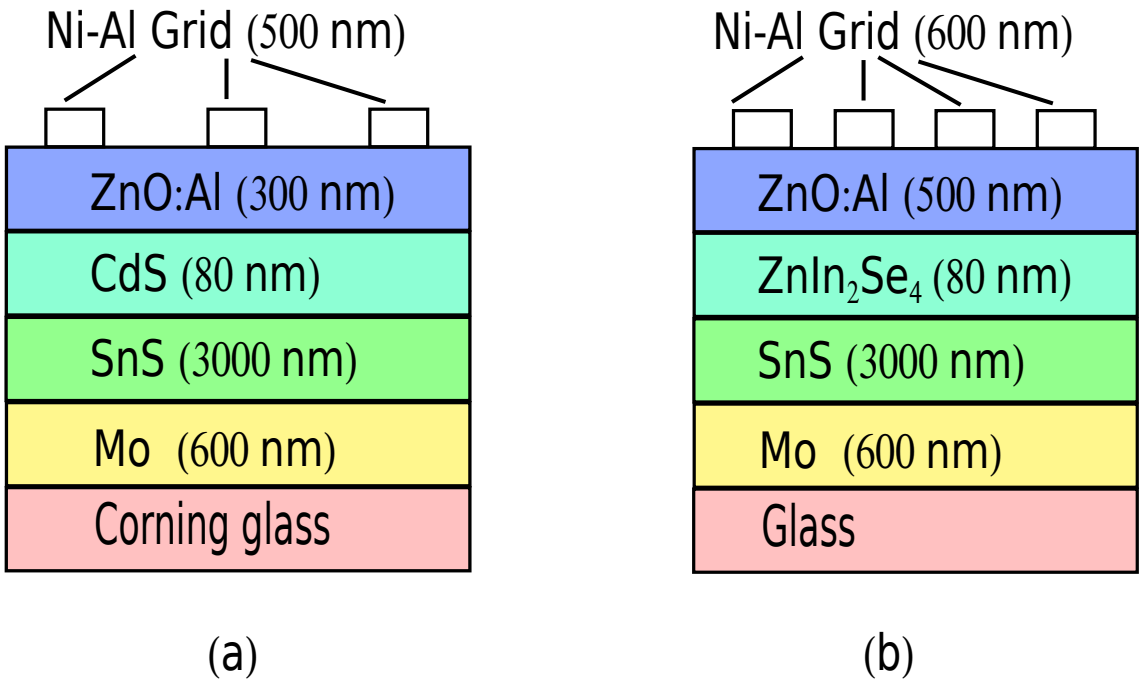

Figure 5.42: Schematic of SnS-based Solar Cells; (a) SnS/CdS/ZnO:Al (b) SnS/ZIS/ZnO:Al.

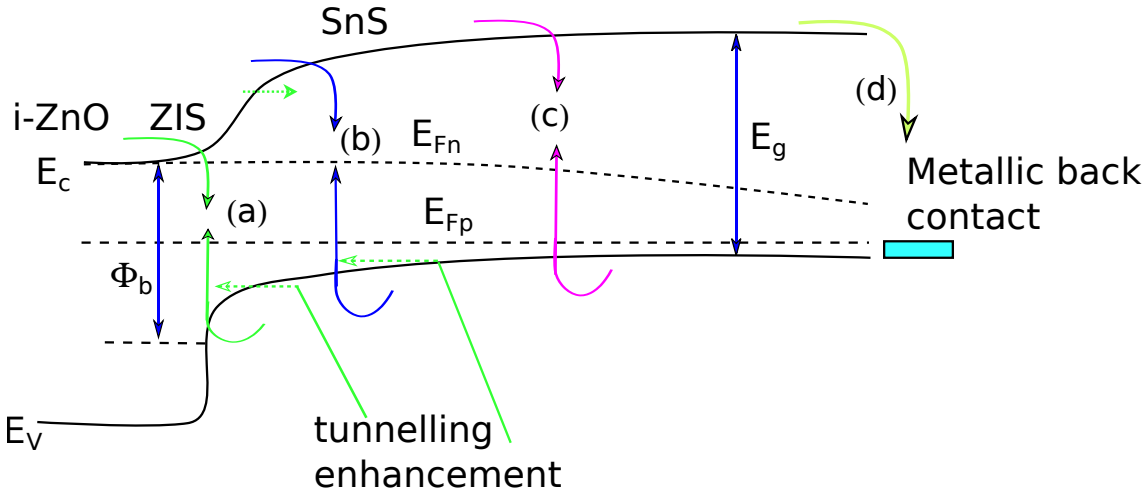

Figure 5.43: Possible Recombination Routes; (a) Interface Recombination Between the ZIS and SnS (b) Recombination at the Space Charge Region (c) Neutral Bulk Recombination (d) Back Contact Recombination.

observed that at higher temperatures (> 268 K), the ideality factor was relatively constant and varied in the range 1.85–1.94 while the saturation current density changed from $4.7 \times 10^{-7}\,\mathrm{A\,cm^{-2}}$ to $4.3 \times 10^{-7}\,\mathrm{A\,cm^{-2}}$. Such behaviour is typical of current transport limited by recombination in the depletion region. For temperatures > 268 K, the current transport is modelled as a combination of interface recombination and tunnelling. This is illustrated in Figure (5.43). Within this temperature range, the value of E_a estimated from the slope of $\ln(J_o)$ against $10^3/T(K)$ yielded 0.46 eV. From the foregoing, the current transport equation in this device can be adequately represented by Equation (2.85), in line with the discussion in [100]. Back contact recombination is not significant in these devices since the minority carrier diffusion length obtained in this work is less than the absorber layer thickness.

5.1.7.2 Current-Voltage Properties (Illuminated Current-Voltage Analysis)

All the junctions fabricated were characterised using an illuminated current density-voltage characteristics under a simulated AM1.5 spectrum. The data extracted from the measurements were used to determine the photovoltaic indicators such as open circuit voltage (V_{oc}), short circuit current density (J_{sc}), Fill factor (FF) and the conversion efficiency (η). The solar cell efficiency was calculated using the relation:

$$\eta = \frac{P_{out}}{P_{in}} \times 100 \tag{5.20}$$

where P_{out} = [V_{oc} x J_{sc} x FF] and P_{in} is the input power in $\mathrm{mW/cm^2}$. Results from I-V measurements under a simulated AM1.5 spectrum for the SnS/CdS based devices gives an open circuit voltage of 170 mV and a short circuit current density of 7.2 $\mathrm{mA/cm^2}$ with a fill factor of 0.28 for separate devices and a conversion efficiency of 1.0 %. These values are within the range reported by other researchers in the literature [32, 102–104]. The low values exhibited by the device are associated to the high density of interface states present at the CdS/SnS interface ($3.06 \times 10^{11} FC^{-1} cm^{-2}$) indicating that CdS is not a good partner material to SnS. It is possible that either producing buried homojunctions or making heterojunctions with materials other than CdS is a good way forward to improve SnS–based devices.

SnS junctions were then fabricated with ZnO as the buffer layer. For such devices, the photovoltaic parameters were found to be lower with the V_{oc} = 83 mV, J_{sc} = 2.7 mA/cm^2, FF = 0.14 and an efficiency < 1%. This was mainly due to the low fill factor value probably due to the high series and low shunt resistances. Low photovoltaic parameters was also recorded for the SnS/ZnCdS junction and was attributed to the low fill factor although better values of V_{oc} and J_{sc} were obtained for this junction.

Solar cells developed with ZIS film as the buffer layer and SnS layer, that was annealed followed by chemical treatment, resulted in a substantial increase of the conversion efficiencies, up to 2.9%. The best device had V_{oc} = 472 mV, J_{sc} = 16.1 mA/cm^2 and FF = 0.38. Table 5.8 gives a summary of the photovoltaic parameters of the best solar cell devices produced in this study and by other authors for SnS–based solar cells while Figure (5.44) gives the illuminated I-V curve of the best cells produced.

	Technique	V_{oc} (mV)	J_{sc} (mA/cm^2)	FF	η (%)	Ref
SnS/CdS	current work	170	7.2	0.28	1.00	current work
SnS/ZnO	current work	83	2.7	1.4	< 1.00	current work
SnS/ZIS	current work	472	16.1	0.38	2.90	current work
SnS/Zn(O,S)	CVD/ALD	244	19.4	0.4297	2.46	[105]
Inorganic-organic	–	850	7.35	0.45	2.81	[106]
SnS/CdS	evaporation/RFS	217	19.0	0.392	1.60	[107]
Homojunction	–	650	7.64	0.39	1.95	[108]
SnS/ZnMgO	RF/Co-sputtering	270	12.1	0.64	2.10	[109]

Table 5.8: Photovoltaic Parameters of the Best Laboratory Scale SnS-based Solar Cell Devices.

5.1.7.3 Electro-optical Properties

One of the most critical parameters among other factors governing the suitability of materials as absorbers for solar cell is the minority carrier diffusion length since diffusion is the mechanism through which minority carriers move to the space charge region and contribute to the photogenerated current. This makes it a diagnostic tool for assessing the suitability of materials as absorbers for photovoltaic solar cell applications. Different methods of determining the minority carrier diffusion length include the surface photo voltage method [110], P-C method (photocurrent versus capacitance method), photo-

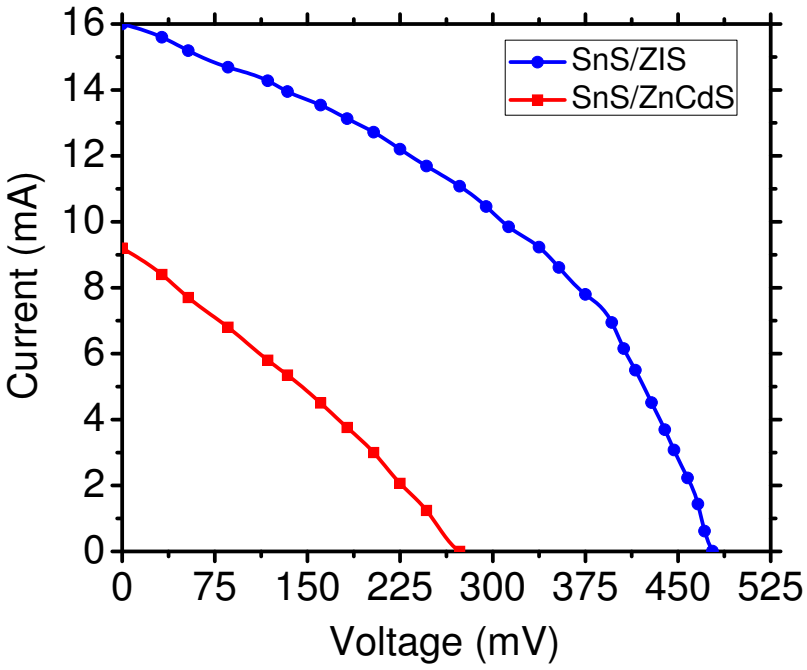

Figure 5.44: I-V Characteristics of SnS-based Heterojunction Devices.

induced open-circuit voltage decay (OCVD) [111] and electron beam induced current (EBIC) method [112]. The minority carrier diffusion length of SnS has been determined here for the first time using an electro-optical method [113, 114]. The measurement of quantum efficiency is a major basis for understanding the origin of the short circuit current and yields information on the optical cell properties and on the electronic properties. The quantum efficiency is a spectral quantity that depends on the wavelength of the incident photons. It is defined as the number of collected electrons per photon impinging on the solar cell device at a given wavelength. The theory behind the spectral response measurement has been discussed earlier in subsection 2.7.2. The variation of the spectral response of the devices are shown in Figure (5.45) and were as expected in that the current responsivity was zero for regions of wavelength less than the cut-off wavelength of the window layer and for wavelengths greater than the cut-off wavelength of the absorber layer. This behaviour is that of the so-called "heterojunction window effect". The behaviour is similar to that reported by other authors in the literature [115, 116].

Following the discussion from Equation (2.94) – Equation (2.96), the minority carrier diffusion length can be obtained from the spectral response by assuming that the short

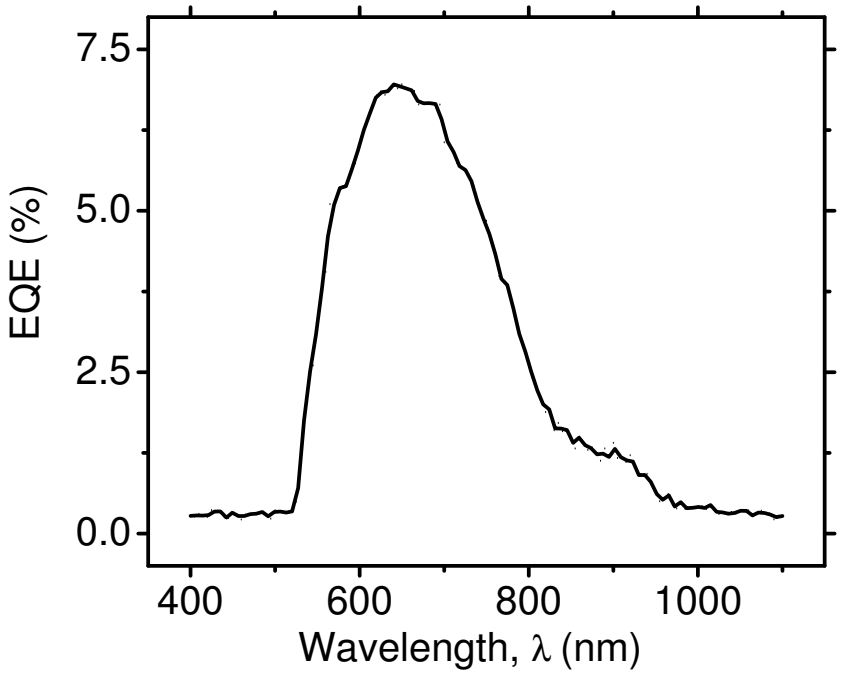

Figure 5.45: Spectral Response Plot of CdS/SnS Junction [24].

circuit current contribution can be approximated by [110, 114]:

$$J_{SC}(\lambda) \;=\; q(I-R)N_{ph}\left[\frac{L_n}{(L_n+\frac{1}{\alpha})}\right] \tag{5.21}$$

where $J_{sc}(\lambda)$ is the total photogenerated short circuit current density at any given λ and N_{ph} is the incident photon flux, R is the reflectance of the cell, α is the optical absorption coefficient and L_n is the minority carrier diffusion length in the SnS. This formula is expected to be valid in the range of wavelengths where α is small, such that the corresponding absorption length of the absorbed photons is within the SnS layer, away from both the CdS/SnS junction and the SnS/back contact. It follows that a plot of EQE^{-1} versus α^{-1} should be a straight line with an intercept on the α^{-1} axis equal to the minority carrier diffusion length. The behaviour observed is very similar to that reported by other workers for other heterojunction devices, in that as expected, the plots are linear for lower values of α (higher values of α^{-1}) and become non-linear for higher values of α (lower values of α^{-1}). Extrapolating the straight lines to the α^{-1} axis indicated a value of minority carrier diffusion length of 0.23 µm for the best SnS sample annealed in forming gas. This is the first time the minority carrier diffusion length has been determined for

SnS-based devices and is shown on Figure (5.46).

For the other junctions, the minority carrier diffusion length was in the range 0.18 µm to 0.25 µm. The values for the diffusion length obtained is within the range expected for polycrystalline thin films e.g. values have been reported to be in the range 0.1 µm to 0.5 µm for CdTe and CIGS, with the higher values obtained for the absorber layers used in the more efficient devices [114, 115]. Most recently, work done by Sinsermsuksakul et al. [105] on SnS-based heterojunction solar cell fabricated using a different technique, indicated that the minority carrier diffusion length of SnS lies within 0.2 µm to 0.4 µm.

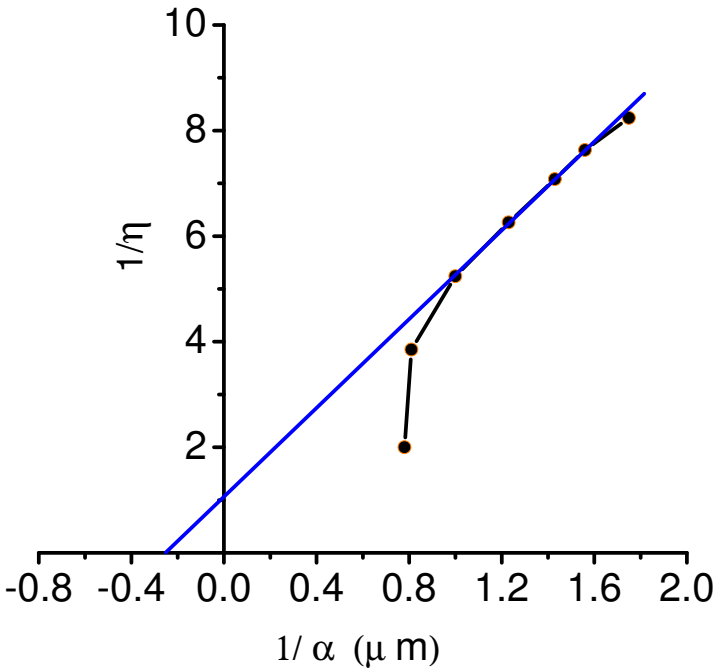

Figure 5.46: $1/\eta$ Versus $1/\alpha$ Plot of CdS/SnS Device [24].

5.1.7.4 Capacitance–Voltage Properties

It has been understood that charges in the depletion region are voltage dependent and hence from the a-c response of the p-n junction, salient information on the junction behaviour such as the carrier densities, depletion widths, deep trap densities and the potential barriers can be extracted. The basic theory behind the C-V measurements have been indicated in subsection 2.3.1. Figure (5.47) gives the variation of capacitance (±5 % measurement error) versus reverse bias voltage at different frequencies for room temperature measurements in the dark. The density of interface states N_{IS} present in the device can be determined

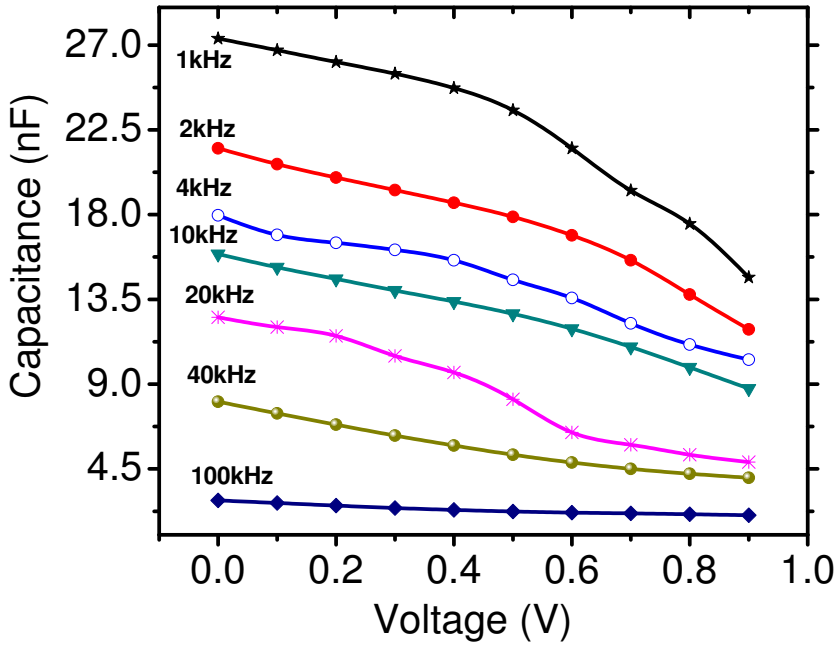

Figure 5.47: Variation of Capacitance-voltage-frequency Plots for CdS/SnS Junction [34].

using the relation [117]:

$$N_{IS} = \frac{C_{LF} - C_{HF}}{Aq} \tag{5.22}$$

where N_{IS} is the density of interface states, C_{LF} is the low frequency capacitance, C_{HF} is the high frequency capacitance, A is the cross-sectional cell area which was $0.5\,cm^2$ for this study, and q is the electronic charge. This gives a N_{IS} value of $3.06 \times 10^{11} FC^{-1}cm^{-2}$.

Figure (5.48) gives the variation of $\frac{1}{C^2}$ versus reverse bias voltage for a typical junction at the highest frequency for this study. The plot is a straight line for reverse bias voltages $< 0.5\ V$ indicating uniform doping of the SnS near to the SnS/CdS interface. Assuming an n^+p device, the slope of the plot of $\frac{1}{C^2}$ versus V gives a doping concentration of 10^{14} – $10^{15}cm^{-3}$ near to the interface. Extrapolating the plot to the voltage axis corresponds to a built-in-voltage of 0.85 V. The zero bias capacitance of this device corresponds to a depletion region of $0.38\,\mu m$. The value of N_{IS} obtained in the C-V studies is of the same order with the value of the dislocation density obtained from the structural studies as indicated in [1, 34].

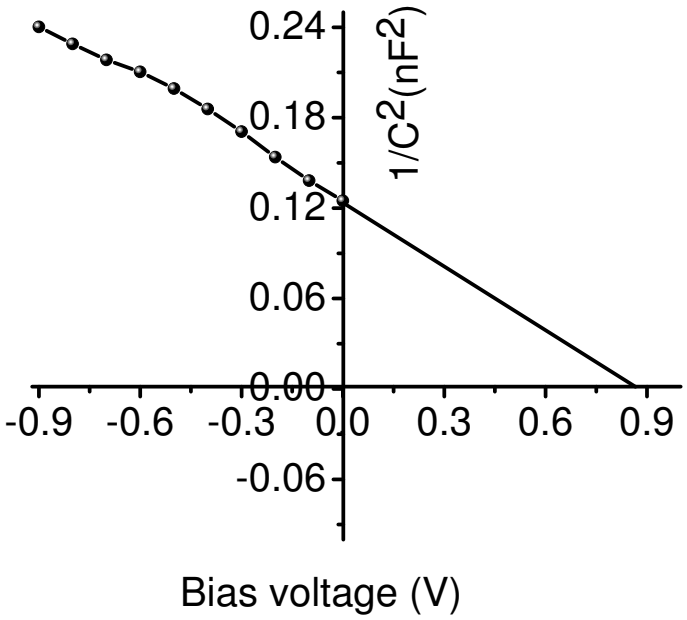

Figure 5.48: Plot of $1/C^2$ Versus Reverse Bias Voltage [34].

5.1.8 Band-alignment Properties

As indicated in subsection 3.3.4, there are very few reports on the band alignment studies on SnS-based devices probably because of the novelty of this material. It has been generally understood that band offsets mostly affect the electronic transport properties of heterojunction solar cell devices by acting as barriers to the charge carriers at the interface thereby reducing the conversion efficiency. This makes investigations on the band discontinuities a very important step in the device design since the valence and conduction band offsets determine the electrical transport properties at the interface, hence an in-depth understanding or control of the discontinuities at the band edges to align the valence and conduction bands of both semiconductors with more precision is very crucial in solar cell fabrication. The relevance of X-ray photoelectron spectroscopy (XPS) as a direct tool for the measurement of valence band discontinuities in hetero-junctions has been highlighted in subsubsection 4.4.4.4 and by other authors [118, 119]. Hence the energy band offsets at the different interfaces are investigated using XPS measurements and the related energy band diagrams developed are in line with the discussions in subsection 2.6.

5.1.8.1 CdS/SnS Junction

Results from the XPS narrow scan done to obtain the spectra of the Cd 4d core level and the Sn 4d core level of CdS and SnS films indicated that ${E_{Sn}^{SnS}}_{4d} = 30.03\,\text{eV}$ and ${E_{Cd}^{CdS}}_{4d} = 16.6\,\text{eV}$. The energy corresponding to the valence band maximum (E_{VBM}) positions were determined by linear extrapolation of the leading edge of the expanded spectra and were obtained as $E_{VBM}^{SnS} = 2.595\,\text{eV}$ and $E_{VBM}^{CdS} = 4.055\,\text{eV}$. From the XPS spectrum measured at the interface of the SnS/CdS junction, the difference between the core levels at the interface is obtained as $E_{CL}^{SnS/CdS} = 13.43\,\text{eV}$. Substituting accordingly in Equation (5.23) and Equation (5.24) [120, 121]:

$$\Delta {E_V}^{SnS/CdS} = ({E_{Sn}^{SnS}}_{4d} - E_{VBM}^{SnS}) - ({E_{Cd}^{CdS}}_{4d} - E_{VBM}^{CdS}) - \Delta E_{Sn-Cd} \tag{5.23}$$

$$\Delta {E_V}^{SnS/CdS} = \Delta E_{VBM-Sn}^{SnS} - \Delta E_{VBM-Cd}^{CdS} - \Delta E_{CL}^{SnS/CdS} \tag{5.24}$$

where ΔE_{VBM-Sn}^{SnS} is the energy separation between the valence band maximum (VBM) and the Sn 4d core level for SnS, ΔE_{VBM-Cd}^{CdS} is the energy separation between the VBM and the Cd 4d core level for CdS and $\Delta E_{CL}^{SnS/CdS}$ is the energy difference across the interface between the Sn 4d core level in the SnS side and Cd 4d core level in the CdS side of the junction. The valance band offset $\Delta {E_V}^{SnS/CdS}$ at the interface can be deduced as:

$$\Delta {E_V}^{SnS/CdS} = (30.03 - 2.595) - (16.6 - 4.055) - 13.43 = 1.46\,\text{eV} \tag{5.25}$$

The conduction band discontinuities can then be calculated from:

$$\Delta {E_C}^{SnS/CdS} = \Delta {E_g}^{SnS/CdS} - \Delta {E_V}^{SnS/CdS} \tag{5.26}$$

where $\Delta {E_g}^{SnS/CdS}$ is the difference in the energy gap values of SnS and CdS. From Figure 5.49 it follows that,

$$\Delta {E_C}^{SnS/CdS} = (2.4 - 1.3) - 1.46 = -0.36\,\text{eV} \tag{5.27}$$

The negative sign implies that the conduction band minimum (CBM) of CdS lies below that of SnS. The photoemission measurements indicated that the CBM and VBM were lower on the CdS side which is typical of a type-II heterojunction. Such junction can enhance electron transport from the SnS-side to the CdS-side substantially. The values obtained from the calculated band offsets were compared with the reported data and found to be in good correlation with the literature as evidenced in [121–123]. However Abdel Haleem and Ichimura [121] argued that a type II heterojunction can be affected by an increased recombination of the majority carriers at the interface leading to a drop in the open circuit voltage to consequently reduce the solar conversion efficiency.

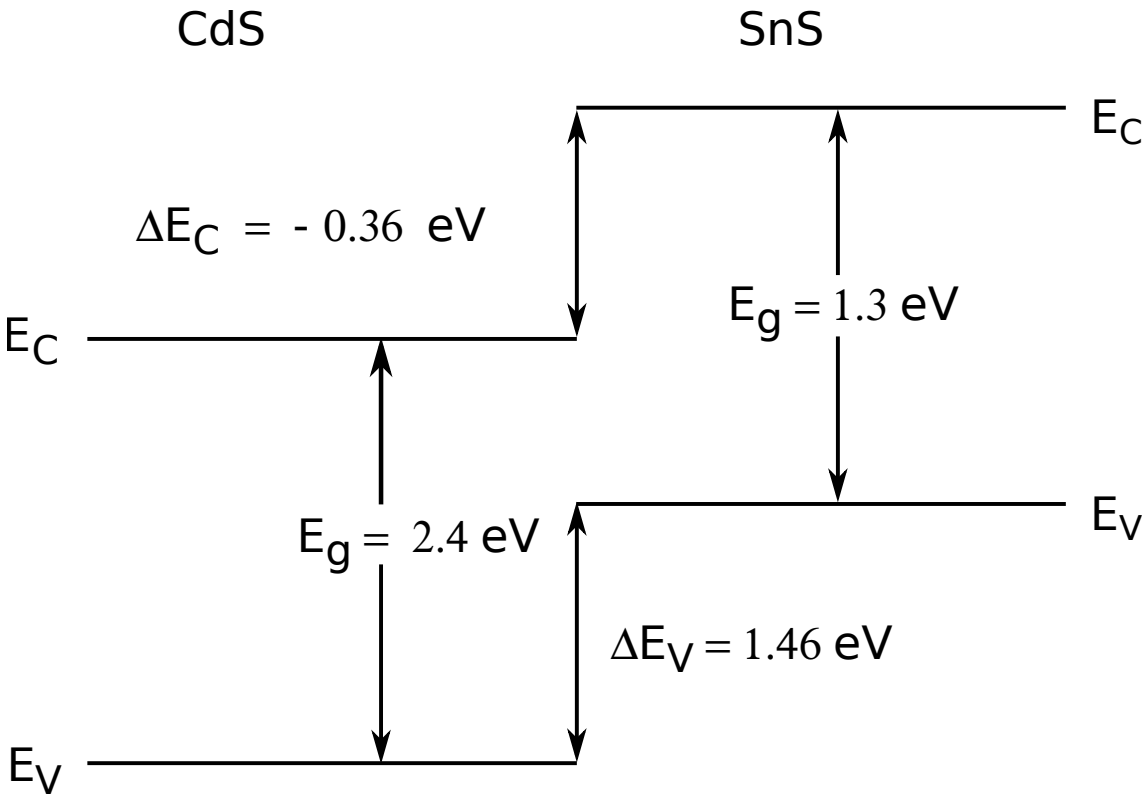

Figure 5.49: Energy Band Diagram of the CdS/SnS Heterojunction.

References

[1] P. A. Nwofe, K. T. Ramakrishna Reddy, G. Sreedevi, J. K. Tan, I. Forbes, and R. W. Miles. “Single phase, large grain, p-conductivity-type SnS layers produced using the thermal evaporation method”. In: *Energy Procedia* 15 (2012), pp. 354–360 (cit. on pp. 154, 155, 157, 158, 161, 162, 166–168, 175, 204).

[2] P. A. Nwofe, K. T. Ramakrishna Reddy, J. K. Tan, I. Forbes, M. Leach, D. Y. Jang, and R. W. Miles. "Investigating the Potential of SnS for Use in Photovoltaic Solar Cell Applications". In: *Proceedings of the Solar Energy Society and PV-Net UK on Photovoltaic Science, Applications and Technology (PVSAT-8), Northumbria University, UK, 2-4 April 2012*. Ed. by M. G. Hutchins, N. Pearsall, and A. Cole. Solar Energy Society, UK, 2012, pp. 89–92 (cit. on pp. 154, 157, 161, 167, 177, 181, 183, 186, 191).

[3] P. A. Nwofe, K. T. Ramakrishna Reddy, and R. W. Miles. "Influence of deposition time on the properties of highly-oriented SnS thin films prepared using the thermal evaporation method". In: *Advanced Materials Research* 602 (2013), pp. 1409–1412 (cit. on pp. 154, 156, 157, 159, 161, 162, 165–167, 179).

[4] P. A. Nwofe, K. T. Ramakrishna Reddy, G. Sreedevi, J. K. Tan, and R. W. Miles. "Structural, optical, and electro-optical properties of thermally evaporated tin sulphide layers". In: *Japanese Journal of Applied Physics* 51 (2012), 10NC36 (cit. on pp. 154, 157, 161, 162, 164, 165).

[5] P. A. Nwofe, K. T. Ramakrishna Reddy, J. K. Tan, I. Forbes, and R. W. Miles. "On the Structural and Optical Properties of SnS Films Grown by Thermal Evaporation Method". In: *Journal of Physics: Conference Series*. Vol. 417. IOP Publishing. 2013, p. 012039 (cit. on pp. 154, 157, 159, 161, 170, 174, 178, 179).

[6] M. Devika, K. T. Ramakrishna Reddy, N. Koteeswara Reddy, K. Ramesh, R. Ganesan, E. S. R. Gopal, and K. R. Gunasekhar. "Microstructure dependent physical properties of evaporated tin sulfide films". In: *Journal of Applied Physics* 100 (2006), p. 23518 (cit. on pp. 154, 157, 161, 162, 170, 189).

[7] O. E. Ogah, G. Zoppi, I. Forbes, and R. W. Miles. "Thin films of tin sulphide for use in thin film solar cell devices". In: *Thin Solid Films* 517 (2009), pp. 2485–2488 (cit. on pp. 154, 157, 161).

[8] M. Devika, N. Koteeswara Reddy, K. Ramesh, H. R. Sumana, K. R. Gunasekhar, E. S. R. Gopal, and K. T. Ramakrishna Reddy. "The effect of substrate surface on the physical properties of SnS films". In: *Semiconductor Science and Technology* 21 (2006), pp. 1495–1501 (cit. on pp. 154, 157).

[9] S. Cheng, Y. Chen, Y. He, and G. Chen. "The structure and properties of SnS thin films prepared by pulse electro-deposition". In: *Materials Letters* 61 (2007), pp. 1408–1412 (cit. on p. 154).

[10] S. Cheng, Y. He, and C. Chen. "Structure and properties of SnS films prepared by electro-deposition in presence of EDTA". In: *Materials Chemistry and Physics* 110 (2008), pp. 449–453 (cit. on pp. 154, 157).

[11] K. Hartman, J.L. Johnson, M.I. Bertoni, D. Recht, M.J. Aziz, M.A. Scarpulla, and T. Buonassisi. "SnS thin-films by RF sputtering at room temperature". In: *Thin Solid Films* 519 (2011), pp. 7421–7424 (cit. on p. 154).

[12] G. H. Yue, W. Wang, L. S. Wang, X. Wang, P. X. Yan, Y. Chen, and D. L. Peng. "The effect of anneal temperature on physical properties of SnS films". In: *Journal of Alloys and Compounds* 474 (2009), pp. 445–449 (cit. on pp. 154, 162).

[13] K. Takeuchi, M. Ichimura, E. Arai, and Y. Yamazaki. "SnS thin films fabricated by pulsed and normal electrochemical deposition". In: *Solar Energy Materials and Solar Cells* 75 (2003), pp. 427–432 (cit. on p. 154).

[14] E. Guneri, C. Ulutas, F. Kirmizigul, G. Altindemir, F. Gode, and C. Gumus. "Effect of deposition time on structural, electrical, and optical properties of SnS thin films deposited by chemical bath deposition". In: *Applied Surface Science* 257 (2010), pp. 1189–1195 (cit. on pp. 154, 162, 167, 177).

[15] P. K. Nair, M. T. S. Nair, V. M. Garcia, O. L. Arenas, A. Castillo Y. Pena, I. T. Ayala, O. Gomezdaza, A. Sanchez, J. Campos, H. Hu, R. Suarez, and M. E. Rincon. "Semiconductor thin films by chemical bath deposition for solar energy related applications". In: *Solar Energy Materials and Solar Cells* 52 (1998), pp. 313–344 (cit. on p. 154).

[16] M. Sugiyama, K. Miyauchi, T. Minemura, and H. Nakanishi. "Sulfurization growth of SnS films and fabrication of CdS/SnS heterojunction for solar cells". In: *Japanese Journal of Applied Physics* 47 (2008), pp. 8723–8725 (cit. on p. 154).

[17] N. Koteeswara Reddy and K. T. Ramakrishna Reddy. “Electrical properties of spray pyrolytic tin sulfide films”. In: *Solid State Electronics* 49 (2005), pp. 902–906 (cit. on pp. 157, 162).

[18] C. Gao and H. Shen. “Influence of the deposition parameters on the properties of orthorhombic SnS films by chemical bath deposition”. In: *Thin Solid Films* 520 (2012), pp. 3523–3527 (cit. on p. 157).

[19] Z. Xu and Y. Chen. “Fabrication of SnS thin films by a novel multilayer-based solid-state reaction method”. In: *Semiconductor Science and Technology* 27 (2012), p. 035007 (cit. on p. 157).

[20] M. Devika, N. K. Reddy, K. Ramesh, K. R. Gunasekhar, E. S. R. Gopal, and K. T. Ramakrishna Reddy. “Influence of annealing on physical properties of evaporated SnS films”. In: *Semiconductor Science and Technology* 21 (2006), pp. 1125–1131 (cit. on pp. 157, 180, 188, 189).

[21] M. Devika, N. Koteeswara Reddy, S. Venkatramana Reddy, K. Ramesh, and K. R. Gunasekhar. “Influence of rapid thermal annealing (RTA) on the structural and electrical properties of SnS films”. In: *Journal of Materials Science: Materials in Electronics* 20 (2009), pp. 1129–1134 (cit. on pp. 157, 170, 188).

[22] M. Devika, N. K. Reddy, D. S. Reddy, S. V. Reddy, K . Ramesh, E. S. R. Gopal, K. R. Gunasekhar, V. Ganesan, and Y. B. Hahn. “Optimization of the distance between source and substrate for device-grade SnS films grown by the thermal evaporation technique”. In: *Journal of Physics: Condensed Matter* 19 (2007), p. 306003 (cit. on pp. 157, 170).

[23] *Powder Diffraction File: 00-039-0354 (1985)*. ICDD (cit. on pp. 157, 161).

[24] K. T. Ramakrishna Reddy, P. A. Nwofe, and R. W. Miles. “Determination of the minority carrier diffusion length of SnS using electro-optical measurements”. In: *Electronic Materials Letters* 9 (2013), pp. 336–366 (cit. on pp. 157, 202, 203).

[25] E. R. Shaaban, M. S. Abd El-Sadek, M. El-Hagary, and I. S. Yahia. “Spectroscopic ellipsometry investigations of the optical constants of nanocrystalline SnS thin films”. In: *Physica Scripta* 86 (2012), p. 015702 (cit. on pp. 157, 174, 176, 193, 194).

[26] V. Dhanasekaran, T. Mahalingam, J. K. Rhee, and J. P. Chu. “Bath Temperature Effects on the Microstructural and Morphological Properties of SnS Thin Films”. In: *Journal of Advanced Microscopy Research* 6.2 (2011), pp. 126–130 (cit. on p. 157).

[27] B. G. Jeyaprakash, R. Ashok Kumar, K. Kesavan, and A. Amalarani. “STRUCTURAL AND OPTICAL CHARACTERISATION OF SPRAY DEPOSITED SnS THIN FILM”. In: *Journal of American Science* 6 (2010), pp. 22–26 (cit. on pp. 157, 174, 177).

[28] Yanuar, G. Moussa, F. Guastavino, and C. LIinares. “Preparation and Characterization of SnS Thin Films Obtained by Close-Spaced Vapor Transport for Solar Cell Application”. In: *IEEE Proceedings* (2000), pp. 66–68. DOI: doi:10.1109/CMPLES.2000.939863 (cit. on p. 157).

[29] S. A. Bashkirov, V. F. Gremenok, V. A. Ivanov, and V. V. Shevtsova. “Microstructure and electrical properties of SnS thin films”. In: *Physics of the Solid State* 54 (2012), pp. 2497–2502 (cit. on pp. 157, 170).

[30] H. Zhu, D. Yang, Y. Ji, H. Zhang, and X. Shen. “Two-dimensional SnS nanosheets fabricated by a novel hydrothermal method”. In: *Journal of Materials Science* 40 (2005), pp. 591–595 (cit. on p. 157).

[31] H. Zhu. “Elevated performances of SnS anodes with MWNTs as conductive agent for rechargeable lithium-ion batteries”. In: *Ionics* 17 (2011), pp. 641–645 (cit. on p. 157).

[32] H. Noguchi, A. Setiyadi, H. Tanamura, T. Nagatomo, and O. Omoto. “Characterization of vacuum-evaporated tin sulfide film for solar cell materials”. In: *Solar Energy Materials and Solar Cells* 35 (1994), pp. 325–331 (cit. on pp. 157, 199).

[33] P. A. Nwofe, K. T. Ramakrishna Reddy, and R. W. Miles. “Type Conversion of p-SnS to n-SnS Using a $SnCl_4/CH_3OH$ Heat Treatment”. In: *Proceedings of 39 IEEE Photoltaic Specialsts Conference*. 2013 (cit. on pp. 160, 163, 167, 169, 178, 179).

[34] P. A. Nwofe, R. W. Miles, and K. T. Ramakrishna Reddy. “Effects of sulphur and air annealing on the properties of thermally evaporated SnS layers for application in

thin film solar cell devices". In: *J. Renewable Sustainable Energy* 5 (2013), p. 011204 (cit. on pp. 161, 182, 184, 186, 192, 195, 204, 205).

[35] A. Mendez-Vilas. *Fuelling the Future: Advances in Science and Technologies for Energy Generation, Transmission and Storage*. Brown Walker Press (FL), 2012 (cit. on pp. 161, 167, 180, 190, 191).

[36] M. Devika, N. Koteeswara Reddy, K. Ramesh, R. Ganesan, K. R. Gunasekhar, E. S. R. Gopal, and K. T. Ramakrishna Reddy. "Thickness Effect on the Physical Properties of Evaporated SnS Films". In: *Journal of The Electrochemical Society* 154 (2007), H67–H73 (cit. on p. 161).

[37] M. Devika, N. Koteeswara Reddy, and K. R. Gunasekhar. "Structural, electrical, and optical properties of as-grown and heat treated ultra-thin SnS films". In: *Thin Solid Films* 520 (2011), pp. 628–632 (cit. on pp. 161, 184).

[38] M. Devika, N. K. Reddy, K. Ramesh, V. Ganesan, E. S. R. Gopal, and K. T. Ramakrishna Reddy. "Influence of substrate temperature on surface structure and electrical resistivity of the evaporated tin sulphide films". In: *Applied Surface Science* 253 (2006), pp. 1673–1676 (cit. on pp. 161, 162, 180).

[39] N. Koteeswara Reddy, Y. B. Hahn, M. Devika, H. R. Sumana, and K. R. Gunasekhar. "Temperature-dependent structural and optical properties of SnS films". In: *Journal of Applied Physics* 101 (2007), p. 093522 (cit. on pp. 161, 162, 170, 193).

[40] N. K. Reddy. "Growth-Temperature Dependent Physical Properties of SnS Nanocrystalline Thin Films". In: *ECS Journal of Solid State Science and Technology* 2 (2013), P259–P263 (cit. on p. 161).

[41] *Powder Diffraction File: 00-014-0619 (1961)*. ICDD (cit. on pp. 161, 184).

[42] B. Ghosh, R. Bhattacharjee, P. Banerjee, and S. Das. "Structural and optoelectronic properties of vacuum evaporated SnS thin films annealed in argon ambient". In: *Applied Surface Science* 257 (2011), pp. 3670–3676 (cit. on pp. 161, 191).

[43] R.W. Miles, O.E. Ogah, G. Zoppi, and I. Forbes. "Thermally evaporated thin films of SnS for application in solar cell devices". In: *Thin Solid Films* 517 (2009), pp. 4702–4705 (cit. on p. 161).

[44] C. An, K. Tang, G. Shen, C. Wang, Q. Yang, B. Hai, and Y. Qian. "Growth of belt-like SnS crystals from ethylenediamine solution". In: *Journal of Crystal Growth* 244 (2002), pp. 333–338 (cit. on p. 162).

[45] S. Cheng and H. Zhang. "Influence of thickness on structural and optical properties of evaporated tin sulphide films". In: *Micro & Nano Letters, IET* 6 (2011), pp. 473–475 (cit. on p. 162).

[46] G. H. Yue, Y. D. Lin, X. Wen, L. S. Wang, Z. Y. Chen, and D. L. Peng. "Synthesis and characterisation of the SnS nanowires via chemical vapour deposition". In: *Applied Physics A* 106 (2012), pp. 87–91 (cit. on p. 162).

[47] S. Sohila, M. Rajalakshmi, C. Gosh, A. K. Arora, and C. Muthamizhchelvan. "Optical and Raman scattering on SnS nanoparticles". In: *Journal of Alloys and Compounds* 509 (2011), pp. 5843–5847 (cit. on pp. 162, 177).

[48] L. L. Cheng, M. H. Liu, M. X. Wang, S. C. Wang, G. D. Wang, Q. Y. Zhou, and Z. Q. Chen. "Preparation of SnS films using solid sources deposited by the PECVD method with controllable film characters". In: *Journal of Alloys and Compounds* 545 (2012), pp. 122–129 (cit. on p. 162).

[49] J. Malaquias, P.A. Fernandes, P.M.P. Salomé, and A.F. da Cunha. "Assessment of the potential of tin sulphide thin films prepared by sulphurization of metallic precursors as cell absorbers". In: *Thin Solid Films* 519 (2011), pp. 7416–7420 (cit. on pp. 162, 193).

[50] L. I. Maissel and R. Glang. *Handbook of Thin Film Technology*. McGraw-Hill, New York, 1970 (cit. on pp. 162, 174, 176, 189).

[51] E. F. Kaelble. *Handbook of X-rays*. McGraw-Hill, New York, 1967 (cit. on p. 162).

[52] B. E. Warren. *X-ray Diffraction*. Dover Publications, Inc., New York, 1969 (cit. on p. 162).

[53] A. L. Fahrenbruch and R. H. Bube. *Fundamentals of Solar Cells: Photovoltaic Solar Energy Conversion*. Academic Press, New York, 1983 (cit. on p. 162).

[54] G. H. Yue, D. L. Peng, P. X. Yan, L. S. Wang, W. Wang, and X. H. Luo. "Structure and optical properties of SnS thin film prepared by pulse electrodeposition". In: *Journal of Alloys and Compounds* 468 (2009), pp. 254–257 (cit. on p. 162).

[55] M. Botero, C. Cifuentes, E. Romero, J. Clavijo, and G. Gordillo. "Properties of SnS thin films grown by a two-step process". In: *Photovoltaic Energy Conversion, Conference Record of the 2006 IEEE 4th World Conference on*. Vol. 1. 2006, pp. 79–82. DOI: doi:10.1109/WCPEC.2006.279351 (cit. on p. 162).

[56] H. B. M. Anaya, I. Z. Torres, and N. R. Mathews. "Pulse electrodeposited tin sulfide films for photovoltaic applications". In: *Proc. of SPIE*. Vol. 7409. 2009, pp. 740914–1 (cit. on p. 162).

[57] V. Malathy, S. Sivaranjani, V. S. Vidhya, J. J. Prince, T. Balasubramanian, C. Sanjeeviraja, and M. Jayachandran. "Amorphous to crystalline transition and optoelectronic properties of nanocrystalline induim tin oxide (ITO) films sputtered with rf power at room temperature". In: *Journal of Non-Crystalline Solids* 355 (2009), pp. 1508–1516 (cit. on p. 167).

[58] M. Reghima, A. Akkari, C. Guasch, and N. Kamoun-Turki. "Effect of indium doping on physical properties of nanocrystallized SnS zinc blend thin films grown by chemical bath deposition". In: *Journal of Renewable and Sustainable Energy* 4 (2012), p. 011602 (cit. on pp. 167, 176).

[59] F. K. Lotgering. "Topotactical reactions with ferrimagnetic oxides having hexagonal crystal structures—I". In: *Journal of Inorganic and Nuclear Chemistry* 9 (1959), pp. 113–123 (cit. on p. 167).

[60] H. R. Moutinho, F. S. Hasoon, F. Abulfotuh, and L. L. Kazmerski. "Investigation of polycrystalline CdTe thin films deposited by physical vapor deposition, close-spaced sublimation, and sputtering". In: *Journal of Vacuum Science & Technology A: Vacuum, Surfaces, and Films* 13 (1995), pp. 2877–2883 (cit. on pp. 167, 169, 170).

[61] H. R. Moutinho, M. M. Al-Jassim, D. H. Levi, P. C. Dippo, and L. L. Kazmerski. "Effects of CdCl treatment on the recrystallization and electro-optical properties

of CdTe thin films". In: *Journal of Vacuum Science & Technology A: Vacuum, Surfaces, and Films* 16 (1998), pp. 1251–1257 (cit. on pp. 167, 169).

[62] C. S. Barrett and T. B. Massalski. *Structure of Metals*. 3rd Edition. Pergamon Press, Oxford, 1980 (cit. on p. 167).

[63] K. H. Kim and J. S. Chun. "X-ray studies of SnO_2 prepared by chemical vapour deposition". In: *Thin Solid Films* 141 (1986), pp. 287–295 (cit. on pp. 167, 169–171).

[64] G. B. Harris. "X. Quantitative measurement of preferred orientation in rolled uranium bars". In: *Philosophical Magazine* 43 (1952), pp. 113–123 (cit. on p. 167).

[65] G. Zoppi, K. Durose, S. J. C. Irvine, and V. Barrioz. "Grain and crystal texture properties of absorber layers in MOCVD-grown CdTe/CdS solar cells". In: *Semiconductor Science and Technology* 21 (2006), pp. 763–770 (cit. on p. 169).

[66] E. P. Zaretskaya, V. F. Gremenok, V. A. Ivanov, S. A. Bashkirov, V. B. Zalesski, and B. I. Kovalevski. "Physical Properties of Polycrystalline SnS Thin Films for Solar Cells". In: *EU-PVSEC Proceedings*. 2009, pp. 262–265. DOI: doi:10.4229/24thEUPVSEC2009-1CV.3.10 (cit. on p. 170).

[67] K. T. Ramakrishna Reddy and P. Purandhra Reddy. "Structural studies on SnS films grown by a two-stage process". In: *Materials Letters* 56 (2002), pp. 108–111 (cit. on p. 170).

[68] A. Tanuševski and D. Poelman. "Optical and photoconductive properties of SnS thin films prepared by electron beam evaporation". In: *Solar Energy Materials and Solar Cells* 80 (2003), pp. 297–303 (cit. on p. 171).

[69] N. R. Mathews, C. Colın Garcıa, and I. Z. Torres. "Effect of annealing on structural, optical and electrical properties of pulse electrodeposited tin sulfide films". In: *Materials Science in Semiconductor Processing* 16 (2013), pp. 29–37 (cit. on p. 171).

[70] M. A. Contreras, K. M. Jones, L. Gedvilas, and R. Matson. *Preferred Orientation in Polycrystalline Cu(In, Ga)Se_2 and Its Effect on Absorber Thin-Films and Devices*. National Renewable Energy Laboratory, 2000 (cit. on p. 171).

[71] N. Revathi, P. Prathap, and K. T. Ramakrishna Reddy. “Thickness dependent physical properties of close space evaporated In_2S_3 films”. In: *Solid State Sciences* 11 (2009), pp. 1288–1296 (cit. on p. 174).

[72] B. Ghosh, M. Das, P. Banerjee, and S. Das. “Fabrication of SnS thin films by the successive ionic layer adsorption and reaction (SILAR) method”. In: *Semiconductor Science and Technology* 23 (2008), p. 125013 (cit. on p. 174).

[73] R. Mariappan, T. Mahalingam, and V. Ponnuswamy. “Preparation and characterization of electrodeposited SnS thin films”. In: *Optik-International Journal for Light and Electron Optics* 122 (2011), pp. 2216–2219 (cit. on pp. 174, 176).

[74] R. Mariappan, M. Ragavendar, and V. Ponnuswamy. “Structural and optical characterization of SnS thin films by electrodeposition technique”. In: *Optica Applicata* 41 (2011), pp. 989–997 (cit. on p. 174).

[75] G. K. Williamson and R. E. Smallman. “III. Dislocation densities in some annealed and cold-worked metals from measurements on the X-ray debye-scherrer spectrum”. In: *Philosophical Magazine* 1 (1956), pp. 34–46 (cit. on p. 176).

[76] C. K. De and N. K. Misra. “X-ray diffraction analysis of lattice defects of ZnSe thin films deposited at different substrate temperatures”. In: *Indian Journal of Physics*. Vol. 71. 1997, pp. 530–535 (cit. on p. 176).

[77] N. J. Suthan Kissinger, M. Jayachandran, K. Perumal, and C. Sanjeevi Raja. “Structural and optical properties of electron beam evaporated CdSe thin films”. In: *Bulletin of Materials Science* 30 (2007), pp. 547–551 (cit. on p. 176).

[78] H. Metin and R. Esen. “Annealing studies on CBD grown CdS thin films”. In: *Journal of Crystal Growth* 258 (2003), pp. 141–148 (cit. on p. 177).

[79] C. Cifuentes, M. Botero, E. Romero, C. Caldern, and G. Gordillo. “Optical and structural studies on SnS films grown by co-evaporation”. In: *Brazilian Journal of Physics* 36 (2006), pp. 1046–1049 (cit. on pp. 177, 193, 194).

[80] A. Akkari, C. Guasch, M. Castagne, and N. Kamoun-Turki. “Optical study of zinc blend SnS and cubic In_2S_3: Al thin films prepared by chemical bath deposition”. In: *Journal of Materials Science* 46 (2011), pp. 6285–6292 (cit. on pp. 177, 194).

[81] A. Tanuševski. "Optical and photoelectric properties of SnS thin films prepared by chemical bath deposition". In: *Semiconductor Science and Technology* 18 (2003), pp. 501–505 (cit. on pp. 177, 191).

[82] S. Sohila, M. Rajalakshmi, C. Muthamizhchelvan, S. Kalavathi, C. Ghosh, R. Divakar, C. N. Venkiteswaran, N. G. Muralidharan, A. K. Arora, and E. Mohandas. "Synthesis and characterization of SnS nanosheets through simple chemical route". In: *Materials Letters* 65 (2011), pp. 1148–1150 (cit. on p. 177).

[83] Y. Azizian-Kalandaragh, A. Khodayari, Z. Zeng, C. S. Garoufalis, S. Baskoutas, and L. C. Gontard. "Strong quantum confinement effects in SnS nanocrystals produced by ultrasound-assisted method". In: *Journal of Nanoparticle Research* 15 (2013), pp. 1–9 (cit. on p. 177).

[84] M. Calixto-Rodriguez, H. Martinez, A. Sanchez-Juarez, J. Campos-Alvarez, A. Tiburcio-Silver, and M. E. Calixto. "Structural, optical, and electrical properties of tin sulfide thin films grown by spray pyrolysis". In: *Thin Solid Films* 517 (2009), pp. 2497–2499 (cit. on p. 177).

[85] T.H. Sajeesh, A.R. Warrier, C.S. Kartha, and K.P. Vijayakumar. "Optimization of parameters of chemical spray pyrolysis technique to get n and p-type layers of SnS". In: *Thin Solid Films* 518 (2010), pp. 4370–4374 (cit. on p. 179).

[86] N. Koteeswara Reddy and K.T. Ramakrishna Reddy. "SnS films for photovoltaic applications: Physical investigations on sprayed Sn_xS_y films". In: *Physica B: Condensed Matter* 368 (2005), pp. 25–31 (cit. on p. 179).

[87] P. A. Nwofe, K. T. Ramakrishna Reddy, J. K. Tan, I. Forbes, and R. W. Miles. "Thickness dependent optical properties of thermally evaporated SnS thin films". In: *Physics Procedia* 25 (2012), pp. 150–157 (cit. on p. 179).

[88] *Powder Diffraction File: 01-083-1706 (1978)*. ICDD (cit. on p. 184).

[89] O. E. Ogah, K. R. Reddy, G. Zoppi, I. Forbes, and R. W. Miles. "Annealing studies and electrical properties of SnS-based solar cells". In: *Thin Solid Films* 519 (2011), pp. 7425–7428 (cit. on p. 188).

[90] N. K. Reddy, M. Devika, Y. Hahn, and K. R. Gunasekhar. “Impact of chemical treatment on the surface, structure, optical and electrical properties of SnS thin films”. In: *Applied Surface Science* 268 (2013), pp. 317–322 (cit. on pp. 188, 191).

[91] Z. Qiao, R. Latz, and D. Mergel. “Thickness dependence of In_2O_3:Sn film growth”. In: *Thin Solid Films* 466 (2004), pp. 250–258 (cit. on p. 189).

[92] B. Ghosh, R. Roy, S. Chowdhury, P. Banerjee, and S. Das. “Synthesis of SnS thin films via galvanostatic electrodeposition and fabrication of CdS/SnS heterostructure for photovoltaic applications”. In: *Applied Surface Science* 256 (2010), pp. 4328–4333 (cit. on p. 193).

[93] J. C. Manifacier, M. De Murcia, J. P. Fillard, and E. Vicario. “Optical and electrical properties of SnO_2 thin films in relation to their stoichiometric deviation and their crystalline structure”. In: *Thin Solid Films* 41 (1977), pp. 127–135 (cit. on p. 193).

[94] A. P. Lambros, D. Geraleas, and N. A. Economou. “Optical absorption edge in SnS”. In: *Journal of Physics and Chemistry of Solids* 35 (1974), pp. 537–541 (cit. on p. 193).

[95] M. S. Selim, M. E. Gouda, M. G. El-Shaarawy, A. M. Salem, and W. A. Abd El-Ghany. “Effect of thickness on optical properties of thermally evaporated SnS films”. In: *Thin Solid Films* 527 (2012), 164–169 (cit. on pp. 193, 194).

[96] M. Patel, I. Mukhopadhyay, and A. Ray. “Annealing influence over structural and optical properties of sprayed SnS thin films”. In: *Optical Materials* 35 (2013), pp. 1693–1699 (cit. on pp. 193, 194).

[97] M. M. El-Nahass, H. M. Zeyada, M. S. Aziz, and N. A. El-Ghamaz. “Optical properties of thermally evaporated SnS thin films”. In: *Optical Materials* 20 (2002), pp. 159–170 (cit. on p. 193).

[98] R. Swanepoel. “Determination of the thickness and optical constants of amorphous silicon”. In: *Journal of Physics E: Scientific Instruments* 16 (1983), pp. 1214–1222 (cit. on p. 193).

[99] B. Subramanian, C. Sanjeeviraja, and M. Jayachandran. "Cathodic electrodeposition and analysis of SnS films for photoelectrochemical cells". In: *Materials Chemistry and Physics* 71 (2001), pp. 40–46 (cit. on p. 194).

[100] B. L. Sharma and R. K. Purohit. *Semiconductor Heterojunctions*. Pergamon Press, Oxford, 1974 (cit. on pp. 197, 199).

[101] U. Rau and H. W. Schock. "Electronic properties of Cu(In,Ga)Se_2 heterojunction solar cells–recent achievements, current understanding, and future challenges". In: *Appl. Phys. A* 69 (1999), pp. 131–147 (cit. on p. 197).

[102] M. Ristov, G. Sinadinovski, M. Mitreski, and M. Ristova. "Photovoltaic cells based on chemically deposited p-type SnS". In: *Solar Energy Materials and Solar Cells* 69 (2001), pp. 17–24 (cit. on p. 199).

[103] M. Gunasekaran and M. Ichimura. "Photovoltaic cells based on pulsed electrochemically deposited SnS and photochemically deposited CdS and $Cd_{1-x}Zn_xS$". In: *Solar Energy Materials and Solar Cells* 91 (2007), pp. 774–778 (cit. on p. 199).

[104] J. J. M. Vequizo and M. Ichimura. "Fabrication of electrodeposited SnS/SnO_2 heterojunction solar cells". In: *Japanese Journal of Applied Physics* 51 (2012), 10NC38 (cit. on p. 199).

[105] P. Sinsermsuksakul, K. Hartman, S. D. Kim, J. Heo, L. Sun, H. H. Park, R. Chakraborty, T. Buonassisi, and R. G. Gordon. "Enhancing the efficiency of SnS solar cells via band-offset engineering with a zinc oxysufide buffer layer". In: *Applied Physics Letters* 102 (2013), p. 053901 (cit. on pp. 200, 203).

[106] W. Guo, Y. Shen, M. Wu, and T. Ma. "Highly efficient inorganic-organic heterojunction solar cells based on SnS-senitized spherical TiO_2 electrodes". In: *Chemical Communications* 48 (2012), pp. 6133–6135 (cit. on p. 200).

[107] A. Schneikart, H. J. Schimper, A. Klein, and W. Jaegermann. "Efficiency limitations of thermally evaporated thin-film SnS solar cells". In: *Journal of Physics D: Applied Physics* 46 (2013), p. 305109 (cit. on p. 200).

[108] G. Yue, Y. Lin, X. Wen, L. Wang, and D. Peng. "SnS homojunction nanowire-based solar cells". In: *Journal of Materials Chemistry* 22 (2012), pp. 16437–16441 (cit. on p. 200).

[109] T. Ikuno, R. Suzuki, K. Kitazumi, N. Takahashi, N. Kato, and K. Higuchi. "SnS thin film solar cells with $Zn_{1-x}Mg_xO$ buffer layers". In: *Applied Physics Letters* 102 (2013), p. 193901 (cit. on p. 200).

[110] C. L. Chiang, R. Schwarz, D. E. Slobodin, J. Kolodzey, and S. Wagner. "Measurement of the minority-carrier diffusion length in thin semiconductor films". In: *Electron Devices, IEEE Transactions on* 33 (1986), pp. 1587–1592 (cit. on pp. 200, 202).

[111] U. Stutenbaeumer and E. Lewetegn. "Comparison of minority carrier diffusion length measurements in silicon solar cells by the photo-induced open-circuit voltage decay (OCVD) with different excitation sources". In: *Renewable Energy* 20 (2000), pp. 65–74 (cit. on p. 201).

[112] G. Brown, V. Faifer, A. Pudov, S. Anikeev, E. Bykov, M. Contreras, and J. Wu. "Determination of the minority carrier diffusion length in compositionally graded Cu (In, Ga) Se solar cells using electron beam induced current". In: *Applied Physics Letters* 96 (2010), p. 022104 (cit. on p. 201).

[113] P. K. Basu, S. N. Singh, N. K. Arora, and B. C. Chakravarty. "A new method of determination of minority carrier diffusion length in the base region of silicon solar cells". In: *Electron Devices, IEEE Transactions on* 41 (1994), pp. 367–372 (cit. on p. 201).

[114] O. Vigil-Galán, A. Arias-Carbajal, R. Mendoza-Pérez, G. Santana, J. Sastré-Hernández, G. Contreras-Puente, A. Morales-Acevedo, and M. Tufiño-Velázquez. "Spectral response of CdS/CdTe solar cells obtained with different S/Cd ratios for the CdS chemical bath". In: *Solar Energy Materials and Solar Cells* 90 (2006), pp. 2221–2227 (cit. on pp. 201–203).

[115] K. T. Ramakrishna Reddy, N. Koteswara Reddy, and R. W. Miles. "Photovoltaic properties of SnS based solar cells". In: *Solar Energy Materials and Solar Cells* 90 (2006), pp. 3041–3046 (cit. on pp. 201, 203).

[116] B. Ghosh, M. Das, P. Banerjee, and S. Das. “Fabrication of vacuum-evaporated SnS/CdS heterojunction for PV applications”. In: *Solar Energy Materials and Solar Cells* 92 (2008), pp. 1099–1104 (cit. on p. 201).

[117] A. S. Grove. *Physics and technology of semiconductor devices.* Wiley, New York, 1967 (cit. on p. 204).

[118] G. Martin, A. Botchkarev, A. Rockett, and H. Morkoc. “Valence-band discontinuities of wurtzite GaN, AlN, and InN heterojunctions measured by x-ray photoemission spectroscopy”. In: *Applied Physics Letters* 68 (1996), pp. 2541–2543 (cit. on p. 205).

[119] J. J. Chen, B. P. Gila, M. Hlad, A. Gerger, F. Ren, C. R. Abernathy, and S. J. Pearton. “Determination of MgO/ GaN heterojunction band offsets by x-ray photoelectron spectroscopy”. In: *Applied Physics Letters* 88 (2006), p. 042113 (cit. on p. 205).

[120] J. Li, Q. Du, G. Jiang, X. Feng, W. Zhang, J. Zhu, and C. Zhu. “The Band Offset at CdS/Cu_2ZnSnS_4 Heterojunction Interface”. In: *Electronic Materials Letters* 8 (2012), pp. 365–367 (cit. on p. 206).

[121] A. M. Abdel Haleem and M. Ichimura. “Experimental determination of band offsets at the SnS/CdS and SnS/InSxOy heterojunctions”. In: *Journal of Applied Physics* 107 (2010), p. 034507 (cit. on pp. 206, 207).

[122] M. Sugiyama, K. T. R. Reddy, N. Revathi, Y. Shimamoto, and Y. Murata. “Band offset of SnS solar cell structure measured by X-ray photoelectron spectroscopy”. In: *Thin Solid Films* 519 (2011), pp. 7429–7431 (cit. on p. 207).

[123] M. Sugiyama, Y. Murata, T. Shimizu, K. Ramya, C. Venkataiah, T. Sato, and K. T. Ramakrishna Reddy. “Sulfurization Growth of SnS Thin Films and Experimental Determination of Valence Band Discontinuity for SnS-Related Solar Cells”. In: *Japanese Journal of Applied Physics* 50 (2011), 05FH03 (cit. on p. 207).

Chapter 6

Conclusions

The aims and objectives of this work were to deposit thin films of SnS using the thermal evaporation technique, characterise accordingly and develop SnS-based solar cells using toxic-free and more environmentally acceptable buffer layer materials. The work presented clearly indicate that:

- It is possible to produce thin films of tin sulphide using the thermal evaporation method and that this method yields high quality layers of SnS that are free from pin-holes and cracks, are made of densely packed grains and adhere strongly to the substrates used. The properties of the films were observed to vary with the deposition conditions [1–6].

- The films are mostly bluish-black when grown using substrate temperatures $\geq 300\,^{\circ}\mathrm{C}$ and film thicknesses $> 40\,\mathrm{nm}$, and brownish-black colour when grown using substrate temperature $< 300\,^{\circ}\mathrm{C}$ and for thicknesses $40\,\mathrm{nm}$. The films are stoichiometric for a wide range of deposition conditions with a slight deviation for substrate temperatures $\geq 350\,^{\circ}\mathrm{C}$. This is attributed to the difference in vapour pressure of the Sn and S atoms.

- X-ray diffractrometry and Raman studies confirm that single phase SnS can be produced over a wide range of deposition conditions. XRD studies also confirms that the layers have the orthorhombic crystal structure (Powder Diffraction File:00-039-0354) [7]. The films are of very high crystallinity with the (111)/(040) appearing as the most prominent peak. The former is more associated to lower deposition factors

(substrate temperature or film thicknesses) while the latter is common at higher substrate temperatures or film thicknesses.

- Information extracted from the XRD data can be used to deduce other important structural parameters such as the crystallite size (C), number of crystallites (N_c), texture coefficient $T_{C(hkl)}$, degree of preferred orientation σ, strain ε, angular broadening and the dislocation density δ. The variation of each of these parameter with the deposition condition was critically investigated and the results are in line with the literature.

- The layers all show p-conductivity type which is a desirable electrical property for making solar cells.

- Results from optical data give the energy bandgap in the range 1.30 eV to 1.35 eV and confirmed it to be direct with the optical absorption coefficient $\alpha > 10^5 cm^{-1}$ for photons with energies greater than the energy bandgap. The near optimum energy bandgap and high optical absorption coefficient confirm that only a few microns of SnS (like CdTe and CIGS) are needed to absorb most of the incident solar radiation.

- Post deposition heat treatments of the layers done in the environments: air, elemental sulphur, 5% hydrogen sulphide in argon (H_2S/Ar), and air annealing after a dip in a saturated solution of tin (iv) chloride in methanol ($SnCl_4/CH_3OH$) result in a further improvement in the crystallinity of the layers especially in the (H_2S/Ar) ambient. However although air annealing can lead to further loss of stoichiometry, annealing in sulphur acts to restore the stoichiometry. A reduction in the resistivity of the films is observed for the layers dipped in ($SnCl_4/CH_3OH$) and then annealed in air. Some significant findings are reported in [8–11].

- The minority carrier diffusion length in p-type SnS is 0.23 µm.

- Devices made with CdS-based buffer layers exhibit low photovoltaic parameters due to the high density of interface states present at the CdS/SnS interface ($3.06 \times 10^{11} FC^{-1} cm^{-2}$) indicating that CdS is not a good partner material to SnS. Also XPS studies done on the CdS/SnS heterojunction gives a band-offset of −0.36 eV,

indicating the possibility of an increased recombination of the majority carriers at the interface.

- Amongst the different buffer layers used, $ZnIn_2Se_4$ deposited by a novel chemical bath deposition (CBD) process proves to be most successful buffer material when used in substrate configuration devices with rf sputtered Mo as the back contact material. Devices with efficiencies up to 2.9% have been produced, a world record efficiency for SnS-based solar cells till date.

6.1 Future Work

From the foregoing, the properties determined for the SnS and the achievement of an efficiency of 2.9% for $SnS/ZnIn_2Se_4$ cells demonstrate the high promise of SnS for making highly efficient, low-cost and more environmentally acceptable PV solar cells. Research of SnS-based solar cells is still at infancy stage hence the efficiency of SnS-based devices can be enhanced by:

- Improving the bulk minority carrier diffusion length through improved passivation of the grain boundaries in the SnS.
- Use of an antireflection coating to help minimise reflection losses in the device structure.
- Passivation of the surfaces of the SnS by developing suitable improved surface etching methods will act to reduce the interface and surface recombination effects.
- Improved doping of the layers and by developing a more suitable low resistance contact to the SnS will minimise series resistance losses.
- Reducing shunting at the periphery of the layers will also improve device performance substantially.
- Use of a more suitable buffer layer and/or variation of the constituent element of the current buffer layer used in this work.

Taking the aformentioned points into consideration will possibly lead to producing small area devices with efficiencies $> 10\%$, and to subsequently:

- Fabricate mini-modules with efficiencies > 10% after which,
- An extensive stability testing of the mini-modules should be carried out.

References

[1] P. A. Nwofe, K. T. Ramakrishna Reddy, G. Sreedevi, J. K. Tan, I. Forbes, and R. W. Miles. "Single phase, large grain, p-conductivity-type SnS layers produced using the thermal evaporation method". In: *Energy Procedia* 15 (2012), pp. 354–360 (cit. on p. 222).

[2] P. A. Nwofe, K. T. Ramakrishna Reddy, J. K. Tan, I. Forbes, M. Leach, D. Y. Jang, and R. W. Miles. "Investigating the Potential of SnS for Use in Photovoltaic Solar Cell Applications". In: *Proceedings of the Solar Energy Society and PV-Net UK on Photovoltaic Science, Applications and Technology (PVSAT-8), Northumbria University, UK, 2-4 April 2012*. Ed. by M. G. Hutchins, N. Pearsall, and A. Cole. Solar Energy Society, UK, 2012, pp. 89–92 (cit. on p. 222).

[3] P. A. Nwofe, K. T. Ramakrishna Reddy, and R. W. Miles. "Influence of deposition time on the properties of highly-oriented SnS thin films prepared using the thermal evaporation method". In: *Advanced Materials Research* 602 (2013), pp. 1409–1412 (cit. on p. 222).

[4] P. A. Nwofe, K. T. Ramakrishna Reddy, J. K. Tan, I. Forbes, and R. W. Miles. "Thickness dependent optical properties of thermally evaporated SnS thin films". In: *Physics Procedia* 25 (2012), pp. 150–157 (cit. on p. 222).

[5] P. A. Nwofe, K. T. Ramakrishna Reddy, G. Sreedevi, J. K. Tan, and R. W. Miles. "Structural, optical, and electro-optical properties of thermally evaporated tin sulphide layers". In: *Japanese Journal of Applied Physics* 51 (2012), 10NC36 (cit. on p. 222).

[6] P. A. Nwofe, K. T. Ramakrishna Reddy, J. K. Tan, I. Forbes, and R. W. Miles. "On the Structural and Optical Properties of SnS Films Grown by Thermal Evaporation Method". In: *Journal of Physics: Conference Series*. Vol. 417. IOP Publishing. 2013, p. 012039 (cit. on p. 222).

[7] *Powder Diffraction File: 00-039-0354 (1985)*. ICDD (cit. on p. 222).

[8] K. T. Ramakrishna Reddy, P. A. Nwofe, and R. W. Miles. "Determination of the minority carrier diffusion length of SnS using electro-optical measurements". In: *Electronic Materials Letters* 9 (2013), pp. 336–366 (cit. on p. 223).

[9] P. A. Nwofe, R. W. Miles, and K. T. Ramakrishna Reddy. "Effects of sulphur and air annealing on the properties of thermally evaporated SnS layers for application in thin film solar cell devices". In: *J. Renewable Sustainable Energy* 5 (2013), p. 011204 (cit. on p. 223).

[10] A. Mendez-Vilas. *Fuelling the Future: Advances in Science and Technologies for Energy Generation, Transmission and Storage*. Brown Walker Press (FL), 2012 (cit. on p. 223).

[11] P. A. Nwofe, K. T. Ramakrishna Reddy, and R. W. Miles. "Type Conversion of p-SnS to n-SnS Using a $SnCl_4/CH_3OH$ Heat Treatment". In: *Proceedings of 39 IEEE Photoltaic Specialsts Conference*. 2013 (cit. on p. 223).

Appendix A

Original Contributions to Knowledge

- Determination of the minority carrier diffusion length of electrons in the SnS absorber layer using electro-optical measurements.
- Post deposition heat treatments in the environments: elemental sulphur, 5% hydrogen sulphide in argon (H_2S/Ar), and air annealing after a dip in a saturated solution of tin (iv) chloride in methanol ($SnCl_4/CH_3OH$).
- Type conversion of p-SnS to n-SnS using a $SnCl_4/CH_3OH$ heat treatment.

Appendix B

List of Publications

1. K. T. Ramakrishna Reddy, P. A. Nwofe and R. W. Miles. *"Determination of the Minority Carrier Diffusion Length of SnS Using Electro-optical Measurements"* Electronic Materials Letters, **9(3)**, 363-366 (2013). doi: http://dx.doi.org/10.1007/s13391-013-2194-3

2. P. A. Nwofe, K. T. Ramakrishna Reddy and R. W. Miles. *"Effects of sulphur and air annealing on the properties of thermally evaporated SnS layers for application in thin film solar cell devices"* J. Renewable Sustainable Energy, **5**, 011204 (2013). doi: http://dx.doi.org/10.1063/1.4791784

3. P. A. Nwofe, K. T. Ramakrishna Reddy and R. W. Miles. *"Influence of Deposition Time on the Properties of Highly-oriented SnS Thin Films Prepared Using the Thermal Evaporation Method"* Adv. Mater. Res., **602–604**, 1409-1412 (2013). doi:10.4028/www.scientific.net/AMR.602-604.1409

4. P. A. Nwofe, K. T. Ramakrishna Reddy, J. K. Tan, I. Forbes and R. W. Miles. *"On the Structural and Optical Properties of SnS Films Grown by Thermal Evaporation Method"* J. Phys.: Conf. Ser., **417**, 012039 (2013). doi: http://dx.doi:10.1088/1742-6596/417/1/012039

5. P. A. Nwofe, K. T. Ramakrishna Reddy, G. Sreedevi, J. K. Tan and R. W. Miles. *" Structural, Optical, and Electro-Optical Properties of Thermally Evaporated Tin Sulphide Layers"* Jpn. J. Appl. Phys., **51**, 10NC36 (2012).
doi: http://dx.doi.org/10.1143/JJAP.51.10NC36

6. P. A. Nwofe, K. T. Ramakrishna Reddy, G. Sreedevi, J. K. Tan, I. Forbes and R. W. Miles. *"Single Phase, Large Grain, p-Conductivity-type SnS Layers Produced using the Thermal Evaporation Method"* Energy Procedia, **15**, 354–360 (2012). doi: http://dx.doi:10.1016/j.egypro.2012.02.043

7. P. A. Nwofe, K. T. Ramakrishna Reddy, J. K. Tan, I. Forbes and R. W. Miles. *"Thickness Dependent Optical Properties of Thermally Evaporated SnS Thin Films"* Physics Procedia, **25**, 150–157 (2012).
doi: http://dx.doi:10.1016/j.phpro.2012.03.064

Book Chapter

8. P. A. Nwofe, K. T. Ramakrishna Reddy, J. K. Tan, I. Forbes, M. Leach, D. Y. Jang and R. W. Miles. *"Fuelling the future: advances in science and technologies for energy generation, transmission and storage"* BrownWalker Press Publishers, Boca Raton, Florida, USA, ISBN-10: 1-61233-558-6, ISBN-13: 978-1-61233-558-2, pp. 194-198, (2012).

Original Research Conference Proceedings

9. P. A. Nwofe, K. T. Ramakrishna Reddy, K. Ramya, K. Tan, G. Zoppi, I. Forbes and R. W. Miles. *"Determination of the minority carrier diffusion length of SnS using electro-optical measurements"* in: Proceedings of the European Materials Research Society, Nice, France, May 9-13, 2011, Symposium Z.

10. P. A. Nwofe, K. T. Ramakrishna Reddy, G. Sreedevi, J. K. Tan, I. Forbes and R. W. Miles. *"Structural, Optical, and Electro-Optical Properties of Thermally Evaporated SnS Layers"* in: Technical Digest of the PVSEC21, Fukuoka, Japan, 2011, p. 126.

11. P. A. Nwofe, K. T. Ramakrishna Reddy, G. Sreedevi, J. K. Tan, I. Forbes and R. W. Miles. *"Single Phase, Large Grain, p-Conductivity-type SnS Layers Produced using the Thermal Evaporation Method"* in: Proceedings of the International Conference on Materials and Advanced Technologies, Suntec, Singapore, June 26-July 1, 2011, p. 38.

12. P. A. Nwofe, K. T. Ramakrishna Reddy, J. K. Tan, I. Forbes and R. W. Miles. *"Structural and Optical Properties of SnS Films Grown by Thermal Evaporation Method"* in: Technical Digest of the ICTF-15, Kyoto-Terrsa, Japan, 2011, p. 40.

13. P. A. Nwofe, K. T. Ramakrishna Reddy, J. K. Tan, I. Forbes and R. W. Miles. *"Thickness Dependent Optical Properties of Thermally Evaporated SnS Thin Films"* in: Proceedings of the 2012 International Conference on Solid State Devices and Materials Science, Macao, Japan, April 1-2, 2012, p. 112.

14. P. A. Nwofe, K. T. Ramakrishna Reddy, J. K. Tan, I. Forbes, M. Leach, D. Y. Jang and R. W. Miles. *"Investigating the Potential of SnS for Use in Photovoltaic Solar Cell Applications"* in: Photovoltaic Science, Applications and Technology (PVSAT-8): Proceedings of the Solar Energy Society and PV-Net UK, Northumbria University, UK, 2 - 4 April 2012, edited by M.G. Hutchins, N. Pearsall, and A. Cole (Solar Energy Society, UK, 2012), pp. 89-92.

15. P. A. Nwofe, K. T. Ramakrishna Reddy, J. K. Tan, I. Forbes, M. Leach, D. Y. Jang and R. W. Miles. *"Effects of Thermal Annealing in Different Environments on the Properties of SnS Thin Films Prepared by the Thermal Evaporation Method"* in: Proceedings of the European Materials Research Society (EMRS), Strasbourg, France, May 14-18, 2012, p. B-25.

16. V. P. Geetha Vani, K. T. Ramakrishna Reddy, P. A. Nwofe and R. W. Miles. *"Influence of Substrate Temperature on the Properties of Cu_4SnS_4 Films Grown by Co-evaporation"* in: Proceedings of the European Materials Research Society (EMRS), Strasbourg, France, May 14-18, 2012, p. B-6.

17. P. A. Nwofe, K. T. Ramakrishna Reddy and R. W. Miles. *"Properties of Thermally Evaporated SnS Layers for Application in Thin Film Solar Cell Devices"* in: Proceedings of the Photovoltaic Technical Conference, PVTC 2012, Aix-ene Provence, France, June 6-8, 2012, p. 46.

18. P. A. Nwofe, K. T. Ramakrishna Reddy, J. K. Tan, I. Forbes, M. Leach, D. Y. Jang and R. W. Miles. *"Highly oriented SnS thin films: preparation, post deposition heat*

treatments and characterisation" in: Proceedings of The Energy & Materials Research Conference (EMR2012) Book of Abstracts, Torremolinos, Spain, June 20-22, 2012, p. 129.

19. P. A. Nwofe, K. T. R. Reddy, J. K. Tan, I. Forbes, M. Leach, D. Y. Jang and R. W. Miles. *"Influence of Thickness on the Properties of SnS Thin Films Prepared Using the Thermal Evaporation Method"* in: Proceedings of the Thin Films Society (TFS), The 6th International Conference on Technological Advances of Thin Films & Surface Coatings, Singapore Management University(SMU) at Stamford Road, Singapore, July 14-17, 2012.

20. K. T. Ramakrishna Reddy, R. W. Miles and P. A. Nwofe. *"Influence of deposition time on the properties of highly-oriented SnS thin films prepared using the thermal evaporation method"* in: Proceedings of 18th International Conference on Ternary and Multinary Compounds, (18 ICMTC), Salzburg, Austria, August 27–31, 2012, P08-P05, p. 125.

21. P. A. Nwofe, K. T. Ramakrishna Reddy and R. W. Miles. *"Type Conversion of p-SnS to n-SnS Using a $SnCl_4/CH_3OH$ Heat Treatment"* in: Proceedings of 39th IEEE Photovoltaic Specialists Conference, June 16-21, 2013

Glossary of Symbols

Symbol	Meaning	Unit
α	Optical absorption coefficient	cm^{-1}
AM	Air Mass	–
λ	Wavelength	μm or Å
CB	Conduction band	–
VB	Valence band	–
E_g	Energy bandgap	electron volt (eV)
$\underline{k}$	Crystal momentum	–
E_F	Fermi energy level	eV
V_{bi}	Built-in potential	V
E_i	Intrinsic Fermi energy level	eV
q	Electronic charge	coulombs (C)
k	Boltzmann constant	JK^{-1}
n_i	Intrinsic carrier density	cm^{-3}
N_A	Acceptor concentration	cm^{-3}
N_D	Donor concentration	cm^{-3}
N_B	N_A or N_D	cm^{-3}
E_V	Energy at the valence band	eV
E_C	Energy at the conduction band	eV
ϵ_s	Semiconductor permittivity	Fcm^{-1}
w	Depletion region width	μm
V_R	Reverse-biased voltage	V
V_F	Forward-biased voltage	V
ε_s	Static dielectric constant ($\varepsilon_s = \epsilon_s/\varepsilon_o$)	–

ε_o	Permittivity of free space	$\mathrm{Fcm^{-1}}$
C	Capacitance	F
C	Capacitance per unit area	$\mathrm{Fcm^{-2}}$
p_{no}	Equilibrium hole density in n-side	$\mathrm{cm^{-3}}$
p_{po}	Equilibrium hole density in p-side	$\mathrm{cm^{-3}}$
n_{po}	Equilibrium electron density in p-side	$\mathrm{cm^{-3}}$
n_{no}	Equilibrium electron density in n-side	$\mathrm{cm^{-3}}$
L_p	Minority carrier diffusion length of holes	μm
L_n	Minority carrier diffusion length of electrons	μm
D_n	Diffusion constant for electrons	$\mathrm{cm^2s^{-1}}$
D_p	Diffusion constant for holes	$\mathrm{cm^2s^{-1}}$
G_n	Carrier generation rate (electrons)	$\mathrm{cm^{-3}s^{-1}}$
G_p	Carrier generation rate (holes)	$\mathrm{cm^{-3}s^{-1}}$
μ_n	Electron mobility	$\mathrm{cm^2V^{-1}s^{-1}}$
μ_p	Hole mobility	$\mathrm{cm^2V^{-1}s^{-1}}$
kT	Thermal energy	eV
J_s or J_o	Saturation current density	$\mathrm{Acm^{-2}}$
τ_r	Recombination lifetime	s
τ_n	Electron minority carrier lifetime	s
τ_p	Hole minority carrier lifetime	s
A	Ideality factor	–
τ_g	Generation lifetime	s
χ	Electron affinity	eV
ϕ	Work function	eV
J_{oo}	Pre-exponential factor of J_s or J_o	$\mathrm{Acm^{-2}}$
$\mathrm{m_n}^*$	Electron effective mass	kg
Φ or E_a	Activation energy	eV
$(\phi_B)_n$	Barrier height, n-type side	V
$(\phi_B)_p$	Barrier height, p-type side	V
V_{oc}	Open circuit voltage	V

I_{sc}	Short circuit current	A
FF	Fill factor	%
I_L	Light generated current	A
V_{mp}	Voltage at maximum power point	V
I_{mp}	Current at maximum power point	A
P_{max}	Maximum power extracted from the solar cell	W
P_{in}	Incident illumination per unit area	Wcm^{-2}
η	Solar conversion efficiency or quantum efficiency	%
R_s	Series resistance	Ω
R_{sh}	Shunt resistance	Ω
N_{ph}	Incident photon flux	Wcm^{-2}
c	Speed of light in vacuum	ms^{-1}
EQE	External quantum efficiency	%
IQE	Internal quantum efficiency	%
ρ_s	Sheet resistivity	$\Omega\square^{-1}$
ρ_b	Bulk resistivity	Ωcm
CBM	Conduction band minimum	–
VBM	Valence band maximum	–
UNSW	University of New South Wales	–

Index